DOCTORAL SCHOOL IN CIVIL, ENVIRONMENTAL AND MECHANICAL ENGINEERING

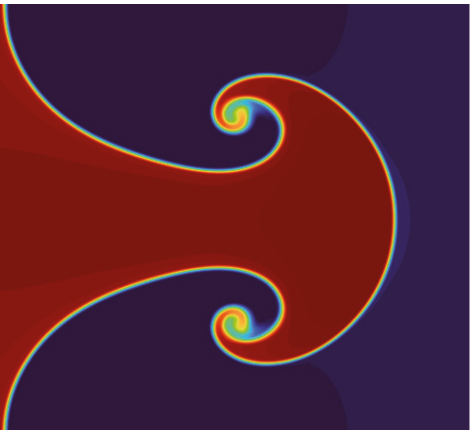

NUMERICAL METHODS FOR MULTIPHASE FLOWS: FROM A SIMPLIFIED INCOMPRESSIBLE BAER-NUNZIATO MODEL TO A UNIFIED THEORY OF COMPRESSIBLE MULTIPHASE FLUID AND SOLID MECHANICS

DAVIDE FERRARI

UNITN

Doctoral thesis in
Civil, Environmental, and Mechanical Engineering,
Cycle XXXVI

Departement of Civil, Environmental, and Mechanical Engineering
University of Trento
Academic year 2022/2023

Advisor **Prof. Dr.-Ing. Michael Dumbser**
Co-advisor **Prof. Dr. Ilya Peshkov**

University of Trento,
Trento, Italy,
January 2024

Ai miei genitori
A mia sorella Serena

Preface

This thesis has been developed during the three-year Doctoral program of the Doctoral School in Environmental Engineering at the Department of Civil, Environmental and Mechanical (DICAM) Engineering of the University of Trento.

The presented research was funded by the Italian Ministry of Education, University and Research (MIUR) in the frame of the Departments of Excellence Initiative 2018–2027 attributed to DICAM of the University of Trento (grant L. 232/2016) and in the frame of the PRIN 2017 project *Innovative numerical methods for evolutionary partial differential equations and applications.*

Most of the work was carried out in Trento supervised by Prof. Dr.-Ing. Michael Dumbser. In addition, for three months (September 2023 - November 2023) my work was carried out at the Institut de Recherche Mathematique Avancee (IRMA) of the Universite de Strasbourg with Dr. Andrea Thomann, thanks to which I obtained the *Doctor Europaeus* label.

Trento, January 2024

Davide Ferrari

Acknowledgements

This page is meant to sincerely thank the people who have helped me, in Science and in Life, during my doctoral studies.

I start by expressing my gratitude to my outstanding advisor Michael Dumbser, for his extreme helpfulness and patience in steering me in the right direction. I must thank him for all the opportunities he has given me, which have been a unique growth experience and through which he has introduced me to this world of research that I still can hardly believe I am a part of. It has been a pleasure to share results with him as videos and, above all, good bottles of wine.

I would also like to thank my second brilliant advisor Ilya Peshkov, who among the thousands of intriguing models he could formulate, still found the time and patience to explain even the most basic things, constantly showing interest and enthusiasm for the achievements of these PhD years.

A sincere thanks to Dr. Andrea Thomann for hosting me in Strasbourg in the warmest way, for spending a lot of time patiently reading my writings, for the interest she showed in my work and for the pleasant time we spent together in that almost German city.

Then, I would like to acknowledge Firas, for his extreme willingness to help and find a solution no matter what he is doing and for your firm belief in science, which is always inspiring. Thanks to Laura, for her empathic flair and for always being able to squeeze a smile out of even the most difficult situations, and Simone, for always being an inspiration with his genuine desire and enthusiasm to learn new things.

To the friends from the fourth and fifth floors that I have met in Mesiano over the years, especially Alessia, Cristian, Enrico, Olindo, Ilya, Elena, Saray, Simone, thank you.

Thanks to my life companions Niccolò and Valeria, and to all the friends I met over the years. (Sorry I don't have enough space, but thanks Angela).

Finally, the most heartfelt thanks go to my sister Serena, my mother Lidia and my father Giovanni, for always being unconditionally present and for (in the end) always supporting me in every possible aspect of my choices. To my mother, for being the kindest person I know and for her marvellous strength in holding everything together.

Contents

Abstract

In this thesis, I detail my contribution to the development of both the theoretical aspects of modelling compressible and incompressible multi-phase flows and the design of suitable numerical algorithms for solving such models. Currently, there is no universally accepted mathematical model to describe two-phase flows, consequently the extension to multi-phase flows (with more than two phases) is even less clear. A popular approach to describe two-phase flows is to use so-called homogenised mixture models, which are based on the diffuse interface approach. One of the most established ones is the Baer-Nunziato (BN) model. Due to its relatively simple mathematical structure, it is possible to derive reduced models, such as a model for incompressible two-phase flows, with straightforward assumptions. However, there are modelling and numerical reasons for the need to develop a mathematical model formulated in a well-defined mixture theory. Therefore, the derivation of a multi-phase and multi-material model within the framework of Symmetric Hyperbolic Thermodynamically Compatible (SHTC) theory and its numerical solution are of relevant interest in the work presented in this thesis.

Concerning the details of my research work, I begin by addressing the problem of a reduced BN-type model for incompressible two-phase flows. In incompressible models, the pressure acts as a Lagrange multiplier which ensures the divergence free condition of the velocity field. A natural numerical approach is to treat pressure-related terms implicitly, thus in this context two efficient mass and momentum conservative semi-implicit FV schemes for different applications are developed, e.g. for complex non-hydrostatic free surface flows, or for flows interacting with moving solid obstacles. These new numerical algorithms are implemented in a distributed memory MPI-parallel Fortran code. In addition, the semi-implicit discretisation adopted for the pressure subsystem, rather than a fully implicit one for the complete Partial Differential Equation (PDE) system, leads to a small-size, symmetric positive definite discrete linear system that can be solved efficiently with a preconditioned, matrix-free conjugate gradient method. This directly results in a much higher parallel scalability compared to fully implicit schemes.

A semi-implicit scheme boils down to the solution of a discrete linear system that takes into account the contributions of implicitly treated terms involved in the governing equations. As a result, understanding the numerical problems associated with the discretization of each term is more complex. Some of the numerical problems usually encountered in the numerical solution of compressible multi-phase model are related to the presence of complex interfaces described by the volume fraction of each phase. Therefore, to become more familiar with and better address these challenges, explicit schemes are considered. In particular, the numerical scheme initially adopted is an explicit second order FV method combined with the path-conservative technique of Castro and Pares for the treatment of the non-conservative products appearing in BN-type models. With the insights from this numerical scheme, the complete seven-equation BN model for compressible two phase flows is discretized. However, despite the variety of literature addressing this model, it still presents some problems, such as the fact that the model is not closed (in the sense that it requires the specification of an interface pressure and an interface velocity, the choice of which is not unique) and that it is not clear how to generalise the BN formulation to mixtures with an arbitrary number of phases. This is mainly due to the fact that the derivation procedure of the BN model is based on phenomenological and heuristic observations.

To overcome these problems, a model based on a well-defined mixture theory and derived from first principles as causality and the laws of thermodynamics is considered. This model can be written in a conservative form and, as formulated, is already generalised to an arbitrary number of constituents. It takes the form of a monolithic system of first order hyperbolic PDEs that include a unified multi-phase description of fluids and solids. The origins of this model go back to the SHTC theory of mixtures firstly proposed by Romenski for the case of two fluids, and then generalized to the case of an arbitrary number of constituents. Furthermore, the Eulerian hyperelasticity equations of Godunov and Romenski (GPR) are used to introduce viscous and elastic forces. These Eulerian equations of solid mechanics are characterised by algebraic relaxation source terms that are capable of extending the applicability of the model not only to elasto-plastic solids but also to viscous and inviscid fluid flows. Within this theoretical framework, a first order hyperbolic multi-phase model is formulated, by which compressible *Newtonian* and *non-Newtonian*, *inviscid* and *viscous fluids* as well as *elasto-plastic solids* can be described.

The question arises whether it is possible to compare the original BN model with the multi-phase model derived from SHTC theory. This can be done if the SHTC system is rewritten in terms of the equations of conservation of mass, phase momenta and phase energies. This structure can be referred to as form of Baer-Nunziato type. In addition, since the BN model is one of the most popular mathematical models for describing two-phase flow, there are many works that address it numerically. However, only a very limited number of publications exist on the mathematical and computational issues of BN models for multiphase flows describing more than two phases. Therefore, it is very interesting to numerically address the multi-phase BN-type type model derived from SHTC theory, which includes the challenges related to the GPR model of continuum mechanics. The resulting BN-type form is given by a large non-linear PDEs system, which includes highly non-linear stiff algebraic source terms as well as non-conservative products. In this thesis, a simplified version of the SHTC BN-type model is addressed numerically, neglecting the phase pressure relaxation, the temperature relaxation and assuming the absence of phase transformations. The differente challenges presented by the model are tackled by adopting a source operator splitting. The homogeneous part of the PDE system is discretized with a MUSCL-Hancock finite volume scheme using a primitive variable reconstruction and positivity preserving limiting, combined with a path-conservative technique to deal with the non-conservative products. Furthermore, the scheme employs semi-analytical time-integration methods for the stiff source terms governing the various relaxation processes.

Concerning the applicability of the models presented in this thesis for the solution of different problems, the resulting aforementioned semi-implicit algorithms for the BN models are first validated on a set of classical incompressible Navier-Stokes test problems and subsequently also by adding a fixed and moving solid phase. Most importantly, however, in this thesis I provide results for complex flows resulting from the interaction of three different phases including gases, liquids and solids. Therefore, results are shown for multiphase flows in the limit behaviour of the Newtonian inviscid and viscous fluid, as well as in the limit of nonlinear hyperelasticity for phases behaving as elastic and elasto-plastic solids. In both cases the numerical results are comparable with results obtained from established standard models, i.e. the Euler or Navier-Stokes equations for fluids, or the classical hypo-elastic model with plasticity, but, notably, everything within a unified multi-phase model of continuum mechanics.

1 Introduction

Multi-phase flows are very common both in nature as well as in human endeavours. Clouds are liquid droplets moving in a gas. At the earth's surface, solid particles are driven by interaction with air or water, shaping the morphology of the environment. Moreover, in the subsurface, gaseous and liquid phases coexist in solid layers, or, as in the Earth's mantle, solid phases with different properties interact. In the context of human activities, heat transfer by boiling is the core of the energy industry and involves the nucleation, growth and coalescence of gas bubbles and the interaction of this gas with moving solid surfaces such as turbines. Chemical processes involve the mixing, transformation and sedimentation of different phases. In addition, on a small scale, drops and sprays or on a larger scale flows interacting with nautical, civil or energy engineering structures such as ships, bridges, wind or hydroelectric turbines are some examples of phenomena that can be described through a multiphase approach. The widespread occurrence of multi-phase flows in various environmental phenomena, scientific and engineering disciplines as in many industrial applications highlights the need to develop a general mathematical description as well as suitable numerical methods for understanding their behaviour.

One way to describe the behaviour of multiphase flows is to follow the details of the evolution of each component of the mixture and all of their interfaces. However, this solution is often not feasible. For example, a suspension of uniformly shaped rigid particles in a liquid constitutes a very simple two-phase mixture. It is possible to define an initial-boundary-value problem for such a mixture that would only turn out to be a complicated problem in mechanics. However, just defining the initial conditions would consist of an unreasonable amount of information that makes this approach impractical.

Furthermore, in an analogy to gas dynamics, much more sophisticated models exist, oriented towards molecular dynamics eg. [90, 91, 159], or the direct Monte Carlo simulation of gas flows [62, 126, 139, 140]. However, although they have important specific applications, they are computationally too demanding for many practical purposes, in particular at large spatial and temporal scales. It is therefore necessary to develop models at the continuum level, such as the Navier-Stokes equations. These models, in turn, are often supplemented with large eddy models [75, 107, 118, 176] or coarser-scale turbulence models [22, 57] in order to account for phenomena that are not directly solved and to be applicable to the solution of real engineering problems.

Similarly for multi-phase flows, following the details of the evolution of each component of the mixture and all interfaces would be computationally too onerous as well as impractical. In this sense, the practical need for a macroscopic model through a continuum description is undeniable.

A primary task in studying the behaviour of continuous media is the definition of appropriate conservation and balance laws. These consist at least of mass, momentum and energy conservation. In addition, entropy considerations are relevant in order to respect the second law of thermodynamics. However, in the literature, the formulation of conservation laws for multiphase flows has been a controversial topic and so far there is no universally accepted procedure for deriving them in a closed form. Furthermore, past and current research efforts in relation to multiphase flow modelling mostly focus on two-phase models, consequently the extension to multi-phase flows is even less clear.

In this sense, these modelling difficulties will be highlighted in this thesis. By numerically dealing with one of the most historically established models, the two-phase Baer-Nunziato (BN) model [3], it will be clear that there are modelling and numerical reasons for the need to develop a mixture model formulated within a proper mathematical framework of continuum mechanics. The main objective of this work therefore becomes the development and numerical solution of a set of hyperbolic partial differential equations capable of describing a generic multi-phase and multi-material continuum in a unified manner, within the framework of Symmetric Hyperbolic Thermodynamically Compatible (SHTC) theory. In the following section, we briefly describe the approaches generally used in the literature and the problems associated with their closure, in contrast with the advantages of formulating a mixture theory within the SHTC continuum mechanics.

1.1 A continuum approach for multi-phase mixtures

In this thesis, we will focus on a description of multi-phase flows from a macroscopic point of view, i.e. through a continuum description. The description of fluids and solids as continuous media is achieved through the conservation and equilibrium laws for mass, momentum and energy. These laws are used to state the governing equations of the medium as a function of time, within a common mathematical framework established in the 19th century by, among others, Cauchy, Navier, Poisson, Laplace, Stokes, Newton and Euler. However, fluids and solids are generally recognised as different states of matter and studied by two distinct communities, using different approaches. The Eulerian description is most commonly used to describe the field of motion of a fluid, as fluids usually undergo large deformations that are not suitable for a Lagrangian description, while in solid mechanics the Lagrangian description is preferred in order to write the force balance equations on a body, since the stress tensor in a solid depends on the deformation of the medium that is readily available within the Lagrangian framework.

Multiphase flows, i.e. flows of several interacting continua, represent the point at which these two different approaches have to be combined. For instance, some applications employ two or more different models, one for each of the phases involved, with additional coupling rules governing the interaction between the different media. However, it is clear that abandoning the distinction between solids and fluids in favour of adopting a unified continuum mechanics model (UMCM) would yield advantages in a continuum formulation of multiphase flows.

1.1.1 On the classical formulation of conservation laws for multi-phase flows

Theories of multi-phase mixtures stem from the early work of C. Truesdell (1957) [173], who transposed the kinetic theory for gas mixtures, given by Maxwell [108], into a form appropriate for a continuum theory. In fact, underlying multiphase theories is the same concept introduced by Truesdell for gas mixtures, according to which a mixture can be represented by "a sequence of bodies $\mathcal{B}_k$, all of which... occupy regions of space... simultaneously". Thus, the phases are treated as interpenetrating continua and a theory describing them should have a mathematical structure that accounts for the macroscopic phenomena associated with the heterogeneous nature of the mixture.

A first rational treatment of a continuum theory for heterogeneous materials was that of Goodman and Cowin [86], who presented a model for a single-phase granular material with a void in the interstices. They noticed that there are two reasonable definitions of mass density in this case. The bulk density ϱ_s is the ratio of the mass of the sample to the total volume of the sample, while the material density ρ_s is the ratio of mass of the grains to the volume occupied by the grains. The ratio $\alpha_s = \varrho_s/\rho_s$ of these two quantities is the definition of the solid *volume fraction*. The concept of volume fraction quickly became the basic notion for modelling the presence of several components in a continuous multiphase mixture description.

The work presented by Goodman *et al.* has prompted great interest in the development of continuum theories of mixtures, and it is difficult, if not impossible, to account for all the contributions in the literature. However, it is interesting to mention that the derivation of conservation laws, and their final form, has been a controversial topic. Two techniques for deriving the balance equations have been employed, which can be referred to as *averaging* and *postulation* respectively.

The *postulation* approach is adopted in the context of a continuum multiphase mixture theory. An essential step towards the development of such a theory was presented by Passman [128], and stems directly from the axioms laid down by Truesdell [173]. The three main principles are the "Metaphysical Principles":

1. all properties of the mixture must be mathematical consequences of properties of the constituents;
2. to describe the motion of a constituent, we can conceptually isolate it from the rest of the mixture, provided that the actions of the other constituents on it are taken into account;
3. the motion of the mixture is governed by the same equations as for a single body.

Subsequently, this theory was further developed by various authors, e.g. Nunziato and Walsh [122] made modifications taking into account the physical notion that the volume fraction associated with the mixture is the sum of the volume fractions of the constituents, and the constraint that arises if the mixture is saturated. Within this mixture theory the conservation laws are postulated following for each phase the balance principles of continuum mechanic, taking also in account for interaction between phases, i.e. the exchange of mass, momentum and energy. Furthermore, the conservation of mass, momentum and energy are required for the overall mixture and this imposes constraints on the interactions between the phases. It should be specified that much of the work in these articles relates to the formulation of specific closure relationships that satisfy the principles of thermodynamics for two-phase flows of reactive granular materials, see e.g. [3, 58, 136] and references therein.

Another interesting approach for the derivation of conservation laws involves overcoming the discrete nature of the phases that constitute a multiphase mixture through the use of averaging techniques. Within *averaged* approaches, see e.g. [48, 93, 119], the balance equations of each constituent are derived by applying an averaging operation to the equations of motion for different continua separated by an interface across which the densities, velocities, etc., may jump. This integration is done through the use of a component indicator function X_a. This is a concept closely related to the volume averaging process, in fact the average of $\bar{X}_a$ is the average fraction of occurrences of phase component a at point $\mathbf{x}$ and at time t, and this averaged quantity corresponds to what is usually called the volume fraction α_a. This approach using averaged equations for two-phase flows can also be found in a more recent work by Abgrall and Saurel [152].

Furthermore, it should be noted that this controversy concerning the derivation of conservation laws has been overcome in Drew and Passman's book [47] where one of the main results presented is that averaging and postulation give essentially the same results, while the correct prescription of the constitutive closure is the crucial issue. The averaged equations have the same form as those postulated in mixture theories, and can be represented, with minor differences, by the following system of balance laws for each phase constituent a, consisting of the phase conservation of mass, momentum and internal energy,

$$\begin{aligned} &\partial_t(\alpha\rho)_a + \nabla \cdot (\alpha\rho\mathbf{v})_a = \Gamma_a, \\ &\partial_t(\alpha\rho\mathbf{v})_a + \nabla \cdot (\alpha\rho\mathbf{v} \otimes \mathbf{v} - \alpha\mathbf{T})_a = \mathbf{M}_a + \Gamma_a\mathbf{v_a}, \\ &\partial_t(\alpha\rho e)_a + \nabla \cdot (\alpha\rho e\mathbf{v} - \alpha\mathbf{T}\cdot\mathbf{v} + \alpha\mathbf{q})_a = E_a + \mathbf{M}_a\mathbf{v_a} + \Gamma_a e_a, \end{aligned} \tag{1.1}$$

where $\alpha_a, \rho_a, \mathbf{v}_a, e_a, \mathbf{T}_a, \mathbf{q}_a$ are the volume fraction, density, velocity field, internal energy, stress tensor and thermal impulse of each phase, respectively. The terms on the right hand side (RHS), $\Gamma_a, \mathbf{M}_a, E_a$ are, respectively, the rate of production of mass, due to phase change or chemical reaction, the momentum and the energy source to phase a due to interactions or exchanges among constituents. Furthermore, this system is usually coupled with the following constraints

$$\sum_a \Gamma_a = 0 \qquad \sum_a \mathbf{M}_a + \Gamma_a\mathbf{v_a} = 0 \qquad \sum_a E_a + \mathbf{M}_a\mathbf{v_a} + \Gamma_a e_a = 0 \tag{1.2}$$

in order to retrieve the classical mass, momentum and energy balance equations for the mixture. The previous system (1.1) must be supplemented with equations of state, constitutive equations, and boundary and initial conditions to be a *determined system.* Equations of state specify the thermodynamic state of the material in the usual sense. The constitutive equations specify the behaviour of the individual phases and their interaction with each other, and it is in their definition that the complexity of formulating conservation laws for multiphase flows lies.

In an analogy to the Navier Stokes equations of single phase flows, once a constitutive equation is postulated, for example assuming that the stress is a linear function of the strain rate, there are exact solutions to the equations of motion, as in the case of Couette flow, that allow the viscosity to be measured and thus characterise a fluid. For multiphase flows, there are almost no exact solutions or theorems on asymptotic behaviour for slow or other specific flows. One can compare only with the few existing experimental data [153] or with molecular dynamics [90]. Therefore, determining the constants or functions governing the constitutive equations is a subtle and complex task, and other techniques must be considered, for example remembering that correct physical theories must be built on an adequate mathematical basis. This means that the development of the constitutive equations can be aided by "principles", see [38, 174], such as

1. *well-posedness* of the initial value problem (IVP),
2. *separation of components*, which means that a variable expressing a phase self-interaction depends only on the variables associated with that phase,
3. *frame indifference* which states that the constitutive equations cannot depend on the reference frame.

These provide rational means to formulate constitutive equations without inadvertently neglecting important dependencies and without including irrational dependencies. Thus, the first step consists of defining vector and tensor quantities that are objective i.e. frame-indifferent for each phase or component of the mixture. Let 's consider a mixture of N phases $a = 1, \dots, \mathrm{N}$, then the phase velocities $\mathbf{v}_a$ are not frame-independent, but by means of the mixture velocity $\mathbf{v}$ the relative phase velocities can be defined as $\mathbf{w}_a = \mathbf{v}_a - \mathbf{v}$, which are objective quantities. The relative phase accelerations are denoted by $\mathbf{a}_a$, and the phase strain tensor $\mathbf{D}_a$ and the relative one $\mathbf{W}_a$ are objective quantities as well, and read

$$\mathbf{D}_a = \frac{1}{2}(\nabla \mathbf{v}_a + (\nabla \mathbf{v}_a)^{\mathsf{T}}), \qquad \mathbf{W}_a = \frac{1}{2}(\nabla \mathbf{v}_a - (\nabla \mathbf{v})^{\mathsf{T}}). \tag{1.3}$$

Let's consider the definition of the momentum source $\mathbf{M}_a$ due to interactions or exchanges among constituents for the phase a. It is a frame-indifferent vector-valued function, hence can be defined as a function of the objective vectors $\mathcal{V}_a = (\nabla \alpha, \nabla \rho, \nabla p, \nabla T, \mathbf{w}, \mathbf{a})_a$ and the tensors $\mathcal{T}_a = (\mathbf{D}, \mathbf{W})_a$ for $a = 1, \dots, \mathrm{N}$ and in which p_a, T_a are the phase pressure and the temperature. Then $\mathbf{M}_a$ must have the form

$$\mathbf{M}_a = \sum_{a=1} \mathrm{N} \sum_{i=1}^{n} A_{a,i} \mathcal{V}_{a,i} + \sum_{a=1} \mathrm{N} \sum_{i=1}^{n} \sum_{j=1}^{m} (B_{a,i,j} \mathcal{V}_{a,i} \cdot \mathcal{T}_{a,j} + C_{a,i,j} \mathcal{T}_{a,j} \cdot \mathcal{V}_{a,i}), \tag{1.4}$$

where n and m are the dimensions of the two previously defined objective vectors $\mathcal{V}_a, \mathcal{T}_a$ respectively. Thus, in order to close the theory all the scalar coefficients $A_{a,i}, B_{a,i,j}, C_{a,i,j}$ have to be specified. This is usually done by imposing the constraints defined in (1.2), and requiring that the constitutive equations satisfy the appropriate entropy inequalities. However, it is clear that this is a complex task. The problem can be reduced by considering a first-order theory, thus only considering terms that have first-order derivatives in space or time, but still a considerable number of dependencies must be determined.

At this point, the complexity inherent in this formulation of conservation laws for multi-phase flows is evident, which explains why closed models can only be found in the literature for application-specific two-phase flows, see eg. deflagration-to-detonation transition (DDT) in gas-permeable, reactive granular materials [3, 7, 58] and spray modelling [40].

1.1.2 A unified multi-phase model of continuum mechanics

As we have seen, the main challenge in formulating multiphase flow models is associated with the formulation of a closed model that satisfies *a priori* important physical and mathematical properties. This is inherently very complicated, however, unlike classical approaches, through the theory of Symmetric Hyperbolic Thermodynamic Compatible (SHTC) systems of conservation law, it is possible to formulate a model of continuum mechanics based *ab initio* on universally accepted fundamental physical principles, such as the principles of invariance, conservation principles, the principle of causality, the laws of thermodynamics and the well-posedness of the IVP.

The origin of the SHTC formulation of continuum mechanics can be attributed to the work of Godunov [77], who considered "an interesting class" of nonlinear conservation laws. The main motivation for this seminal work was the desire to understand how to ensure the *well-posedness* of the IVP for a nonlinear system of time-dependent PDEs, which should be regarded as a fundamental physical observation on the time evolution of physical systems. The inference is that the only possibility is to deliberately develop the model within the subclass of symmetric first-order hyperbolic PDE systems. Moreover, already in this [77] and subsequent works [79, 81] it was shown that there is an intimate connection between the symmetric hyperbolicity and thermodynamics. In particular, this specific subclass of systems of conservation laws can be written in symmetric hyperbolic Godunov form, and can be shown to satisfy both the first principle of thermodynamics (the law of conservation of total energy) and the second principle of thermodynamics (the entropy inequality).

Within this mathematical framework, it is possible to derive a theory for multiphase flows. The SHTC theory of mixtures was first proposed by Romenski in [149, 150] for the case of two fluids. It was then further developed in a series of works [144–146] and it was generalized to the case of arbitrary number of constituents in [143]. Recently, various numerical schemes were developed to solve the two-fluid SHTC equations, e.g. semi-implicit all-Mach number schemes were developed in [104, 105], high-order discontinuous Galerkin and finite-volume schemes in the ADER framework were developed in [141], a thermodynamically compatible discretization was proposed in [168], and detailed solutions of the Riemann problems for the barotropic two-fluid SHTC equations were studied in [167].

An early product of the very general SHTC formalism is the *unified model of continuum mechanics* introduced by Godunov and Romenski in [80, 82–84] as an hyperbolic Eulerian formulation of elasticity, rather than the Lagrangian framework more commonly adopted in solid mechanics. In [131], Peshkov and Romenski, presented the key insight that the Godunov–Romenski model may be applied not only to elasto-plastic solids, but to fluid flows too. This model, which represents a unified description of fluids and solids, takes the form of a monolithic first order hyperbolic system of PDEs, i.e. all signals propagate in space by means of finite speed waves and each of the system's partial differential equations is first order in space and time. Several numerical schemes have recently been developed to model elasto-plastic solids, e.g. [5, 12, 16, 63, 64, 74], and viscous or inviscid fluids [34, 54, 55, 94, 95], with this modelling approach, however, almost always only one phase is considered. The mathematical model and its many variants have been referred to differently in these various contexts, from Hyperbolic-Peshkov-Romenski (HPR) or Godunov-Peshkov-Romenski (GPR) in [54, 55] to unified model of continuum mechanics (UMCM) in [12]. In this thesis, we adopt the generic terminology Unified Continuum Mechanics Model, or when appropriate for brevity UMCM or GPR.

The unified multi-phase model of continuum mechanics object of this thesis work is derived, as a whole, from *variational principles* and geometrical constraints within the formalism of SHTC systems, following the work of Peshkov *et al.* [132] where the variational nature of the SHTC equations is extensively highlighted. Within this theoretical framework, in order to obtain the equations for a specific medium, it is necessary to identify state variables and to define a thermodynamic potential as a function of these variables. Considering a mixture of N constituents denoted by latin indices a, where $a = 1, \dots, \mathrm{N}$ enumerates the phases, the vector of sought SHTC state variables is

$$\mathbf{Q} = \{\boldsymbol{U}, \mathbf{A}, \rho, \boldsymbol{w}_1, \dots, \boldsymbol{w}_{\mathrm{N}-1}, \varphi_1, \dots, \varphi_{\mathrm{N}-1}, \varrho_1, \dots, \varrho_{\mathrm{N}-1}, \eta_1, \dots, \eta_{\mathrm{N}}\}^{\mathsf{T}}, \tag{1.5}$$

where $\boldsymbol{U}$ is a vector field with the meaning of the mixture momentum, $\mathbf{A}$ is a three by three non-symmetric matrix called *distortion field* or *cobasis* of the mixture, $\boldsymbol{w}_1, \dots, \boldsymbol{w}_{\mathrm{N}-1}$ are the relative velocities of each phase which are defined with respect to the N-th constituent that can be chosen arbitrary, φ_a, ϱ_a and η_a are scalar quantities defined as follows $\varphi_a = \rho\alpha_a, \varrho_a = \rho c_a, \eta_a = \varrho_a s_a$ where α_a, c_a, s_a are the volume fraction, mass fraction and specific entropy of the a-th phase, respectively.

Then, once also a thermodynamic potential is defined as a function of these variables, a first order hyperbolic multi-phase model can be formulated, which satisfies both the first and the second principles of thermodynamics and by which compressible *Newtonian* and *non-Newtonian*, *inviscid* and *viscous fluids* as well as *elasto-plastic solids* can be described.

1.1.3 A comparison of the two approaches

In this brief introduction we have seen, in 1.1.1, that the standard approach of deriving governing equations for multiphase flows leads to a system of governing equations in the form of mass, momentum and energy balance laws for each phase. Then, the phase interactions are described with both differential interaction terms and non-differential source terms that are usually unknown, and their rigorous formulation requires complex additional considerations. The model originally introduced in the context of reactive granular materials by Baer and Nunziato in [3] is one of the most prominent which follows this approach. Nowadays, it is usually referred to a simplified form, for compressible two-phase flows, in which it is assumed that the interaction between the constituents is given only by contributions proportional to the volume fraction gradients of the phases through two so-called interphase pressure and velocity coefficients, see e.g. the following recent works [2, 52, 138, 152, 156] and references therein.

In 1.1.2, we pointed out that a unified multiphase model of continuum mechanics can be formulated within the SHTC systems formalism. More precisely, a mixture can be uniquely described through an appropriate choice of a vector of state variables (1.5) and defining a thermodynamic potential as a function of these variables. It can be seen that the vector of sought SHTC state variables differs from that usually adopted in the classical formulation of conservation laws for multiphase flows. Thus, the governing equations in SHTC theory describe the evolution of different quantities.

The question therefore arises as to whether it is possible to compare these two approaches. This can be done if the SHTC system is rewritten in terms of the equations of conservation of mass, momentum and phase energy. This structure is referred to in the following as *Baer-Nunziato type form* (BN-type form). In this work, the BN-type form of the SHTC mixture model will be derived, and naturally a closed form of the model will be obtained, where the interactions between the constituents are automatically well defined. Initially, this rewriting of the SHTC system will be done by excluding the evolution equation for the mixture distortion field $\mathbf{A}$, since the rigorous derivation of the several distortion fields relating to each phase, which is necessary in a classical description of the mixture through the quantities describing the individual constituents, is not available so far. Then, assuming that the single mixture distortion field can be described through various phase-related distortion fields $\mathbf{A}_a$, by analogy we consider an evolution equation for each of these matrix value fields. In a simplified view, this model can also be seen as an extension of the multi-phase theory of mixtures proposed by Romenski [143] augmented with GPR theory. However, while this simplified, practical viewpoint is correct for this BN-type form of the SHTC mixture model, it is not correct for the SHTC model derived as a whole from variational principles.

1.2 Systems of balance laws

Conservation laws are fundamental to the understanding of the physical world, as they describe which processes can or cannot occur in nature. In physics, a conservation law states that a specific measurable quantity of an isolated system does not change as the system evolves over time. In particular, in continuum mechanics, local balance laws are usually expressed mathematically by systems of PDEs which has the following general structure

$$\partial_t \mathbf{Q} + \nabla \cdot \mathbf{F}(\mathbf{Q}, \nabla \mathbf{Q}) + \mathbf{B}(\mathbf{Q}) \cdot \nabla \mathbf{Q} = \mathbf{S}(\mathbf{Q}). \tag{1.6}$$

Exact solutions to these differential systems very rarely exist, so numerical analysis plays a central role in the development of robust and efficient numerical methods to find accurate solutions to these problems.

1.2.1 Explicit and semi-implicit schemes

The development of new numerical methods is closely tied to the nature of mathematical models. An interesting class of non-linear conservation laws, e.g. the Euler equations of gas-dynamics, is represented by *first-order hyperbolic* PDE systems, whose general structure is

$$\partial_t \mathbf{Q} + \nabla \cdot \mathbf{F}(\mathbf{Q}) = \mathbf{S}(\mathbf{Q}). \tag{1.7}$$

First-order hyperbolic PDE systems satisfy and imitate two important and closely related principles of nature. That is, information propagates by means of waves moving with *finite speed* and consequently the principle of *causality* is satisfied. In other words, causality can be seen as a consequence of the finite speed of propagation of information, in fact if waves originate from the interaction of matter (the interaction is the cause) it is reasonable to require that this interaction takes place in a finite physical space and that there exist zones that are sufficiently distant from the cause that they are not yet influenced by the interaction. These characteristics are also naturally reflected in the development of numerical methods. In the context of explicit numerical schemes, the concept of the finite speed of propagation of information is reflected in the so-called Courant–Friedrichs–Lewy (CFL) condition [39]. This is a necessary condition to ensure the stability of the time integration and expresses the maximum time step size Δt that can be adopted for a given mesh size Δx and a given numerical scheme. The underlying principle of the condition is that the numerical domain of dependence of any point in space and time must include the analytical domain of dependence, which can be related to the maximum signal propagation speed λ; this translates into the following inequality

$$\Delta t/\Delta x \leq \lambda, \tag{1.8}$$

which must be satisfied everywhere in the computational domain.

Considering hyperbolic-parabolic PDE systems, for instance the compressible Navier-Stokes equations, whose general structure is represented in (1.6), a similar time restriction can be derived in the case of explicit numerical integration. However, in this case, the proportionality between the time step and the mesh size is quadratic, $\Delta t \sim \Delta x^2$, and such a condition can become prohibitive on fine meshes, which is why implicit or semi-implicit schemes are needed. In general, solving nonlinear systems of PDEs using fully implicit schemes is computationally expensive, since strongly nonlinear algebraic systems with a huge number of unknowns and with rather high condition number must be solved. Therefore, the semi-implicit approach is a viable strategy to retain a *mild stability condition* and to increase computational efficiency.

On the other hand, the nature of PDE systems tends to change depending on the flow regimes that occur and this requires the design of different and specific numerical methods. These different flow regimes can be characterised by the *Mach number* $M = ||\mathbf{v}||/\mathrm{C}$, defined through the ratio of the flow velocity $\mathbf{v}$ to the sound speed C, which expresses the influence of compressibility on a flow field. The physical interpretation is that in the low Mach number regime the sound velocity, related to pressure waves, is much larger than the fluid velocity. Therefore, rapid pressure equalisation takes place and, as a result, density changes due to compression cannot occur and the fluid flow becomes incompressible in the limit.

Focusing for instance on compressible Navier–Stokes equations, with the aid of asymptotic analysis [98, 99, 114], it can be shown that in the low Mach number limit $M \to 0$ their counterpart are the incompressible Navier-Stokes equations, which are a hyperbolic-parabolic-elliptic PDE systems with infinite propagation rates. In this limit pressure results in a Lagrange multiplier that adapts itself to ensure the divergence free condition of the velocity field. A classical numerical approach consists of applying an operator splitting strategy to yield a hyperbolic dominated subsystem for the unknown velocities and an elliptic Poisson-type problem for the pressure [129, 160]. Various finite volume, finite difference and finite element methods have been developed for incompressible flows, see e.g. [8, 29, 30, 37, 88, 161] also in a hybrid form, in order to solve each subproblem with the most suitable scheme [23]. Furthermore, some of these algorithms have been extended to the weakly compressible and low Mach regimes [9, 112], and to all Mach number flows too [24, 127, 164], retaining a reasonable time step restriction that depends only on the velocity field, rather than on the sound speed.

1.3 Structure of the thesis

The remainder of the thesis is divided into four main parts, initially the various mathematical models are introduced or derived, then the numerical modeling aspects are discussed through the development of various numerical schemes closely related to the mathematical nature of the models, and finally ample space is devoted to the obtained numerical results. In detail, the structure is as follows.

In **Chapter 2**, the different mathematical modelling approaches adopted in this thesis for multiphase mixtures are presented. I illustrate the main features of the so-called BN model, from a brief characteristic analysis to a non-dimensional formulation for deriving the low Mach limit model, as done for the (isentropic) Euler equations in [98–100]. In the same chapter, I also describe how a unified multiphase model of continuum mechanics can be derived from variational principles and geometric constraints within the SHTC formalism [132]. Through this approach, the main problem of the classical formulation of conservation laws for multi-phase flows, inherent in the definition of a *closed* model generalised to an arbitrary number of constituents, is overcome. Furthermore these two approaches are compared by rewriting the SHTC model in a BN-type form.

Chapter 3 is entirely devoted to the derivation of various numerical methods, tailored to the different mathematical models addressed in this thesis. I introduce a novel staggered, semi-implicit, finite-volume method derived starting from the works of Casulli *et al.* [29, 51], for the solution of a simplified BN model. This method is the basis of a highly efficient Fortran MPI-parallel code that in terms of applicability is a step forward for the study of real-world problems related to complex non-hydrostatic free-surface flows interacting with solid moving obstacles.
A substantial part of this chapter is devoted to the development of a robust numerical scheme capable of addressing the various difficulties inherent in a unified theory of compressible multiphase fluid and solids mechanics. I detail the numerical techniques I adopted to address a reduced form of the BN-type SHTC model capable of describing a continuum consisting of up to three phases.

In **Chapter 4** provides and discusses an extensive collection of numerical experiments, with the aim of validating the numerical methods developed in this work, as well as providing some rather unique results related to the behaviour of multiphase flows for more than two phases, described through the unified model of fluid mechanics and compressible multiphase solids presented here. The computational results obtained in this thesis are published in [69, 70], and [71] is, at the time of writing of this manuscript, to be submitted for publication.

Finally, the **Chapter 5** list the main achievements of the work presented in this thesis and discuss future research directions regarding numerical algorithms and modelling perspectives provided within a unified theory of compressible multiphase fluid and solid mechanics.

2 Towards a unified theory of multiphase fluid and solid mechanics

This chapter is entirely devoted to the presentation and formulation of the mathematical models which will then be addressed numerically. The development of a multiphase model following the classical formulation presents difficulties that are inherent in the approach, as we have seen in Section 1.1.1. There is no attempt to provide an exhaustive and rigorous derivation of the governing equations of a mixture following this approach; such a task is beyond the scope of this thesis. However, it is useful to introduce and mathematically describe one of the most widely used and studied formulations for modelling compressible two-phase flow, namely the one originally proposed by Baer and Nunziato [3].

In this work, there are two main reasons for the introduction of this model. First, the BN model was the starting point of my research work on modeling and numerical solution of multiphase flows. In fact, through its non-dimensional formulation, the low Mach limit model was recovered. Moreover, by considering only rigid body motion for the solid phase, a reduced incompressible BN model is obtained, which, as we shall see, can be applied for the solution of complex non-hydrostatic free-surface flows interacting with moving solid bodies.

The second motivation is comparative; in fact, the need to adopt a formulation different from the classical one becomes apparent noting the modelling limitations associated with a rather simplistic definition of interphase terms and understanding the difficulties associated with generalization to the case of an arbitrary number of constituents. Therefore, ample space will be devoted in this chapter to formulating a theory of mixtures within the SHTC framework derived from variational principles [132]. This approach overcomes the main problem of the classical formulation of conservation laws for multiphase flows, inherent in defining a closed model generalized to an arbitrary number of constituents. However, a classical reformulation of the new SHTC model, i.e., considering the mathematical structure of the BN model, can be useful in practice to recognize and isolate terms associated with phase interactions and compare them with those already present in the original BN model.

2.1 The Baer-Nunziato equations of compressible two-phase flow

The Baer-Nunziato model is one of the most popular nonconservative models for two-phase flows. In its original formulation [3] it is a two-phase model specifically designed for applications describing the deflagration-to-detonation (DDT) transition in reactive, gas-permeable granular materials. However, nowadays this model is usually referred to by considering only the homogeneous part of the original system, i.e., without the algebraic phase interaction terms, see e.g. the following recent works [2, 52, 138, 152, 156]. This is equivalent assuming that the interaction between the constituents is given only by contributions proportional to the volume fraction gradients of the phases through two so-called interphase pressure and velocity coefficients. This simplification, in some sense, makes the model less specific and applicable to a wider range of two-phase flows, see. e.g. [49, 72] for a reduced model for free surface flows or [97] for the interaction of compressible fluids with solids. The complete seven-equation Baer-Nunziato model, without algebraic source terms, is a fist-order system of nonlinear PDEs, which reads

$$\begin{aligned}
&\partial_t(\alpha\,\rho)_a + \nabla\cdot(\alpha\,\rho\,\mathbf{v})_a = 0,\\
&\partial_t(\alpha\,\rho\,\mathbf{v})_a + \nabla\cdot(\alpha\,\rho\,\mathbf{v}\otimes\mathbf{v} + \alpha\,p\,\mathbf{I})_a = p_{\mathrm{I}}\,\nabla\alpha_a,\\
&\partial_t(\alpha\,\rho E)_a + \nabla\cdot(\alpha\,\rho\,\mathbf{v}\,E + \alpha\,\mathbf{v}\,p)_a = -p_{\mathrm{I}}\,\partial_t\alpha_a,\\
&\partial_t\alpha_a + \mathbf{v}_{\mathrm{I}}\cdot\nabla\alpha_a = 0
\end{aligned} \tag{2.1}$$

where the subscript a denotes each phase, thus in this two-phase model $a = 1, 2$; ρ_a is the mass density, $\mathbf{v}_a = (v_{a,1}, v_{a,2}, v_{a,3})^{\intercal}$ the velocity vector, p_a the pressure and E_a the total energy per unit mass and α_a the volume fraction of each phase a, respectively. Furthermore, the model requires a proper choice of the interface velocity $\mathbf{v}_{\mathrm{I}}$ and the interface pressure p_{I}. Baer and Nunziato, in their original work, proposed the following choice

$$\mathbf{v}_{\mathrm{I}} = v_2, \qquad p_{\mathrm{I}} = p_1, \tag{2.2}$$

where, since in this work the model describes flame propagation in gas-permeable granular solids, the two phases considered are a gaseous and a solid one; in this order we are denoting them with subscripts 1 and 2, respectively. Thus, these assumptions are equivalent to assuming the interphase pressure p_I equal to that of the most compressible phase and the interphase velocity $\mathbf{v}_{\mathrm{I}}$ corresponding to the velocity of the least compressible phase, that is, the solid phase, phase 2. Another choice of p_{I} and $\mathbf{v}_{\mathrm{I}}$ will lead to a different mathematical model. It should also be noted that the volume fractions α_a

must satisfy the saturation constraint, i.e., $\alpha_1 + \alpha_2 = 1$, therefore, it is clear that formally the nonconservative convection equation for the second volume fraction function, in (2.1), must be excluded from the system of PDEs since it is equivalent to that for phase 1. In order to close the system (2.1), we need to provide additional relations, namely the equations of state (EOS) for each phase. For instance, an ideal EOS for the gas phase and a stiffened EOS for the solid phase can be chosen

$$e_1 = \frac{p_1}{\rho_1(\gamma_1 - 1)}, \qquad e_2 = \frac{p_2 + \gamma_2 \pi_2}{\rho_2(\gamma_2 - 1)}, \tag{2.3}$$

where e_1, e_2 are the specific internal energies, γ_1, γ_2 are the specific heat ratios of the gas and solid phases, respectively, and π_2 is a known constant.

From a modelling perspective, it is easy to see how the BN model (2.1) reflects the structure outlined in (1.1), and it is essentially formulated as a system of two Euler sub-systems, with extra terms describing the interaction of the two constituents. Therefore each phase has its own pressure, velocity and temperature, which is why it is said to be a full non-equilibrium model. Moreover, the interphase terms are defined in a very simplified form, compared to the form of interphase terms presented in (1.4) where all combinations of the vector and tensor quantities that are objective are considered. In (2.1) the interaction between the constituents is given only by contributions proportional to the volume fraction gradients $\nabla \alpha_a$ of the phases through two so-called interphase pressure p_{I} and velocity $\mathbf{v}_{\mathrm{I}}$ coefficients.

2.1.1 Characteristic analysis

The characteristic analysis of the BN model was comprehensively studied by Embid and Baer [58]. Therefore, here we will only briefly present the results. As a consequence of the presence of the differential interaction terms, the overall system of governing equations (2.1) cannot be written in divergence form. The system is said to be non-conservative, and the phase interaction terms are called non-conservative terms. Defining the state variable vector $\mathbf{Q}$ as

$$\mathbf{Q} = (\, \alpha_1 \rho_1,\ \alpha_1 \rho_1 \mathbf{v}_1{}^{\mathsf{T}},\ \alpha_1 \rho_1 E_1,\ \alpha_2 \rho_2,\ \alpha_2 \rho_2 \mathbf{v}_2{}^{\mathsf{T}},\ \alpha_2 \rho_2 E_2,\ \alpha_2 \,)^{\mathsf{T}}, \tag{2.4}$$

the governing PDE system (2.1) can be written in compact matrix-vector notation as

$$\partial_t \mathbf{Q} + \nabla \cdot \mathbf{F}(\mathbf{Q}) + \mathbf{B}(\mathbf{Q})\, \nabla \mathbf{Q} = \mathbf{0}, \tag{2.5}$$

where $\mathbf{F}(\mathbf{Q})$ is a non-linear conservative flux tensor and $\mathbf{B}(\mathbf{Q})\,\nabla\mathbf{Q} = \mathbf{B}_i\,\partial_{x_k}\mathbf{Q}$, with $k = 1,\ 2,\ 3$, represent the non-conservative products, and read

$$\mathbf{F}(\mathbf{Q}) = \begin{pmatrix} \alpha_1\,\rho_1\,\mathbf{v}_1 \\ \alpha_1\,(\rho_1\,\mathbf{v}_1 \otimes \mathbf{v}_1 + p_1\,\mathbf{I}) \\ \alpha_1\,\left(\rho_1\,E_1 + p_1\right)\,\mathbf{v}_1 \\ \alpha_2\,\rho_2\,\mathbf{v}_2 \\ \alpha_2\,(\rho_2\,\mathbf{v}_2 \otimes \mathbf{v}_2 + p_2\,\mathbf{I}) \\ \alpha_2\,\left(\rho_2\,E_2 + p_2\right)\,\mathbf{v}_2 \\ 0 \end{pmatrix}, \quad \mathbf{B}(\mathbf{Q})\,\nabla\mathbf{Q} = \begin{pmatrix} 0 \\ -p_1\,\nabla\alpha_1 \\ -p_1\,\mathbf{v}_2\cdot\nabla\alpha_1 \\ 0 \\ +p_1\,\nabla\alpha_1 \\ +p_1\,\mathbf{v}_2\cdot\nabla\alpha_1 \\ \mathbf{v}_2\cdot\nabla\alpha_2 \end{pmatrix}. \tag{2.6}$$

The PDE system (2.1) can also be rewritten in the following quasi-linear form in terms of the conservative variables $\mathbf{Q}$

$$\partial_t\mathbf{Q} + \mathbf{A}(\mathbf{Q})\,\nabla\mathbf{Q} = \mathbf{0}, \tag{2.7}$$

with

$$\mathbf{A}(\mathbf{Q}) = (\mathbf{A}_1,\ \mathbf{A}_2,\ \mathbf{A}_3) = \frac{\partial\mathbf{F}}{\partial\mathbf{Q}} + \mathbf{B}(\mathbf{Q}), \tag{2.8}$$

while in terms of the vector of primitive variables $\mathbf{V}$

$$\mathbf{V} = \left(\,\rho_1,\ \mathbf{v}_1{}^{\mathsf{T}},\ p_1,\ \rho_2,\ \mathbf{v}_2{}^{\mathsf{T}},\ p_2,\ \alpha_2\,\right)^{\mathsf{T}}, \tag{2.9}$$

it can be rewritten as

$$\partial_t\mathbf{V} + \mathbf{C}(\mathbf{V})\,\nabla\mathbf{V} = \mathbf{0}, \tag{2.10}$$

with

$$\mathbf{C}(\mathbf{V}) = (\mathbf{C}_1,\ \mathbf{C}_2,\ \mathbf{C}_3), \qquad \mathbf{C}_k = \frac{\partial\mathbf{V}}{\partial\mathbf{Q}}\,\mathbf{A}_k\,\frac{\partial\mathbf{Q}}{\partial\mathbf{V}}. \tag{2.11}$$

To compute the eigenstructure of the system, and thus assess its hyperbolicity, we can consider the equations projected along a generic direction k specified by a unit vector $\hat{\mathbf{e}}_k$. This can be done, without loss of generality, due to the rotational invariance of the system (2.1); thus the matrix of coefficients appearing in (2.10) will be given by the following projection $\mathbf{C}_1 = \mathbf{C}\cdot\hat{\mathbf{e}}_1$, which results

$$\mathbf{C}_1 = \begin{pmatrix} v_{1,1} & \rho_1 & 0 & 0 & 0 & 0 & 0 & 0 & 0 & 0 & \frac{\rho_1\,\Delta u}{\alpha_1} \\ 0 & v_{1,1} & 0 & 0 & 1/\rho_1 & 0 & 0 & 0 & 0 & 0 & 0 \\ 0 & 0 & v_{1,1} & 0 & 0 & 0 & 0 & 0 & 0 & 0 & 0 \\ 0 & 0 & 0 & v_{1,1} & 0 & 0 & 0 & 0 & 0 & 0 & 0 \\ 0 & \rho_1\,a_1^2 & 0 & 0 & v_{1,1} & 0 & 0 & 0 & 0 & 0 & \frac{\rho_1\,a_1^2\,\Delta u}{\alpha_1} \\ 0 & 0 & 0 & 0 & 0 & v_{2,1} & \rho_2 & 0 & 0 & 0 & 0 \\ 0 & 0 & 0 & 0 & 0 & 0 & v_{2,1} & 0 & 0 & 1/\rho_2 & \frac{\Delta p}{\alpha_1\,\rho_2} \\ 0 & 0 & 0 & 0 & 0 & 0 & 0 & v_{2,1} & 0 & 0 & 0 \\ 0 & 0 & 0 & 0 & 0 & 0 & 0 & 0 & v_{2,1} & 0 & 0 \\ 0 & 0 & 0 & 0 & 0 & 0 & \rho_2\,a_2^2 & 0 & 0 & v_{2,1} & 0 \\ 0 & 0 & 0 & 0 & 0 & 0 & 0 & 0 & 0 & 0 & v_{2,1} \end{pmatrix}, \quad (2.12)$$

where $\Delta u = (u_{2,1} - u_{1,1})$ and $\Delta p = (p_2 - p_1)$, while a_1, a_2 are the sound speeds of the gas and solid phases, respectively, and can be calculated according to each EOS as follows

$$a_1 = \sqrt{\gamma_1\,p_1/\rho_1}, \qquad a_2 = \sqrt{\gamma_2\,(p_2 + \pi_2)/\rho_2}. \quad (2.13)$$

The following eigenvalues $\boldsymbol{\lambda}$ can be computed for the matrix $\mathbf{C}_1$

$$\begin{aligned} &\lambda_1 = u_1 - a_1, \quad \lambda_2 = \lambda_3 = \lambda_4 = u_1, \quad \lambda_5 = u_1 + a_1, \\ &\lambda_6 = u_2 - a_2, \quad \lambda_7 = \lambda_8 = \lambda_9 = u_2, \quad \lambda_{10} = u_2 + a_2, \\ &\lambda_{11} = u_2. \end{aligned} \quad (2.14)$$

Therefore, since all eigenvalues (2.14) are real, system (2.1) is hyperbolic; the right eigenvectors of $\mathbf{C}_1$, corresponding to these eigenvalues are

$$\mathbf{R}_1 = \begin{pmatrix} 0 & 0 & 0 & 0 & 0 & 0 & 0 & 0 & 0 & 0 & 1 \\ 0 & 0 & 0 & 0 & 0 & \rho_2 & 1 & 0 & 0 & \rho_2 & 0 \\ 0 & 0 & 0 & 0 & 0 & -a_2 & 0 & 1 & 0 & a_2 & 0 \\ 0 & 0 & 0 & 0 & 0 & 0 & 0 & 0 & 1 & 0 & 0 \\ 0 & 0 & 0 & 0 & 0 & 0 & 0 & 0 & 0 & 0 & 0 \\ 0 & 0 & 0 & 0 & 0 & \rho_2\,a_2^2 & 0 & 0 & 0 & \rho_2\,a_2^2 & -\frac{\Delta p}{\alpha_2} \\ \rho_1 & 1 & 0 & 0 & \rho_1 & 0 & 0 & 0 & 0 & 0 & \frac{\rho_1(\Delta u)^2}{\alpha_1\,(a_1^2-(\Delta u)^2)} \\ -a_1 & 0 & 0 & 0 & a_1 & 0 & 0 & 0 & 0 & 0 & \frac{-a_1^2(\Delta u)}{\alpha_1\,(a_1^2-(\Delta u)^2)} \\ 0 & 0 & 1 & 0 & 0 & 0 & 0 & 0 & 0 & 0 & 0 \\ 0 & 0 & 0 & 1 & 0 & 0 & 0 & 0 & 0 & 0 & 0 \\ \rho_1\,a_1^2 & 0 & 0 & 0 & \rho_1\,a_1^2 & 0 & 0 & 0 & 0 & 0 & \frac{\rho_1\,a_1^2(\Delta u)}{\alpha_1\,(a_1^2-(\Delta u)^2)} \end{pmatrix}. \quad (2.15)$$

As shown in [58], observing (2.15) it is straightforward to see that the eigenvectors become linearly dependent if one of the following conditions is realized

$$\alpha_1 = 0, \quad \alpha_2 = 0, \quad a_1^2 - (\Delta u)^2 = 0. \tag{2.16}$$

Furthermore, for the Riemann problem consisting of system (2.1) and the following initial conditions, considering a generic direction x,

$$\mathbf{Q}(x,0) = \begin{cases} \mathbf{Q}_L(x), & x < 0, \\ \mathbf{Q}_R(x), & x > 0, \end{cases} \tag{2.17}$$

the first inverse Riemann exact solver was proposed by Andrianov and Warnecke [2], while the first forward exact solvers were published by Schwendeman *et al.* [156] and Deledicque and Papalexandris [43]. Moreover the structure of the exact solution of the Riemann problem (2.1) and (2.17) is described in the work of Tokareva and Toro[169] by examining the right eigenvalues of the system (2.15) with generalized Riemann invariants.

2.1.2 Non-dimensional formulation and low-Mach limit

In this section, with the aim of obtaining a simplified model describing the behaviour of incompressible phases, the low Mach limit of the BN model is derived with the aid of a classical asymptotic expansion approach, e.g. [44, 98].

As stated in the introduction 1.2.1, different flow regimes can be characterised by the *Mach number* $M = ||\mathbf{v}||/\mathrm{C}$, given by the ratio of the local flow velocity $\mathbf{v}$ to the sound speed C. Thus, in principle, in a multiphase context, given a homogeneous velocity field for the phases, a different flow regime will be found for each phase. For instance, a compressible behaviour may be assumed by a gas phase, while a liquid phase may exhibit an almost incompressible response. Consequently, in order not to lose generality in a non-dimensional analysis it would be necessary to choose different reference quantities for each phase, leading to different Mach numbers characterising the flow regime of each phase, as was done by Lukáčová *et al.* in [105]. However, in the specific application of interest for this thesis work, the low Mach limit of the most compressible phase is of interest. (The limit is even more strictly satisfied for the solid phase, the least compressible of the two.) Therefore, the simultaneous limit for both phases is considered in the non-dimensionalisation stage, assuming a flow regime described by a single Mach number associated with both phases.

To represent and identify the different scales present in model (2.1), we denote the non-dimensional quantities by $(\tilde{\cdot})$ and the corresponding reference value by $(\cdot)^r$. The following reference quantities can be assumed. The convective scale is denoted by $u^r = x^r/t^r$ which can be expressed by means of a reference length x^r and time t^r. Further we define the reference density ρ^r and the reference pressure p^r from which one can define the reference sound speed given by $(\mathrm{C}^r)^2 = p^r/\rho^r$. With these definitions, we can express the dimensional variables with the product of the non-dimensional quantity and the reference value, for each phase, as follows

$$\begin{aligned}
&x = \tilde{x}\, x^r, \quad t = \tilde{t}\, t^r, \quad M = u^r/\mathrm{C}^r, \\
&\mathbf{v}_a = \tilde{\mathbf{v}}_a \frac{x^r}{t^r}, \quad \rho_a = \tilde{\rho}_a\, \rho^r, \quad p_a = \tilde{p}_a\, \rho^r\, (\mathrm{C}^r)^2, \quad e_a = \tilde{e}_a\, (\mathrm{C}^r)^2,
\end{aligned} \tag{2.18}$$

where e_a is the specific internal energy of each phase and M is the reference Mach number.

By inserting expressions (2.18) into (2.1) and dropping $(\tilde{\cdot})$, we obtain the following non-dimensional formulation of the BN system

$$\begin{aligned}
&\partial_t(\alpha\,\rho)_a + \nabla\cdot(\alpha\,\rho\,\mathbf{v})_a = 0, \\
&\partial_t(\alpha\,\rho\,\mathbf{v})_a + \nabla\cdot\left(\alpha\,\rho\,\mathbf{v}\otimes\mathbf{v} + \frac{\alpha\,p}{M^2}\,\mathbf{I}\right)_a = \frac{p_{\mathrm{I}}}{M^2}\,\nabla\alpha_a, \\
&\partial_t(\alpha\,\rho E)_a + \nabla\cdot(\alpha\,\rho\,\mathbf{v}\,E + \alpha\,\mathbf{v}\,p)_a = -p_{\mathrm{I}}\,\partial_t\alpha_a, \\
&\partial_t\alpha_a + \mathbf{v}_{\mathrm{I}}\cdot\nabla\alpha_a = 0,
\end{aligned} \tag{2.19}$$

where the non-dimensional total energy is given by

$$E_a = \left(\frac{1}{2}|\mathbf{v}|^2\, M^2 + e\right)_a. \tag{2.20}$$

The presence of the Mach number in the non-dimesional momentum equation of the system (2.19) leads to a change in the eigenvalues related to acoustic waves, which now read

$$\begin{aligned}
&\lambda_1 = u_1 - a_1/M, \quad \lambda_2 = \lambda_3 = \lambda_4 = u_1, \quad \lambda_5 = u_1 + a_1/M, \\
&\lambda_6 = u_2 - a_2/M, \quad \lambda_7 = \lambda_8 = \lambda_9 = u_2, \quad \lambda_{10} = u_2 + a_2/M, \\
&\lambda_{11} = u_2.
\end{aligned} \tag{2.21}$$

Furthermore, it can be seen that pressure-related terms in the momentum equations become dominant and that acoustic waves propagate significantly faster than the material ones, for low Mach numbers.

Through an asymptotic analysis of the non-dimensional model (2.19), it is possible to gain a better understanding of the behaviour of the solution in the low Mach number limit and formally obtain the incompressible equations.

According to [44, 98], for the derivation of the low Mach limit model, we focus on the scales induced by the Mach number, considering a time and space asymptotic expansion of the variables $\rho_a, p_a, \mathbf{v}_a$, for each phase, which read

$$\begin{aligned}
&\rho_a(x,t) = \rho_a^{(0)}(x,t) + \mathcal{O}(M),\\
&p_a(x,t) = p_a^{(0)}(x,t) + p_a^{(1)}(x,t)\,M + p_a^{(2)}(x,t)\,M^2 + \mathcal{O}(M^3),\\
&\mathbf{v}_a(x,t) = \mathbf{v}_a^{(0)}(x,t) + \mathcal{O}(M).
\end{aligned} \tag{2.22}$$

By introducing these expansions into the non-dimensional equations (2.19) and sorting by Mach number orders, we find the following system for the leading order $\mathcal{O}(M^0)$

$$\partial_t(\alpha\,\rho^{(0)})_a + \nabla\cdot(\alpha\,\rho^{(0)}\,\mathbf{v}^{(0)})_a = 0, \tag{2.23}$$

$$\partial_t(\alpha\,\rho^{(0)}\,\mathbf{v}^{(0)})_a + \nabla\cdot(\alpha\,\rho^{(0)}\,\mathbf{v}^{(0)}\otimes\mathbf{v}^{(0)} + \alpha\,p^{(2)}\,\mathbf{I})_a = p_{\mathrm{I}}^{(2)}\,\nabla\alpha_a, \tag{2.24}$$

$$\partial_t(\alpha\,\rho^{(0)}e^{(0)})_a + \nabla\cdot(\alpha\,\rho^{(0)}\,\mathbf{v}^{(0)}\,e^{(0)} + \alpha\,\mathbf{v}^{(0)}\,p^{(0)})_a = -p_{\mathrm{I}}^{(0)}\,\partial_t\alpha_a, \tag{2.25}$$

$$\partial_t\alpha_a + \mathbf{v}_{\mathrm{I}}{}^{(0)}\cdot\nabla\alpha_a = 0, \tag{2.26}$$

where $e_a^{(0)}$ is a function of $\rho_a^{(0)}, p_a^{(0)}$ and the following two PDEs for the orders $\mathcal{O}(M^{-1})$ and $\mathcal{O}(M^{-2})$

$$\nabla\cdot(\alpha\,p^{(1)}\,\mathbf{I})_a = p_{\mathrm{I}}^{(1)}\,\nabla\alpha_a, \qquad \nabla\cdot(\alpha\,p^{(0)}\,\mathbf{I})_a = p_{\mathrm{I}}^{(0)}\,\nabla\alpha_a. \tag{2.27}$$

Considering the choices of Baer and Nunziato in defining the interphase quantities (2.2), we can rewrite (2.27) for the first and the second phase as

$$\begin{aligned}
\nabla(\,\alpha_1\,p_1^{(1)}) &= p_1^{(1)}\,\nabla\alpha_1, & \nabla(\,\alpha_1\,p_1^{(0)}) &= p_1^{(0)}\,\nabla\alpha_1,\\
\nabla(\,\alpha_2\,p_2^{(1)}) &= -p_1^{(1)}\,\nabla\alpha_1, & \nabla(\,\alpha_2\,p_2^{(0)}) &= -p_1^{(0)}\,\nabla\alpha_1,
\end{aligned} \tag{2.28}$$

which imply that $\nabla p_1^{(1)} = 0$ and $\nabla p_1^{(0)} = 0$, therefore the pressure for the first phase is constant in space up to a perturbation in M^2. The same consideration can be made for the second phase only assuming that $p_2^{(1)} = p_1^{(1)}$ and $p_2^{(0)} = p_1^{(0)}$, for instance considering a pressure relaxation term. At this stage we can rewrite the system (2.29) at the leading order $\mathcal{O}(M^0)$, introducing these consideration about phase pressures, and reads

$$\partial_t(\alpha\,\rho^{(0)})_a + \nabla\cdot(\alpha\,\rho^{(0)}\,\mathbf{v}^{(0)})_a = 0, \tag{2.29}$$

$$\partial_t(\alpha\,\rho^{(0)}\,\mathbf{v}^{(0)})_a + \nabla\cdot(\alpha\,\rho^{(0)}\,\mathbf{v}^{(0)}\otimes\mathbf{v}^{(0)} + \alpha\,p^{(2)}\,\mathbf{I})_a = p_1^{(2)}\,\nabla\alpha_a, \tag{2.30}$$

$$\begin{aligned}
&\alpha_a\partial_t(\rho^{(0)}e^{(0)})_a + (\rho^{(0)}e^{(0)} + p_1^{(0)})_a\,(\mathbf{v}_a^{(0)} - \mathbf{v}_1^{(0)})\cdot\nabla\alpha_a +\\
&\qquad + (\alpha\rho^{(0)}e^{(0)} + \alpha\,p^{(0)})_a\,\nabla\cdot\mathbf{v}_a^{(0)} = 0,
\end{aligned} \tag{2.31}$$

$$\partial_t\alpha_a + \mathbf{v}_2^{(0)}\cdot\nabla\alpha_a = 0. \tag{2.32}$$

Assuming further that the phase velocities coincide in this limit, $\mathbf{v}_1^{(0)} = \mathbf{v}_2^{(0)}$ (e.g. due to the inter-phase drag terms present in the original model), the phase energy conservation equation (2.31) reduces to

$$\alpha_a \partial_t (\rho^{(0)} e^{(0)})_a + (\alpha \rho^{(0)} e^{(0)} + \alpha\, p^{(0)})_a \, \nabla \cdot \mathbf{v}_a^{(0)} = 0. \tag{2.33}$$

Integrating (2.33) over the domain Ω with periodic or no-flux boundary conditions, as done in [44, 98], we obtain that $(\rho^{(0)} e^{(0)})_a$ is constant in time. Therefore it follows directly that $\nabla \cdot \mathbf{v}_a^{(0)} = 0$ for each phase. This means the pressure of each phase is given by

$$p_a(x,t) = p_a^{(0)} + p_a^{(2)}(x,t)\, M^2 + \mathcal{O}(M^3), \tag{2.34}$$

where the leading order $p_a^{(0)}$ is a constant which plays the role of the thermodynamic variable, and the second-order term $p_a^{(2)}(x,t)$ is the pressure whose fluctuations account for local force balancing and, for $M \to 0$, satisfies the Poisson equation. This leads to a system of incompressible Euler equations with friction coupled through a source term that is a function of the second-order term $p_a^{(2)}(x,t)$

$$\begin{aligned}
&\partial_t (\alpha\, \rho^{(0)})_a + \nabla \cdot (\alpha\, \rho^{(0)}\, \mathbf{v}^{(0)})_a = 0, \\
&\partial_t (\alpha\, \rho^{(0)}\, \mathbf{v}^{(0)})_a + \nabla \cdot (\alpha\, \rho^{(0)}\, \mathbf{v}^{(0)} \otimes \mathbf{v}^{(0)} + \alpha\, p^{(2)}\, \mathbf{I})_a = p_1^{(2)}\, \nabla \alpha_a, \\
&\nabla \cdot \mathbf{v}_a^{(0)} = 0, \\
&\partial_t \alpha_a + \mathbf{v}_2^{(0)} \cdot \nabla \alpha_a = 0.
\end{aligned} \tag{2.35}$$

2.2 The unified SHTC multiphase model of continuum mechanics

The seminal ideas about an SHTC theory of mixtures was proposed by Romenski in [149, 150] for the case of two fluids. It was then further developed in a series of works [144–146] and it was generalized to the case of arbitrary number of constituents in [143]. This theory is characterized by its remarkable ability to describe multiphase flow in closed form as formulated, in contrast to more conventional formulations (e.g. BN model). However, even if correct, the derivation is somewhat complicated, mainly due to the fact that terms related to the existence of geometric stationary compatibility constraints, e.g., for the vorticity of relative velocities, are added a posteriori to prevent the source terms from violating them.

This theory, can be rewritten simply and clearly in light of the work on the re-derivation of SHTC theory from variational principle presented in the recent work of Peshkov *et al.* [132]. Indeed, this work reveals that the original structure of SHTC systems, which goes back to the work of Godunov and Romenski [80, 82–84], is rather related to conservation laws written in the Lagrangian framework, while their Eulerian counterparts are inherently non-conservative time evolutions and have a more complicated structure that intimately includes geometric aspects.

Moreover, in this thesis, the SHTC multiphase model is extended with additional physical effects, deriving it as a whole from variational principles, while retaining its first-order hyperbolic nature. Specifically, in this re-formulation of an SHTC mixture theory, the unified model of continuum mechanics introduced in [131], based on the Eulerian hyperbolic formulation of elasticity by Godunov and Romenski [82–84], is included from the beginning. This particular formulation of continuum mechanics is notable for its ability to describe liquids and solids in a unified manner, with the two states of matter differing simply by the choice of a material-specific time scale τ, that governs the rate at which deformation, in a given control volume, are dissipated through a process of relaxation.

2.2.1 General structure of the SHTC formulation

The origin of the SHTC formulation of continuum mechanics can be attributed to the fundamental work of Godunov [77] who asked what mathematical requirements can guarantee IVP well-posedness, i.e. what requirements can guarantee that the solution of a PDE system with initial data exists, is unique and continuously depends on the initial data, for a new model of non-linear continuum mechanics. Stressing that the well-posedness of the IVP should be considered as a fundamental physical principle, in the same way that causality, conservation and thermodynamic principles or Galilean invariance are regarded when considering classical smooth solutions of time-dependent PDEs.

As has been shown by Godunov [77–79], for the important subclass of *symmetric hyperbolic systems* of PDEs, one can guarantee that such systems are globally hyperbolic by definition, and consequently that IVP is locally well-posed in time. In fact, if we consider a first order system of conservation laws, for $\mathbf{q} = (q_1, q_2, \dots, q_n)$,

$$\frac{\partial \mathbf{q}}{\partial t} + \frac{\partial \mathbf{F}^k(\mathbf{q})}{\partial x_k} = 0, \tag{2.36}$$

which admits an additional conservation law for a *strictly convex total energy density potential* $\mathcal{E}(\mathbf{q})$

$$\frac{\partial \mathcal{E}(\mathbf{q})}{\partial t} + \frac{\partial G^k(\mathbf{q})}{\partial x_k} = 0. \tag{2.37}$$

Then, such a system (2.36)-(2.37) can be parametrized in terms of a new state variables vector $\mathbf{p} = (p_1, p_2, \dots, p_n)$ and a new potential $L(\mathbf{p})$. These new quantities $(\mathbf{p}, L)$ are thermodynamically conjugate to $(\mathbf{q}, \mathcal{E})$ via the following definitions

$$\mathbf{p} = \mathcal{E}_{\mathbf{q}}\,, \qquad L(\mathbf{p}) = \mathbf{q} \cdot \mathcal{E}_{\mathbf{q}} - \mathcal{E}(\mathbf{q}) = \mathbf{q} \cdot \mathbf{p} - \mathcal{E}(\mathbf{q}), \tag{2.38}$$

namely, via the definition of L, which is Legendre's transformation of $\mathcal{E}(\mathbf{q})$; the subscript denotes partial derivatives with respect to the latter, i.e. $\mathbf{p}$ is a vector of components $p_i = \partial \mathcal{E} / \partial q_i$. The inverse relations also exist

$$\mathbf{q} = L_{\mathbf{p}}\,, \qquad \mathcal{E}(\mathbf{q}) = \mathbf{p} \cdot L_{\mathbf{p}} - L(\mathbf{p}) = \mathbf{p} \cdot \mathbf{q} - L(\mathbf{p}), \tag{2.39}$$

and (2.38)-(2.39) are one-to-one relations since $\mathcal{E}(\mathbf{q})$ is assumed to be a convex function, i.e. the Hessian $\partial \mathbf{p}/\partial \mathbf{q} = \mathcal{E}_{\mathbf{qq}} = (L_{\mathbf{pp}})^{-1} > 0$ is symmetric and positive definite. By also introducing the Legendre-conjugation of the energy flux $L^k(\mathbf{p})$, which reads

$$L^k(\mathbf{p}) = \mathcal{E}_{\mathbf{q}} \cdot \mathbf{F}^k(\mathbf{q}) - G^k(\mathbf{q}) = \mathbf{p} \cdot \mathbf{F}^k(\mathbf{q}) - G^k(\mathbf{q}), \tag{2.40}$$

the previous system (2.36)-(2.37) can be parametrized as

$$\frac{\partial L_{\mathbf{p}}}{\partial t} + \frac{\partial L^k_{\mathbf{p}}}{\partial x_k} = 0, \tag{2.41}$$

and this form can be easily rewritten as a *symmetric* quasilinear one

$$L_{\mathbf{p}_i\mathbf{p}_j}\frac{\partial p_j}{\partial t}+L^k_{\mathbf{p}_i\mathbf{p}_j}\frac{\partial p_j}{\partial x_k}=0. \tag{2.42}$$

Therefore, the parametrization of the governing equations in terms of the conjugate variables $\mathbf{p}$ and generating potential $L(\mathbf{p})$ allows to rewrite the system in a symmetric hyperbolic quasilinear form, if the energy potential is convex.

Moreover, one usually refers to (2.41) as Godunov's form of the conservation laws. However, in light of the re-derivation work of SHTC theory from variational principle, in [132], it is clear that the original Godunov structure (2.41) refers to conservation laws written in the Lagrangian framework; while their Eulerian counterparts are, in general, non-conservative time evolutions and have a more complicated structure, that can be represented by generalizing (2.41) as follows

$$\frac{\partial L_{\mathbf{p}}}{\partial t}+\frac{\partial(v_k\,L)_{\mathbf{p}}}{\partial x_k}+C_k\frac{\partial\mathbf{p}}{\partial x_k}=0, \tag{2.43}$$

where C_k are some symmetric matrices and v_k is the velocity field. The presence of the non-conservative terms, represented by $C_k\,\partial\mathbf{p}/\partial x_k$, is related to the fact that involution constraints in the Eulerian framework are not auxiliary equations derived from stationary laws as in the Lagrangian framework, but are an intrinsic part of the structure of the Eulerian SHTC equations. Furthermore, these constraints cannot be omitted, otherwise the Galilean invariance property would be violated and the characteristic structure would also change. In [132], it is also shown how the conjugate form of the Eulerian SHTC equations can still be written as a symmetric quasilinear system, even including these geometrical involution constraints.

The second key observation in Godunov's work [77] is that for this specific subclass of conservation law systems, there is an intimate connection with thermodynamics. Specifically, the system (2.36) and the conservation law of the total energy (2.37) costitute and overdetermined system of PDEs, which means that

$$\mathcal{E}_{\mathbf{q}}\cdot\left(\frac{\partial\mathbf{q}}{\partial t}+\frac{\partial\mathbf{F}^k(\mathbf{q})}{\partial x_k}\right)\equiv\frac{\partial\mathcal{E}(\mathbf{q})}{\partial t}+\frac{\partial G^k(\mathbf{q})}{\partial x_k}. \tag{2.44}$$

Thus, this subclass of symmetric hyperbolic PDEs can be associated with the *thermodynamically compatible systems* of first order nonlinear conservation laws.

2.2.2 Mixture description: composition characteristics

We consider a mixture of N constituents denoted by latin indices a, where $a = 1, \dots, \mathrm{N}$ enumerates the phases. Denoting by M and V the total mass and the volume of the infinitesimal element of the mixture, respectively, we can write

$$M = \sum_{a=1}^{\mathrm{N}} m_a, \qquad V = \sum_{a=1}^{\mathrm{N}} \nu_a, \tag{2.45}$$

where m_a is the mass and ν_a is the volume of the a-th constituent in the mixture control volume V. The mixture mass density is then defined as

$$\rho = \frac{M}{V} = \frac{m_1 + m_2 + \dots + m_{\mathrm{N}}}{V} = \sum_{a=1}^{\mathrm{N}} \varrho_a, \tag{2.46}$$

where

$$\varrho_a := \frac{m_a}{V} \tag{2.47}$$

denotes the density of the a-th phase inside the control volume V.

To characterise the volume and mass content of the a-th constituent inside the mixture control volume V, it is also convenient to introduce two non-dimensional scalars: the volume fraction

$$\alpha_a := \frac{\nu_a}{V}, \qquad \sum_{a=1}^{\mathrm{N}} \alpha_a = 1, \tag{2.48}$$

and the mass fraction

$$c_a := \frac{m_a}{M} = \frac{\varrho_a}{\rho}, \qquad \sum_{a=1}^{\mathrm{N}} c_a = 1. \tag{2.49}$$

Although ϱ_a represents the true mass density of the a-th constituent inside the control volume V, the equations of state of the constituents are usually given in the single-phase context, i.e. as if the phase a would occupy the entire volume V. Therefore, to use the standard single-phase equations of state, we shall also need the mass density of the a-th phase not of the entire mixture control volume V, but of the partial volume ν_a, i.e.

$$\rho_a = \frac{m_a}{\nu_a} = \frac{m_a V}{\nu_a V} = \frac{\varrho_a}{\alpha_a}. \tag{2.50}$$

In other words, for phase a, its mass density ρ_a of the partial volume ν_a and its true mass density ϱ_a of the control volume V are related by

$$\varrho_a = \alpha_a \rho_a. \tag{2.51}$$

The mixture entropy density $\eta = \rho S$ is defined as

$$\eta := \sum_{a=1}^{\mathrm{N}} \eta_a = \sum_{a=1}^{\mathrm{N}} \varrho_a s_a \tag{2.52}$$

where s_a is the specific entropy of the a-th phase. Hence, the specific mixture entropy can be computed as

$$S = \frac{\eta}{\rho} = c_1 s_1 + c_2 s_2 + \dots + c_{\mathrm{N}} s_{\mathrm{N}}. \tag{2.53}$$

2.2.3 Mixture description: the kinematic quantities

Due to the conservation principle, the total momentum of a control volume is defined as the sum of the momenta of its parts. Thus the linear momentum $\boldsymbol{U} = \{U_k\}$ of the mixture control volume V, where k denotes the component in space, is defined as the sum of the linear momenta $\boldsymbol{u}_a = \{u_{a,k}\} := \varrho_a \boldsymbol{v}_a$ of the constituents

$$\boldsymbol{U} := \boldsymbol{u}_1 + \boldsymbol{u}_2 + \dots + \boldsymbol{u}_{\mathrm{N}} = \varrho_1 \boldsymbol{v}_1 + \varrho_2 \boldsymbol{v}_2 + \dots + \varrho_{\mathrm{N}} \boldsymbol{v}_{\mathrm{N}}, \tag{2.54}$$

where $\boldsymbol{v}_a = \{v_{a,k}\}$ is the velocity of the a-th phase. The velocity $\boldsymbol{V} = \{V_k\} := \boldsymbol{U}/\rho$ of the mixture control volume is therefore defined as the center of mass velocity

$$\boldsymbol{V} := \frac{\boldsymbol{U}}{\rho} = \frac{\varrho_1 \boldsymbol{v}_1 + \varrho_2 \boldsymbol{v}_2 + \dots + \varrho_{\mathrm{N}} \boldsymbol{v}_{\mathrm{N}}}{\rho} = c_1 \boldsymbol{v}_1 + c_2 \boldsymbol{v}_2 + \dots + c_{\mathrm{N}} \boldsymbol{v}_{\mathrm{N}}. \tag{2.55}$$

For the SHTC formulation of the mixture equations, in addition to the mixture momentum $\boldsymbol{U}$, one also needs the relative velocity $\boldsymbol{w} = \{w_{a,k}\}$

$$\boldsymbol{w}_a = \boldsymbol{v}_a - \boldsymbol{v}_{\mathrm{N}}, \qquad w_{a,k} = v_{a,k} - v_{\mathrm{N},k}, \qquad k = 1, \dots, 3. \tag{2.56}$$

which is defined with respect to the N-th constituent that can be chosen arbitrarily. Whereas, in order to derive a BN-type formulation it is useful to define the relative velocity with respect to the mixture velocity

$$\bar{\boldsymbol{v}}_a := \boldsymbol{v}_a - \boldsymbol{V}, \qquad \bar{v}_{a,k} = v_{a,k} - V_k, \qquad k = 1, \dots, 3. \tag{2.57}$$

In the SHTC theory, the relative velocity $\boldsymbol{w}_a$ is the preferred choice because it is dictated by the variational formulation as well as by the symmetrization of the governing equations [145, 150].

2.2.4 Mixture description: deformation characteristics

In order to describe the elastic and inelastic deformations of a single material in the SHTC framework, one needs to introduce the concept of the *distortion field* $\mathbf{A}$, by means of which the evolution of elastic and elastoplastic solids and the dynamics of Newtonian and non-Newtonian fluids can be formulated in the SHTC formalism [83, 94, 131, 133, 134].

In the classical formulation of ideal elastic solids the distortion matrix is interpreted as the inverse of the *deformation gradient tensor*, commonly denoted in the literature as $\boldsymbol{F} = \partial \boldsymbol{x}/\partial \boldsymbol{X}$, or, in index notations $F_{iK} = \partial x_i/\partial X_K$, and hence, $\mathbf{A} = \partial \boldsymbol{X}/\partial \boldsymbol{x}$ or $A_{Ki} = \partial X_K/\partial x_i$, for the dynamics of pure elastic solids. Here, as usual, we denote the coordinates of the reference configuration by $\mathbf{X}$ and the coordinates in the current configuration by $\mathbf{x}$. In the case of inelastic deformations (viscous flows, plastic deformations), the distortion field can be interpreted as the inverse of the elastic part $\boldsymbol{F}^{\mathrm{e}}$ of the multiplicative decomposition $\boldsymbol{F} = \boldsymbol{F}^{\mathrm{e}}\boldsymbol{F}^{\mathrm{i}}$ of the deformation gradient into elastic and inelastic part, e.g. see [131, 133]. In this case, the distortion field $\mathbf{A}$ is free to have a non-zero curl component, therefore the reference configuration loses its physical significance and it plays merely the role of an initial condition, i.e. one can not reconstruct the original Lagrangian frame. In other words, in general, the distortion field should be viewed as a local field attached to each material element, providing its complete time and space local information about deformation and rotation.

Note that in the notation of the distortion matrix entries, we distinguish between the Eulerian (lowercase) index i, j, k and the Lagrangian (uppercase) index I, J, K so that the distortion matrix can be seen as a triad of three basis vectors $\mathbf{A} = \{\mathbf{A}_1, \mathbf{A}_2, \mathbf{A}_3\}$, where for each $K = 1, 2, 3$, $\mathbf{A}_K$ is a 3-vector $\mathbf{A}_K = (A_{K1}, A_{K2}, A_{K3})$.

It is also useful to introduce the definition of a positive definite symmetric tensor, the *metric tensor* $\mathbf{G}$, which has been shown to be useful for describing complex fluids [87, 131]. This rank-2 tensor can be defined as $\mathbf{G} = \mathbf{A}^{\mathsf{T}}\,\mathbf{A}$, or, in index notations $G_{ij} = A_{Ji}\,A_{Jj}$, and identifies the direction and magnitude of deformations in the continuum. Again, in an analogy with the solid mechanics, it coincides with the inverse of the left Cauchy-Green deformation tensor $\mathbf{B} = \mathbf{F}\,\mathbf{F}^{\mathsf{T}}$ and is sometimes called Piola tensor or Finger tensor.

According to the unified model of continuum mechanics [131] and SHTC formulation for multiphase flows [143, 145], a true non-equilibrium multiphase model should have, in general, different pressures, temperatures, velocities, distortion fields, and etc. for each phase. However, at the moment, following [147, 148], we only know how to derive the SHTC multiphase model for the case when the phase distortions are equal, $\mathbf{A}_1 = \mathbf{A}_2 = ... = \mathbf{A}_{\mathrm{N}} = \mathbf{A}$. Moreover, a multiphase single-distortion model was successfully used in [120, 121] for transient shock-dominated problems in 1D as well in multiple space dimensions.

Yet, from our computational experience with the model, it has appeared that it is beneficial to evolve individual distortions for every phase. Therefore, in Section 2.3.2 a heuristic extension of the SHTC multiphase model in its BN-form (2.3) to the case of different phase distortions $\mathbf{A}_a$ is discussed, and this formulation was used to obtain all the numerical results presented in Section 4.2.

2.2.5 Mixture description: SHTC state variables

The SHTC mixture governing equations are naturally formulated in terms of state variables, which are usually represented by scalar and vectors densities, e.g. mass density, momentum density, entropy density, etc. The set of SHTC state variables for mixtures is partly different from the conventionally used state variables, for example, in the BN-type formulations, e.g. mixture momentum and relative velocities $\{\boldsymbol{U}, \boldsymbol{w}_a\}$, $a = 1, \dots, \mathrm{N}-1$ in the SHTC formulation versus phase momenta $\boldsymbol{u}_a$, $a = 1, \dots, \mathrm{N}$ in the BN-type formulations. The SHTC choice is conditioned by the variational nature of the equations and their symmetrization procedure. Thus, the vector of sought conservative SHTC variables is

$$\mathbf{Q} = (\boldsymbol{U}, \mathbf{A}, \rho, \varrho_1, \dots, \varrho_{\mathrm{N}-1}, \boldsymbol{w}_1, \dots, \boldsymbol{w}_{\mathrm{N}-1}, \eta_1, \dots, \eta_{\mathrm{N}}, \varphi_1, \dots, \varphi_{\mathrm{N}-1})^T, \tag{2.58}$$

which is related to the vector of primitive SHTC variables

$$\boldsymbol{P} = (\boldsymbol{V}, \mathbf{A}, \rho, c_1, \dots, c_{\mathrm{N}-1}, \boldsymbol{w}_1, \dots, \boldsymbol{w}_{\mathrm{N}-1}, s_1, \dots, s_{\mathrm{N}}, \alpha_1, \dots, \alpha_{\mathrm{N}-1})^T, \tag{2.59}$$

as

$$\varphi_a = \rho\alpha_a, \qquad \boldsymbol{U} = \rho\boldsymbol{V}, \qquad \varrho_a = \rho c_a \qquad \eta_a = \rho c_a s_a. \tag{2.60}$$

One should pay attention to that φ_{N}, ϱ_{N}, and $\boldsymbol{w}_{\mathrm{N}}$ are excluded from the set of state variables because they can be expressed as

$$\varphi_{\mathrm{N}} = \rho - \varphi_1 - \dots - \varphi_{\mathrm{N}-1}, \qquad \varrho_{\mathrm{N}} = \rho - \varrho_1 - \dots - \varrho_{\mathrm{N}-1}, \qquad \boldsymbol{w}_{\mathrm{N}} = 0, \tag{2.61}$$

likewise their primitive counterparts

$$\alpha_{\mathrm{N}} = 1 - \alpha_1 - \dots - \alpha_{\mathrm{N}-1}, \qquad c_{\mathrm{N}} = 1 - c_1 - \dots - c_{\mathrm{N}-1}, \qquad \boldsymbol{w}_{\mathrm{N}} = 0. \tag{2.62}$$

2.2.6 Closure relations

To design the equations of a multiphase model, the main ingredient, within the SHTC formalism, is related to the definition of a total energy density $\mathcal{E}(\mathbf{Q})$ defined with respect to the state vector $\mathbf{Q}$. According to the principle of energy conservation, the total energy density $\mathcal{E}$ of the mixture, in the control volume V, can be defined as the sum of the mixture energy density associated with the elastic-shear stress ε^{e} and the energy densities $\mathcal{E}_a = \varepsilon^{\mathrm{i}}_a + \varepsilon^{\mathrm{k}}_a$ of its constituents

$$\mathcal{E}(\mathbf{Q}) = \varepsilon^{\mathrm{e}} + \sum_{a=1}^{\mathrm{N}} \mathcal{E}_a, \tag{2.63}$$

where $\varepsilon^{\mathrm{e}}(\rho, \mathbf{A})$ is the elastic-shear energy and, for each phase $a = 1, 2, \dots, \mathrm{N}$, $\varepsilon^{\mathrm{i}}_a(\rho, \varrho_a, \varphi_a, \eta_a)$ is the internal energy, and $\varepsilon^{\mathrm{k}}_a(\varrho_a, \boldsymbol{u}_a)$ is the kinetic energy.

Mixture elastic energy, ε^{e}

Recalling that according to the unified model of continuum mechanics [131], the Navier-Stokes equations can be considered as a the stiff relaxation limit of the SHTC viscoelastic model [54], and thus, like in elastic solids, their response to shear deformations is characterized by the elastic energy.

In this work, the part of the energy density associated with the elastic-shear stress, ε^{e}, is assumed to be proportional to the second invariant of the deviator $\mathrm{dev}G_{ij} = G_{ij} - (G_{kk}/3)\delta_{ij}$ of the metric tensor of elastic deformations $G_{ij} = A_{Ji}A_{Jj}$, and reads

$$\varepsilon^{\mathrm{e}}(\rho, \mathbf{A}_a) = \frac{1}{4}\rho\,\mathrm{Cs}^2\ \left(\mathrm{dev}G_{ik}\mathrm{dev}G_{ki}\right), \tag{2.64}$$

where Cs is a parameter representing the propagation speed of small-amplitude shear waves in the mixture, here it is referred to as *shear sound velocity.*

The definition of strain energy in (2.64) is a choice, then other definitions can be used freely, such as the one given in [116], which produces a sharper separation between spherical and deviatoric stresses.

At the moment, an SHTC formulation for multiphase flows with different distortion fields $\mathbf{A}_a$ is unknown, and in the theoretical part, we assume a single-distortion approximation $\mathbf{A} = \mathbf{A}_1 = \mathbf{A}_2 = \dots = \mathbf{A}_{\mathrm{N}}$.

Phase internal energy, $\varepsilon^{\mathrm{i}}_a$

The SHTC state variables (2.58) are dictated by the variational formulation of the governing equations. However, these might be not the optimal choice of variables when it comes to expressing the fluxes in terms of the conventional fluid characteristics such as pressure, temperature, etc. Therefore, it is useful to express the total energy density of the mixture through two parametrizations. The first one is in terms of the state vector $\mathbf{Q}$ in (2.58), and the second one in terms of the individual phase state parameters ρ_a and s_a. The latter, only concerns the internal energies $\varepsilon^{\mathrm{i}}_a$. Thus, we shall use the following notations

$$\begin{aligned}\varepsilon^{\mathrm{i}}_a(\rho, \varrho_a, \varphi_a, \eta_a) &= \hat{\varepsilon}^{\mathrm{i}}_a(\rho_a, s_a) = \varrho_a \hat{e}^{\mathrm{i}}_a(\rho_a, s_a) = \\ &= \varrho_a \hat{e}^{\mathrm{i}}_a\left(\frac{\varrho_a \rho}{\varphi_a}, \frac{\eta_a}{\varrho_a}\right), \qquad a = 1, 2, \dots, \mathrm{N}-1\end{aligned} \tag{2.65}$$

and for $a = \mathrm{N}$

$$\hat{\varepsilon}^{\mathrm{i}}_{\mathrm{N}}(\rho_{\mathrm{N}}, s_{\mathrm{N}}) = \left(\rho - \sum_{a=1}^{\mathrm{N}-1} \varrho_a\right) \hat{e}^{\mathrm{i}}_{\mathrm{N}}\left(\frac{\rho(\rho - \sum_{a=1}^{\mathrm{N}-1} \varrho_a)}{\rho - \sum_{a=1}^{\mathrm{N}-1} \varphi_a}, \frac{\eta_{\mathrm{N}}}{\rho - \sum_{a=1}^{\mathrm{N}-1} \varrho_a}\right). \tag{2.66}$$

With this parametrization of the internal energies, the phase pressures and temperatures are defined as

$$p_a := \rho_a^2 \frac{\partial \hat{e}^{\mathrm{i}}_a}{\partial \rho_a}, \qquad T_a := \frac{\partial \hat{e}^{\mathrm{i}}_a}{\partial s_a}. \tag{2.67}$$

In this work, several test problems for multiphase flows of interacting gases, liquids, and solids will be presented. Each of these states of matter has its own equation of state which are described below. We remark that it is not the goal of the thesis to provide a comprehensive list of equations of state for all possible materials, but rather to illustrate the flexibility of the SHTC model in handling different types of materials.

- For the gas phases, the equation of state of perfect gases is used in the form
$$\hat{e}^{\mathrm{i}}_a(\rho_a, s_a) = \frac{\mathrm{Co}_a^2}{\gamma_a(\gamma_a - 1)} \left(\frac{\rho_a}{\rho_{\mathrm{o}a}}\right)^{\gamma_a - 1} e^{s_a/\mathrm{Cv}_a}, \tag{2.68}$$
where $\rho_{\mathrm{o}a}$ is the reference density, γ_a is the adiabatic exponent, Co_a is the velocity of sound at normal atmospheric conditions, Cv_a is the specific heat capacity at constant volume. Then, according to (2.67), the pressure and temperature are computed as
$$p_a = \rho_a^2 \frac{\partial \hat{e}_a}{\partial \rho_a} = \frac{\rho_{\mathrm{o}a} \mathrm{Co}_a^2}{\gamma_a} \left(\frac{\rho_a}{\rho_{\mathrm{o}a}}\right)^{\gamma_a} e^{s_a/\mathrm{Cv}_a}, \tag{2.69}$$
$$T_a = \frac{\partial \hat{e}_a}{\partial s_a} = \frac{\mathrm{Co}_a^2}{\mathrm{Cv}_a \gamma_a(\gamma_a - 1)} \left(\frac{\rho_a}{\rho_{\mathrm{o}a}}\right)^{\gamma_a - 1} e^{s_a/\mathrm{Cv}_a}, \tag{2.70}$$
and the phase velocity of sound C_a can be computed as
$$\mathrm{C}_a^2 := \frac{\partial p_a}{\partial \rho_a} = \mathrm{Co}_a^2 \left(\frac{\rho_a}{\rho_{\mathrm{o}a}}\right)^{\gamma_a - 1} e^{s_a/\mathrm{Cv}_a}. \tag{2.71}$$

- For the liquid and solid phases, the stiffened gas equation of state will be used in the form

$$\hat{e}^{\mathrm{i}}_a(\rho_a, s_a) = \frac{\mathrm{Co}_a^2}{\gamma_a(\gamma_a - 1)} \left(\frac{\rho_a}{\rho_{\mathrm{o}a}}\right)^{\gamma_a - 1} e^{s_a/\mathrm{Cv}_a} + \frac{\rho_{\mathrm{o}a}\mathrm{Co}_a^2 - \gamma_a p_{\mathrm{o}a}}{\gamma_a \rho_a}, \qquad (2.72)$$

denoting with $p_{\mathrm{o}a}$ the reference (atmospheric) pressure. In this case, the pressure and temperature are given by

$$p_a = \rho_a^2 \frac{\partial \hat{e}_a}{\partial \rho_a} = \frac{\rho_{\mathrm{o}a}\mathrm{Co}_a^2}{\gamma_a} \left(\frac{\rho_a}{\rho_{\mathrm{o}a}}\right)^{\gamma_a} e^{s_a/\mathrm{Cv}_a} - \frac{\rho_{\mathrm{o}a}\mathrm{Co}_a^2 - \gamma_a p_{0a}}{\gamma_a}, \qquad (2.73)$$

$$T_a = \frac{\partial \hat{e}_a}{\partial s_a} = \frac{\mathrm{Co}_a^2}{\mathrm{Cv}_a \gamma_a(\gamma_a - 1)} \left(\frac{\rho_a}{\rho_{\mathrm{o}a}}\right)^{\gamma_a - 1} e^{s_a/\mathrm{Cv}_a} \qquad (2.74)$$

and the phase adiabatic sound speed C_a results in

$$\mathrm{C}_a^2 := \frac{\partial p_a}{\partial \rho_a} = \mathrm{Co}_a^2 \left(\frac{\rho_a}{\rho_{\mathrm{o}a}}\right)^{\gamma_a - 1} e^{s_a/\mathrm{Cv}_a}. \qquad (2.75)$$

Phase kinetic energy, $\varepsilon^{\mathrm{k}}_a$

The phase kinetic energy

$$\varepsilon^{\mathrm{k}}_a = \frac{1}{2\varrho_a} \|\boldsymbol{u}_a\|^2, \qquad (2.76)$$

is defined in terms of the phase momenta $\boldsymbol{u}_a$. However, also in this case, it is useful to express this component of the energy density of the mixture in terms of the state vector $\mathbf{Q}$, to compute the partial derivatives $\partial \mathcal{E}/\partial \mathbf{Q}$. Thus, alternatively, $\varepsilon^{\mathrm{k}}_a$ can be also given, after some algebra, as

$$\sum_{a=1}^{\mathrm{N}} \varepsilon^{\mathrm{k}}_a = \frac{1}{2\rho} \sum_{k=1}^{3} U_k^2 + W(\rho, \varrho_1, \dots, \varrho_{\mathrm{N}-1}, \boldsymbol{w}_1, \dots, \boldsymbol{w}_{\mathrm{N}-1}) \qquad (2.77)$$

where the kinetic energy of relative motion W is defined as

$$W(\rho, \varrho_1, \dots, \varrho_{\mathrm{N}-1}, \boldsymbol{w}_a, \dots, \boldsymbol{w}_{\mathrm{N}-1}) := \frac{1}{2} \sum_{k=1}^{3} \sum_{a=1}^{\mathrm{N}-1} \varrho_a w_{a,k}^2 - \frac{1}{2\rho} \sum_{k=1}^{3} \left(\sum_{a=1}^{\mathrm{N}-1} \varrho_a w_{a,k} \right)^2. \qquad (2.78)$$

Thermodynamic forces, $\mathcal{E}_{\mathbf{Q}}$

At this point we are able to express the total energy density of the mixture completely in terms of the state vector $\mathbf{Q}$. Keping in mind that

$$\varrho_{\rm N} = \rho - \sum_{a=1}^{\rm N-1} \varrho_a \quad \text{and} \quad \varphi_{\rm N} = \rho - \sum_{a=1}^{\rm N-1} \varphi_a, \tag{2.79}$$

the partial derivatives of the energy potential $\mathcal{E}$ with respect to the state vector $\mathbf{Q}$ are given by

$$\begin{aligned}\frac{\partial \mathcal{E}}{\partial \rho} = \sum_{a=1}^{\rm N-1} \frac{\partial \hat{\varepsilon}^{\rm i}_a}{\partial \rho_a}\frac{\varrho_a}{\varphi_a} + \frac{\partial \hat{\varepsilon}^{\rm i}_{\rm N}}{\partial \rho_{\rm N}}\left(\frac{\rho\varphi_{\rm N} - \rho\varrho_{\rm N} + \varrho_{\rm N}\varphi_{\rm N}}{{\varphi_{\rm N}}^2}\right) - \frac{\partial \hat{\varepsilon}^{\rm i}_{\rm N}}{\partial s_{\rm N}}\frac{\eta_{\rm N}}{{\varrho_{\rm N}}^2}& \\ + \frac{1}{2\rho^2}\sum_{k=1}^{3}\sum_{a=1}^{\rm N}(\varrho_a w_{a,k})^2 - \frac{1}{2\rho^2}\sum_{k=1}^{3} U_k^2 + \frac{\partial \varepsilon^{\rm e}}{\partial \rho},&\end{aligned} \tag{2.80a}$$

$$\frac{\partial \mathcal{E}}{\partial U_i} = \frac{1}{\rho}U_i, \tag{2.80b}$$

$$\frac{\partial \mathcal{E}}{\partial A_{Jj}} = \frac{\partial \varepsilon^{\rm e}}{\partial A_{Jj}}, \tag{2.80c}$$

$$\frac{\partial \mathcal{E}}{\partial \varphi_a} = -\frac{\varrho_a\rho}{\varphi_a^2}\frac{\partial \hat{\varepsilon}^{\rm i}_a}{\partial \rho_a} + \frac{\varrho_{\rm N}\rho}{\varphi_{\rm N}^2}\frac{\partial \hat{\varepsilon}^{\rm i}_{\rm N}}{\partial \rho_{\rm N}}, \qquad a = 1,\dots,\text{N}-1, \tag{2.80d}$$

$$\begin{aligned}\frac{\partial \mathcal{E}}{\partial \varrho_a} = \frac{\rho}{\varphi_a}\frac{\partial \hat{\varepsilon}^{\rm i}_a}{\partial \rho_a} - \frac{\eta_a}{\varrho_a^2}\frac{\partial \hat{\varepsilon}^{\rm i}_a}{\partial s_a} - \frac{\rho}{\varphi_{\rm N}}\frac{\partial \hat{\varepsilon}^{\rm i}_{\rm N}}{\partial \rho_{\rm N}} + \frac{\eta_{\rm N}}{\varrho_{\rm N}^2}\frac{\partial \hat{\varepsilon}^{\rm i}_{\rm N}}{\partial s_{\rm N}} + \frac{1}{2}\sum_{k=1}^{3} w_{a,k}^2& \\ - \frac{1}{\rho}\sum_{k=1}^{3}\sum_{b=1}^{\rm N-1}\varrho_b w_{b,k} w_{a,k}, \qquad a = 1,\dots,\text{N}-1,&\end{aligned} \tag{2.80e}$$

$$\frac{\partial \mathcal{E}}{\partial w_{a,k}} = \varrho_a w_{a,k} - \frac{\varrho_a}{\rho}\sum_{b=1}^{\rm N-1}\varrho_b w_{b,k}, \qquad a = 1,\dots,\text{N}-1, \tag{2.80f}$$

$$\frac{\partial \mathcal{E}}{\partial \eta_a} = \frac{1}{\varrho_a}\frac{\partial \hat{\varepsilon}^{\rm i}_a}{\partial s_a}. \tag{2.80g}$$

In addition, a thermodynamic mixture pressure P can be defined in the SHTC formalism

$$P(\mathbf{Q}) := \rho\mathcal{E}_\rho + U_i\mathcal{E}_{U_i} + \varphi_a\mathcal{E}_{\varphi_a} + \varrho_a\mathcal{E}_{\varrho_a} + \eta_a\mathcal{E}_{\eta_a} - \mathcal{E} = \rho^2\hat{E}_\rho := \hat{P}(\boldsymbol{P}), \tag{2.81}$$

and, with the formulas in (2.80), $P(\mathbf{Q})$ can be computed as the following sum

$$P(\mathbf{Q}) = \sum_{a=1}^{\mathrm{N}} \left(\rho_a \frac{\partial \hat{\varepsilon}^{\mathrm{i}}_a}{\partial \rho_a} - \hat{\varepsilon}^{\mathrm{i}}_a \right) := \hat{P}(\boldsymbol{P}), \tag{2.82}$$

which suggests that the quantities

$$P_a := \rho_a \frac{\partial \hat{\varepsilon}^{\mathrm{i}}_a}{\partial \rho_a} - \hat{\varepsilon}^{\mathrm{i}}_a \tag{2.83}$$

can be called the partial phase pressures. Moreover, due to the fact that

$$\rho_a \frac{\partial \hat{\varepsilon}^{\mathrm{i}}_a}{\partial \rho_a} - \hat{\varepsilon}^{\mathrm{i}}_a = \alpha_a \rho_a^2 \frac{\partial \hat{e}_a}{\partial \rho_a}, \tag{2.84}$$

the partial phase pressures P_a and the single phase pressures (2.67) are related by

$$P_a = \alpha_a p_a. \tag{2.85}$$

In other words, the mixture pressure can be computed as

$$P = P_1 + ... + P_{\mathrm{N}} = \alpha_1 p_1 + ... + \alpha_{\mathrm{N}} p_{\mathrm{N}}. \tag{2.86}$$

All the derivatives listed in (2.80) are used in the formulation of the SHTC governing equations and therefore it is more convenient to express them in a more explicit form. Thus, expressions (2.80d) and (2.80f) can be further expanded as follows

$$\frac{\partial \mathcal{E}}{\partial A_{Jj}} = \rho\, \mathrm{Cs}^2\, A_{Ji}\, \mathrm{dev}\, G_{ij}, \tag{2.87a}$$

$$\frac{\partial \mathcal{E}}{\partial \varphi_a} = -\frac{1}{\rho}(p_a - p_{\mathrm{N}}), \tag{2.87b}$$

$$\frac{\partial \mathcal{E}}{\partial \varrho_a} = \mu_a - \mu_{\mathrm{N}} + \frac{1}{2}\sum_{k=1}^{3} w_{a,k}^2 - \frac{1}{\rho}\sum_{k=1}^{3}\sum_{b=1}^{\mathrm{N}-1} \varrho_b w_{b,k} w_{a,k}, \tag{2.87c}$$

$$\frac{\partial \mathcal{E}}{\partial w_{a,k}} = \varrho_a w_{a,k} - \frac{\varrho_a}{\rho}\sum_{b=1}^{\mathrm{N}} \varrho_b w_{b,k} = \varrho_a (v_{a,k} - V_k), \tag{2.87d}$$

$$\frac{\partial \mathcal{E}}{\partial \eta_a} = T_a, \tag{2.87e}$$

where

$$\mu_a := e_a + \frac{p_a}{\rho_a} - s_a T_a = e_a - \alpha_a \frac{\partial e_a}{\partial \alpha_a} - s_a \frac{\partial e_a}{\partial s_a} = \frac{\partial \hat{\varepsilon}^{\mathrm{i}}_a}{\partial \varrho_a} \tag{2.88}$$

is the chemical potential of the a-th constituent.

2.2.7 The SHTC mixture conservation laws

As we have seen in Section 1.1.1 a multiphase continuum is generally described by means of mass, momentum and energy balance laws for each constituent. However, the balance laws of the SHTC mixture consist of the evolution equations for the quantities defined in the state vector of the SHTC variables (2.58). As anticipated in Section 2.2, the SHTC theory of mixtures was first proposed by Romenski *et al.* in [143] for an arbitrary number of constituents, based simply on the requirements listed at the beginning of Section 2.2.1. However, this theory can be rewritten simply and clearly in light of the work on the re-derivation of the SHTC theory from the variational principle, [132], in which involution constraints are an intrinsic part of the structure of the Eulerian SHTC equations. Furthermore, in the variational framework, the original theory in [143] can be extended by including the unified model of continuum mechanics, i.e. by including A_{Ji} in the formulation of the following mixture theory.

In order to understand the variational nature of the SHTC governing equations, i.e. that the master system can also be obtained from Hamilton's stationary action principle, let us consider a vector potential referred to the mixture and $\mathrm{N}-1$ scalar potentials

$$x_i(t, X_I), \qquad \chi_a(t, X_I). \tag{2.89}$$

where t is time, $\mathbf{X} = X_I$ and $\mathbf{x} = x_i$ are the Lagrangian and Eulerian spatial coordinates respectively, while the potentials χ_a are needed to characterise each phase in the mixture, with $a = 1, ...\mathrm{N}-1$. We denote the derivatives of the potentials in (2.89) as follows

$$\begin{aligned} \hat{v}_i &= \frac{\partial x_i}{\partial t}, & \hat{f}_{iJ} &= \frac{\partial x_i}{\partial X_J}, \\ \hat{e}_a &= \frac{\partial \chi_a}{\partial t}, & \hat{h}_{aJ} &= \frac{\partial \chi_a}{\partial X_J}, \end{aligned} \tag{2.90}$$

and we define the action integral

$$\mathcal{L} = \int \Lambda \, \mathrm{d}\mathbf{X} \, \mathrm{d}t, \tag{2.91}$$

where $\Lambda = \Lambda(\hat{v}_i, \hat{f}_{iJ}, \hat{e}_a, \hat{h}_{aJ})$ is the Lagrangian. The first variation is

$$\delta\mathcal{L} = \int \left(-\left(\frac{\partial \Lambda_{\hat{v}_i}}{\partial t} + \frac{\partial \Lambda_{\hat{f}_{iJ}}}{\partial X_J} \right) \delta x_i - \left(\frac{\partial \Lambda_{\hat{e}_a}}{\partial t} + \frac{\partial \Lambda_{\hat{h}_{aJ}}}{\partial X_J} \right) \delta \chi_a \right) \mathrm{d}\mathbf{X} \, \mathrm{d}t, \tag{2.92}$$

and the $\delta\mathcal{L}$ is null for every possible perturbation if the individual integrands are null, i.e. if and only if the following Euler-Lagrange equations are valid

$$\frac{\partial \Lambda_{\hat{v}_i}}{\partial t} + \frac{\partial \Lambda_{\hat{f}_{iJ}}}{\partial X_J} = 0, \tag{2.93}$$

$$\frac{\partial \Lambda_{\hat{e}_a}}{\partial t} + \frac{\partial \Lambda_{\hat{h}_{aJ}}}{\partial X_J} = 0, \tag{2.94}$$

and the following integrability conditions, which are trivial consequences of definitions (2.90),

$$\frac{\partial \hat{f}_{iJ}}{\partial t} - \frac{\partial \hat{v}_i}{\partial X_J} = 0, \quad \frac{\partial \hat{f}_{iJ}}{\partial X_K} - \frac{\partial \hat{f}_{iK}}{\partial X_J} = 0, \tag{2.95}$$

$$\frac{\partial \hat{h}_{aJ}}{\partial t} - \frac{\partial \hat{e}_a}{\partial X_J} = 0, \quad \frac{\partial \hat{h}_{aI}}{\partial X_J} - \frac{\partial \hat{h}_{aJ}}{\partial X_I} = 0, \qquad a = 1, \dots, \mathrm{N}{-}1 \tag{2.96}$$

are satisfied. In order to obtain the fully conservative Lagrangian master system, that admits the original Godunov structure (2.41) we have to introduce a potential $\mathcal{U}$ as a partial Legendre transformation of the Lagrangian Λ

$$\begin{aligned} \mathrm{d}\mathcal{U} &= \mathrm{d}\left(\hat{v}_i \Lambda_{\hat{v}_i} + \hat{e}_a \Lambda_{\hat{e}_a} - \Lambda\right) \\ &= \hat{v}_i \mathrm{d}\Lambda_{\hat{v}_i} + \hat{e}_a \mathrm{d}\Lambda_{\hat{e}_a} - \Lambda_{\hat{f}_{iJ}} \mathrm{d}\hat{f}_{iJ} - \Lambda_{\hat{h}_{aJ}} \mathrm{d}\hat{h}_{aJ} \\ &= \hat{v}_i \mathrm{d}\Lambda_{\hat{v}_i} + \hat{e}_a \mathrm{d}\Lambda_{\hat{e}_a} + \Lambda_{\hat{f}_{iJ}} \mathrm{d}(-\hat{f}_{iJ}) + \Lambda_{\hat{h}_{aJ}} \mathrm{d}(-\hat{h}_{aJ}). \end{aligned} \tag{2.97}$$

which, denoting $\hat{m}_i = \Lambda_{\hat{v}_i}$, $\hat{\varrho}_a = \Lambda_{\hat{e}_a}$, $\hat{F}_{iJ} = -\hat{f}_{iJ}$, $\hat{w}_{aJ} = -\hat{h}_{aJ}$, yields the thermodynamic identity

$$\mathrm{d}\mathcal{U} = \mathcal{U}_{\hat{m}_i} \mathrm{d}\hat{m}_i + \mathcal{U}_{\hat{\varrho}_a} \mathrm{d}\hat{\varrho}_a + \mathcal{U}_{\hat{F}_{iJ}} \mathrm{d}\hat{F}_{iJ} + \mathcal{U}_{\hat{w}_{aJ}} \mathrm{d}\hat{w}_{aJ}\,. \tag{2.98}$$

Now, by collecting these quantities into a new Lagrangian vector of state variables $\hat{\mathbf{q}} = (\hat{m}_i, \hat{F}_{iJ}, \hat{w}_{aJ}, \hat{\varrho}_a)$ and using the potential $\mathcal{U} = \mathcal{U}(\hat{\mathbf{q}})$, equations (2.93),(2.94),(2.95),(2.96) can be transformed into the following minimal Lagrangian master system

$$\frac{\mathrm{d}\hat{m}_i}{\mathrm{d}t} - \frac{\partial \mathcal{U}_{\hat{F}_{iJ}}}{\partial X_J} = 0, \tag{2.99a}$$

$$\frac{\mathrm{d}\hat{F}_{iJ}}{\mathrm{d}t} - \frac{\partial \mathcal{U}_{\hat{m}_i}}{\partial X_J} = 0, \tag{2.99b}$$

$$\frac{\mathrm{d}\hat{w}_{aJ}}{\mathrm{d}t} + \frac{\partial \mathcal{U}_{\hat{\varrho}_a}}{\partial X_J} = 0, \qquad a = 1, \dots, \mathrm{N}{-}1, \tag{2.99c}$$

$$\frac{\mathrm{d}\hat{\varrho}_a}{\mathrm{d}t} + \frac{\partial \mathcal{U}_{\hat{w}_{aJ}}}{\partial X_J} = 0, \qquad a = 1, \dots, \mathrm{N}{-}1, \tag{2.99d}$$

which should be supplemented by stationary constraints (2.95) and (2.96) which now read as

$$\frac{\partial \hat{F}_{iJ}}{\partial X_K} - \frac{\partial \hat{F}_{iK}}{\partial X_J} = 0, \quad \frac{\partial \hat{w}_{aI}}{\partial X_J} - \frac{\partial \hat{w}_{aJ}}{\partial X_I} = 0, \qquad a = 1, \dots, \mathrm{N}{-}1. \tag{2.100}$$

The conversion from the SHTC Lagrangian master system (2.99) and (2.100), which admits the original Godunov (2.41) structure, to the Eulerian equations can be carried out by means of the Lagrange-to-Euler change of the spatial variables which results in the change of the time and spatial derivatives

$$\frac{\mathrm{d}}{\mathrm{d}t} = \frac{\partial}{\partial t} + v_k \frac{\partial}{\partial x_k}, \qquad \frac{\partial}{\partial X_J} = \hat{F}_{iJ} \frac{\partial}{\partial x_i}, \tag{2.101}$$

while the Lagrangian total energy density $\mathcal{U}(\hat{\mathbf{q}})$ is related to Eulerian total energy density $\mathcal{E}(\mathbf{q})$ as

$$\mathcal{U}(\hat{\mathbf{q}}) = \iota\, \mathcal{E}(\mathbf{q}) \quad \text{with} \quad \iota = \det(F_{iJ}) \tag{2.102}$$

Similarly, Lagrangian state variables $\hat{\mathbf{q}}$ are related to Eulerian fields $\mathbf{q} = (U_i,\, A_{Ji},\, w_{a,i},\, \varrho_a)$ by the formulae

$$\hat{m}_i = \iota\, U_i, \quad \hat{F}_{iJ} = A^{-1}_{Ji}, \quad \hat{w}_{aI} = \iota\, w_{a,i}, \quad \hat{\varrho}_a = \iota\, \varrho_a \tag{2.103}$$

Despite these simple definitions, the conversion to Eulerian equations is a non-trivial task and details can be found, for example, in [81], or in Appendix C of [55].

The resulting Eulerian master system has a more complicated structure than the fully conservative Lagrangian system (2.99), in fact the Eulerian equations are inherently non-conservative and admit only the generalized Godunov structure in (2.43). The resulting system of non-conservative Eulerian equations, formulated in terms of the state variables vector $\mathbf{q}$ and the total energy density $\mathcal{E}(\mathbf{q})$, reads

$$\frac{\partial U_i}{\partial t} + \frac{\partial}{\partial x_k}\Big(U_i\mathcal{E}_{U_k} + (\rho\mathcal{E}_\rho + U_i\mathcal{E}_{U_i} + \varrho_a\mathcal{E}_{\varrho_a} - \mathcal{E})\delta_{ik} + \\ + w_{a,i}\mathcal{E}_{w_{a,k}} + A_{Jk}\mathcal{E}_{A_{Ji}}\Big) = 0, \tag{2.104a}$$

$$\frac{\partial A_{Jk}}{\partial t} + \frac{\partial A_{Jl}\mathcal{E}_{U_l}}{\partial x_k} + \mathcal{E}_{U_i}\left(\frac{\partial A_{Jk}}{\partial x_i} - \frac{\partial A_{Ji}}{\partial x_k}\right) = 0, \tag{2.104b}$$

$$\frac{\partial w_{a,k}}{\partial t} + \frac{\partial\left(w_{a,l}\mathcal{E}_{U_l} + \mathcal{E}_{\varrho_a}\right)}{\partial x_k} + \mathcal{E}_{U_l}\left(\frac{\partial w_{a,k}}{\partial x_l} - \frac{\partial w_{a,l}}{\partial x_k}\right) = 0, \quad a=1,\dots,\mathrm{N}-1, \tag{2.104c}$$

$$\frac{\partial \varrho_a}{\partial t} + \frac{\partial\left(\varrho_a\mathcal{E}_{U_k} + \mathcal{E}_{w_{a,k}}\right)}{\partial x_k} = 0, \qquad a=1,\dots,\mathrm{N}-1, \tag{2.104d}$$

$$\frac{\partial \rho}{\partial t} + \frac{\partial\left(\rho\mathcal{E}_{U_k}\right)}{\partial x_k} = 0. \tag{2.104e}$$

where it should be noted that, with respect to the Lagrangian framework, here we usually also consider the mass conservation of the mixture Eq.(2.104e). In fact, especially for numerical reasons, it is useful to treat ρ as an independent state variable governed by its own time evolution.

Despite this consideration, it should be specified that, in this Eulerian framework, as was shown for example in [80, 135], the conservation of mass (2.104e) is the consequence of the time evolution (2.104b) for the distortion matrix $\mathbf{A}$ and therefore also in this case could be excluded from the governing system. Whereas, let's recall that in the Lagrangian framework it is not necessary to consider the mass conservation equation since the mass density is $\rho = \rho_o\,\iota^{-1}$. In this sense, the complementary equations of the Lagrangian pair (2.99a) and (2.99b) are the three equations (2.104a), (2.104b) and (2.104e) of the Eulerian SHTC master system.

Note also that an arbitrary number of equations with the structure of (2.104e) can be added to the system (2.104). In the specific case concerning the formulation of a unified multiphase model of continuum mechanics, the variables under consideration are specified in the state vector $\mathbf{Q}$. Accordingly, the resulting system formulated in terms of the state variables $\mathbf{Q}$ and the total energy density $\mathcal{E}(\mathbf{Q})$, the entropy conservation laws η_a and the time evolution of the volume fraction through φ_a are considered, therefore (2.104) becomes

$$\frac{\partial U_i}{\partial t}+\frac{\partial\left(U_iV_k+P\delta_{ik}+w_{a,i}\mathcal{E}_{w_{a,k}}+A_{Jk}\mathcal{E}_{A_{Ji}}\right)}{\partial x_k}=0, \tag{2.105a}$$

$$\frac{\partial A_{Jk}}{\partial t}+\frac{\partial A_{Jl}V_l}{\partial x_k}+V_i\left(\frac{\partial A_{Jk}}{\partial x_i}-\frac{\partial A_{Ji}}{\partial x_k}\right)=0, \tag{2.105b}$$

$$\frac{\partial w_{a,k}}{\partial t}+\frac{\partial\left(w_{a,l}V_l+\mathcal{E}_{\varrho_a}\right)}{\partial x_k}+V_l\left(\frac{\partial w_{a,k}}{\partial x_l}-\frac{\partial w_{a,l}}{\partial x_k}\right)=0, \qquad a{=}1,\dots,\mathrm{N}{-}1, \tag{2.105c}$$

$$\frac{\partial\varrho_a}{\partial t}+\frac{\partial\left(\varrho_aV_k+\mathcal{E}_{w_{a,k}}\right)}{\partial x_k}=0, \qquad a{=}1,\dots,\mathrm{N}{-}1, \tag{2.105d}$$

$$\frac{\partial\varphi_a}{\partial t}+\frac{\partial\left(\varphi_aV_k\right)}{\partial x_k}=0, \qquad a{=}1,\dots,\mathrm{N}{-}1, \tag{2.105e}$$

$$\frac{\partial\rho}{\partial t}+\frac{\partial\left(\rho V_k\right)}{\partial x_k}=0, \tag{2.105f}$$

$$\frac{\partial\eta_a}{\partial t}+\frac{\partial(\eta_aV_k)}{\partial x_k}=0, \qquad a{=}1,\dots,\mathrm{N}, \tag{2.105g}$$

where the velocity field V_k is introduced since is always the conjugate field of the total momentum, i.e., $V_k=\mathcal{E}_{U_k}$, and where the definition of thermodynamic mixture pressure P, in (2.81), was also used. Equations (2.105) are the multiphase, multi-pressure, and multi-speed SHTC governing equations in a Cartesian coordinate system, with $k=1,2,3$, for an arbitrary number of non-heat conducting phases, denoted by $a=1,\dots,\mathrm{N}$, which can describe Newtonian and non-Newtonian, inviscid and viscous fluids, as well as elasto-plastic solids.

The governing system (2.105) for multiphase fluid and solid mechanics is not a system of conservation laws because of the presence of non-conservative differential terms,

$$V_i\left(\frac{\partial A_{Jk}}{\partial x_i}-\frac{\partial A_{Ji}}{\partial x_k}\right), \qquad V_l\left(\frac{\partial w_{a,k}}{\partial x_l}-\frac{\partial w_{a,l}}{\partial x_k}\right), \tag{2.106}$$

in equations (2.105b) and (2.105c), respectively. As we have already mentioned, the terms in (2.106) are an intrinsic part of the structure of the Eulerian SHTC equations and are a result of the following stationary geometric involution constraints

$$\nabla\times\mathbf{A}=\mathbf{B}, \qquad \nabla\times\mathbf{w}_a=\boldsymbol{\omega}_a, \tag{2.107}$$

which are satisfied by the solutions of (2.105), if they hold true at time $t = 0$. In component-wise notations, these involution constraints, by means of the Levi-Civita symbol ϵ_{ijk}, read

$$\epsilon_{ijk}\frac{\partial A_{Jk}}{\partial x_j} = B_{Ji}, \qquad \epsilon_{ijk}\frac{\partial w_{a,k}}{\partial x_j} = \omega_{a,k}, \tag{2.108}$$

where the quantities B_{Ji} and $\omega_{a,k}$ satisfy the following conservation laws

$$\frac{\partial B_{Ji}}{\partial t} + \frac{\partial \left(B_{Ji}V_k - B_{Jk}V_i\right)}{\partial x_k} + V_i\frac{\partial B_{Jk}}{\partial x_k} = 0, \tag{2.109}$$

$$\frac{\partial \omega_{a,j}}{\partial t} + \frac{\partial \left(\omega_{a,j}V_k - \omega_{a,k}V_j\right)}{\partial x_k} + V_j\frac{\partial \omega_{a,k}}{\partial x_k} = 0. \tag{2.110}$$

and have a certain physical meaning. For instance, $\mathbf{B}$, has the meaning of a dislocation density tensor [135] in elatoplasticity theory. In general, for plasticity or viscosity, if the phase has undergone an irreversible dissipative process, one has $\nabla \times \mathbf{A} \neq 0$, and since usually this *irreversible dynamics* is time-dependent, the system (2.105) has non-trivial time-dependent solutions in which these involution constraints are non-zero terms.

2.2.8 Irreversible dynamics, dissipative processes

In the SHTC theory, a dissipative process is associated with the irreversible part of the time evolution equations that increases the entropy of the system and that is modeled via algebraic relaxation source terms [132], i.e. the hyperbolic nature of PDEs is not affected. They are defined in terms of the gradients of the energy $\mathcal{E}_{\mathbf{Q}}$, (i.e. in terms of the conjugate state variables), thus the irreversible part of the SHTC equations can be called the gradient dynamics [130, 132].

Therefore, the following arbitrary functions of the conjugate state variables can be added

$$Z_{Jk}(\mathcal{E}_{A_{Jk}}), \quad \Lambda_{a,k}(\mathcal{E}_{w_{b,k}}), \quad \chi_a(\mathcal{E}_{\varrho_b}), \quad \Phi_a(\mathcal{E}_{\varphi_b}), \quad \pi_a(\mathcal{E}_{\eta_b}), \tag{2.111}$$

in the right-hand side of the system equations (2.105)

$$\frac{\partial U_i}{\partial t} + \frac{\partial \left(U_i V_k + P\delta_{ik} + w_{a,i}\mathcal{E}_{w_{a,k}} + A_{Jk}\mathcal{E}_{A_{Ji}}\right)}{\partial x_k} = 0, \tag{2.112a}$$

$$\frac{\partial A_{Jk}}{\partial t} + \frac{\partial A_{Jl}V_l}{\partial x_k} + V_i\left(\frac{\partial A_{Jk}}{\partial x_i} - \frac{\partial A_{Ji}}{\partial x_k}\right) = Z_{Jk}, \tag{2.112b}$$

$$\frac{\partial w_{a,k}}{\partial t} + \frac{\partial \left(w_{a,l}V_l + \mathcal{E}_{\varrho_a}\right)}{\partial x_k} + V_l\left(\frac{\partial w_{a,k}}{\partial x_l} - \frac{\partial w_{a,l}}{\partial x_k}\right) = \Lambda_{a,k}, \quad a = 1, \dots, \mathrm{N}{-}1, \tag{2.112c}$$

$$\frac{\partial \varrho_a}{\partial t} + \frac{\partial \left(\varrho_a V_k + \mathcal{E}_{w_{a,k}}\right)}{\partial x_k} = \chi_a, \qquad a = 1, \dots, \mathrm{N}{-}1, \tag{2.112d}$$

$$\frac{\partial \varphi_a}{\partial t} + \frac{\partial \left(\varphi_a V_k\right)}{\partial x_k} = \Phi_a, \qquad a = 1, \dots, \mathrm{N}{-}1, \tag{2.112e}$$

$$\frac{\partial \rho}{\partial t} + \frac{\partial \left(\rho V_k\right)}{\partial x_k} = 0, \tag{2.112f}$$

$$\frac{\partial \eta_a}{\partial t} + \frac{\partial (\eta_a V_k)}{\partial x_k} = \pi_a + \Pi_a, \qquad a = 1, \dots, \mathrm{N}, \tag{2.112g}$$

where no sources are considered for the conservation of momentum and mass of the mixture, since mass and momentum must always be exactly conserved. Moreover, since the terms in (2.111) are quite arbitrary, Π_a must be introduced in (2.112g) to ensure consistency with the first and second laws of thermodynamics. For instance, this term is necessary to guarantee that

$$A_{Jk}Z_{Jk} + w_{b,k}\Lambda_{a,k} + \varrho_b\chi_a + \varphi_b\Phi_a + \eta_b\pi_a \equiv 0, \tag{2.113}$$

which is required by the energy summation rule in (2.44), see detail in Section 2.2.9.

Strain relaxation, Z_{Jk}

The strain relaxation source Z_{Jk}, for the distortion field A_{Jk}, takes the form

$$Z_{Jk} := -\frac{1}{\rho}\Upsilon\,\mathcal{E}_{A_{Jk}}, \qquad \mathcal{E}_{A_{Jk}} = \rho\,\mathrm{Cs}^2\,A_{Ji}\,\mathrm{dev}\,G_{ik}, \tag{2.114}$$

where Υ it's a positive relaxation scaling functions, which according to [131], is taken equal to

$$\Upsilon = \frac{3}{\tau^{\mathrm{e}}}\,\mathrm{Cs}^{-2}\,\det(A_{Jk})^{5/3}. \tag{2.115}$$

The parameter τ^{e} is the so-called *strain relaxation time*, which governs the rate at which the strain, in a given control volume, is dissipated trough this dissipative process. When $\tau^{\mathrm{e}} \to 0$ a state of strain equilibrium is achieved instantaneously and therefore inviscid flow is retrieved, while for $\tau^{\mathrm{e}} \to \infty$ the relaxation process is infinitely slow and the behaviour of a pure elastic solid is retrieved.

Interphase friction, $\Lambda_{a,k}$

The second dissipative process considered is the relative velocity relaxation towards zero, due to the interfacial friction, and appear as source terms in the relative velocity equations. This is modelled by the functions

$$\Lambda_{a,k} := -\frac{1}{\rho}\sum_{b=1}^{\mathrm{N}-1}\lambda_{ab,k}\mathcal{E}_{w_{b,k}}, \qquad \mathcal{E}_{w_{b,k}} = \frac{\partial \mathcal{E}}{\partial w_{b,k}} = \varrho_b(v_{b,k} - V_k), \tag{2.116}$$

where the kinetic coefficients $\lambda_{ab,k} = \lambda_{ab,k}(\mathbf{Q})$ are the entries of three ($k = 1, 2, 3$) symmetric positive semi-definite matrices.

Pressure relaxation, Φ_a

The dissipative process related to the pressure relaxation towards a common pressure are introduced as source terms in the volume fraction conservation laws of the phases by the functions

$$\Phi_a := -\rho\sum_{b=1}^{\mathrm{N}-1}\varphi_{ab}\mathcal{E}_{\varphi_b}, \qquad \mathcal{E}_{\varphi_a} = \frac{\partial \mathcal{E}}{\partial \varphi_a} = -\frac{p_a - p_{\mathrm{N}}}{\rho}, \tag{2.117}$$

where $\varphi_{ab} = \varphi_{ab}(\mathbf{Q})$ are the kinetic coefficients which again are the entries of a symmetric positive semi-definite matrix.

Kinetics of phase transformation, χ_a

For the sake of completeness, we also mention how chemical kinetics can be introduced into the SHTC mixture equations. In order to achieve this, it is necessary to introduce the χ_a sources into the true mass density equations, which are defined as

$$\chi_a := -\rho\sum_{b=1}^{\mathrm{N}-1}\chi_{ab}\mathcal{E}_{\varrho_b}, \quad \mathcal{E}_{\varrho_a} = \frac{\partial \mathcal{E}}{\partial \varrho_a} = \mu_a - \mu_{\mathrm{N}} + \frac{1}{2}\sum_{k=1}^{3} w_{a,k}^2 - \frac{1}{\rho}\sum_{k=1}^{3}\sum_{b=1}^{\mathrm{N}-1}\varrho_b w_{b,k} w_{a,k} \tag{2.118}$$

where the kinetic coefficients $\chi_{ab} = \chi_{ab}(\mathbf{Q})$ form a symmetric positive semi-definite matrix.

Temperature relaxation, π_a

Finally, the source terms π_a in the phase entropy equations are defined as

$$\pi_a := -\varrho_a \frac{\mathcal{E}_{\eta_a} - \sum\limits_{b=1}^{\mathrm{N}} \frac{\varrho_b}{\rho}\mathcal{E}_{\eta_b}}{\tau^{\mathrm{h}}\mathcal{E}_{\eta_a}} = \varrho_a \frac{T_a - \sum\limits_{b=1}^{\mathrm{N}} c_b T_b}{\tau^{\mathrm{h}}\, T_a}, \tag{2.119}$$

and they model the phase temperature relaxation towards the common temperature

$$T := \sum_{a=1}^{\mathrm{N}} c_a T_a \tag{2.120}$$

which can be called the temperature of the mixture control volume. Here, τ^{h} is a relaxation parameter that characterizes the rate at which the temperature equilibrium $T_1 = ... = T_{\mathrm{N}} = T$ is approached by the system.

The dissipative processes Φ_a, $\Lambda_{a,k}$, and χ_a are defined in such a way that they diminish the thermodynamic forces $\mathcal{E}_{\varphi_a}$, $\mathcal{E}_{w_{a,k}}$, and $\mathcal{E}_{\chi_a}$, i.e they lead the mixture towards a thermodynamic equilibrium state at which these forces must vanish $\mathcal{E}_{\varphi_a} = 0$, $\mathcal{E}_{w_{a,k}} = 0$, and $\mathcal{E}_{\chi_a} = 0$, while the temperature relaxation π_a tends to make the phase temperatures equal.

Entropy production terms, Π_a

The remaining undefined dissipative terms, the entropy production terms Π_a, $a = 1, ..., \mathrm{N}$, serve the goal of making the system compatible with the two laws of thermodynamics. Therefore, to fulfill the first and second law of thermodynamics (see the next section for the details), Π_a must be defined as

$$\Pi_a := \frac{\varrho_a}{\mathcal{E}_{\eta_a}\rho}\sigma \geq 0 \tag{2.121}$$

where

$$\begin{aligned}\sigma := \frac{1}{\mathrm{N}}\mathcal{E}_{A_{Ji}} Z_{Jk} + \sum_{b=1}^{\mathrm{N}-1}\left(\mathcal{E}_{\varphi_b}\Phi_b + \sum_{k=1}^{3}\mathcal{E}_{w_{b,k}}\Lambda_{b,k} + \mathcal{E}_{\varrho_b}\chi_b\right) = \\ \frac{1}{\rho\,\mathrm{N}}\mathcal{E}_{A_{Ji}}\Upsilon\,\mathcal{E}_{A_{Jk}} + \sum_{b=1}^{\mathrm{N}-1}\sum_{c=1}^{\mathrm{N}-1}\left(\rho\mathcal{E}_{\varphi_b}\varphi_{bc}\mathcal{E}_{\varphi_c} + \sum_{k=1}^{3}\rho^{-1}\mathcal{E}_{w_{b,k}}\lambda_{bc,k}\mathcal{E}_{w_{c,k}} + \right. \\ \left. + \rho\mathcal{E}_{\varrho_b}\chi_{bc}\mathcal{E}_{\varrho_c}\right) \geq 0.\end{aligned} \tag{2.122}$$

Remark that, in general, the sign of each $\Pi_a \geq 0$ is definite due to the choice of the kinetic coefficients φ_{ab}, $\lambda_{ab,k}$, and χ_{ab} that are the entries of the positive semi-definite matrices.

Yet, the phase entropies may decrease due to the presence of the temperature relaxation terms π_a that makes the sign of $\Pi_a - \pi_a$, in general, indefinite. This of course doesn't contradict the second law because the mixture constituents are not isolated systems. However, as discussed in the next section, this choice of Π_a guaranties the fulfillment of the second law of thermodynamics for the entire mixture.

2.2.9 Consistency with the first and second laws of thermodynamics

One may notice that the total energy conservation law (first law of thermodynamics) is not listed within the set of equations (2.112). In fact, one of the main features of all the SHTC models [81, 85, 132, 149, 150] is that the energy conservation law

$$\frac{\partial \mathcal{E}}{\partial t} + \frac{\partial}{\partial x_k}\Big(\mathcal{E} V_k + V_k(P\delta_{ik} + w_{a,i}\mathcal{E}_{w_{a,k}} + A_{Jk}\mathcal{E}_{A_{Ji}}) + \mathcal{E}_{\varrho_a}\mathcal{E}_{w_{a,k}}\Big) = 0 \quad (2.123)$$

is automatically fulfilled for solutions of system (2.112). In other words, the energy conservation law can be obtained as a linear combination of the governing equations (2.112) multiplied with certain coefficients (the thermodynamic conjugate variables or main-field variables [111]), as stated in (2.44). Thus, Eq.(2.123) can be obtained as the following linear combination of equations (2.112) multiplied by the corresponding factors, which are the thermodynamic forces $\mathcal{E}_{\mathbf{Q}}$

$$\begin{aligned}(2.123) \equiv \mathcal{E}_\rho \cdot (2.112\text{f}) + \mathcal{E}_{U_i} \cdot (2.112\text{a}) + \mathcal{E}_{A_{Jk}} \cdot (2.112\text{b}) + \mathcal{E}_{\varphi_a} \cdot (2.112\text{e}) + \\ + \mathcal{E}_{\varrho_a} \cdot (2.112\text{d}) + \mathcal{E}_{w_{a,k}} \cdot (2.112\text{c}) + \mathcal{E}_{\eta_a} \cdot (2.112\text{g}).\end{aligned} \quad (2.124)$$

However, we can obtain zero in the right hand-side of (2.123) by these means only if we define the phase entropy production terms Π_a as in (2.121). Note that the temperature relaxation terms π_a are defined in such a way that

$$\sum_{a=1}^{\mathrm{N}} \mathcal{E}_{\eta_a}\pi_a = \sum_{a=1}^{\mathrm{N}} T_a\pi_a = 0. \quad (2.125)$$

As we have already mentioned, if the relaxation processes discussed in the previous section are taken into account, our choice (2.121) of the phase entropy production terms Π_a cannot guarantee positive sign of $\Pi_a - \pi_a$. However, the mixture itself (in the absence of exchange with the exterior) is an isolated system and the second law must hold. Thus, our choice of the phase entropy production terms Π_a not only guarantees the energy conservation law for the entire mixture (the first law of thermodynamics) but also the second law. Indeed, the mixture entropy density is defined as

$$\eta = \eta_1 + ... + \eta_{\mathrm{N}} \tag{2.126}$$

and fulfills the entropy balance law

$$\frac{\partial \eta}{\partial t} + \frac{\partial (\eta V_a)}{\partial x_k} = \Pi + \pi \geq 0, \tag{2.127a}$$

$$\Pi := \sum_{a=1}^{\mathrm{N}} \Pi_a = \left(\frac{c_1}{T_1} + ... + \frac{c_{\mathrm{N}}}{T_{\mathrm{N}}} \right) \sigma \geq 0, \tag{2.127b}$$

$$\pi = -\sum_{a=1}^{\mathrm{N}} \pi_a = \frac{1}{2} \mathrm{tr} \left(M^{\mathrm{T}} M \right) \geq 0, \tag{2.127c}$$

where M_{ab} is a symmetric matrix with the entries

$$M_{ab} = \sqrt{\frac{\varrho_a \varrho_b}{\rho \tau} \frac{(T_a - T_b)^2}{T_a T_b}}, \qquad a, b = 1, ..., \mathrm{N}, \tag{2.128}$$

and the sign on the right hand side of (2.127b) is guarantied by the choice of the kinetic coefficients φ_{ab}, $\lambda_{ab,k}$, and χ_{ab} that form positive semi-definite matrices.

2.3 The SHTC model compared with the classical approach, a BN-type form

As anticipated in the Introduction 1, it is of particular interest to compare the structure of the newly derived model within the SHTC formalism, presented in Section 2.2, with the structure of models obtained through a classical approach. In particular, comparing it with one of the most prominent ones that follows this approach, which is the model originally introduced by Baer and Nunziato [3], also briefly analysed in Section 2.1.

We have seen that the standard approach of deriving governing equations for multiphase flows leads to a system of governing equations in the form of mass, momentum, and energy balance laws for each phase, coupled with some terms that account for interactions or exchanges among constituents. These interactions are described with differential terms that are usually unknown and whose rigorous formulation requires complex additional considerations. This structure is referred to in the following as *BN-type form* of the governing equations. Moreover, we have seen in Section 2.1 that the BN model [3] is nowadays usually referred to in a simplified form, for compressible two-phase flows, in which the interactions between constituents are assumed to be given only by contributions proportional to the gradients of volume fraction of the phases through two so-called interphase pressure and velocity coefficients. Finally, the difficulties inherent in formulating a generalized *closed* model to mixtures with an arbitrary number of phases, both historically and conceptually following the classical approach, are evident.

In Section 2.2, we showed how a unified theory of multiphase fluid and solid mechanics can be formulated within the SHTC formalism. More specifically, we saw how a mixture can be uniquely described through the appropriate choice of a vector of state variables (2.58) and the definition of a thermodynamic potential (2.77). It can be seen that the vector of SHTC state variables sought differs from that usually adopted in the classical formulation of conservation laws for multiphase flows. Therefore, the governing equations of the SHTC theory describe the evolution of different quantities than those of the BN model. Thus, in order to compare the two models, a rewriting of the SHTC governing equations is necessary.

Furthermore, another important consideration concerns the interaction between the constituents. In the theory of SHTC systems, dissipative processes are formulated through gradients of the total energy potential, which is defined rigorously in the mixture theory, and give rise to strictly algebraic source terms that satisfy the thermodynamic laws and that do not affect the hyperbolic nature of PDEs.

2.3.1 A BN-type form of the SHTC multiphase model

In order to compare the structure of the multiphase SHTC model (2.112) with the BN-type structure, the system of PDEs in (2.112) is rewritten in terms of mass, momentum and phase energy balance laws.

All the dissipative source terms of the SHTC model are deliberately kept in the BN-type form. While, this rewriting of the SHTC system is done by excluding the evolution equation for the distortion field of the mixture A_{Ji}, since the rigorous derivation of the different distortion fields $A_{a,Ji}$ related to each phase, which are required in a classical description of the mixture through the quantities describing the individual constituents, from a single mixture distortion field is so far under investigation.

In the following BN-type form of the SHTC mixture equations all the resulting Euler-like terms are collected on the left-hand side, while the *interphase exchange terms* and the terms arising from the dissipative processes considered in Section 2.2.8 are collected on the right-hand side.

The phase mass balance equations

The evolution equations in (2.112d) can be immediately rewritten in a more traditional form using the definition of the mixture velocity $\boldsymbol{V}$ and the expression of $\mathcal{E}_{w_{a,k}}$, given in (2.87d),

$$\frac{\partial \varrho_a}{\partial t} + \frac{\partial \left(\varrho_a v_{a,k}\right)}{\partial x_k} = \chi_a. \tag{2.129}$$

The phase volume fraction equation

The phase volume fraction equations can be retrieved from the equations (2.112e), using the conservation of total mass and balance laws of the phase densities (2.129), and read

$$\frac{\partial \alpha_a}{\partial t} + V_k \frac{\partial \alpha_a}{\partial x_k} = \frac{1}{\rho} \Phi_a. \tag{2.130}$$

Thus, comparing with the BN model, one can conclude that the interface velocity $v_{\mathrm{I},k}$ of the BN model is replaced by the mixture velocity V_k in the SHTC model, as was already noticed in [145, 146].

The phase momentum equations

The balance laws for the phase momenta can be obtained from the mixture momentum conservation and relative velocity equations in the following way.

Let $\mathcal{D}^U_i$ represents the mixture momentum equation (2.105a), $\mathcal{D}^w_{a,i}$ represents the relative velocity equations (2.105c), and $\mathcal{D}^u_{a,i}$ represents the phase momentum equations that we need to derive. Then, the phase momentum balance equations can be obtained as

$$\mathcal{D}^u_{a,i} = \frac{\varrho_a}{\rho}\mathcal{D}^U_i - \frac{\varrho_a}{\rho}\sum_{b=1}^{\mathrm{N}} \varrho_b \mathcal{D}^w_{b,i} + \varrho_a \mathcal{D}^w_{a,i}. \tag{2.131}$$

After lengthy but rather straightforward manipulations of the terms in (2.131), the individual phase momentum balance equations can be written as

$$\frac{\partial u_{a,i}}{\partial t} + \frac{\partial}{\partial x_k}\left(u_{a,i}v_{a,k} + P_a\delta_{ki}\right) = - c_a \sum_{b=1}^{\mathrm{N}} p_b \frac{\partial \alpha_b}{\partial x^i} + p_a \frac{\partial \alpha_a}{\partial x^i} \tag{2.132a}$$

$$- c_a \sum_{b=1}^{\mathrm{N}} \varrho_b \bar{v}_{b,k}\omega_{b,k,i} + \varrho_a \bar{v}_{a,k}\omega_{a,k,i} \tag{2.132b}$$

$$- c_a \sum_{b=1}^{\mathrm{N}} \varrho_b s_b \frac{\partial T_b}{\partial x^i} + \varrho_a s_a \frac{\partial T_a}{\partial x^i} \tag{2.132c}$$

$$+ c_a \sum_{b=1}^{\mathrm{N}} \varrho_b \Lambda_{b,i} - \varrho_a \Lambda_{a,i} \tag{2.132d}$$

$$+ c_a \sum_{b=1}^{\mathrm{N}} v_{b,i}\chi_b - v_{a,i}\chi_a, \tag{2.132e}$$

where

$$\omega_{a,k,i} := \frac{\partial w_{a,i}}{\partial x_k} - \frac{\partial w_{a,k}}{\partial x_i} \tag{2.133}$$

and $\bar{v}_{a,k}$ as previously defined in (2.57). Here, the presence of the phase transformation terms χ_a is due to appearance of $\partial \varrho_a / \partial t$ and the need to replace them by their expressions from (2.129).

The phase momentum equations (2.132) derived from the SHTC mixture equations can be compared with those of the original BN model in order to understand some differences between the two approaches. The main one concerns the fact that in the momentum equations derived from the SHTC mixture theory (2.132), a closed form of the terms resulting from the interaction of the constituents is naturally obtained. These interphase exchange terms are collected on the right-hand side of (2.132). The last two (2.132d) and (2.132e) are contributions from the dissipative processes considered in the previous paragraph, respectively concerning relative velocity relaxation and the presence of the phase transformation. Whereas the other terms, (2.132a, 2.132b, 2.132c), arise naturally by deriving a BN-type form of the SHTC mixture equations, i.e. they are naturally univocally defined from a mixture theory described by a set of variables capable of capturing the multiphase character of the flow.

The first term, given by (2.132a), is the only one directly comparable with the original BN model, since in this model inter-phase exchange terms are only given by a contributions proportional to the volume fraction gradients. Similarly, in the equations derived from the SHTC theory, the terms in (2.132a) contain the phase volume fraction gradients, however, with known coefficients which can be seen as an unambiguous way to evaluate an interphase pressure, in an analogy with the BN formalism.

The second, given by (2.132b), contains the gradients of the phase velocities organised to express the phase velocity vortices and represents the so-called lift forces.

The last one, (2.132c), is proportional to the phase temperature gradient, and can also be expressed, after some manipulation, as the phase entropy gradient.

Since there is no rigorous derivation of the original BN model, the similarity found in the interphase terms proportional to volume fraction suggests that in a more complete BN-type multiphase model one should consider all the terms that appear in closed form thanks to the SHTC mixture theory.

The phase energy equations

The phase energy balance laws can be obtained from the conservation equations of mixture momentum, relative velocity and entropy, similarly to the phase momentum equations, after a lengthy manipulation.

However, this procedure is not illustrated in this work, since the energy equations depend directly on the momenta PDEs, and the latter already fulfill the comparative purpose of this section by making the interphase terms clear.

2.3.2 Multi-distortion extension of the BN formulation of SHTC equations

According to the unified model of continuum mechanics [131] and SHTC formulation for multiphase flows [143, 145], a true non-equilibrium multiphase model should have, in general, different pressures, temperatures, velocities, distortion fields, and etc. for each phase. However, at the moment, it is only known how to derive the SHTC multiphase model for the case when the phase distortions are equal, $\mathbf{A}_1 = \mathbf{A}_2 = ... = \mathbf{A}_{\mathrm{N}} = \mathbf{A}$. Therefore, in this section a heuristic extension of the SHTC multiphase model in its BN form to the case of different phase distortions $\mathbf{A}_a$ is discussed.

Thus, to extend the SHTC multiphase model in its BN form to the multi-distortion formulation, we employ a heuristic approach and simply introduce the phase distortion fields $\mathbf{A}_a = \{A_{a,Jk}\}$ for each phase $a = 1, \dots, \mathrm{N}$ and assume that each $\mathbf{A}_a$ is advected by the phase velocity $\boldsymbol{v}_a$, i.e. we add to system (2.129,2.130, 2.132,) the following equations for the phase distortion fields

$$\frac{\partial A_{a,Jk}}{\partial t} + \frac{\partial \left(A_{a,Jl} v_{a,l}\right)}{\partial x_k} + v_{a,i}\left(\frac{\partial A_{a,Jk}}{\partial x_i} - \frac{\partial A_{a,Ji}}{\partial x_k}\right) = Z_{a,Jk}, \tag{2.134}$$

for the dynamic of $A_{a,Jk}$ should be added for each phase. Specifically, with this extension to continuous mechanics, the total energy density $\mathcal{E}$ of the mixture (2.77) should be modified by taking into account the energy density associated with the elastic shear stresses $\varepsilon_{s,a}$ of the constituents, rather than of the mixture, and would result

$$\mathcal{E} = \sum_{a=1}^{\mathrm{N}} \varepsilon_{s,a} + \varepsilon_a + W(\rho, \varrho_1, \dots, \varrho_{\mathrm{N}-1}, \boldsymbol{w}_a, \dots, \boldsymbol{w}_{\mathrm{N}-1}) + \frac{1}{2\rho}\sum_{k=1}^{3} U_k^2. \tag{2.135}$$

As previously introduced in Section 2.2.6, the phase energy densities associated with the elastic-shear stresses, $\varepsilon_{s,a}$, are assumed to be proportional to the second invariant of the deviator $\operatorname{dev} G_{a,ij} = G_{a,ij} - (\operatorname{tr} G_{a,ik}/3)\,\delta_{ki}$ of the metric tensor $G_{a,ij} = A_{a,Ji}\,A_{a,Jj}$, and read

$$\varepsilon_{a,s} = \varrho_a\,\mathrm{Cs}_a^2\ \operatorname{tr}\left(\operatorname{dev} G_{a,ik}\operatorname{dev} G_{a,kj}\right)/4, \tag{2.136}$$

where Cs_a, in this case, represent the phase shear sound velocity. Thus, the conjugate variables of the phase distortion fields $A_{a,Jk}$ are

$$\mathcal{E}_{A_{a,Jk}} = \varrho_a\,\mathrm{Cs}_a^2\,A_{a,Ji}\operatorname{dev} G_{a,ik}, \tag{2.137}$$

by which the phase moment equations (2.132) can be modified introducing, by analogy, the elastic shear stresses $\sigma_{a,ik}$

$$
\begin{aligned}
\frac{\partial u_{a,i}}{\partial t}+\frac{\partial(u_{a,i}v_{a,k}+P_a\delta_{ki}+\sigma_{a,ik})}{\partial x_k} =&-c_a\sum_{b=1}^{\mathrm{N}} p_b\frac{\partial\alpha_b}{\partial x^i}+p_a\frac{\partial\alpha_a}{\partial x^i}+\\
&-c_a\sum_{b=1}^{\mathrm{N}}\varrho_b\bar{v}_{b,k}\omega_{b,k,i}+\varrho_a\bar{v}_{a,k}\omega_{a,k,i}\\
&-c_a\sum_{b=1}^{\mathrm{N}}\varrho_b s_b\frac{\partial T_b}{\partial x^i}+\varrho_a s_a\frac{\partial T_a}{\partial x^i}+\\
&+c_a\sum_{b=1}^{\mathrm{N}}\varrho_b\Lambda_{b,i}-\varrho_a\Lambda_{a,i}\\
&+c_a\sum_{b=1}^{\mathrm{N}}v_{b,i}\chi_b-v_{a,i}\cdot\chi_a,
\end{aligned}
\tag{2.138}
$$

which are defined as follows

$$
\begin{aligned}
\sigma_{a,ik}=A_{a,Ji}\mathcal{E}_{A_{a,Jk}} &= A_{a,Ji}(\varrho_a\,\mathrm{Cs}_a^2\,A_{a,Jj}\,\mathrm{dev}\,G_{a,jk})\\
&=\varrho_a\,\mathrm{Cs}_a^2\,G_{a,ij}\,\mathrm{dev}\,G_{a,jk}.
\end{aligned}
\tag{2.139}
$$

It should also be noted that there are likely to be phase interaction terms due to $A_{a,Jk}$ in the RHS of (2.138), but since we do not yet have a rigorous derivation of the multiple distortions, they are neglected at this point.

The dissipative process related to the strain relaxation source $Z_{a,Jk}$ in (2.134), must again be defined by conjugate variables, as done in 2.2.8. Specifically, for each constituent, $Z_{a,Jk}$ takes the form

$$
Z_{a,Jk}:=-\frac{1}{\varrho_a}\,\Upsilon_a\,\mathcal{E}_{A_{a,Jk}},
\tag{2.140}
$$

where Υ_a now is a positive relaxation scaling functions, which is taken equal to

$$
\Upsilon_a=\frac{3}{\tau_a^{\mathrm{e}}}\,\mathrm{Cs}_a^{-2}\,\det(A_{a,Jk})^{5/3}.
\tag{2.141}
$$

The parameter τ_a^{e} is the phase-specific strain relaxation time. Namely, it is a timescale that governs the rate at which the strain, in a given control volume, is dissipated trough a relaxation process for the phase a. This timescale defines the stiff nature of the strain relaxation source term towards an equilibrium state of material deformation, e.g.

i for $\tau_a^{\mathrm{e}} \to 0$, the so-called stiff relaxation limit, a state of strain equilibrium is achieved instantaneously and therefore inviscid flow is retrieved;

ii for τ_a^{e} small with respect to the timescale of flow convection the model reproduces the Navier-Stokes equations of viscous fluids, for the chosen shear energy, it can be computed to fit the kinematic viscosity ν_a of a fluid as $\tau_a^{\mathrm{e}} = 6\nu_a/\mathrm{Cs}_a^2$;

iii for $\tau_a^{\mathrm{e}} \to \infty$ the relaxation process is infinitely slow and the behaviour of a pure elastic solid is retrieved.

The relaxation time τ_a^{e}, in principle can be a function of the state variables, but often is assumed to be a fixed parameter. In the multiphase context, it is useful to define it as a function of the volume fraction α_a for each phase, by means of a smooth logarithmic interpolation, which can be computed as follows

$$\tau_a^{\mathrm{e}} = \tau_a^{\mathrm{e}\,\xi}\ \tau_{\mathrm{o}}^{(e)\,1-\xi}, \tag{2.142}$$

where ξ can be evaluated by

$$\delta\alpha = \frac{\alpha_a - \alpha_{\mathrm{m}}}{\alpha_{\mathrm{M}} - \alpha_{\mathrm{m}}}, \quad \delta\alpha = \max\big(0,\, \min(1,\, \delta\alpha)\big), \quad \xi = \delta\alpha^2\,(3 - 2\,\delta\alpha), \tag{2.143}$$

which results in a smooth transition from τ_a^{e} to $\tau_{\mathrm{o}}^{\mathrm{e}}$, where $\tau_{\mathrm{o}}^{\mathrm{e}}$ is usually assumed to be a small constant like 10^{-14}. Then, α_{M} and α_{m} represent the extrema at which this operator makes the transition. In this way, where a phase is not present, the *strain is dissipated instantaneously*, as for a prefect fluid, and no stresses are generated in the respective momentum conservation equation. This rescaling of the relaxation time is well suited to multimaterial problems, and in the rest of the paper is referred to as *vanishing ghost solid relaxation time.*

3 Numerical methods

This chapter is devoted to the derivation of various numerical methods, tailored to the different mathematical models presented in Chapter 2.

The numerical methods that will be presented in this chapter must deal with the difficulties involved in describing more than one phase. Overall, there are three different families of numerical methods for dealing with multi-material and multiphase problems: (i) Lagrangian and Arbitrary-Lagrangian-Eulerian (ALE) methods on moving meshes, where the free surface of the fluid and the fluid-solid interface are exactly solved by the moving computational grid, see e.g. [11, 15, 17, 21, 50, 73, 101, 102]; (ii) Eulerian sharp interface methods on fixed meshes with explicit interface reconstruction, see for instance the volume of fluid (VOF) method originally developed by Hirt and Nichols [89], or the ghost fluid method of Fedkiw *et al.* [65, 66] together with the level set approach [110, 124], or the remarkable work of Menshov *et al.* in [109, 178, 179] which is also generalised to arbitrary number of immiscible compressible fluids; (iii) Eulerian diffuse interface methods on fixed grids, where the presence of each material is represented only by a scalar function, see e.g. [49, 63, 64, 72, 97, 117] and references therein.

First, a new semi-implicit, staggered finite-volume method is introduced to solve a simplified BN model, based on the incompressible BN model derived in (2.1.2) in the low Mach number limit. Specifically, by considering only rigid body motion for the solid phase, a reduced BN model is obtained, which, can be applied for the solution of complex non-hydrostatic free-surface flows interacting with moving solid bodies. The numerical discretization of this model extends the algorithm already used in the work of Casulli *et al.* [29, 51] to a fully FV framework.

Then, a substantial part of this chapter is devoted to the development of a robust numerical scheme capable of addressing the various difficulties inherent in a unified theory of compressible multiphase fluid and solids mechanics, presented in Section 2.2. I detail the numerical techniques I adopted to address a reduced form of the SHTC BN-type model capable of describing a continuum consisting of three phases which can describe freely Newtonian and non-Newtonian, inviscid and viscous fluids, as well as elasto-plastic solids.

All these methods are the basis of efficient MPI-parallel Fortran codes that, in terms of applicability, are a valuable tool for the study of complex non-hydrostatic free-surface flows interacting with moving solid obstacles, but more importantly, a further step toward the applicability of the multiphase unified continuum mechanics model in real problems.

3.1 Semi-implicit FV schemes for free-surface two-phase flows

In this section a numerical method tailored to a simplified BN model is presented. This underling model is based on the incompressible BN model (2.35) derived in (2.1.2) with the aid of a classical asymptotic expansion in the low Mach number limit. As we saw in (2.1.2), in this limit the BN model leads to a system of incompressible Euler equations in which the second-order pressure terms $p_a^{(2)}(x,t)$ satisfy a Poisson equation taking into account the local balance of forces. Thus, the resulting model is hyperbolic-parabolic-elliptic, like the original incompressible Navier-Stokes equations, and numerically requires special approaches, such as those provided in Section 1.2.1, e.g. [8, 23, 29, 37, 160, 161]. Furthermore, the simplified Baer-Nunziato type model considered in this section cannot be defined as strictly incompressible, since in order to consider two-phase free-surface flows, i.e. two-phase flows containing a liquid phase, a solid phase and the surrounding void, the divergence-free conditions for the velocity field are not directly included in the governing system.

The numerical method presented in this section follows the so-called *diffuse interface approach* to describe the two phase free surface flow. This can be done thanks to the adoption of a suitable mathematical model, as indeed the BN model is. In fact, according to the so-called diffuse interface approach, the domain is covered by the liquid phase, the solid phase, and the surrounding void via a scalar volume fraction function for each phase. This approach allows arbitrarily complex geometries and complex free-surface flows to be discretized, despite using simple uniform Cartesian meshes.

The scheme presented in this section is completely formulated in a FV framework. Moreover, it is important form the beginning to emphasise that the dynamics of the liquid phase and the motion of the solid are decoupled. The solid is assumed to be a moving rigid body, whose motion is prescribed. Only after the advection of the solid volume fraction, the dynamics of the liquid phase is considered employing an operator splitting strategy. As usual in semi-implicit schemes, we employ staggered Cartesian control volumes and treat the nonlinear convective terms explicitly, while the pressure terms are treated implicitly. The non-conservative products arising in the transport equation for the solid volume fraction are treated by a path-conservative approach, see e.g. [27, 125]. The resulting semi-implicit FV discretization of the mass and momentum equations leads to a mildly nonlinear system for the pressure which can be efficiently solved with a nested Newton-type technique recently introduced and analysed by Casulli *et al.* in [18, 19]. The time step size is only limited by the velocities of the two phases contained in the domain, and not by the gravity wave speed nor by the stiff algebraic relaxation source term, which requires an implicit discretization.

3.1.1 Governing Partial Differential Equations

The two-phase solid-liquid flows of interest in this work can be mathematically described by means of a reduced BN model, formulated starting from the low Mach limit of the BN model (2.35) derived with the aid of a classical asymptotic expansion in Section 2.1.2. Specifically, considering only rigid-body motion for the solid phase, assuming a constant density at time $t = 0$ for the liquid phase, and considering an interphase velocity relaxation source term, the two incompressible Euler systems in (2.35) can be strongly simplified to a reduced three-equation model. It can be written in terms of a solid volume fraction α_s and a liquid volume fraction α_l, according to the so-called diffuse interface approach, and reads

$$\frac{\partial \alpha_s}{\partial t} + v_{s,k}\,\frac{\partial \alpha_s}{\partial x_k} = 0, \tag{3.1}$$

$$\frac{\partial \alpha_l}{\partial t} + \frac{\partial (\alpha_l\, v_{l,k})}{\partial x_k} = 0, \tag{3.2}$$

$$\frac{\partial (\alpha_l\, v_{l,i})}{\partial t} + \frac{\partial (\alpha_l\, v_{l,i}\, v_{l,k})}{\partial x_k} + \alpha_l \frac{\partial p_l}{\partial x_i} - \frac{\partial \sigma_{l,ik}}{\partial x_k} = -\alpha_l\, g_i - \frac{1}{\lambda}(v_{l,i} - V_i), \tag{3.3}$$

where $v_{l,i}$ is the velocity field of the liquid, $v_{s,i}$ the (known) velocity of the solid phase, p_l is the normalized pressure with respect to the constant density, $\boldsymbol{g} = g\,(0,-1)^{\mathsf{T}}$ is the vector of gravity acceleration, λ is a time scale for the velocity relaxation kinetics and the shear stress tensor is denoted by $\sigma_{l,ik}$, assuming a viscous incompressible Newtonian fluid. It is given by

$$\sigma_{l,ik} = \alpha_l\, \nu_l\, \frac{\partial v_{l,i}}{\partial x_k}, \tag{3.4}$$

where $\nu_l = \mu_l/\rho_l$ denotes the kinematic viscosity coefficient.

It has to be noted that with respect to the previous low Mach limit of the BN model in (2.35), the divergence free conditions for both the phases

$$\frac{\partial v_{l,k}}{\partial x_k} = 0, \qquad \frac{\partial v_{s,k}}{\partial x_k} = 0, \tag{3.5}$$

are not included in the system (3.1)-(3.3). This, clearly, is not done for the solid phase since the velocity field of this phase is prescribed. However, the divergence free condition is not considered for the liquid phase either, to obtain a more general system capable of describing free surface flows within a diffuse interface approach.

It can be observed that near the free surface, i.e. only in the narrow zone when $1 > \alpha_l > 0$, the velocity field needs not to be discrete divergence free. In fact, from (3.2) we can see that the velocity field, in this diffused interface area, satisfies the following equation

$$\frac{\partial v_{l,k}}{\partial x_k} = -\frac{1}{\alpha_l}\left(\frac{\partial \alpha_l}{\partial t} + v_{l,k}\frac{\partial \alpha_l}{\partial x_k}\right) \tag{3.6}$$

describing the correct free-surface dynamics. On the other hand, in most of the domain occupied by the liquid, excluding interfaces, i.e. when $\alpha_l = 1$ the equation (3.2) simplifies to

$$\frac{\partial v_{l,k}}{\partial x_k} = 0, \tag{3.7}$$

which is the divergence free conditions related to the incompressibility.

In agreement with the assumption that the phase velocities coincide in the low Mach limit of the BN model (2.35), the inter-phase drag term represented by the *velocity relaxation* source term in (3.3) is considered. In Eq. (3.3) this source is expressed through the velocity of the mixture V_i, but can be rearranged as follows

$$\frac{1}{\lambda}(v_{l,i} - V_i) = \frac{1}{\lambda}((1-\alpha_l)v_{l,i} - \alpha_s v_{s,i}). \tag{3.8}$$

It represents one of the reciprocal interactions that can be defined between the two phases, describing the fact that the velocity of the fluid tends to that of the solid at the interphase interfaces, if λ is sufficiently small.

The non-conservative system (3.1)-(3.3) can be expressed in a more compact notation by defining a column vector $\mathbf{Q}$ of state variables, a flux tensor $\mathbf{F}(\mathbf{Q})$ which includes the purely conservative part of the PDE system, a so-called non-conservative product $\mathbf{B}(\mathbf{Q})\cdot\nabla\mathbf{Q}$ and the vector of potentially stiff algebraic relaxation source terms $\mathbf{S}(\mathbf{Q})$,

$$\partial_t\mathbf{Q} + \nabla\cdot\mathbf{F}(\mathbf{Q}) + \mathbf{B}(\mathbf{Q})\cdot\nabla\mathbf{Q} = \mathbf{S}(\mathbf{Q}). \tag{3.9}$$

As proposed in some recent works, in which new families of *conservative* pressure-based semi-implicit schemes were introduced on staggered Cartesian and general unstructured meshes, see e.g. [14, 22, 34, 51, 56, 61, 105, 163–165], the flux tensor and the non-conservative products are now split into different tensors depending on the discretization that will be adopted, i.e. $(*)^i$ denotes a term that will be discretized implicitly, while $(*)^e$ denotes one that will be discretized explicitly. Hence, eq.(3.9) can be rewritten as

$$\partial_t \mathbf{Q} + \nabla\cdot\Big(\mathbf{F}_c^i(\mathbf{Q}) + \mathbf{F}_c^e(\mathbf{Q}) + \mathbf{F}_\nu^e(\mathbf{Q})\Big) + \Big(\mathbf{B}_c^e(\mathbf{Q}) + \mathbf{B}_p^i(\mathbf{Q})\Big)\cdot\nabla\mathbf{Q} = \mathbf{S}(\mathbf{Q}), \quad (3.10)$$

where the vector of state variables $\mathbf{Q} = (\alpha_s,\, \alpha_l,\, \alpha_l \boldsymbol{v}_l)^\intercal$, the flux tensors and the non-conservative products are given as

$$\mathbf{F}_c^i(\mathbf{Q}) = \begin{pmatrix} 0 \\ \alpha_l\,\boldsymbol{v}_l \\ 0 \end{pmatrix}, \quad \mathbf{F}_c^e(\mathbf{Q}) = \begin{pmatrix} 0 \\ 0 \\ \alpha_l\,\boldsymbol{v}_l \otimes \boldsymbol{v}_l \end{pmatrix}, \quad \mathbf{F}_\nu^e(\mathbf{Q}) = \begin{pmatrix} 0 \\ 0 \\ -\alpha_l\,\nu_l\,\nabla\boldsymbol{v}_l \end{pmatrix},$$

$$\mathbf{B}_c^e(\mathbf{Q})\cdot\nabla\mathbf{Q} = \begin{pmatrix} \boldsymbol{v}_s\,\nabla\alpha_s \\ 0 \\ 0 \end{pmatrix}, \quad \mathbf{B}_p^i(\mathbf{Q})\cdot\nabla\mathbf{Q} = \begin{pmatrix} 0 \\ 0 \\ \alpha_l\,\nabla p_l \end{pmatrix}, \quad (3.11)$$

and $\mathbf{S}(\mathbf{Q})$, the algebraic source term reads

$$\mathbf{S}(\mathbf{Q}) = \begin{pmatrix} 0 \\ 0 \\ -\alpha_l \boldsymbol{g} - \frac{1}{\lambda}\big((1-\alpha_l)\boldsymbol{v}_l - \alpha_s \boldsymbol{v}_s\big) \end{pmatrix}. \quad (3.12)$$

Terms related to the convection are denoted by $(*)_c$, with $(*)_\nu$ the viscous one and with $(*)_p$ the pressure related. The flux splitting procedure is quite useful to decouple the complete evolution system (3.10) into a convection-diffusion subsystem, a pressure subsystem and an algebraic source term subsystem, which will be discretized explicitly or implicitly according to their properties. Note that, the resulting split convective fluxes represent the advection system of the flux-vector splitting scheme of Toro and Vázquez-Cendón [172] also used in [23, 24].

Throughout this work, for simplicity the two-dimensional case is considered. The computational domain is denoted by $\Omega \subset \mathbb{R}^2$ in which $x_1 = x$ and $x_2 = y$, where the x-axis is horizontal and the vertical y-axis is oriented upward against the gravity direction.

3.1.2 Computational grid and constitutive relationship for the liquid phase

Within the computational domain $\Omega \subset \mathbb{R}^2$ three staggered overlapping Cartesian control volumes are defined, a primal control volume and two staggered edge-based cells in x and y-directions, see e.g. [60]. In such a control volume Ω, the liquid and the solid volume fractions α_l and α_s are related to the volume occupied respectively by the liquid V_l or by solid V_s by

$$V_l = \int_\Omega \alpha_l \, d\Omega \qquad \text{and} \qquad V_s = \int_\Omega \alpha_s \, d\Omega. \tag{3.13}$$

Figure 3.2 (left) shows all three types of control volumes with their respective barycenters. The primal control volumes are

$$\Omega_{i,j} = [x_{i-\frac{1}{2}}, x_{i+\frac{1}{2}}] \times [y_{j-\frac{1}{2}}, y_{j+\frac{1}{2}}], \tag{3.14}$$

with the barycenters denoted by $\mathbf{x}_{i,j} = (x_i, y_j)$ and having width and height

$$\Delta x_i = x_{i+\frac{1}{2}} - x_{i-\frac{1}{2}}, \qquad \Delta y_j = y_{j+\frac{1}{2}} - y_{j-\frac{1}{2}}. \tag{3.15}$$

The elements of the edge-based staggered mesh in x-direction are denoted by

$$\Omega_{i+\frac{1}{2},j} = [x_i, x_{i+1}] \times [y_{j-\frac{1}{2}}, y_{j+\frac{1}{2}}], \tag{3.16}$$

having barycenters in $\mathbf{x}_{i+\frac{1}{2},j} = (x_{i+\frac{1}{2}}, y_j)$. Their width is $\Delta x_{i+\frac{1}{2}} = x_{i+1} - x_i$ and their height is Δy_j. The volumes of the edge-based staggered mesh in the y-direction are denoted by

$$\Omega_{i,j+\frac{1}{2}} = [x_{i-\frac{1}{2}}, x_{i+\frac{1}{2}}] \times [y_j, y_{j+1}]. \tag{3.17}$$

Their barycenters are located in $\mathbf{x}_{i,j+\frac{1}{2}} = (x_i, y_{j+\frac{1}{2}})$ and they have width Δx_i and height $\Delta y_{j+\frac{1}{2}} = y_{j+1} - y_j$, respectively. In the following description of the numerical method and for all the tests that will be presented, uniform Cartesian control volumes with uniform mesh spacing, at least according to each direction, are taken into account, hence $\Delta x_i = \Delta x_{i+\frac{1}{2}} = \Delta x$ and $\Delta y_j = \Delta y_{j+\frac{1}{2}} = \Delta y$.

In order to simplify the subscripts notation, let's denote the discrete liquid phase related variables as

$$\alpha_l v_{l,1} := \alpha^l u, \qquad \alpha_l v_{l,2} := \alpha^l v, \qquad p_l := p, \tag{3.18}$$

and in general the subscripts of liquid l and solid s will henceforth be denoted by superscripts, since subscripts i, j will denote the discretization indices.

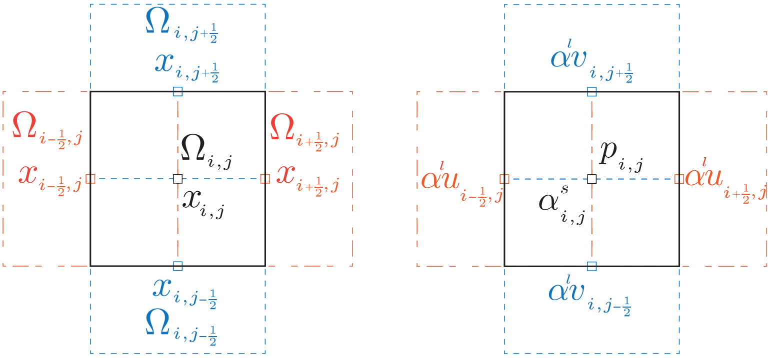

Fig. 3.1. Representation of the three overlapping Cartesian control volumes, in black the primal control volume, in red the elements of the edge-based staggered mesh in x-direction and in blue the volumes of the edge-based staggered mesh in the y-direction (left). Location of the liquid and solid phase related variables over the control volumes (right).

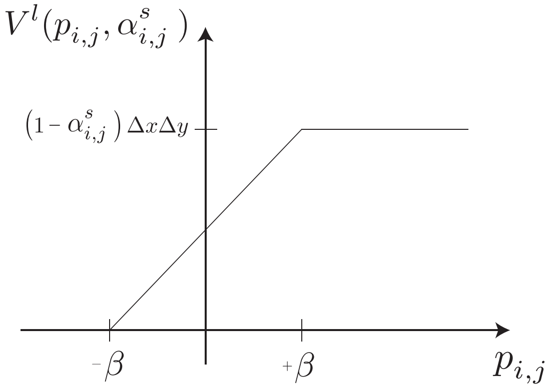

Fig. 3.2. Fluid volume defined as a piecewise linear function of the local cell pressure $p_{i,j}$ and of the local solid phase volume fraction $\alpha^s_{i,j}$.

The discrete quantities in (3.18) at time level t^n will be defined at staggered locations, within the three introduced overlapping Cartesian control volumes, as represented in Fig. 3.2 (center). The discrete pressure $p^n_{i,j}$ and the liquid volume fractions $\alpha^n_{l,i,j}$ will be defined as cell-averaged quantities over the primal control volumes $\Omega_{i,j}$. The state variables $\alpha^l u^n_{l,i\pm\frac{1}{2},j}$ will be defined in the barycenters of the edge-based staggered mesh in x-direction $\Omega_{i\pm\frac{1}{2},j}$, while the state quantity associated with the vertical components of the velocity $\alpha^l v^n_{i,j\pm\frac{1}{2}}$, will be defined in the barycenters of the edge-based staggered mesh in y-direction $\Omega_{i,j\pm\frac{1}{2}}$.

The system of equations (3.1)-(3.3) needs a closure relation that relates the pressure to the quantities that are actually evolved by the system. In this thesis work we assume a linear variability of the pressure in the gravity direction within each cell with respect to the value in the center

$$p(x, y, t^n) = p^n_{i,j} + g(y_j - y), \quad \forall (x, y) \in \Omega_{i,j}. \tag{3.19}$$

which despite its simplicity has proven to be a very effective choice in gravity-driven free-surface flows, see e.g. [29]. In general, it is possible to specify a non-linear volume-pressure relationship, such as when solving the mixed form of the Richards equation, see [32] for details. For the sake of clarity, we specify that in the former constitutive relationship (3.19), the cell-centered pressure values $p^n_{i,j}$ are the solution of the fully non-hydrostatic problem. The assumption of a cell-local linear pressure (3.19) is needed in order to define the following integral (3.20) of the liquid phase volume in the case of partially wet cells in such a way to describe the correct free-surface dynamics with the transition towards fully wet cells $\alpha^l = 1$. Moreover, thanks to this closure relation, the overall method reduces to a semi-implicit scheme for the shallow water equations in the special case where the fluid covers only one single layer of cells, see [28, 29] for further details.

According to [29], the volume of the liquid phase $V^{l,n}_{i,j}$, within the cell $\Omega_{i,j}$, is related to the local cell pressure $p^n_{i,j}$ and to the solid volume fraction $\alpha^s_{i,j}$ by the following *constitutive relationship*,

$$V^{l,n}_{i,j} = \int_{\Omega_{i,j}} \left(1 - \alpha^{s,n}_{i,j}\right) \, \mathcal{H}(p^n_{i,j} + g(y_j - y)) \; dx \; dy, \tag{3.20}$$

defined by the Heaviside step function

$$\mathcal{H} = \begin{cases} 1 & \text{if } \; p^n_{i,j} + g(y_j - y) \geqslant 0, \\ 0 & \text{otherwise.} \end{cases} \tag{3.21}$$

Eq.(3.20) can be more conveniently expressed in terms of a Jordan decomposition as

$$V^{l,n}_{i,j} = P(p^n_{i,j}, \alpha^{s,n}_{i,j})(p^n_{i,j} + \beta) - Q(p^n_{i,j}, \alpha^{s,n}_{i,j})(p^n_{i,j} - \beta), \tag{3.22}$$

where $\beta = g\frac{\Delta y}{2}$, and P and Q are step functions defined as

$$P(p^n_{i,j}, \alpha^{s,n}_{i,j}) = \begin{cases} \left(1 - \alpha^{s,n}_{i,j}\right) \frac{\Delta x}{g} & \text{if } \; p^n_{i,j} \geqslant -\beta, \\ 0 & \text{otherwise} \end{cases} \tag{3.23}$$

and

$$Q(p_{i,j}^n, \alpha_{i,j}^{s,n}) = \begin{cases} \left(1 - \alpha_{i,j}^{s,n}\right) \frac{\Delta x}{g} & \text{if } p_{i,j}^n > \beta, \\ 0 & \text{otherwise.} \end{cases} \tag{3.24}$$

The discrete solid phase volume fraction $\alpha_{i,j}^{s,n}$ and also the velocities $u_{i,j}^{s,n}$, $v_{i,j}^{s,n}$ related to this phase are defined in the centers of the cells $\Omega_{i,j}$. Moreover, for $\alpha_{i,j}^s = 1$ the corresponding cell, obviously, cannot be occupied by the liquid phase. Thus, as illustrated in Fig. 3.2 (right), the liquid phase volume is defined, for each cell, as a piecewise linear function of the local cell pressure $p_{i,j}^n$ and of the local solid phase volume fraction $\alpha_{i,j}^{s,n}$.

3.1.3 Structure of the FV semi-implicit scheme

In this numerical scheme, the dynamics of the liquid phase and the solid phase motion are decoupled. By solving the solid advection equation

$$\partial_t \mathbf{Q} + \mathbf{B}_c^e(\mathbf{Q}) \cdot \nabla \mathbf{Q} = \mathbf{0}, \tag{3.25}$$

with a prescribed solid velocity field u_k^s, one obtains the new solid volume fraction distribution $\alpha^{s,n+1}$, which is needed in the constitutive relationship of the liquid phase volume and in the relaxation source term. This is numerically done with the aid of a path conservative second order in space and time MUSCL-Hancock method, see [171] for details.

Furthermore, to solve the liquid phase related subsystem

$$\partial_t \mathbf{Q} + \nabla \cdot \Big(\mathbf{F}_c^i(\mathbf{Q}) + \mathbf{F}_c^e(\mathbf{Q}) + \mathbf{F}_\nu^e(\mathbf{Q})\Big) + \mathbf{B}_p^i(\mathbf{Q}) \cdot \nabla \mathbf{Q} = \mathbf{S}(\mathbf{Q}), \tag{3.26}$$

which can be obtained from the flux splitting approach, a specific combination of explicit and implicit FV discretization on staggered Cartesian control volumes is introduced. A fully implicit finite volume discretization of the liquid mass conservation

$$\partial_t \mathbf{Q} + \mathbf{F}_c^i(\mathbf{Q}) = \mathbf{0}, \tag{3.27}$$

is adopted, while for the momentum equations a semi-implicit finite volume discretization will be employed. The convective and viscous subsystem, referred to convective and viscous fluxes,

$$\partial_t \mathbf{Q} + \nabla \cdot \Big(\mathbf{F}_c^e(\mathbf{Q}) + \mathbf{F}_\nu^e(\mathbf{Q})\Big) = \mathbf{0}, \tag{3.28}$$

is discretized with the aid of an explicit FV method, thus obtaining an intermediate approximation of the conservative variables vector.

Differently the non-conservative pressure subsystem

$$\partial_t \mathbf{Q} + \mathbf{B}_p^i(\mathbf{Q}) \cdot \nabla \mathbf{Q} = \mathbf{S}(\mathbf{Q}), \tag{3.29}$$

is discretized using an implicit discretization over edge staggered grids, based on the path-conservative approach of Pares and Castro [125], [27]. Moreover, the algebraic relaxation source term, in $\mathbf{S}(\mathbf{Q})$, may also become stiff and thus require an integral implicit discretization again based on an edge staggered volume. These implicit subsystem are then coupled to the implicit liquid mass conservation law, leading to a mildly nonlinear system for the pressure. The diagonal nonlinearity of this system stems from the definition of volume of fluid, while the remaining linear part of the system is symmetric and at least positive semi-definite. Hence, the pressure can be efficiently obtained with the family of nested Newton-type techniques introduced by Casulli *et al.* in [18, 19, 32, 33].

3.1.4 Implicit FV discretization of the liquid mass conservation

To discretise implicitly the conservation of the mass of the liquid, represented in matrix vector notation by the subsystem

$$\partial_t \mathbf{Q} + \nabla \cdot \mathbf{F}_c^i(\mathbf{Q}) = \mathbf{0}, \tag{3.30}$$

a two-dimensional physical domain is considered, thus it simply reads

$$\partial_t \alpha^l + \partial_x(\alpha^l u) + \partial_y(\alpha^l v) = 0. \tag{3.31}$$

The integration of this mass conservation equation (3.31) over the primal space-time control volume $\Omega_{i,j} = [x_{i-\frac{1}{2}}, x_{i+\frac{1}{2}}] \times [y_{j-\frac{1}{2}}, y_{j+\frac{1}{2}}] \times [t^n, t^{n+1}]$ and the use of the Gauss theorem yield

$$\begin{aligned}
&\int\limits_{x_{i-\frac{1}{2}}}^{x_{i+\frac{1}{2}}} \int\limits_{y_{i-\frac{1}{2}}}^{y_{j+\frac{1}{2}}} \Big(\alpha^l(x,y,t^{n+1}) - \alpha^l(x,y,t^n)\Big)\, dydx + \\
&\qquad + \int\limits_{t^n}^{t^{n+1}} \int\limits_{y_{j-\frac{1}{2}}}^{y_{j+\frac{1}{2}}} \Big(\alpha^l u(x_{i+\frac{1}{2}},y,t) - \alpha^l u(x_{i-\frac{1}{2}},y,t)\Big)\, dydt + \\
&\qquad + \int\limits_{t^n}^{t^{n+1}} \int\limits_{x_{i-\frac{1}{2}}}^{x_{i+\frac{1}{2}}} \Big(\alpha^l v(x,y_{j+\frac{1}{2}},t) - \alpha^l v(x,y_{j-\frac{1}{2}},t)\Big)\, dxdt = 0
\end{aligned} \tag{3.32}$$

With the definitions of the liquid cell volume

$$V_{i,j}^{l} = \int_{x_{i-\frac{1}{2}}}^{x_{i+\frac{1}{2}}} \int_{y_{j-\frac{1}{2}}}^{y_{j+\frac{1}{2}}} \alpha^{l}(x,y,t)dydx, \tag{3.33}$$

and the liquid fluxes

$$f_{i+\frac{1}{2},j}^{l} = \frac{1}{\Delta t \Delta y} \int_{t^{n}}^{t^{n+1}} \int_{y_{j-\frac{1}{2}}}^{y_{j+\frac{1}{2}}} \alpha^{l} u(x_{i+\frac{1}{2}},y,t)dydt, \tag{3.34}$$

and

$$g_{i,j+\frac{1}{2}}^{l} = \frac{1}{\Delta t \Delta x} \int_{t^{n}}^{t^{n+1}} \int_{x_{i-\frac{1}{2}}}^{x_{i+\frac{1}{2}}} \alpha^{l} v(x,y_{j+\frac{1}{2}},t)dxdt \tag{3.35}$$

the following integral form of (3.31) is obtained

$$V_{i,j}^{l,n+1} = V_{i,j}^{l,n} - \Delta t \Delta y (f_{i+\frac{1}{2},j}^{l} - f_{i-\frac{1}{2},j}^{l}) - \Delta t \Delta x (g_{i,j+\frac{1}{2}}^{l} - g_{i,j-\frac{1}{2}}^{l}). \tag{3.36}$$

Introducing the liquid cell-average of the liquid volume fraction

$$\alpha_{i,j}^{l} = \frac{1}{\Delta x \Delta y} \int_{x_{i-\frac{1}{2}}}^{x_{i+\frac{1}{2}}} \int_{y_{j-\frac{1}{2}}}^{y_{j+\frac{1}{2}}} \alpha^{l}(x,y,t)dydx, \tag{3.37}$$

it is possible to rewrite (3.36) as

$$\alpha_{i,j}^{l,n+1} = \alpha_{i,j}^{l,n} - \frac{\Delta t}{\Delta x}(f_{i+\frac{1}{2},j}^{l} - f_{i-\frac{1}{2},j}^{l}) - \frac{\Delta t}{\Delta y}(g_{i,j+\frac{1}{2}}^{l} - g_{i,j-\frac{1}{2}}^{l}), \tag{3.38}$$

which is a discrete form of (3.31). Assuming the liquid velocity field constant along each edge, denoting these velocities at the new time t^{n+1} by $u_{i+\frac{1}{2},j}^{l,n+1}$ and $v_{i,j+\frac{1}{2}}^{l,n+1}$, and defining the effective edge lengths which are occupied by the liquid as

$$\delta y_{i+\frac{1}{2},j}^{n+1} = \int_{y_{j-\frac{1}{2}}}^{y_{j+\frac{1}{2}}} \alpha^{l}(x_{i+\frac{1}{2}},y,t^{n+1})dy, \qquad \delta x_{i,j+\frac{1}{2}}^{n+1} = \int_{x_{i-\frac{1}{2}}}^{x_{i+\frac{1}{2}}} \alpha^{l}(x,y_{j+\frac{1}{2}},t^{n+1})dx, \tag{3.39}$$

it is possible to define the following edge-averaged liquid volume fractions

$$\alpha^{l,n+1}_{i+\frac{1}{2},j} = \frac{\delta y^{n+1}_{i+\frac{1}{2},j}}{\Delta y}, \qquad \text{and} \qquad \alpha^{l,n+1}_{i,j+\frac{1}{2}} = \frac{\delta x^{n+1}_{i,j+\frac{1}{2}}}{\Delta x}. \tag{3.40}$$

Defining the liquid fluxes in terms of the edge velocities and the edge-averaged volume fractions as

$$f^l_{i+\frac{1}{2},j} = \alpha^{l,n+1}_{i+\frac{1}{2},j}\, u^{n+1}_{i+\frac{1}{2},j}, \qquad \text{and} \qquad g^l_{i,j+\frac{1}{2}} = \alpha^{l,n+1}_{i,j+\frac{1}{2}}\, v^{n+1}_{i,j+\frac{1}{2}} \tag{3.41}$$

the liquid volume conservation equation (3.38) can finally be written as

$$\begin{aligned} V^{l,n+1}_{i,j} = V^{l,n}_{i,j} &- \Delta t \left((\delta y u)^{n+1}_{i+\frac{1}{2},j} - (\delta y u)^{n+1}_{i-\frac{1}{2},j} \right) \\ &- \Delta t \left((\delta x v)^{n+1}_{i,j+\frac{1}{2}} - (\delta x v)^{n+1}_{i,j-\frac{1}{2}} \right). \end{aligned} \tag{3.42}$$

Equation (3.42) represents an implicit finite volume discretization of the continuity equation, as the semi-implicit method proposed in [29]. Furthermore, it is worth noting that the discrete form of the liquid volume conservation given in Eq. (3.42) implies a consistent discretization of the incompressibility condition in (3.7) if the $\Omega_{i,j}$ cell is a full cell. Namely, Eq. (3.42) simplifies to

$$\frac{u^{n+1}_{i+\frac{1}{2},j} - u^{n+1}_{i-\frac{1}{2},j}}{\Delta x} + \frac{v^{n+1}_{i,j+\frac{1}{2}} - v^{n+1}_{i,j-\frac{1}{2}}}{\Delta y} = 0. \tag{3.43}$$

The effective edge-integrated volume fractions $\delta y^{n+1}_{i+\frac{1}{2},j}$ and $\delta x^{n+1}_{i,j+\frac{1}{2}}$, in (3.42), available to liquid phase through the edges, can be evaluated from the liquid volumes within the cells that share the edge by taking the average, the upwind, or the maximum cell volumes. For instance, if the average is chosen, then $\delta y^{n+1}_{i+\frac{1}{2},j}$ and $\delta x^{n+1}_{i,j+\frac{1}{2}}$ read

$$\begin{aligned} \delta y^{n+1}_{i+\frac{1}{2},j} &= \Delta y \frac{1}{2} \left(\alpha^l(p^{n+1}_{i,j}) + \alpha^l(p^{n+1}_{i+1,j}) \right) \\ &= \frac{1}{2\Delta x} \left(V^l(p^{n+1}_{i,j}, \alpha^{s,n+1}_{i,j}) + V^l(p^{n+1}_{i+1,j}, \alpha^{s,n+1}_{i+1,j}) \right), \end{aligned} \tag{3.44}$$

$$\begin{aligned} \delta x^{n+1}_{i,j+\frac{1}{2}} &= \Delta x \frac{1}{2} \left(\alpha^l(p^{n+1}_{i,j}) + \alpha^l(p^{n+1}_{i,j+1}) \right) \\ &= \frac{1}{2\Delta y} \left(V^l(p^{n+1}_{i,j}, \alpha^{s,n+1}_{i,j}) + V^l(p^{n+1}_{i,j+1}, \alpha^{s,n+1}_{i,j+1}) \right), \end{aligned} \tag{3.45}$$

where for the computation of the liquid cell volume V^l the *constitutive relationship* defined in (3.22) has to be used.

3.1.5 Semi-implicit FV discretization of the momentum equations

As illustrated in Section 3.1.3 the system (3.26) is discretized with the aid of a specific combination of explicit and implicit FV methods on staggered Cartesian control volumes.

Explicit discretization of the convective terms

The convective subsystem for the liquid phase is discretized explicitly. In particular, it is useful to integrate this subsystem within the primary control volumes in order to have a classical Godunov-type FV scheme, in which all state variables are defined at the centre of $\Omega_{i,j}$, as illustrated in Fig. 3.2.

Likewise, a FV explicit discretisation is adopted for the advection of the solid phase (3.30) within the primary control volumes $\Omega_{i,j}$. Therefore, although the dynamics of the solid and liquid phases are decoupled, it is useful to illustrate their explicit discretization in a single step. Thus the system considered in this paragraph reads

$$\partial_t \mathbf{Q} + \nabla \cdot \mathbf{F}_c^e(\mathbf{Q}) + \mathbf{B}_c^e(\mathbf{Q}) \cdot \nabla \mathbf{Q} = \mathbf{0}. \tag{3.46}$$

It should be pointed out, however, that while the following explicit FV discretization yields an integral solution for the solid phase $\alpha^{s,n+1}$ at time t^n+1, an intermediate solution is obtained for the state variables related to the liquid phase, due to the fact that the splitting operator is used to evaluate the dynamics of the latter phase. This integral intermediate solution within the primary control volumes $\Omega_{i,j}$ is denoted with $\mathbf{Q}^*_{i,j}$. Specifically, for the sake of clarity, the state variable vector $\mathbf{Q}^*_{i,j}$ solution of the following explicit discretization will be

$$\mathbf{Q}^*_{i,j} = \left(\alpha^{s,n+1}_{i,j},\, \alpha^{l,n}_{i,j},\, (\alpha u)^*_{i,j},\, (\alpha v)^*_{i,j}\right)^{\mathsf{T}}, \tag{3.47}$$

which can be rewritten as

$$\mathbf{Q}^*_{i,j} = \left(\alpha^{s,n+1}_{i,j},\, \alpha^{l,n}_{i,j},\, (\delta y u)^*_{i,j},\, (\delta x v)^*_{i,j}\right)^{\mathsf{T}} \tag{3.48}$$

introducing in the FV discretization the integral definitions of the effective fluxes $(\delta y u)^n_{i,j}$, $(\delta x v)^n_{i,j}$ over the primary control volumes $\Omega_{i,j}$

$$(\delta y u)^n_{i,j} = (\alpha u)^n_{i,j} \Delta y = \frac{1}{\Delta x} \int\limits_{x_i}^{x_{i+1}} \int\limits_{y_j}^{y_{j+1}} \alpha^l u(x,y,t^n)\,dx dy, \tag{3.49}$$

where $(\delta x v)^n_{i,j}$ can be defined similarly.

Furthermore, since the velocity components $u^n_{i\pm\frac{1}{2},j}$, $v^n_{i,j\pm\frac{1}{2}}$ and the fluxes $(\delta yu)^{n+1}_{i\pm\frac{1}{2},j}$ and $(\delta xv)^{n+1}_{i,j\pm\frac{1}{2}}$ are defined over the edges of the primal control volumes in the discrete liquid volume conservation equation (3.42), an interpolation of the velocity field or fluxes from one mesh to another is needed. This interpolation, to evaluate centered values on the primal control volumes, is achieved as follows

$$(\delta yu)^n_{i,j} = \frac{1}{2}\left((\delta yu)^n_{i+\frac{1}{2},j} + (\delta yu)^n_{i-\frac{1}{2},j}\right) \tag{3.50}$$

and

$$(\delta xv)^n_{i,j} = \frac{1}{2}\left((\delta xv)^n_{i,j+\frac{1}{2}} + (\delta xv)^n_{i,j-\frac{1}{2}}\right) \tag{3.51}$$

and an average of the same type can be used to return to staggered values on the edges of the primal control volumes.

Starting from the known solution $\mathbf{Q}^n_{i,j}$ at time t^n, the integration of the subsystem (3.46) over the primal space-time control volume $\Omega_{i,j} \times [t^n, t^{n+1}]$ yields

$$\begin{aligned}\mathbf{Q}^*_{i,j} = \mathbf{Q}^n_{i,j} &- \frac{\Delta t}{\Delta x}\left(\mathbf{f}^c_{i+\frac{1}{2},j} - \mathbf{f}^c_{i-\frac{1}{2},j}\right) - \frac{\Delta t}{\Delta y}\left(\mathbf{g}^c_{i,j+\frac{1}{2}} - \mathbf{g}^c_{i,j-\frac{1}{2}}\right)\\ &- \frac{\Delta t}{\Delta x}\left(\mathbf{D}^c_{i+\frac{1}{2},j} + \mathbf{D}^c_{i-\frac{1}{2},j}\right) - \frac{\Delta t}{\Delta y}\left(\mathbf{D}^c_{i,j+\frac{1}{2}} + \mathbf{D}^c_{i,j-\frac{1}{2}}\right),\end{aligned} \tag{3.52}$$

where fluxes are written as $\mathbf{F}^e_c(\mathbf{Q}) = (\mathbf{f}^c(\mathbf{Q}), \mathbf{g}^c(\mathbf{Q}))^\intercal$. The FV discretization in (3.52) has to be completed with the definition of the numerical fluxes and path-conservative jump terms. In this work, a Rusanov-type flux is chosen in x and y-direction and is defined as

$$\mathbf{f}^c_{i+\frac{1}{2},j} = \frac{1}{2}\left(\mathbf{f}^c(\mathbf{Q}^-_{i+\frac{1}{2},j}) + \mathbf{f}^c(\mathbf{Q}^+_{i+\frac{1}{2},j})\right) - \frac{1}{2}|s^x_{max}|\left(\mathbf{Q}^+_{i+\frac{1}{2},j} - \mathbf{Q}^-_{i+\frac{1}{2},j}\right) \tag{3.53}$$

and

$$\mathbf{g}^c_{i,j+\frac{1}{2}} = \frac{1}{2}\left(\mathbf{g}^c(\mathbf{Q}^-_{i,j+\frac{1}{2}}) + \mathbf{g}^c(\mathbf{Q}^+_{i,j+\frac{1}{2}})\right) - \frac{1}{2}|s^y_{max}|\left(\mathbf{Q}^+_{i,j+\frac{1}{2}} - \mathbf{Q}^-_{i,j+\frac{1}{2}}\right) \tag{3.54}$$

where the maximum signal speeds s^x_{max} and s^y_{max} are computed as the maximum of the eigenvalues of the explicit convective subsystem in x and y, respectively. The path-conservative jump terms [27, 125] read

$$\mathbf{D}^c_{i+\frac{1}{2},j} = \frac{1}{2}\tilde{\mathbf{B}}_{c,x}(\tilde{\mathbf{Q}}_{i+\frac{1}{2},j})\left(\mathbf{Q}^+_{i+\frac{1}{2},j} - \mathbf{Q}^-_{i+\frac{1}{2},j}\right), \tag{3.55}$$

$$\mathbf{D}^{c}_{i,j+\frac{1}{2}} = \frac{1}{2}\mathbf{B}_{c,y}(\tilde{\mathbf{Q}}_{i,j+\frac{1}{2}})\left(\mathbf{Q}^{+}_{i,j+\frac{1}{2}} - \mathbf{Q}^{-}_{i,j+\frac{1}{2}}\right), \tag{3.56}$$

with $\tilde{\mathbf{Q}}_{i+\frac{1}{2},j} = \frac{1}{2}(\mathbf{Q}^{+}_{i+\frac{1}{2},j} + \mathbf{Q}^{-}_{i+\frac{1}{2},j})$, $\tilde{\mathbf{Q}}_{i,j+\frac{1}{2}} = \frac{1}{2}(\mathbf{Q}^{+}_{i,j+\frac{1}{2}} + \mathbf{Q}^{-}_{i,j+\frac{1}{2}})$ and

$$\mathbf{B}_{c,x}(\mathbf{Q}) = \begin{pmatrix} u^s & 0 & 0 \\ 0 & 0 & 0 \\ 0 & 0 & 0 \end{pmatrix}, \qquad \mathbf{B}_{c,y}(\mathbf{Q}) = \begin{pmatrix} v^s & 0 & 0 \\ 0 & 0 & 0 \\ 0 & 0 & 0 \end{pmatrix}. \tag{3.57}$$

Furthermore, in order to reach second order of accuracy the boundary-extrapolated and time-evolved values are computed via a standard total variation diminishing (TVD) MUSCL-Hancock scheme as follows

$$\mathbf{Q}^{\mp}_{i+\frac{1}{2},j} = \mathbf{Q}^{n}_{i,j} \pm \frac{1}{2}\Delta x \partial_x \mathbf{Q}^{n}_{i,j} + \frac{1}{2}\Delta t \partial_t \mathbf{Q}^{n}_{i,j}, \tag{3.58}$$

$$\mathbf{Q}^{\mp}_{i,j+\frac{1}{2}} = \mathbf{Q}^{n}_{i,j} \pm \frac{1}{2}\Delta y \partial_y \mathbf{Q}^{n}_{i,j} + \frac{1}{2}\Delta t \partial_t \mathbf{Q}^{n}_{i,j} \tag{3.59}$$

with the gradient in space approximated using the classical *minmod* slope limiter

$$\partial_x \mathbf{Q}^{n}_{i,j} = \text{minmod}\left(\frac{\mathbf{Q}^{n}_{i+1,j} - \mathbf{Q}^{n}_{i,j}}{\Delta x}, \frac{\mathbf{Q}^{n}_{i,j} - \mathbf{Q}^{n}_{i-1,j}}{\Delta x}\right), \tag{3.60}$$

$$\partial_y \mathbf{Q}^{n}_{i,j} = \text{minmod}\left(\frac{\mathbf{Q}^{n}_{i,j+1} - \mathbf{Q}^{n}_{i,j}}{\Delta y}, \frac{\mathbf{Q}^{n}_{i,j} - \mathbf{Q}^{n}_{i,j-1}}{\Delta y}\right), \tag{3.61}$$

while the derivative in time is computed as

$$\begin{aligned} \partial_t \mathbf{Q}^{n}_{i,j} = & -\frac{\mathbf{f}^c(\mathbf{Q}^{n}_{i,j} + \frac{1}{2}\Delta x \partial_x \mathbf{Q}^{n}_{i,j}) - \mathbf{f}^c(\mathbf{Q}^{n}_{i,j} - \frac{1}{2}\Delta x \partial_x \mathbf{Q}^{n}_{i,j})}{\Delta x} \\ & - \frac{\mathbf{g}^c(\mathbf{Q}^{n}_{i,j} + \frac{1}{2}\Delta y \partial_y \mathbf{Q}^{n}_{i,j}) - \mathbf{g}^c(\mathbf{Q}^{n}_{i,j} - \frac{1}{2}\Delta y \partial_y \mathbf{Q}^{n}_{i,j})}{\Delta y} \\ & - \mathbf{B}_{c,x}\left(\mathbf{Q}^{n}_{i,j}\right)\partial_x \mathbf{Q}^{n}_{i,j} - \mathbf{B}_{c,y}\left(\mathbf{Q}^{n}_{i,j}\right)\partial_y \mathbf{Q}^{n}_{i,j}, \end{aligned} \tag{3.62}$$

see the Toro textbook [171] for details.

From this explicit finite volume scheme the intermediate solution $(\delta yu)^{*}_{i,j}$, $(\delta xv)^{*}_{i,j}$ will be obtained, and from this average values on primal control volume it it possible to go back to staggered values on the edges by interpolation obtaining $(\delta yu)^{*}_{i+\frac{1}{2},j}, (\delta xv)^{*}_{i,j+\frac{1}{2}}$.

Explicit discretization of the viscous terms

The parabolic viscous subsystem

$$\partial_t \mathbf{Q} + \nabla \cdot (\mathbf{F}^e_\nu(\mathbf{Q})) = 0 \tag{3.63}$$

is discretized explicitly as well. Notably, the subsystem in (3.63) represents an evolution law for the momentum variables only, which is why the other state variables contained in $\mathbf{Q}$ can be excluded in this discretisation step. Thus, the two equations which constitute the viscous subsystem (3.63) are

$$\begin{aligned} \partial_t(\alpha^l u) + \partial_x(\nu\, \alpha^l \partial_x u) + \partial_y(\nu\, \alpha^l \partial_y u) = 0, \\ \partial_t(\alpha^l v) + \partial_x(\nu\, \alpha^l \partial_x v) + \partial_y(\nu\, \alpha^l \partial_y v) = 0. \end{aligned} \tag{3.64}$$

The equations in (3.64) are discretized on two different edge based staggered cells in the x and y-directions, respectively. In fact, as it has been done in the previous section when considering the convective terms, it is necessary at the end of this further explicit step to obtain new intermediate states $(\delta y u)^{**}_{i+\frac{1}{2},j}$ and $(\delta x v)^{**}_{i,j+\frac{1}{2}}$ for flows defined in staggered positions, on the edges of the primary control volumes $\Omega_{i,j}$. To have discrete quantities that can then be cast in the discrete liquid volume conservation equation (3.42) in order to get a final pressure based system.

Let us consider the discretization of the first equation in (3.64), in the x-direction. Starting from the known solution at time t^n, the FV integration of this equation over the edge-based staggered space-time control volume $\Omega_{i+\frac{1}{2},j} \times [t^n, t^{n+1}]$ yields

$$\begin{aligned} (\alpha u)^{**}_{i+\frac{1}{2},j} = (\alpha u)^{n}_{i+\frac{1}{2},j} &+ \frac{\Delta t}{\Delta x}\left(f^\nu_{i+1,j} - f^\nu_{i,j}\right) \\ &+ \frac{\Delta t}{\Delta y}\left(g^\nu_{i+\frac{1}{2},j+\frac{1}{2}} - g^\nu_{i+\frac{1}{2},j-\frac{1}{2}}\right) \end{aligned} \tag{3.65}$$

with the definitions

$$(\alpha u)^{**}_{i+\frac{1}{2},j} = \frac{1}{\Delta x \Delta y} \int\limits_{x_i}^{x_{i+1}} \int\limits_{y_{j-\frac{1}{2}}}^{y_{j+\frac{1}{2}}} \alpha^l u(x, y, t^n) dx dy, \tag{3.66}$$

$$f^\nu_{i+1,j} = \frac{1}{\Delta t \Delta y} \int\limits_{t^n}^{t^{n+1}} \int\limits_{y_{j-\frac{1}{2}}}^{y_{j+\frac{1}{2}}} f^\nu_{(x_{i+1},y,t)} dy dt, \tag{3.67}$$

and

$$g^{\nu}_{i+\frac{1}{2},j+\frac{1}{2}} = \frac{1}{\Delta t \Delta x} \int\limits_{t^n}^{t^{n+1}} \int\limits_{x_i}^{x_{i+1}} g^{\nu}_{(x,y_{j+\frac{1}{2}},t)} dx dt. \tag{3.68}$$

As in the previous paragraph, the liquid cell-average flux in x-direction $(\alpha u)^{**}_{i+\frac{1}{2},j}$ can be expressed by the the effective edge-integrated volume fraction $(\delta y)^{**}_{i+\frac{1}{2},j}$ as follows

$$(\delta y u)^{**}_{i+\frac{1}{2},j} = (\alpha u)^{**}_{i+\frac{1}{2},j} \Delta y = \frac{1}{\Delta x} \int\limits_{x_i}^{x_{i+1}} \int\limits_{y_{j-\frac{1}{2}}}^{y_{j+\frac{1}{2}}} \alpha^l u(x,y,t^n) dx dy, \tag{3.69}$$

and assuming constant fluxes along each edge, it is possible to rewrite the discrete eqn.(3.65) in terms of effective volume fractions

$$\begin{aligned} (\delta y u)^{**}_{i+\frac{1}{2},j} = (\delta y u)^{*}_{i+\frac{1}{2},j} &+ \frac{\Delta t}{\Delta x}\left(f^{\nu}_{i+1,j} - f^{\nu}_{i,j}\right) \\ &+ \frac{\Delta t}{\Delta y}\left(g^{\nu}_{i+\frac{1}{2},j+\frac{1}{2}} - g^{\nu}_{i+\frac{1}{2},j-\frac{1}{2}}\right), \end{aligned} \tag{3.70}$$

where, for the sake of brevity, the initial value $(\delta y u)^{n}_{i+\frac{1}{2},j}$ has been replaced by the preliminary quantities obtained from the explicit discretisation of the convective terms $(\delta y u)^{*}_{i+\frac{1}{2},j}$ in order to have a final update formula for all explicitly discretized terms.

To complete the FV discretization in (3.70), classical *two*-point fluxes based on mid-point rule are chosen and defined in x and y-direction as

$$\begin{aligned} f^{\nu}_{i+1,j} &= \nu \delta y^n_{i+1,j} \frac{u^n_{i+\frac{3}{2},j} - u^n_{i+\frac{1}{2},j}}{\Delta x}, \\ g^{\nu}_{i+\frac{1}{2},j+\frac{1}{2}} &= \nu \delta y^n_{i+\frac{1}{2},j+\frac{1}{2}} \frac{u^n_{i+\frac{1}{2},j+1} - u^n_{i+\frac{1}{2},j}}{\Delta y}, \end{aligned} \tag{3.71}$$

with

$$\begin{aligned} \delta y^n_{i+1,j} &= \frac{1}{2}(\delta y^n_{i+1/2,j} + \delta y^n_{i+3/2,j}), \\ \delta y^n_{i+\frac{1}{2},j+\frac{1}{2}} &= \frac{1}{2}(\delta y^n_{i+1/2,j+1} + \delta y^n_{i+1/2,j}). \end{aligned} \tag{3.72}$$

The same can be done in the y-direction. The discretization of the gravity contribution, included in the source term, is explicitly added to these intermediate states $(\delta y u)^{**}_{i+\frac{1}{2},j}, (\delta x v)^{**}_{i,j+\frac{1}{2}}$.

Implicit discretization of the pressure subsystem and source term

The non-conservative pressure subsystem

$$\partial_t \mathbf{Q} + \mathbf{B}_p^i(\mathbf{Q}) \cdot \nabla \mathbf{Q} = \mathbf{S}(\mathbf{Q}), \tag{3.73}$$

is discretized using an implicit discretization over edge staggered grids, based on the path-conservative approach of Pares and Castro [125], [27]. Similarly to the viscous subsystem described in the previous paragraph, even the subsystem in (3.73) represents an evolution law for the momentum variables only, which is why the other state variables contained in Q can be excluded at this stage of discretization. Thus, the two equations in x and y-direction which constitute the viscous subsystem (3.63) are

$$\partial_t(\alpha^l u) + \alpha^l \partial_x p = 0 \qquad \text{and} \qquad \partial_t(\alpha^l v) + \alpha^l \partial_y p = 0. \tag{3.74}$$

Again, for the same reasons as described in the previous paragraph for the viscous subsystem, the equations in (3.74) are discretized on two different staggered edge based cells in the directions x and y-direction, respectively. In x-direction, the PDE is integrated over the staggered edge-based cells $\Omega_{i+\frac{1}{2},j} \times [t^n, t^{n+1}]$, which is represented in Figure 3.3, and reads

$$\int_{t^{**}}^{t^{n+1}} \int_{x_i}^{x_{i+1}} \int_{y_{j-\frac{1}{2}}}^{y_{j+\frac{1}{2}}} \frac{\partial \alpha^l u}{\partial t} dxdydt + \int_{t^{**}}^{t^{n+1}} \int_{x_i}^{x_{i+1}} \int_{y_{j-\frac{1}{2}}}^{y_{j+\frac{1}{2}}} \alpha^l \frac{\partial p}{\partial x} dxdydt = 0. \tag{3.75}$$

Assuming that the discrete pressure is piecewise constant in each cell

$$p(x) = \begin{cases} p_{i,j} & \text{if } x \leqslant x_{i+\frac{1}{2}}, \\ p_{i+1,j} & \text{if } x > x_{i+\frac{1}{2}}, \end{cases} \quad \text{then} \quad \frac{\partial p}{\partial x} = \delta(x - x_{i+\frac{1}{2}})\,(p_{i+1,j} - p_{i,j}), \tag{3.76}$$

and integrating in x-direction, the non-conservative product reads

$$\Delta x \Delta y \Big((\alpha^l u)^{n+1}_{i+\frac{1}{2},j} - (\alpha^l u)^{**}_{i+\frac{1}{2},j} \Big) + \int_{t^{**}}^{t^{n+1}} \int_{y_{j-\frac{1}{2}}}^{y_{j+\frac{1}{2}}} \tilde{\alpha}_{i+\frac{1}{2},j}\,(p_{i+1,j} - p_{i,j})\, dydt = 0, \tag{3.77}$$

where the $\tilde{\alpha}_{i+\frac{1}{2},j}$ is defined with the path integral along the straight-line segment path $\varphi = \alpha_i + s(\alpha_{i+1} - \alpha_i)$ and results $\tilde{\alpha}_{i+\frac{1}{2},j} = \frac{1}{2}(\alpha_{i+1,j} + \alpha_{i,j})$.

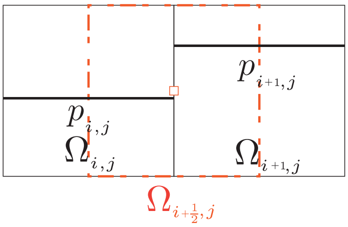

Fig. 3.3. Representation of the discrete states over the different staggered control volumes, in black the primal control volumes, in red the element of the edge-based staggered mesh in x-direction over which the pressure subsystem is integrated.

Then introducing this definition in (3.77) and integrating, the following implicit discretization of the pressure terms is obtained

$$\Delta x \Delta y \left((\alpha^l u)^{n+1}_{i+\frac{1}{2},j} - (\alpha^l u)^{**}_{i+\frac{1}{2},j} \right) + \Delta t \Delta y \, \delta y^{n+1}_{i+\frac{1}{2},j} \left(p^{n+1}_{i+1,j} - p^{n+1}_{i,j} \right) = 0, \quad (3.78)$$

where $\delta y^{n+1}_{i+\frac{1}{2},j} = \Delta y \, \tilde{\alpha}_{i+\frac{1}{2},j} = \Delta y \, \frac{1}{2}({\alpha^l}_{i+1,j} + {\alpha^l}_{i,j})$.

The two discrete momentum equations, in x and y-direction, including the discretization of the non-conservative pressure terms therefore read

$$(\delta y u)^{n+1}_{i+\frac{1}{2},j} = (\delta y u)^{**}_{i+\frac{1}{2},j} - \Delta t \, \delta y^{n+1}_{i+\frac{1}{2},j} \frac{\left(p^{n+1}_{i+1,j} - p^{n+1}_{i,j} \right)}{\Delta x} \quad (3.79)$$

and

$$(\delta x v)^{n+1}_{i,j+\frac{1}{2}} = (\delta x v)^{**}_{i,j+\frac{1}{2}} - \Delta t \, \delta x^{n+1}_{i,j+\frac{1}{2}} \frac{\left(p^{n+1}_{i,j+1} - p^{n+1}_{i,j} \right)}{\Delta y}. \quad (3.80)$$

The algebraic velocity relaxation source term contained in $\mathbf{S}(\mathbf{Q})$ still needs to be discretized. It requires an implicit discretization on the same staggered control volumes, where a simple backward Euler scheme is used. By adding this contribution to (3.79- 3.80), the final semi-implicit discretization of the momentum equations is obtained as

$$\begin{aligned} (\delta y u)^{n+1}_{i+\frac{1}{2},j} = (\delta y u)^{**}_{i+\frac{1}{2},j} &- \frac{\Delta t}{\Delta x} \delta y^{n+1}_{i+\frac{1}{2},j} \, (p^{n+1}_{i+1,j} - p^{n+1}_{i,j}) \\ &- \frac{\Delta t}{\lambda} \, \delta y^{n+1}_{i+\frac{1}{2},j} \, (u^{n+1}_{i+\frac{1}{2},j} - u^{s,n+1}_{i+\frac{1}{2},j}) \alpha^{s,n+1}_{i+\frac{1}{2},j}, \end{aligned} \quad (3.81)$$

$$\begin{aligned} (\delta x v)^{n+1}_{i,j+\frac{1}{2}} = (\delta x v)^{**}_{i,j+\frac{1}{2}} &- \frac{\Delta t}{\Delta y} \delta x^{n+1}_{i,j+\frac{1}{2}} \, (p^{n+1}_{i,j+1} - p^{n+1}_{i,j}) \\ &- \frac{\Delta t}{\lambda} \, \delta x^{n+1}_{i,j+\frac{1}{2}} \, (v^{n+1}_{i,j+\frac{1}{2}} - v^{s,n+1}_{i,j+\frac{1}{2}}) \alpha^{s,n+1}_{i,j+\frac{1}{2}}, \end{aligned} \quad (3.82)$$

where $\alpha^{s,n+1}_{i+\frac{1}{2},j}$ and $\alpha^{s,n+1}_{i,j+\frac{1}{2}}$ are referring to the edge, then can be evaluated either as the maximum or the average of the ones in the adjacent cells.
Manipulating the previous equations, $(\delta yu)^{n+1}_{i+\frac{1}{2},j}$ and $(\delta xv)^{n+1}_{i,j+\frac{1}{2}}$ can be expressed as follows:

$$\begin{aligned}
(\delta yu)^{n+1}_{i+\frac{1}{2},j}\left(1+\frac{\Delta t}{\lambda}\ \alpha^{s,n+1}_{i+\frac{1}{2},j}\right) &= (\delta yu)^{**}_{i+\frac{1}{2},j}-\frac{\Delta t}{\Delta x}\delta y^{n+1}_{i+\frac{1}{2},j}\ (p^{n+1}_{i+1,j}-p^{n+1}_{i,j}) \\
&\quad +\frac{\Delta t}{\lambda}\ \delta y^{n+1}_{i+\frac{1}{2},j}\ u^{s,n+1}_{i+\frac{1}{2},j}\alpha^{s,n+1}_{i+\frac{1}{2},j}, \qquad (3.83) \\
(\delta xv)^{n+1}_{i,j+\frac{1}{2}}\left(1+\frac{\Delta t}{\lambda}\ \alpha^{s,n+1}_{i,j+\frac{1}{2}}\right) &= (\delta xv)^{**}_{i,j+\frac{1}{2}}-\frac{\Delta t}{\Delta y}\delta x^{n+1}_{i,j+\frac{1}{2}}\ (p^{n+1}_{i,j+1}-p^{n+1}_{i,j}) \\
&\quad +\frac{\Delta t}{\lambda}\ \delta x^{n+1}_{i,j+\frac{1}{2}}\ v^{s,n+1}_{i,j+\frac{1}{2}}\alpha^{s,n+1}_{i,j+\frac{1}{2}}, \qquad (3.84)
\end{aligned}$$

which can be re-written as

$$\begin{aligned}
(\delta yu)^{n+1}_{i+\frac{1}{2},j} &= \frac{\lambda}{\alpha^{s,n+1}_{i+\frac{1}{2},j}\Delta t+\lambda}\left((\delta yu)^{**}_{i+\frac{1}{2},j}-\frac{\Delta t}{\Delta x}\delta y^{n+1}_{i+\frac{1}{2},j}\ (p^{n+1}_{i+1,j}-p^{n+1}_{i,j})\right) \\
&\quad +\frac{\alpha^{s,n+1}_{i+\frac{1}{2},j}\Delta t}{\alpha^{s,n+1}_{i+\frac{1}{2},j}\Delta t+\lambda}\ \delta y^{n+1}_{i+\frac{1}{2},j}\ u^{s,n+1}_{i+\frac{1}{2},j}, \qquad (3.85) \\
(\delta xv)^{n+1}_{i,j+\frac{1}{2}} &= \frac{\lambda}{\alpha^{s,n+1}_{i,j+\frac{1}{2}}\Delta t+\lambda}\left((\delta xv)^{**}_{i,j+\frac{1}{2}}-\frac{\Delta t}{\Delta y}\delta x^{n+1}_{i,j+\frac{1}{2}}\ (p^{n+1}_{i,j+1}-p^{n+1}_{i,j})\right) \\
&\quad +\frac{\alpha^{s,n+1}_{i,j+\frac{1}{2}}\Delta t}{\alpha^{s,n+1}_{i,j+\frac{1}{2}}\Delta t+\lambda}\ \delta x^{n+1}_{i,j+\frac{1}{2}}\ v^{s,n+1}_{i,j+\frac{1}{2}}. \qquad (3.86)
\end{aligned}$$

Two different types of coefficients can be identified, for both equations, as $\beta^{n+1}_{i+\frac{1}{2},j}$, $\gamma^{n+1}_{i+\frac{1}{2},j}$ and $\beta^{n+1}_{i,j+\frac{1}{2}}$, $\gamma^{n+1}_{i,j+\frac{1}{2}}$; they read:

$$\begin{aligned}
\beta^{n+1}_{i+\frac{1}{2},j} &= \frac{\lambda}{\alpha^{s,n+1}_{i+\frac{1}{2},j}\Delta t+\lambda}, \qquad & \gamma^{n+1}_{i+\frac{1}{2},j} &= \frac{\alpha^{s,n+1}_{i+\frac{1}{2},j}\Delta t}{\alpha^{s,n+1}_{i+\frac{1}{2},j}\Delta t+\lambda}, \\
\beta^{n+1}_{i,j+\frac{1}{2}} &= \frac{\lambda}{\alpha^{s,n+1}_{i,j+\frac{1}{2}}\Delta t+\lambda}, \qquad & \gamma^{n+1}_{i,j+\frac{1}{2}} &= \frac{\alpha^{s,n+1}_{i,j+\frac{1}{2}}\Delta t}{\alpha^{s,n+1}_{i,j+\frac{1}{2}}\Delta t+\lambda}.
\end{aligned}$$

Note the behaviour of these coefficients as $\epsilon \to 0$, assuming $\alpha^s = 1$, i.e. inside the solid phase, or assuming $\alpha^s = 0$ in the liquid phase

$$\begin{aligned} \lim_{\epsilon \to 0} \beta^{n+1}_{i+\frac{1}{2},j}\Big|_{\alpha^s=1} &= 0, \qquad \lim_{\epsilon \to 0} \gamma^{n+1}_{i+\frac{1}{2},j}\Big|_{\alpha^s=1} = 1, \\ \lim_{\epsilon \to 0} \beta^{n+1}_{i+\frac{1}{2},j}\Big|_{\alpha^s=0} &= 1, \qquad \lim_{\epsilon \to 0} \gamma^{n+1}_{i+\frac{1}{2},j}\Big|_{\alpha^s=0} = 0. \end{aligned} \tag{3.87}$$

Thus, when a cell is completely occupied by the solid phase, the momentum equations automatically and naturally force the velocity of the residual liquid phase to tend to the velocity of the solid phase.

3.1.6 Final pressure system

Inserting the discrete momentum equations (3.86) into the finite volume discretization of the continuity equation (3.42) yields the following system for the unknown pressure $p^{n+1}_{i,j}$

$$\begin{aligned} V(p^{n+1}_{i,j}) &- \frac{\Delta t^2}{\Delta x}\left(\beta^{n+1}_{i+\frac{1}{2},j}\delta y^{n+1}_{i+\frac{1}{2},j}(p^{n+1}_{i+1,j} - p^{n+1}_{i,j}) - \beta^{n+1}_{i-\frac{1}{2},j}\delta y^{n+1}_{i-\frac{1}{2},j}(p^{n+1}_{i,j} - p^{n+1}_{i-1,j})\right) \\ &- \frac{\Delta t^2}{\Delta y}\left(\beta^{n+1}_{i,j+\frac{1}{2}}\delta x^{n+1}_{i,j+\frac{1}{2}}(p^{n+1}_{i,j+1} - p^{n+1}_{i,j}) - \beta^{n+1}_{i,j-\frac{1}{2}}\delta x^{n+1}_{i,j-\frac{1}{2}}(p^{n+1}_{i,j} - p^{n+1}_{i,j-1})\right) \\ &= b^n_{i,j}, \end{aligned} \tag{3.88}$$

with the known right hand side $b^n_{i,j}$

$$\begin{aligned} b^n_{i,j} = V(p^n_{i,j}) &- \Delta t\left(\gamma^{n+1}_{i+\frac{1}{2},j}(\delta yu)^{s,n+1}_{i+\frac{1}{2},j} - \gamma^{n+1}_{i-\frac{1}{2},j}(\delta yu)^{s,n+1}_{i-\frac{1}{2},j}\right) \\ &- \Delta t\left(\gamma^{n+1}_{i,j+\frac{1}{2}}(\delta xv)^{s,n+1}_{i,j+\frac{1}{2}} - \gamma^{n+1}_{i,j-\frac{1}{2}}(\delta xv)^{s,n+1}_{i,i-\frac{1}{2}}\right) \\ &- \Delta t\left(\beta^{n+1}_{i+\frac{1}{2},j}(\delta yu)^{*}_{i+\frac{1}{2},j} - \beta^{n+1}_{i-\frac{1}{2},j}(\delta yu)^{**}_{i-\frac{1}{2},j}\right) \\ &- \Delta t\left(\beta^{n+1}_{i,j+\frac{1}{2}}(\delta xv)^{*}_{i,j+\frac{1}{2}} - \beta^{n+1}_{i,j-\frac{1}{2}}(\delta xv)^{**}_{i,j-\frac{1}{2}}\right). \end{aligned} \tag{3.89}$$

Discretizing the edge-integrated volume fractions $\delta x^{n+1}_{i,j+\frac{1}{2}}$, $\delta y^{n+1}_{i+\frac{1}{2},j}$ and the velocities of the objects $u^{s,n+1}$, $v^{s,n+1}$ implicitly, the system (3.88) becomes strongly nonlinear and thus difficult to solve. Actually, the solid related variables $u^{s,n+1}$, $v^{s,n+1}$ and $\alpha^{s,n+1}$ are known at at time t^{n+1} due to the fact that the kinematics of the solid is decoupled from the dynamics of the liquid phase, thus the non-linearity affects only the edge-integrated volume fractions. Therefore, a *Picard iteration* technique has to be adopted in order to make the edge-integrated volume fractions $\delta x^{n+1}_{i,j+\frac{1}{2}}$, $\delta y^{n+1}_{i+\frac{1}{2},j}$ explicit again, as suggested in [32].

Introducing k to denote the index of the Picard iterations, the following *mildly nonlinear* system for the pressure $p^{n+1,k+1}_{i,j}$ is obtained

$$\begin{aligned} V(p^{n+1,k+1}_{i,j}) &- \frac{\Delta t^2}{\Delta x}\left(\beta^{n+1}_{i+\frac{1}{2},j}\delta y^{n+1,k}_{i+\frac{1}{2},j}\,\Delta p^{n+1,k+1}_{i+\frac{1}{2},j} - \beta^{n+1}_{i-\frac{1}{2},j}\delta y^{n+1,k}_{i-\frac{1}{2},j}\,\Delta p^{n+1,k+1}_{i-\frac{1}{2},j}\right)\\ &- \frac{\Delta t^2}{\Delta y}\left(\beta^{n+1}_{i,j+\frac{1}{2}}\delta x^{n+1,k}_{i,j+\frac{1}{2}}\,\Delta p^{n+1,k+1}_{i,j+\frac{1}{2}} - \beta^{n+1}_{i,j-\frac{1}{2}}\delta x^{n+1,k}_{i,j-\frac{1}{2}}\,\Delta p^{n+1,k+1}_{i,j-\frac{1}{2}}\right)\\ &= b^n_{i,j}, \end{aligned} \tag{3.90}$$

with $\Delta p^{n+1,k+1}_{i+\frac{1}{2},j} = p^{n+1,k+1}_{i+1,j} - p^{n+1,k+1}_{i,j}$ and $\Delta p^{n+1,k+1}_{i,j+\frac{1}{2}} = p^{n+1,k+1}_{i,j+1} - p^{n+1,k+1}_{i,j}$.

The system (3.90) needs to be solved for the pressure $p^{n+1,k+1}_{i,j}$ at each Picard iteration. Using a more compact notation, the above system can be written as follows

$$\mathbf{V}(\mathbf{p}^{n+1,k+1}) + \mathbf{T}\,\mathbf{p}^{n+1,k+1} = \mathbf{b}^n, \tag{3.91}$$

with the vector of the unknown new pressure $\mathbf{p}^{n+1,k+1} = (p^{n+1,k+1}_{i,j})$ and where $\mathbf{V}(\mathbf{p}^{n+1,k+1}) = V(p^{n+1,k+1}_{i,j})$ denotes the corresponding fluid volumes; $\mathbf{b}^n$ is the known right hand side vector and $\mathbf{T}$ is a sparse, symmetric and penta-diagonal matrix which arises from the linear terms in equation (3.90). The matrix $\mathbf{T}$ in the system (3.91) is symmetric and at least positive semi-definite. For the solution of system (3.91), we apply the nested Newton-type technique introduced by Casulli *et al.* in [18, 19, 32, 33], associated with a matrix-free implementation of the conjugate gradient method. For implementation details and the convergence proofs of these Newton-type techniques applied to mildly nonlinear systems the reader is referred to the above references.

Once the pressures $p^{n+1,k+1}_{i,j}$ are evaluated, the quantities $\delta y^{n+1,k}_{i+\frac{1}{2},j}$ and $\delta x^{n+1,k}_{i,j+\frac{1}{2}}$ at the next Picard iteration can be easily obtained from (3.44) and (3.45). As confirmed by numerical simulations, only very few Picard iterations are needed to obtain an accurate solution. At the end of the last Picard iteration $p^{n+1}_{i,j} := p^{n+1,k+1}_{i,j}$ is set and the velocity field is easily obtained from the discrete momentum equations (3.86). The time step is only limited by a *mild* CFL condition based on the liquid and solid phase velocities and on the kinematic viscosity. Since the solid phase is also governed by an advection equation which is explicitly discretized and since the velocity of the solid phase is prescribed *a priori*, a stability condition that is valid for both phases can be easily formulated. For the explicit advection terms of both phases and for all the test problems shown in this thesis the CFL time restriction reads:

$$\Delta t \leq \frac{\text{CFL}}{\frac{s_x^{\max}}{\Delta x} + \frac{2\nu}{\Delta x^2} + \frac{s_y^{\max}}{\Delta y} + \frac{2\nu}{\Delta y^2}}, \tag{3.92}$$

where the choice of the maximum wave speed is $s_x^{\max} = 2\max(|u|, |u^s|)$ and $s_y^{\max} = 2\max(|v|, |v^s|)$ and ν is the kinematic viscosity coefficient. The stability condition is not affected by the gravity wave speed, thus the method is efficient for *low Froude number* flows, too.

3.1.7 Advection of the solid volume fraction using a subgrid

The solid phase kinematics is prescribed and is evaluated through an advection equation, as described in (3.1). However, it is necessary for the advection of the solid phase to be accurately computed in order to preserve the properties of a solid, i.e. to remain sharply defined and to spread only slightly over time due to the numerical viscosity of the scheme. Usually, a numerical method is able to produce better solutions as the mesh size is refined. However, the adoption of a too severe grid refinement, to ensure an accurate advection of the solid phase, can easily become computationally prohibitive for the evaluation of the liquid phase dynamics, which requires, at each time-step the solution of the pressure based system described in Section 3.1.6. A practical solution, which is adopted in all the test problems shown in this work, is to keep the main computational grid at a reasonable size and adopt a *sub-grid* strategy to evaluate the advection of the solid volume fraction α^s and the effective edge-integrated volume fractions $\delta y^{n+1}_{i+\frac{1}{2},j}$ and $\delta x^{n+1}_{i,j+\frac{1}{2}}$, similar to the subgrid methods introduced in other contexts in [31, 53].

As represented in Fig. 3.4, starting from the main grid, which consists of rectangular control volumes $\Omega_{i,j} = [x_{i-\frac{1}{2}}, x_{i+\frac{1}{2}}] \times [y_{j-\frac{1}{2}}, y_{j+\frac{1}{2}}]$ with barycenters in (x_i, y_j) and having width Δx_i and height Δy_j, a sub-grid consisting of N×M sub-elements for each rectangular control volumes $\Omega_{i,j}$ is defined.

The cell-averaged solid volume fraction α^s is defined on this sub-grid as follows

$$\alpha^s_{n,m} = \frac{\text{NM}}{\Delta x \Delta y} \int\limits_{x_{n-\frac{1}{2}}}^{x_{n+\frac{1}{2}}} \int\limits_{y_{m-\frac{1}{2}}}^{y_{m+\frac{1}{2}}} \alpha^s(x,y)\, dy\, dx, \tag{3.93}$$

while on the main grid, a cell-averaged solid volume fraction $\alpha^s_{i,j}$ can be evaluated by means of the values in these subcells

$$\alpha^s_{i,j} = \frac{1}{\text{NM}} \sum_{n,m=1}^{\text{N,M}} \alpha^s_{n,m}. \tag{3.94}$$

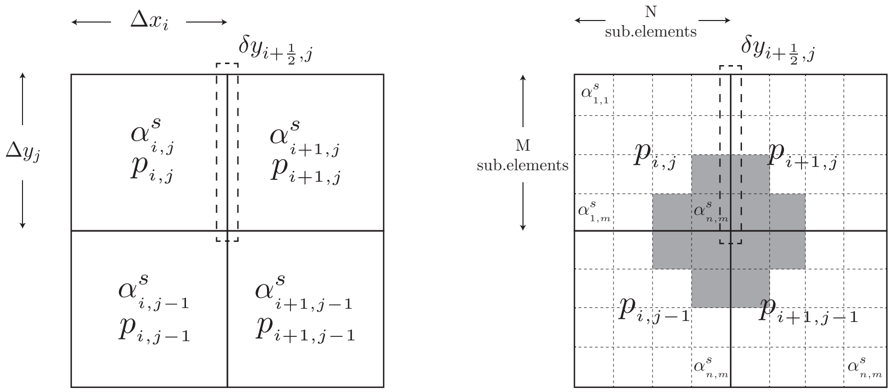

Fig. 3.4. Representation of the main grid for the evaluation of the liquid phase related variables (left). Representation of the sub-grid within the main grid for the evaluation of the refined solid phase variables (right). In gray is depicted the variability of the solid volume fraction $\alpha^s_{n,m}$ over the sub-grid.

Furthermore, the edge-integrated effective volume fractions can be more accurately assessed, in agreement with the more accurate distribution of the solid phase on the sub-grid. Considering for instance the edge-integrated effective volume fraction $\delta y^{n+1}_{i+\frac{1}{2},j}$ shown in Fig. 3.4, it can be evaluated over the sub-grid as follows:

$$\delta y_{i+\frac{1}{2},j} = \frac{\mathrm{N}}{2\Delta x} \sum_{m=1}^{\mathrm{M}} \Big(V^l(p_{i,j}, \alpha^s_{n,m}) + V^l(p_{i+1,j}, \alpha^s_{1,m}) \Big) \,, \tag{3.95}$$

where the liquid cell volume V^l is evaluated by the *constitutive relationship* scaled for the sub-grid and where the sub-grid cell-averages of the solid volume fraction $\alpha^s_{n,m}$ which shares the same edge are involved.
Furthermore, for the sake of clarity, let us recall that the advection of the solid phase is solved through a second-order FV method in space and time by means of a MUSCL-Hancock TVD method, illustrated in the 3.1.5 section, even though the dynamics of the solid and liquid phases are decoupled.

3.1.8 Remark

When the vertical mesh spacing Δy is large enough to contain the entire water layer of depth H, we can drop the vertical index j and set $(\delta y)^n_{i+1/2} = H^n_{i+1/2}$. Since for one single layer $p^n_i = g(\eta^n_i - y_b)$ with η^n_i the free surface elevation and y_b the location of the barycenters of the only row of cells in y direction, the previous scheme reduces to

$$V_i^{n+1} = V_i^n - \Delta t \left((Hu)_{i+\frac{1}{2}}^{n+1} - (Hu)_{i-\frac{1}{2}}^{n+1} \right), \tag{3.96}$$

$$(Hu)_{i+\frac{1}{2}}^{n+1} = (Hu)_{i+\frac{1}{2}}^{*} - \frac{\Delta t}{\Delta x} H_{i+\frac{1}{2}}^{n} \, (p_{i+1}^{n+1} - p_i^{n+1}), \tag{3.97}$$

which is a consistent and mass and momentum conservative discretization of the 1D shallow water equations

$$\begin{aligned} \frac{\partial \eta}{\partial t} + \frac{\partial (Hu)}{\partial x} &= 0, & (3.98) \\ \frac{\partial (Hu)}{\partial t} + \frac{\partial (Hu^2)}{\partial x} + gH\frac{\partial \eta}{\partial x} &= 0. & (3.99) \end{aligned}$$

3.2 Explicit FV scheme for compressible multiphase fluid and solid mechanics

As the BN model is one of the most popular mathematical models for describing two-phase flow, there are many works that address this problem numerically. However, only a very limited number of publications exist on the mathematical and computational issues of BN models for multi-phase flows describing *more* than two phases. It is therefore very attractive to numerically address the BN-type SHTC multi-phase model presented in the previous Section 2.3, which has been generalised to fluid and solid mechanics.

In this section we numerically address a simplified version of the BN-type SHTC model introduced in Section 2.3. The mixture considered here consist at most of three phases. However, they can be freely chosen as gaseous, viscous or inviscid liquid, or elasto-plastic solid.

The numerical method presented in this section will follow the so-called *diffuse interface approach*, thanks to the suitable mathematical description of the mixture through volume fractions. An *operator splitting* approach is employed, in order to numerically solve the resulting simplified system, which will be detailed in the next section. The procedure consists of two steps. At each time step, the homogeneous part of the PDEs system, which also includes all non-conservative terms, is discretized with the aid of an explicit second-order path-conservative FV scheme, [171]. A preliminary solution is thus obtained. Then, since the time scales associated with the relaxation sources are much shorter than those given by the stability condition of the explicit scheme used to solve the homogeneous part of the PDE, two different implicit methods are employed. Namely, for the stiff, but linear, sources related to velocity relaxation, an time integrator based on backward Euler is employed. While a semi-analytical time integration method is adopted for the nonlinear stiff source governing the relaxation of the distortion matrix $\mathbf{A}_a$. Moreover, as we shall see, the accurate integration of the distortion matrix evolution equation is a rather challenging task, especially in the context of multiphase flows, thus some additional efforts will be required.

3.2.1 Three phase reduced BN-type SHTC model

The numerical test problems, presented below, concern one and two-dimensional three-phase flow. Thus, the BN-type form of the SHTC mixture equations for $a = 1, 2, 3$, presented in Section 2.3, and further extended with the generalization to elasto-plastic solids and viscous fluid constituents, is considered.

As stated in the introduction of this numerical section, the mathematical model is further simplified, but in such a way as to preserve its multi-phase and multi-material properties. In this thesis, we restrict ourselves to relatively low Mach number flows, e.g. $M \simeq 0.1$. In this context shock waves are either totally absent, or very weak. Thus considering the conservation of phase entropy, which has much simpler dynamics, rather than phase energy leads to a negligible error. Therefore, the *phase entropy equations* can be retrieved from the SHTC equations (2.112g), using the conservation of total mass (2.112f), and read

$$\frac{\partial s_a}{\partial t} + V_k \frac{\partial s_a}{\partial x_k} = \Pi_a - \pi_a. \tag{3.100}$$

Then, neglecting the phase pressure relaxation towards a common pressure for all the phases ($\Phi_a = 0$), assuming the absence of phase transformations ($\chi_a = 0$), temperature relaxation ($\pi_a = 0$), and assuming the isotropy of the phase velocity relaxation process ($\lambda_{ab,k} = \text{diag}(\lambda_1, \lambda_2, \dots, \lambda_{\text{N}})$, $k = 1, 2, 3$), the mathematical model, that is numerically addressed, can be represented by the following system of PDEs

$$\frac{\partial \varrho_a}{\partial t} + \frac{\partial u_{a,k}}{\partial x_k} = 0 \tag{3.101a}$$

$$\frac{\partial A_{a,Jk}}{\partial t} + \frac{\partial \left(A_{a,Jl} v_{a,l}\right)}{\partial x_k} + v_{a,i}\left(\frac{\partial A_{a,Jk}}{\partial x_i} - \frac{\partial A_{a,Ji}}{\partial x_k}\right) = Z_{a,Jk}, \tag{3.101b}$$

$$\frac{\partial u_{a,i}}{\partial t} + \frac{\partial}{\partial x_k}\left(u_{a,i} v_{a,k} + P_a \delta_{i,k} - \sigma_{a,ik}\right) = -c_a \sum_{b=1}^{\text{N}} p_b \frac{\partial \alpha_b}{\partial x_i} + p_a \frac{\partial \alpha_a}{\partial x_i} \tag{3.101c}$$

$$- c_a \sum_{b=1}^{\text{N}} \varrho_b \bar{v}_{b,k} \omega_{b,k,i} + \varrho_a \bar{v}_{a,k} \omega_{a,k,i} \tag{3.101d}$$

$$+ c_a \sum_{b=1}^{\text{N}} \lambda_b \varrho_b \left(v_{b,i} - V_i\right) - \lambda_a \varrho_a \left(v_{a,i} - V_i\right), \tag{3.101e}$$

$$\frac{\partial s_a}{\partial t} + V_k \frac{\partial s_a}{\partial x_k} = \frac{\lambda_a}{T_a} c_a \left(v_{a,k} - V_k\right)^2, \tag{3.101f}$$

$$\frac{\partial \alpha_a}{\partial t} + V_k \frac{\partial \alpha_a}{\partial x_k} = 0, \tag{3.101g}$$

In order to simplify notation for discussing the numerical method, we introduce a compact matrix-vector notation so that system (3.101) can be written as

$$\partial_t \mathbf{Q} + \nabla \cdot \mathbf{F}(\mathbf{Q}) + \mathbf{B}(\mathbf{Q}) \cdot \nabla \mathbf{Q} = \mathbf{S}(\mathbf{Q}) \tag{3.102}$$

with $\mathbf{Q} = \{\mathbf{Q}_1, \mathbf{Q}_2, \mathbf{Q}_3\}$ being the vector of conservative state variables, and

$\mathbf{Q}_a$ being the conservative variables for each phase $a = 1, 2, 3$

$$\mathbf{Q}_a = (\varrho_a, \boldsymbol{u}_a, s_a, \alpha_a, \mathbf{A}_{a,1}, \mathbf{A}_{a,2}, \mathbf{A}_{a,3}), \tag{3.103}$$

where we use the fact that each distortion matrix $\mathbf{A}_a$ is in fact a triad of three basis vectors, i.e. $\mathbf{A}_a = \{\mathbf{A}_{a,1}, \mathbf{A}_{a,2}, \mathbf{A}_{a,3}\}$ and for each $J = 1, 2, 3$, $\mathbf{A}_{a,J} = \{A_{a,J1}, A_{a,J2}, A_{a,J3}\}$ is a 3-vector.

The flux tensor $\mathbf{F}(\mathbf{Q})$ in (3.102) is decoupled with respect to the phases, i.e. $\mathbf{F}(\mathbf{Q}) = \{\mathbf{F}_1(\mathbf{Q}_1), \mathbf{F}_2(\mathbf{Q}_2), \mathbf{F}_3(\mathbf{Q}_3)\}$, and can be written as the sum of several contributions as follows

$$\mathbf{F}_a(\mathbf{Q}_a) = \mathbf{F}^{\mathrm{c}}_a(\mathbf{Q}_a) + \mathbf{F}^{\mathrm{p}}_a(\mathbf{Q}_a) + \mathbf{F}^{\mathrm{s}}_a(\mathbf{Q}_a) + \mathbf{F}^{\mathrm{d}}_a(\mathbf{Q}_a), \tag{3.104}$$

where each term depends only on $\mathbf{Q}_a$ and is defined as

$$\begin{gathered}
\mathbf{F}^{\mathrm{c}}_a(\mathbf{Q}_a) = \begin{pmatrix} \boldsymbol{u}_a \\ \boldsymbol{u}_a \otimes \boldsymbol{v}_a \\ \mathbf{0}_{3\times1} \\ \mathbf{0}_{3\times1} \\ \mathbf{0}_{3\times1} \\ \mathbf{0}_{3\times1} \\ \mathbf{0}_{3\times1} \end{pmatrix}, \quad \mathbf{F}^{\mathrm{p}}_a(\mathbf{Q}_a) = \begin{pmatrix} \mathbf{0}_{3\times1} \\ P_a\mathbf{I} \\ \mathbf{0}_{3\times1} \\ \mathbf{0}_{3\times1} \\ \mathbf{0}_{3\times1} \\ \mathbf{0}_{3\times1} \\ \mathbf{0}_{3\times1} \end{pmatrix}, \\
\mathbf{F}^{\mathrm{s}}_a(\mathbf{Q}_a) = \begin{pmatrix} \mathbf{0}_{3\times1} \\ \boldsymbol{\sigma}^{\mathrm{e}}_a \\ \mathbf{0}_{3\times1} \\ \mathbf{0}_{3\times1} \\ \mathbf{0}_{3\times1} \\ \mathbf{0}_{3\times1} \\ \mathbf{0}_{3\times1} \end{pmatrix}, \quad \mathbf{F}^{\mathrm{d}}_a(\mathbf{Q}_a) = \begin{pmatrix} \mathbf{0}_{3\times1} \\ \mathbf{0}_{3\times3} \\ \mathbf{0}_{3\times1} \\ \mathbf{0}_{3\times1} \\ \mathbf{A}_{a,1}\boldsymbol{v}_a\mathbf{I} \\ \mathbf{A}_{a,2}\boldsymbol{v}_a\mathbf{I} \\ \mathbf{A}_{a,3}\boldsymbol{v}_a\mathbf{I} \end{pmatrix}.
\end{gathered} \tag{3.105}$$

The tensor $\mathbf{F}^{\mathrm{c}}_a(\mathbf{Q}_a)$ contains the convective terms for the mass and momentum balance equations, $\mathbf{F}^{\mathrm{p}}_A(\mathbf{Q}_a)$ is the phase related pressure flux tensor, $\mathbf{F}^{\mathrm{s}}_a(\mathbf{Q}_a)$ is the flux tensor containing contribution due to shear viscous and elastic stresses, while $\mathbf{F}^{\mathrm{d}}_a(\mathbf{Q}_a)$ contains advective terms from the distortion PDE.

The so-called non-conservative matrix-vector product in (3.102) contains the phase coupling terms and can be presented as a sum of the following contributions

$$\mathbf{B}(\mathbf{Q}) \cdot \nabla\mathbf{Q} = \Big[\mathbf{B}^{\mathrm{c}}(\mathbf{Q}) + \mathbf{B}^{\mathrm{p}}(\mathbf{Q}) + \mathbf{B}^{\mathrm{w}}(\mathbf{Q}) + \mathbf{B}^{\mathrm{d}}(\mathbf{Q})\Big] \cdot \nabla\mathbf{Q}, \tag{3.106}$$

where the convective part is given by (components restricted to phase a)

$$(\mathbf{B}^{\mathrm{c}}(\mathbf{Q}) \cdot \nabla\mathbf{Q})_a = (0, \mathbf{0}, \boldsymbol{V} \cdot \nabla s_a, \boldsymbol{V} \cdot \nabla\alpha_a, \mathbf{0}, \mathbf{0}, \mathbf{0})^{\mathsf{T}}, \tag{3.107}$$

while the non-conservative products related to the multiphase and multi-material nature of the model read

$$\left(\mathbf{B}^{\mathrm{p}}(\mathbf{Q})\cdot\nabla\mathbf{Q}\right)_a = \begin{pmatrix} 0 \\ c_a\sum_{b=1}^{3} p_b\nabla\alpha_b - p_a\nabla\alpha_a \\ 0 \\ 0 \\ \mathbf{0} \\ \mathbf{0} \\ \mathbf{0} \end{pmatrix}, \tag{3.108}$$

$$\left(\mathbf{B}^{\mathrm{w}}(\mathbf{Q})\cdot\nabla\mathbf{Q}\right)_a = \begin{pmatrix} 0 \\ c_a\sum_{b=1}^{3} \varrho_b(\nabla\boldsymbol{v}_b-\nabla\boldsymbol{v}_b^{\mathsf{T}})(\boldsymbol{v}_b-\boldsymbol{V})-\varrho_a(\nabla\boldsymbol{v}_a-\nabla\boldsymbol{v}_a^{\mathsf{T}})(\boldsymbol{v}_a-\boldsymbol{V}) \\ 0 \\ 0 \\ \mathbf{0} \\ \mathbf{0} \\ \mathbf{0} \end{pmatrix}, \tag{3.109}$$

$$\left(\mathbf{B}^{\mathrm{d}}(\mathbf{Q})\cdot\nabla\mathbf{Q}\right)_a = \begin{pmatrix} 0 \\ \mathbf{0} \\ 0 \\ 0 \\ \left(\nabla\mathbf{A}_{a,1}-\nabla\mathbf{A}_{a,1}^{\mathsf{T}}\right)\boldsymbol{v}_a \\ \left(\nabla\mathbf{A}_{a,2}-\nabla\mathbf{A}_{a,2}^{\mathsf{T}}\right)\boldsymbol{v}_a \\ \left(\nabla\mathbf{A}_{a,3}-\nabla\mathbf{A}_{a,3}^{\mathsf{T}}\right)\boldsymbol{v}_a \end{pmatrix}. \tag{3.110}$$

The source term vector $\mathbf{S}(\mathbf{Q})$ can be written as the sum of two different vectors that will be discretized by two different approaches,

$$\mathbf{S}(\mathbf{Q}) = \mathbf{S}^{\mathrm{w}}(\mathbf{Q}) + \mathbf{S}^{\mathrm{s}}(\mathbf{Q}), \tag{3.111}$$

where $\mathbf{S}^{\mathrm{v}}(\mathbf{Q})$ is stiff but linear in $\mathbf{Q}$ (relative velocity relaxation), while $\mathbf{S}^{\mathrm{s}}(\mathbf{Q})$ is related to the strain relaxation source terms of the distortion matrix, which is nonlinear and can be extremely stiff. These source term vectors read

$$\mathbf{S}^{\mathrm{w}}(\mathbf{Q}_a) = \begin{pmatrix} 0 \\ c_a \sum_{b=1}^{3} \lambda_b \varrho_b \left(\boldsymbol{v}_b - \boldsymbol{V}\right) - \lambda_a \varrho_a \left(\boldsymbol{v}_a - \boldsymbol{V}\right) \\ 0 \\ \frac{\lambda_a}{T_a} c_a \left(\boldsymbol{v}_a - \boldsymbol{V}\right)^2 \\ \mathbf{0} \\ \mathbf{0} \\ \mathbf{0} \end{pmatrix}, \quad \mathbf{S}^{\mathrm{s}}(\mathbf{Q}_a) = \begin{pmatrix} 0 \\ 0 \\ 0 \\ 0 \\ \mathbf{Z}_{a,1} \\ \mathbf{Z}_{a,2} \\ \mathbf{Z}_{a,3} \end{pmatrix}, \tag{3.112}$$

where $\boldsymbol{Z}_a = \{\boldsymbol{Z}_{a,1}, \boldsymbol{Z}_{a,2}, \boldsymbol{Z}_{a,3}\}$ is the phase strain relaxation matrix defined in (2.140). Furthermore, to better address some of the specific problems usually encountered in the numerical solution of multiphase flow models. In these models there are complex interfaces described by the volume fractions of the different phases and usually through conserved variables $\mathbf{Q}$ one tends to consider the evolution of combined quantities, such as ϱ_a and $\mathbf{u}_a$, i.e. expressed in terms of $\mathbf{V}$, $\alpha_a \rho_a$ and $\alpha_a \rho_a \boldsymbol{v}_a$. Thus, a cell-local conservative variable polynomial reconstruction could give rise to non-physical discontinuities, e.g. in the reconstructed evaluation of velocity and density fields, as well as violations of positivity in the reconstructed mass fraction values. Whereas, a reconstruction in the primitive variable space, for a second-order MUSCL-Hancock TVD scheme, significantly mitigates these problems, see e.g. [36, 113, 177] and references therein.

Therefore, alongside with the vector of conservative variables $\mathbf{Q} = (\mathbf{Q}_a, \mathbf{Q}_2, \mathbf{Q}_3)$ a vector of primitive variables $\mathbf{V} = (\mathbf{V}_1, \mathbf{V}_2, \mathbf{V}_3)$ is considered, where for each phase $a = 1, 2, 3$,

$$\mathbf{Q}_a = (\varrho_a, \boldsymbol{u}_a, s_a, \alpha_a, \mathbf{A}_a), \qquad \mathbf{V}_a = (\rho_a, \boldsymbol{v}_a, p_a, \alpha_a, \mathbf{A}_a), \tag{3.113}$$

The *primitive-to-conservative* transformation operator will be denoted by $\mathcal{C}$ and its complementary *conservative-to-primitive* by $\mathcal{P}$, i.e.

$$\mathbf{V}_a(x, y) = \mathcal{P}[\mathbf{Q}_a(x, y)], \qquad \text{and} \qquad \mathbf{Q}_a(x, y) = \mathcal{C}[\mathbf{V}_a(x, y)]. \tag{3.114}$$

In the mixture context, these operators must be defined with care to avoid division by zero when a phase vanishes. In the following, we illustrate how these conversion operators are defined in our numerical method to address this issue and to satisfy the unit sum constraints on the volume fractions.

First, a sum of the volume fractions over the phases is evaluated

$$\alpha_{tot} = \sum_{a=1}^{\mathrm{N}} \alpha_a, \tag{3.115}$$

from which a preliminary phase volume fraction is computed as

$$\alpha_a^* = \max(\epsilon, \min(1, \alpha_a/\alpha_{tot}^*)) , \tag{3.116}$$

where $\epsilon = 10^{-14}$ is a small constant introduced to avoid division by zero in the following formula. Then the conservative-to-primitive $\mathcal{P}$ operator reads

$$\mathcal{P}[\mathbf{Q}_a] = \begin{pmatrix} \varrho_a/\alpha_a^* \\ \boldsymbol{u}_a\varrho_a/(\varrho_a^2+\epsilon^2) \\ P[\varrho_a/\alpha_a^*, s_a] \\ \max(\epsilon, \min(1, \alpha_a/\alpha_{tot}^*)) \\ \mathbf{A}_a \end{pmatrix} , \tag{3.117}$$

where $P[\varrho_a/\alpha_a^*, s_a]$ is the pressure function that can be defined according to the EOS chosen for the phase.

3.2.2 Eigenvalue estimates

From the very nature of the hyperbolic equations, it is important to understand the *characteristic* structure of the PDE system (3.101) under consideration. However, even if simplified with respect to the full SHTC model in (2.112), this system remains too complex for analytical calculation of all eigenvalues due to coupling of convective, acoustic, and shear parts, as well as due to coupling between the phases. Therefore, since the FV method requires the knowledge of the maximum sound speeds, some estimates for the eigenvalues discussed below will be used.

To get some estimates of the eigenvalues of the Jacobian $\mathbf{C}_k = \mathbf{C} \cdot \hat{\boldsymbol{n}}_k$, where the direction x_k is specified by the unit vector $\hat{\boldsymbol{n}}_k$. The complete matrix $\mathbf{C}$, can be formally defined from the general first order balance law (3.102) considering the vector of primitive variables for each phase $\mathbf{V}_a$, defined in (3.113), as

$$\mathbf{C} = \left(\frac{\partial \mathbf{Q}_a}{\partial \mathbf{V}_a}\right)^{-1} \left(\frac{\partial \mathbf{F}(\mathbf{Q}_a)}{\partial \mathbf{V}_a} + \widetilde{\mathbf{B}}(\mathbf{V}_a)\right), \quad \text{and} \quad \widetilde{\mathbf{B}} = \mathbf{B}(\mathbf{Q}_a)\frac{\partial \mathbf{Q}_a}{\partial \mathbf{V}_a} \tag{3.118}$$

and, therefore, with (3.118), the system of PDEs (3.102) can be written in a quasi-linear form

$$\partial_t \mathbf{V}_a + \mathbf{C}\,\nabla \mathbf{V}_a = \mathbf{S}(\mathbf{V}_a). \tag{3.119}$$

Because the Jacobian matrix is large it is also computationally very expensive to numerically calculate the eigenvalues at each time and at every cell. For this reason, as will be seen in the next sub-section, a Rusanov Riemann solver will be chosen, which only requires an estimate of the maximum absolute eigenvalue λ_k^M of the Jacobian (3.118).

As has been suggested in [34], a practical and effective choice for estimating the spectral radius of the Jacobian matrix of a two-fluid model coupled with the GPR model is to compute the maximum sound speed λ_k^M in each direction x_k as

$$\lambda_k^M = \max_a \left(|\boldsymbol{v}_a \cdot \hat{\boldsymbol{n}}_k + \lambda|, |\boldsymbol{v}_a \cdot \hat{\boldsymbol{n}}_k - \lambda| \right), \qquad \text{with} \qquad \lambda = \sqrt{\lambda_p^2 + \lambda_s^2} \tag{3.120}$$

where λ_p accounts for pressure waves of the multiphase model, and λ_s is an estimate of the contribution due to shear waves, which are derived in the following.

Let us consider system (3.101), without the extension to elastic solids and viscous fluids (3.101b), i.e. neglecting $\mathbf{A}_a$ and associated shear stresses $\sigma^{\mathrm{e}}_{a,ik}$ for the moment. Then a simplified vector of primitive state variables can be written as

$$\widehat{\mathbf{V}}_a = (\rho_a, v_{a,1}, v_{a,2}, v_{a,3}, p_a, \alpha_a)^{\mathsf{T}}, \tag{3.121}$$

and we can define the matrix $\mathbf{C}_1$, with respect to the first direction x_1, as follows

$$\mathbf{C}_1 = \begin{pmatrix} \mathbf{D}_1 & \mathbf{O}_2 & \mathbf{O}_3 \\ \mathbf{O}_1 & \mathbf{D}_2 & \mathbf{O}_3 \\ \mathbf{O}_1 & \mathbf{O}_2 & \mathbf{D}_3 \end{pmatrix} \tag{3.122}$$

where $\mathbf{D}_a$, $\mathbf{O}_a \in \mathbb{R}^{6x6}$ and are the diagonal and off-diagonal components of $\mathbf{C}_1$ and read

$$\mathbf{D}_a = \begin{pmatrix} v_{a,1} & \rho_a & 0 & 0 & 0 & (v_{a,1}-V_1)\rho_a/\alpha_a \\ 0 & v_{a,1} & (1-c_a)(v_{a,2}-V_2) & (1-c_a)(v_{a,3}-V_3) & 1/\rho_a & p_a/\rho \\ 0 & 0 & c_a(v_{a,1}-V_1)+V_1 & 0 & 0 & 0 \\ 0 & 0 & 0 & c_a(v_{a,1}-V_1)+V_1 & 0 & 0 \\ 0 & p_a\gamma_a & 0 & 0 & v_{a,1} & p_a(v_{a,1}-V_1)\gamma_a/\alpha_a \\ 0 & 0 & 0 & 0 & 0 & V_1 \end{pmatrix}, \tag{3.123}$$

$$\mathbf{O}_a = \begin{pmatrix} 0 & 0 & 0 & 0 & 0 & 0 \\ 0 & 0 & -c_a(v_{a,2}-V_2) & -c_a(v_{a,3}-V_3) & 0 & p_a/\rho \\ 0 & 0 & c_a(v_{a,1}-V_1) & 0 & 0 & 0 \\ 0 & 0 & 0 & c_a(v_{a,1}-V_1) & 0 & 0 \\ 0 & 0 & 0 & 0 & 0 & 0 \\ 0 & 0 & 0 & 0 & 0 & 0 \end{pmatrix}. \tag{3.124}$$

For this simplified system, in which the extension to elastic solids and viscous fluids (3.101b) is excluded, it is possible to explicitly evaluate the eigenvalues. The resulting non-zero and non-repeating eigenvalues are listed in the following vector

$$\lambda_a = (v_{a,1}, V_1, v_{a,1} \pm \sqrt{p_a\gamma_a/\rho_a}), \tag{3.125}$$

where $p_a\gamma_a/\rho_a$ is the adiabatic phase sound velocity C_a^2. Therefore, in the estimate of the spectral radius of the Jacobian matrix of the complete system, the term which takes the pressure waves of the multiphase model into account, is given by

$$\lambda_p = C_a = p_a\gamma_a/\rho_a. \tag{3.126}$$

Regarding the contribution due to shear waves λ_s, analogously to [34, 54] we consider the following estimate

$$\lambda_s = \sqrt{4\ \mathrm{Cs}_a^2/3}. \tag{3.127}$$

The expression (3.127), concerning the contribution of shear waves to the spectral radius evaluation of the Jacobian matrix of the complete system, is obtained considering a fluid (or solid) in its resting state and introducing the assumption of small deformations, i.e. when $\mathbf{A}_a \to \mathbf{I}$. Then linearised estimates for the eigenvalues can be recovered. Moreover, through numerical experiments, it can be verified that (3.127) is quite safe also for the complete problem, leading only to occasional slight overestimates.

Therefore, the time step and the evaluation of the eigenvalues used in Rusanov flux dissipation can be computed by means of the simple evaluation of (3.120).

3.2.3 Data representation, reconstruction and slope limiting

The computational domain $\Omega \subset \mathbb{R}^2$ is partitioned in Cartesian elements, denoted by

$$\Omega_{ij} = \left[x_i - \frac{\Delta x_i}{2}, x_i + \frac{\Delta x_i}{2}\right] \times \left[y_j - \frac{\Delta y_j}{2}, y_j + \frac{\Delta y_j}{2}\right], \tag{3.128}$$

where the indices i and j go from 1 to the total number of elements in each direction. From now on, to avoid possible confusion of spatial and discretization indices, we shall use x for the direction x_1, and y for the direction x_2.

The discrete solution of the conservative and primitive state variables for a generic element Ω_{ij} at time t^n is denoted by $\mathbf{Q}^n_{i,j}$ and $\mathbf{V}^n_{ij}$, and which are defined as volume (area) averaged values, i.e.

$$\mathbf{Q}^n_{i,j} = \frac{1}{|\Omega_{ij}|}\int_{\Omega_{ij}} \mathbf{Q}(x,y,t^n)d\Omega, \qquad \mathbf{V}^n_{i,j} = \frac{1}{|\Omega_{ij}|}\int_{\Omega_{ij}} \mathbf{V}(x,y,t^n)d\Omega. \tag{3.129}$$

In order to achieve a second-order accuracy, it is necessary to perform a data reconstruction that, for each cell, yields a first-degree polynomial representation of the state variables, named $\mathbf{Q}^r_{ij}(x,y,t)$ and $\mathbf{V}^r_{ij}(x,y,t)$.

A cell-local primitive variable polynomial reconstruction $\mathbf{V}^r_{ij}(x, y, t)$ is now reconstructed, for each element Ω_{ij}, from the discrete primitive state vector $\mathbf{V}^n_{ij}$ at time t^n. For each Cartesian cell Ω_{ij}, a jump in primitive variables through each edge can be evaluated. These are then combined in a non-linear fashion in order to obtain a slope in the x and y-direction respectively and to guarantee non-oscillatory properties of the resulting scheme. For instance, in the x-direction, left and right jumps are evaluated as

$$\Delta\mathbf{V}_L = \mathbf{V}^n_{i,j} - \mathbf{V}^n_{i-1,j} \qquad \text{and} \qquad \Delta\mathbf{V}_R = \mathbf{V}^n_{i+1,j} - \mathbf{V}^n_{i,j}, \tag{3.130}$$

respectively. These are then combined in a non-linear fashion to obtain a preliminary slope $\widetilde{\Delta\mathbf{V}}_i$ by means of a slope limiter. In this implmentation, a limiter that is usually referred to as the *Generalised minmod slope limiter* is used, and is given by

$$\begin{aligned}\widetilde{\Delta\mathbf{V}}_i = & \frac{\Delta\mathbf{V}_R \max\left[\, 0,\ \min\left(\, \beta\Delta\mathbf{V}^2_R,\ \Delta\mathbf{V}_R\Delta\mathbf{V}_L\right)\right]}{2\ \Delta\mathbf{V}^2_R + \epsilon^2} \\ & + \frac{\Delta\mathbf{V}_L \max\left[\, 0,\ \min\left(\, \beta\Delta\mathbf{V}^2_L,\ \Delta\mathbf{V}_L\Delta\mathbf{V}_R\right)\right]}{2\ \Delta\mathbf{V}^2_L + \epsilon^2},\end{aligned} \tag{3.131}$$

where ϵ is a small constant that avoids division by zero, e.g. $\epsilon = 10^{-14}$, and β defines a family of *minmod* limiters. For $\beta = 1$, the classic minmod slope limiter is obtained, whereas it reduces to the MUSCL-Barth-Jespersen limiter for $\beta = 3$, and $\beta = 2$ represents an good compromise between robustness and dissipation, and this value will be assumed for all the subsequent numerical tests.

In fact the slope $\widetilde{\Delta\mathbf{V}}_i$ is not the final slope but a *preliminary* one since it was found useful to adopt a slope *rescaling* approach presented in [34]. Thus, after $\widetilde{\Delta\mathbf{V}}_i$ is computed it is then corrected to impose an upper or lower limit for certain variables; in this way, the positivity of the reconstructed density values is guaranteed and the upper and lower bounds of the volume fractions of the phases are respected. We list below the steps to achieve this rescaling

$$\Delta\mathbf{V}_i = \widetilde{\Delta\mathbf{V}}_i \min\left(1,\ \Phi^+_i,\ \Phi^-_i\right), \tag{3.132}$$

with

$$\begin{aligned}\Phi^+_i &= \frac{\left[\left(\mid \widetilde{\Delta\mathbf{V}}_i \mid + \widetilde{\Delta\mathbf{V}}_i\right)\left(\mathbf{V}_M - \mathbf{V}_i\right) + \left(\mid \widetilde{\Delta\mathbf{V}}_i \mid - \widetilde{\Delta\mathbf{V}}_i\right)\left(\mathbf{V}_m - \mathbf{V}_i\right)\right]\widetilde{\Delta\mathbf{V}}_i}{2 \mid \widetilde{\Delta\mathbf{V}}^3_i \mid + \epsilon^3}, \\ \Phi^-_i &= \frac{\left[\left(\mid \widetilde{\Delta\mathbf{V}}_i \mid - \widetilde{\Delta\mathbf{V}}_i\right)\left(\mathbf{V}_i - \mathbf{V}_M\right) + \left(\mid \widetilde{\Delta\mathbf{V}}_i \mid + \widetilde{\Delta\mathbf{V}}_i\right)\left(\mathbf{V}_i - \mathbf{V}_m\right)\right]\widetilde{\Delta\mathbf{V}}_i}{2 \mid \widetilde{\Delta\mathbf{V}}^3_i \mid + \epsilon^3},\end{aligned} \tag{3.133}$$

where, the vectors $\mathbf{V}_m$ and $\mathbf{V}_M$ represent the lower and upper bounds for each variable of the primitive state vector, and are set, for each phase, as

$$\mathbf{V}_{m,\ a} = (0, -\mathbf{h}, -H, 0, -\mathbf{H})_a^{\mathsf{T}}, \quad \text{and} \quad \mathbf{V}_{M,\ a} = (H, \mathbf{h}, H, 1, \mathbf{H})_a^{\mathsf{T}}, \tag{3.134}$$

where the values of H, $\mathbf{h}$ and $\mathbf{H}$ can be set to a scalar, a vector or an arbitrary large matrix to represent the absence of bounds. The analogous steps are performed in y-direction to calculate a reconstruction of the slope $\Delta\mathbf{V}_j$.

After the spatial reconstruction, at a given time instant t^n, the cell-local space-time primitive variable polynomial reconstruction, in each cell Ω_{ij}, is written in terms of a space-time Taylor series expanded about x_i, y_i and t^n as

$$\mathbf{V}^r_{i,j}(x, y, t) = \mathbf{V}^n_{i,j} + (x - x_{i,j})\frac{\Delta\mathbf{V}_i}{\Delta x} + (y - y_{i,j})\frac{\Delta\mathbf{V}_j}{\Delta y} + (t - t^n)\ \partial_t\mathbf{V}_{i,j}. \tag{3.135}$$

The time derivative, in (3.135), is computed in terms of primitive variables in two steps, through a straight-forward application of the operator splitting approach. Thus, to determine $\partial_t\mathbf{V}_{i,j}$, we consider

$$\partial_t\mathbf{V}_{i,j} = -\ (\mathbf{C}\cdot\hat{\boldsymbol{n}}_x)\ \partial_x\mathbf{V} -\ (\mathbf{C}\cdot\hat{\boldsymbol{n}}_y)\ \partial_y\mathbf{V} + \mathbf{S}, \tag{3.136}$$

where $\mathbf{C}$ is defined for the quasi-linear form in (3.118). To solve (3.136), we split it into the homogeneous part

$$\partial_t\mathbf{V}_{i,j} = -\ (\mathbf{C}\cdot\hat{\boldsymbol{n}}_x)\ \partial_x\mathbf{V} -\ (\mathbf{C}\cdot\hat{\boldsymbol{n}}_y)\ \partial_y\mathbf{V}, \tag{3.137}$$

and a source part

$$\frac{\mathrm{d}\mathbf{V}_{i,j}}{\mathrm{d}\hat{t}} = \mathbf{S}(\mathbf{V}_{i,j}), \qquad \hat{t} \in [t^n, t]. \tag{3.138}$$

In order to approximate the spatial derivatives of the primitive state variables in (3.137), we use a central finite difference with respect to the cell center x_{ij} by using the boundary primitive reconstructed values from within the cell $\Omega_{i,j}$, as

$$\partial_t\mathbf{V}_{i,j} \approx \Big(\mathbf{C}(\mathbf{V}^n_{i,j})\cdot\hat{\boldsymbol{n}}_x\Big)\ \frac{\Delta\mathbf{V}_i}{\Delta x} + \Big(\mathbf{C}(\mathbf{V}^n_{i,j})\cdot\hat{\boldsymbol{n}}_y\Big)\ \frac{\Delta\mathbf{V}_j}{\Delta y}. \tag{3.139}$$

Hence, using (3.139), one can compute an update for each cell, such that $\mathbf{V}^*_{i,j}$ is the solution of (3.137) at time t with an initial value $\mathbf{V}^n_{i,j}$, as follows

$$\mathbf{V}^*_{i,j} = \mathbf{V}^n_{i,j} + (t - t^n)\ \partial_t\mathbf{V}_{i,j}. \tag{3.140}$$

In the second step, we consider the contribution of the stiff source terms via solving the initial value problem

$$\frac{d\mathbf{V}_{i,j}}{d\hat{t}} = \mathbf{S}(\mathbf{V}_{i,j}), \qquad \hat{t} \in [t^n, t], \qquad \mathbf{V}_{i,j}(t^n) = \mathbf{V}^*_{i,j}, \tag{3.141}$$

whose solution at time t is denoted by $\mathbf{V}^{**}_{i,j}$. This initial value problem is solved with two different implicit methods discussed in detail in Section 3.2.5.

Finally, by introducing the discrete solution $\mathbf{V}^{**}_{ij}$ of $\partial_t \mathbf{V}_{i,j}$ in (3.135), the cell-local primitive variable polynomial reconstruction reads

$$\mathbf{V}^r_{i,j}(t,x,y) = \mathbf{V}^{**}_{i,j}(t) + (x - x_{i,j})\frac{\Delta \mathbf{V}_i}{\Delta x} + (y - y_{i,j})\frac{\Delta \mathbf{V}_j}{\Delta y}, \tag{3.142}$$

which we also refer to as the *cell-local space-time predictor*.

3.2.4 Explicit finite volume discretization of the homogeneous system

After obtaining the local space-time predictor (3.142), the final solution $\mathbf{Q}^{n+1}_{i,j}$ at t^{n+1} of the MUSCL-Hancock scheme is also computed using the splitting approach, in which we first compute the solution of the homogeneous PDE system

$$\partial_t \mathbf{Q} + \nabla \cdot \mathbf{F}(\mathbf{Q}) + \mathbf{B}(\mathbf{Q}) \cdot \nabla \mathbf{Q} = \mathbf{0}, \tag{3.143}$$

with the initial data obtained by extrapolating the reconstructed polynomials towards the cell boundaries and by applying the standard explicit FV update formula to (3.143).

Considering a space-time control volume $\Omega_{ij} \times [t^n, t^{n+1}]$ on a fixed Cartesian grid, the volume differential element $\mathrm{d}\mathbf{x} = \mathrm{d}x\ \mathrm{d}y$ and the surface element $\mathrm{d}S$ are defined to compactly write integrals on the control volume Ω_{ij} and on its boundary $\partial\Omega_{ij}$ respectively. By integrating the PDE (3.143) over the space-time element and applying Gauss's theorem for integrating the divergence of fluxes in space, we obtain the weak formulation

$$\begin{aligned} \int_{t^n}^{t^{n+1}} \int_{\Omega_{ij}} \partial_t \mathbf{Q}\, d\mathbf{x}\, dt + \int_{t^n}^{t^{n+1}} \int_{\partial\Omega_{ij}} \mathbf{F}(\mathbf{Q}) \cdot \hat{\mathbf{n}}\, dS\, dt& \\ + \int_{t^n}^{t^{n+1}} \int_{\Omega_{ij}} \mathbf{B}(\mathbf{Q}) \cdot \nabla \mathbf{Q}\ d\mathbf{x}\ dt = 0&, \end{aligned} \tag{3.144}$$

where $\hat{\mathbf{n}}$ defines the outward unit normal vector on the element boundary.

Then, by using the reconstructed polynomials $\mathbf{V}^r_{i,j}(t,x,y)$ and treating the non-conservative terms using the path-conservative approach by Castro and Parés [27, 125], the usual *path-conservative* FV discretization is obtained

$$\begin{aligned} \int_{t^n}^{t^{n+1}} \int_{\Omega_{ij}} \partial_t \mathbf{Q}\, d\mathbf{x}\, dt + \int_{t^n}^{t^{n+1}} \int_{\partial\Omega_{ij}} \Big(\mathbf{F}(\mathbf{V}^{r,-}_{i,j}, \mathbf{V}^{r,+}_{i,j}) + \mathbf{D}(\mathbf{V}^{r,-}_{i,j}, \mathbf{V}^{r,+}_{i,j}) \Big) \cdot \hat{\mathbf{n}}\, dS\, dt\ +& \\ + \int_{t^n}^{t^{n+1}} \int_{\Omega_{ij} \setminus \partial\Omega_{ij}} \widetilde{\mathbf{B}}(\mathbf{V}^r_{i,j}) \cdot \nabla \mathbf{V}^r_{i,j}\ d\mathbf{x}\ dt = 0,& \end{aligned} \tag{3.145}$$

where, within the framework of path-conservative schemes, the new term $\mathbf{D}$ was introduced to take into account the jumps of the primitive solution $\mathbf{V}$ across the space-time element boundaries $\partial\Omega_{ij}$, while the last term is the integral over the smooth part of the non-conservative terms.

Using notations (3.129), the fully discrete one-step update formula for the solution $\mathbf{Q}_{i,j}^{(1)}$ of the homogeneous part of the system at time t^{n+1} reads

$$\begin{aligned}\mathbf{Q}_{i,j}^{(1)} = \mathbf{Q}_{i,j}^{n} - \frac{\Delta t}{\Delta x}\Big(\mathbf{F}^{\mathrm{RS}}_{i+1/2,j} - \mathbf{F}^{\mathrm{RS}}_{i-1/2,j} + \mathbf{D}_{i+1/2,j} + \mathbf{D}_{i-1/2,j}\Big) +& \\ - \frac{\Delta t}{\Delta y}\Big(\mathbf{F}^{\mathrm{RS}}_{i,j+1/2} - \mathbf{F}^{\mathrm{RS}}_{i,j-1/2} + \mathbf{D}_{i,j+1/2} + \mathbf{D}_{i,j-1/2}\Big) +& \\ + \frac{\Delta t}{\Delta x}\widetilde{\mathbf{B}}_1\Big[\mathbf{V}^{r}_{i,j}\Big(t^{\,n+1/2}, x_i, y_j\Big)\Big]\,\Delta\mathbf{V}_i +& \\ + \frac{\Delta t}{\Delta y}\widetilde{\mathbf{B}}_2\Big[\mathbf{V}^{r}_{i,j}\Big(t^{\,n+1/2}, x_i, y_j\Big)\Big]\,\Delta\mathbf{V}_j .&\end{aligned} \tag{3.146}$$

where $\mathbf{F}^{\mathrm{RS}}$ is the generic conservative numerical flux, which can be compute with different approximate Riemann solvers.

In order to describe easily each term in (3.146), a compact notation for the boundary-extrapolated primitive states $\mathbf{v}_R$ and $\mathbf{v}_L$, evaluated from the solution of the cell-local space-time predictor (3.142), is introduced. In particular, the space-time midpoint values for each face, of generic index $i+\frac{1}{2}, j$ in the x-direction or $i, j+\frac{1}{2}$ in the y-direction, read

$$\begin{aligned}(\mathbf{V}_L)_{i+\frac{1}{2},j} &= \mathbf{V}^{r}_{i,j}(t^{n+\frac{1}{2}}, x_{i+\frac{1}{2}}, y_j), \quad (\mathbf{V}_R)_{i+\frac{1}{2},j} = \mathbf{V}^{r}_{i+1,j}(t^{n+\frac{1}{2}}, x_{i+\frac{1}{2}}, y_j), \\ (\mathbf{V}_L)_{i,j+\frac{1}{2}} &= \mathbf{V}^{r}_{i,j}(t^{n+\frac{1}{2}}, x_i, y_{j+\frac{1}{2}}), \quad (\mathbf{V}_R)_{i,j+\frac{1}{2}} = \mathbf{V}^{r}_{i,j+1}(t^{n+\frac{1}{2}}, x_i, y_{j+\frac{1}{2}}).\end{aligned} \tag{3.147}$$

Thus, using this simpler notation, we illustrate how conservative numerical $\mathbf{F}^{\mathrm{RS}}$ flows are defined. In this work, the simple Rusanov Riemann solver is employed

$$\begin{aligned}\mathbf{F}^{\mathrm{RS}}_{i+1/2,j}(\mathbf{V}_L, \mathbf{V}_R) &= \frac{1}{2}\Big(\mathbf{F}_1(\mathbf{V}_L) + \mathbf{F}_1(\mathbf{V}_R)\Big) - \frac{1}{2}s_1^{\max}\Big(\mathcal{C}[\mathbf{V}_R] - \mathcal{C}[\mathbf{V}_L]\Big), \\ \mathbf{F}^{\mathrm{RS}}_{i,j+1/2}(\mathbf{V}_L, \mathbf{V}_R) &= \frac{1}{2}\Big(\mathbf{F}_2(\mathbf{V}_L) + \mathbf{F}_2(\mathbf{V}_R)\Big) - \frac{1}{2}s_2^{\max}\Big(\mathcal{C}[\mathbf{V}_R] - \mathcal{C}[\mathbf{V}_L]\Big),\end{aligned} \tag{3.148}$$

where $\mathbf{F}_1$ and $\mathbf{F}_2$ are the conservative fluxes in the first and in the second space direction, in which are included the contributions of the convective, pressure and stress tensor components, as illustrated in (3.149). For clarity, in terms of the primitive state vector, the conservative flux in x-direction reads

$$\mathbf{F}_1(\mathbf{V}_a) = \begin{pmatrix} \alpha_a\ \rho_a\ v_{a,1} \\ \alpha_a\ \rho_a\ v_{a,1}\ v_{a,1} + \alpha_a P_a + \alpha_a \sigma_{1,1} \\ \alpha_a\ \rho_a\ v_{a,2}\ v_{a,1} + \alpha_a \sigma_{2,1} \\ \alpha_a\ \rho_a\ v_{a,3}\ v_{a,1} + \alpha_a \sigma_{3,1} \\ 0 \\ 0 \\ \mathbf{fA}_a \end{pmatrix}, \tag{3.149}$$

with

$$\mathbf{fA}_a, k = \begin{pmatrix} A_{1,1}v_1 + A_{1,2}v_2 + A_{1,3}v_3 & 0 & 0 \\ A_{2,1}v_1 + A_{2,2}v_2 + A_{2,3}v_3 & 0 & 0 \\ A_{3,1}v_1 + A_{3,2}v_2 + A_{3,3}v_3 & 0 & 0 \end{pmatrix}_a . \tag{3.150}$$

Analogously one can obtain F_2 in y-direction.

The Rusanov numerical flux requires the knowledge of an estimate for the maximum wave velocity $s^{\max}$ for each direction. In this paper, keeping in mind that we are interested in problems with not high Mach numbers, the absolute value of the maximum eigenvalue of the PDE system linearized at the states $\mathbf{V}_L$ and $\mathbf{V}_R$ can be a good estimate for $s^{\max}$. Therefore, the maximum wave speed estimates read

$$\begin{aligned} s_1^{\max}(\mathbf{V}_L, \mathbf{V}_R) &= \max\left(\ \lambda_1^{\max}(\mathbf{V}_L),\ \lambda_1^{\max}(\mathbf{V}_R)\ \right), \\ s_2^{\max}(\mathbf{V}_L, \mathbf{V}_R) &= \max\left(\ \lambda_2^{\max}(\mathbf{V}_L),\ \lambda_2^{\max}(\mathbf{V}_R)\ \right). \end{aligned} \tag{3.151}$$

The maximum eigenvalues of (3.101) can be estimated as described in Section 3.2.2.

The nonconservative products appearing in the BN model are treated within the framework of path-conservative schemes [27, 52, 125]. Thus, at each cell interface the following path integrals must be prescribed

$$\begin{aligned} \mathbf{D}_\Psi(\mathbf{V}_L, \mathbf{V}_R) \cdot \hat{\mathbf{n}} &= \frac{1}{2} \int_0^1 \widetilde{\mathbf{B}}\left[\Psi(\mathbf{V}_L, \mathbf{V}_R, s)\right] \cdot \hat{\mathbf{n}}\, \frac{\partial \Psi}{\partial s}\, \mathrm{d}s \\ &= \frac{1}{2} \left(\int_0^1 \widetilde{\mathbf{B}}\left[\Psi(\mathbf{V}_L, \mathbf{V}_R, s)\right] \cdot \hat{\mathbf{n}}\, ds \right) (\mathbf{V}_R - \mathbf{V}_L), \end{aligned} \tag{3.152}$$

in which $\Psi(\mathbf{V}_L, \mathbf{V}_R, s) = \mathbf{V}_L + s(\mathbf{V}_R - \mathbf{V}_L)$ is a simple segment path function connecting the left and right states in the primitive state space. These path integrals, which are denoted by $\mathbf{D}_{i+1/2,j}$ and $\mathbf{D}_{i,j+1/2}$ in (3.146), are computed with a three-point Gauss-Legendre quadrature rule with points $s_k \in [0,1]$ and weights w_k as follows (see [52])

$$\begin{aligned} \mathbf{D}_{i+1/2,j} &= \frac{1}{2}\sum_{k=1}^{3} w_k \ \tilde{\mathbf{B}}_1\Big[\Psi(\mathbf{V}_L,\mathbf{V}_R,s_k)\Big] \ (\mathbf{V}_R-\mathbf{V}_L), \\ \mathbf{D}_{i,j+1/2} &= \frac{1}{2}\sum_{k=1}^{3} w_k \ \tilde{\mathbf{B}}_2\Big[\Psi(\mathbf{V}_L,\mathbf{V}_R,s_k)\Big] \ (\mathbf{V}_R-\mathbf{V}_L) \ . \end{aligned} \tag{3.153}$$

Therefore, by these means we compute the preliminary state vector $\mathbf{Q}^{(1)}_{i,j}$, which is the updated solution of the left hand side of (3.102). To get the final solution $\mathbf{Q}^{n+1}_{i,j}$, it remains to compute the solution of the relaxation source terms, which is done in the next section.

Before describing in detail the implicit solver for the relaxation source terms, we note that in order to guarantee stability of the explicit FV time-stepping described above, the time-step size is restricted by

$$\Delta t \leq k_{\text{CFL}}\frac{1}{\Delta x/\lambda_1^{max}+\Delta y/\lambda_2^{max}}, \tag{3.154}$$

where λ_k^{max} the maximum absolute value of all eigenvalues found in the domain, associated to k-direction and computed according to (3.120). Also, $k_{\text{CFL}} \leq 1$ is a Courant-type number [39], which is typically chosen as $k_{\text{CFL}} = 0.9$ for all the simulations presented in this work.

3.2.5 Integration of relaxations sources

As previously mentioned, to account for the algebraic relaxation source terms in the numerical solution, a splitting approach is adopted. It is a simple but robust strategy since it allows to separate the contribution of relaxation terms from the reversible part of the time evolution equations. Here, we discuss the details of the implicit method that is used to solve the ordinary differential equations (ODE)

$$\frac{\mathrm{d}\mathbf{Q}_{i,j}}{\mathrm{d}t} = \mathbf{S}(\mathbf{Q}_{i,j}), \qquad t\in[t^n,t^{n+1}], \qquad \mathbf{Q}_{i,j}(t^n) = \mathbf{Q}^{(1)}_{i,j}. \tag{3.155}$$

In Section 3.2.1, the source terms were separated into $\mathbf{S}^{\text{w}}(\mathbf{Q}_a)$, which contains the velocity relaxation terms and are stiff, but linear with respect to the relative velocity, and $\mathbf{S}^{\text{s}}(\mathbf{Q}_a)$, which contains the strain relaxation terms of the distortion matrix $\mathbf{A}_a$, and which is non-linear and can be very stiff. The integration of these two different source terms is carried out with two different implicit approaches.

Relative velocity relaxation

In the following, we describe the system of ODEs arising from the source vector $\mathbf{S}^{\mathrm{w}}(\mathbf{Q})$ in (3.112), related to the relative velocity relaxation. Since there are zeros in $\mathbf{S}^{\mathrm{w}}(\mathbf{Q}_a)$ corresponding to the conservation equations of mass, volume fraction, and distortion matrix, they are remained constant over time in (3.155). Therefore, these quantities can be considered as constant parameters and can be omitted from the state vector $\mathbf{Q}_{i,j}$ of the initial value problem (3.155).

The integration of the remaining quantities, the phase momenta $\boldsymbol{u}_a$ and entropies s_a, is carried out in terms of the primitive state variables. More precisely, instead of (3.155) we consider the following reduced ODE system for the vector $\widetilde{\mathbf{V}} = (\boldsymbol{v}_1, \boldsymbol{v}_2, \boldsymbol{v}_3, s_1, s_2, s_3)$

$$\frac{\mathrm{d}\widetilde{\mathbf{V}}_{ij}}{\mathrm{d}t} = \mathbf{S}(\widetilde{\mathbf{V}}_{ij}), \qquad t \in [t^n, t^{n+1}], \qquad \widetilde{\mathbf{V}}_{ij}(t^n) = \widetilde{\mathbf{V}}^{(1)}_{ij}, \tag{3.156}$$

where $\widetilde{\mathbf{V}}^{(1)}$ is the primitive variable reduced state vector obtained in (3.146) as the solution to the the homogeneous PDE system. The later ODE system can be easily integrated by means of the backward Euler method to obtain an updated solution $\widetilde{\mathbf{V}}^{(2)}$ at time t^{n+1}.

For instance, it can be seen that for each spatial direction x_k, $k = 1, 2$, one can decouple the phase velocity equations from the phase entropy ones, and this velocity subsystem reads

$$\begin{aligned}
\frac{\mathrm{d}v_{1,k}}{\mathrm{d}t} &= \lambda\left(c_1(v_{1,k}-V_k) + c_2(v_{2,k}-V_k) + c_3(v_{3,k}-V_k) - (v_{1,k}-V_k)\right),\\
\frac{\mathrm{d}v_{2,k}}{\mathrm{d}t} &= \lambda\left(c_1(v_{1,k}-V_k) + c_2(v_{2,k}-V_k) + c_3(v_{3,k}-V_k) - (v_{2,k}-V_k)\right),\\
\frac{\mathrm{d}v_{3,k}}{\mathrm{d}t} &= \lambda\left(c_1(v_{1,k}-V_k) + c_2(v_{2,k}-V_k) + c_3(v_{3,k}-V_k) - (v_{3,k}-V_k)\right),
\end{aligned} \tag{3.157}$$

where the phase kinetic coefficients $\lambda_{ab,k}$, that define the time scale for friction relaxation dissipative process, are assumed to be equal throughout all phases and directions, i.e. $\lambda_{ab,k} = \lambda$. It is also usually assumed that this parameter is larger than $1/\Delta t$, where Δt is the time-step given by the stability condition in (3.154). Thus, we can say that we have a stiff relaxation source term, and an implicit discretization is needed. For such a system (3.157), in which all the sources are linear, the following discretization can be written for each cell Ω_{ij}

$$\begin{pmatrix} v_{1,k} \\ v_{2,k} \\ v_{3,k} \end{pmatrix}^{(2)}_{ij} = (\mathrm{I} - \Delta t\, \mathcal{M})^{-1} \begin{pmatrix} v_{1,k} \\ v_{2,k} \\ v_{3,k} \end{pmatrix}^{(1)}_{ij} \tag{3.158}$$

where the matrix inverse can be evaluated analytically and, defining $\lambda^* = \Delta t\,\lambda$, reads

$$(\mathrm{I} - \Delta t\,\mathcal{M})^{-1} = \frac{1}{1+\lambda^*}\begin{pmatrix} 1+\lambda^*\,c_1 & \lambda^*\,c_2 & \lambda^*\,c_3 \\ \lambda^*\,c_1 & 1+\lambda^*\,c_2 & \lambda^*\,c_3 \\ \lambda^*\,c_1 & \lambda^*\,c_2 & 1+\lambda^*\,c_3 \end{pmatrix}. \tag{3.159}$$

Now it remains to solve the independent ODEs related to the entropies of the phases, which read

$$\begin{aligned} \frac{\mathrm{d}s_1}{\mathrm{d}t} &= \frac{\lambda\,c_1}{T_1}\left(\left(v_{1,1}-V_1\right)^2 + \left(v_{1,2}-V_1\right)^2 + \left(v_{1,3}-V_1\right)^2\right), \\ \frac{\mathrm{d}s_2}{\mathrm{d}t} &= \frac{\lambda\,c_2}{T_2}\left(\left(v_{2,1}-V_1\right)^2 + \left(v_{2,2}-V_1\right)^2 + \left(v_{2,3}-V_1\right)^2\right), \\ \frac{\mathrm{d}s_3}{\mathrm{d}t} &= \frac{\lambda\,c_3}{T_3}\left(\left(v_{3,1}-V_1\right)^2 + \left(v_{3,2}-V_1\right)^2 + \left(v_{3,3}-V_1\right)^2\right). \end{aligned} \tag{3.160}$$

where we can use the updated velocities evaluated in (3.158). Finally, to discretize the three ODEs in (3.160), a generic implicit backward Euler time integrator based on Newton's method can be used in order to deal with the nonlinearity inherent to the definitions of the phase temperatures $T_a(\rho_a, s_a)$.

Strain relaxation

In contrast to the relative velocity relaxation subsystem (3.156), an accurate integration of the non-linear stiff source $\mathbf{S}^{\mathrm{s}}(\mathbf{Q})$ governing the strain relaxation of the distortion matrix $\mathbf{A}_a$ is a more challenging task, especially in the context of multiphase flows. Let begin with some remarks on the evolution equations of the phase distortion fields $\mathbf{A}_a$, which are defined for each phase $a = 1, 2, 3$.

In the multiphase context, the evolution of the three distortion fields $\mathbf{A}_a$, $a =, 1, 2, 3$ given by

$$\partial_t\mathbf{A}_a + \nabla(\mathbf{A}_a \cdot \boldsymbol{v}_a) + (\nabla\mathbf{A}_a - \nabla\mathbf{A}_a^{\mathsf{T}}) \cdot \boldsymbol{v}_a = -\frac{3}{\tau_a^{\mathrm{e}}}\,(\det\mathbf{A}_a)^{5/3}\,\mathbf{A}_a\mathrm{dev}(\mathbf{A}_a^{\mathsf{T}}\mathbf{A}_a). \tag{3.161}$$

may occur over a very wide range of time scales in a single computational cell Ω_{ij}. Namely, there might be infinitely slow strain relaxation time scale ($\tau_a^{\mathrm{e}} = 10^{14}$) in an elastic solid phase and extremely fast relaxation of shear stresses in the inviscid ($\tau_a^{\mathrm{e}} = 10^{-14}$) and viscous fluid phase ($\tau_a^{\mathrm{e}} \sim 10^{-6} - 10^{-3}$). These different time scales are quantified by means of the relaxation time τ_a^{e} in the evolution equation of the phase distortion field.

The interpretation of the strain relaxation timescale τ_a^{e} and its definition in the multiphase context were described in Section 2.3.2. From that description, it is clear that one of the major difficulties in solving the unified multiphase model of continuum mechanics is conditioned by the presence of these stiff and very non-linear strain relaxation source terms. Therefore, it is necessary to solve the associated ODE systems with care using an appropriate implicit time integrator.

Following the ideas in [83], an efficient and robust method for a semi-analytical implicit integration of the strain relaxation ODE systems was introduced by Chiocchetti and co-authors in [166] in the context of strain relaxation in the damaged solids, and further developed in [34, 35] for finite-rate pressure and strain relaxation in multiphase flows. The *key idea* of this time integrator is a reduction of the problem by using the *polar decomposition* for each phase distortion matrix $\mathbf{A}_a$

$$\mathbf{A}_a = \boldsymbol{R}_a\ \mathbf{G}_a^{1/2} \qquad \text{with} \qquad \mathbf{G}_a^{1/2} = \boldsymbol{E}_a\ \hat{\mathbf{G}}_a^{1/2}\ \boldsymbol{E}_a^{-1}, \tag{3.162}$$

where $\boldsymbol{R}_a$ is an orthogonal matrix with a positive unit determinant, while the matrix square root $\mathbf{G}_a^{1/2}$ can be defined by means of eigen-decomposition of the symmetric positive definite matrix $\mathbf{G}_a$, where $\boldsymbol{E}_a$ is the matrix whose columns are eigenvectors and $\hat{\mathbf{G}}_a^{1/2}$ is the diagonal matrix whose diagonal elements are the roots of the eigenvalues.

Indeed, the distortion field $\mathbf{A}_a$ represents three local basis vectors representing the volume, shape, and the orientation of the phase control volume. Its 9 independent components (degrees of freedom), therefore, encodes two different types of information. Six degrees of freedom are strictly related to the definition of the stress tensor $\boldsymbol{\sigma}_a^{\mathrm{e}} = \varrho_a \mathrm{Cs}_a^2(\mathbf{G}_a \mathrm{dev}\mathbf{G}_a)$ via the six independent components of the metric tensor $\mathbf{G}_a$, and the three remaining degrees of freedom that define the angular orientation of the control volume.

Numerically, the matrix $\mathbf{G}_a^{1/2}$ can be simply evaluated using the Denman-Beavers algorithm. Thus, for any given state $\mathbf{A}_a$, one can easily compute $\mathbf{G}_a$, its square root $\mathbf{G}_a^{1/2}$, and eventually the inverse $\mathbf{G}_a^{-1/2}$. After that, the rotation matrix can be computed as

$$\boldsymbol{R}_a = \mathbf{A}_a\ \mathbf{G}_a^{-1/2}. \tag{3.163}$$

Moreover, the invariance of the rotational component of the distortion matrix under strain relaxation can be proven following the arguments in [34, 83], which means that during the strain relaxation step, one can use the evolution PDE for the metric tensor

$$\partial_t \mathbf{G}_a + (\nabla \mathbf{G}_a)\ \boldsymbol{v}_a + \mathbf{G}_a \nabla \boldsymbol{v}_a - (\nabla \boldsymbol{v}_a)^{\mathsf{T}} \mathbf{G}_a = -\frac{6}{\tau_a^{\mathrm{e}}}\,(\det \mathbf{G}_a)^{5/6}\, \mathbf{G}_a \mathrm{dev}\mathbf{G}_a\ , \tag{3.164}$$

instead of the PDE for the full distortion matrix.

We now have all the ingredients to describe the following steps in order to obtain the final solution for the distortion matrix. First, we calculate the update $\mathbf{A}_a^{(1)}$ of the distortion matrix $\mathbf{A}_a$ obtained from the left hand side of the evolution equation (3.161), as presented in (3.146). From this solution, a rotation matrix can be calculated independently of the non-linear source terms as

$$\boldsymbol{R}_a^{(1)} = \mathbf{A}_a^{(1)} \; \mathbf{G}_a^{(1) \; -1/2} \quad \text{with} \quad \mathbf{G}_a^{(1)} = \left(\mathbf{A}_a^{(1)}\right)^{\mathsf{T}} \mathbf{A}_a^{(1)}, \tag{3.165}$$

with $\mathbf{G}_a^{(1) \; -1/2}$ computed by means of the Denman-Beavers algorithm. Then, the following nonlinear ODE system should be solved

$$\frac{\mathrm{d}\mathbf{G}_a}{\mathrm{d}t} = \boldsymbol{L}_a^{(1)} - \frac{6}{\tau_a^{\mathrm{e}}} \left(\det \mathbf{G}_a \right)^{5/6} \; \mathbf{G}_a \operatorname{dev} \mathbf{G}_a \;, \tag{3.166}$$

where $\boldsymbol{L}_a^{(1)}$ is a constant convective/productive forcing term evaluated simply as

$$\boldsymbol{L}_a^{(1)} = \frac{\mathbf{G}_a^{(1)} - \mathbf{G}_a^n}{\Delta t}, \quad \text{with} \quad \mathbf{G}_a^{(1)} = \left(\mathbf{A}_a^{(1)}\right)^{\mathsf{T}} \mathbf{A}_a^{(1)}, \quad \mathbf{G}_a^n = \mathbf{G}_a\left(t^n\right). \tag{3.167}$$

This term, which takes into account the left-hand side of (3.164), is introduced to converge to the asymptotically correct state in the stiff limit of the equations. This alternative ODE problem (3.166) is then solved by computing the analytical solution of a sequence of linearized problems that approximate the original non-linear ODE, according to the procedure outlined in [34]. Once the source term applied to the metric tensor is integrated, and thus obtaining $\mathbf{G}_a^{(2)}$ at time t^{n+1}, the information can be mapped back to get the updated distortion field as

$$\mathbf{A}_a^{(2)} = \boldsymbol{R}_a^{(1)} \; \left(\mathbf{G}_a^{(2)}\right)^{1/2}. \tag{3.168}$$

3.2.6 Further remarks on the distortion field

Before assembling the final solution of the entire PDE system, we must make some important remarks concerning the challenges related to the numerical computation of the distortion field $\mathbf{A}_a$.

Algebraic constraints

In the numerical solution of the evolution equation (3.162) for the phase distortion field $\mathbf{A}_a$, particularly when describing liquid phases, one must be careful to preserve the nonlinear algebraic constraint

$$\rho_a = \rho_{\text{o}_a} \det \mathbf{A}_a. \tag{3.169}$$

This constrain stems from the fact that the phase mass conservation equation (3.101a) is the consequence of the time evolution (3.162) for the distortion matrix $\mathbf{A}_a$, see e.g. [80, 135]. However, in computational practice it is preferable not to eliminate the mass conservation equation system of governing equations, for the clear reason that (3.101a) is a conservation law, for which therefore the Rankine-Hugoniot jump conditions are clearly defined. Therefore, in order to ensure that the solution is represented by a compatible state with respect to (3.169), the constraint must be actively applied as the numerical scheme can in principle introduce significant errors that grow over time.

A simple but effective approach is to manually impose the constraint at each time iteration, specifically the distortion field, solution of the homogeneous problem, is enforced to satisfy the following ratio

$$\det \mathbf{A}_a^{(1)} = \frac{\rho_a^{(1)}}{\rho_{\text{o}_a}}. \tag{3.170}$$

Similarly, in the procedure for integrating the source term of the distortion field, in Section 3.2.5, i.e., in the semi-analytic solver presented in [34, 35], special care is taken to preserve the nonlinear algebraic constraint $\det \mathbf{G}_a(t, \mathbf{x}) = (\rho_a(t, \mathbf{x})/\rho_{\text{o}_a})^2$.

Linear combination of pure rotational fields

Numerical discretization, in all its parts from data representation to explicit discretization with the FV update formula, is applied to the vector and tensorial quantities in a component-wise manner. This is not a problem for the velocity field, but the distortion field requires more attention due to its rotational component. From our experience, an improper treatment of the rotational matrix $\boldsymbol{R}_a$ can lead to artificial stresses and other numerical artifacts.

It is clear that even in the case of a simple component-by-component linear combination of two rotational matrices, such as that presented by an average operator for example, the resulting matrix is a rotational matrix only in the case of infinitesimal rotations. In this case, in fact, by defining a rotation vector

$\delta\boldsymbol{\vartheta}$, an infinitesimal rotation about an arbitrary axis can be written in the following matrix form by neglecting second order terms of a series expansion,

$$\mathbf{R}_{\delta\vartheta} = \mathbf{I} + \left(\delta\boldsymbol{\vartheta}\cdot\hat{\boldsymbol{n}}_x\,\mathrm{M}_x + \delta\boldsymbol{\vartheta}\cdot\hat{\boldsymbol{n}}_y\,\mathrm{M}_y\right) \equiv \mathbf{I} + \delta\boldsymbol{\vartheta}\cdot\mathbf{M} \tag{3.171}$$

with

$$\mathrm{M}_x = \begin{pmatrix} 0 & 0 & 0 \\ 0 & 0 & -1 \\ 0 & 1 & 0 \end{pmatrix} \quad \mathrm{M}_y = \begin{pmatrix} 0 & 0 & 1 \\ 0 & 0 & 0 \\ -1 & 0 & 0 \end{pmatrix} \tag{3.172}$$

where $\mathbf{M}$ is called the infinitesimal rotation generator as it can be used to generate any infinitesimal rotation matrix $\mathbf{R}_{\delta\vartheta}$ when combined with the rotation vector $\delta\boldsymbol{\vartheta}$. It is straightforward to see how to combine two infinitesimal rotations $\delta\boldsymbol{\vartheta}_1$ and $\delta\boldsymbol{\vartheta}_2$, and it turns out that the order in which infinitesimal rotations are applied is irrelevant,

$$\begin{aligned} \mathbf{R}_{\delta\vartheta_{12}} &= \left(\mathbf{I} + \delta\boldsymbol{\vartheta}_1\cdot\mathbf{M}\right)\left(\mathbf{I} + \delta\boldsymbol{\vartheta}_2\cdot\mathbf{M}\right) \\ &\simeq \mathbf{I} + \left(\delta\boldsymbol{\vartheta}_1 + \delta\boldsymbol{\vartheta}_2\right)\cdot\mathbf{M} \end{aligned} \tag{3.173}$$

where in the last line we have dropped terms quadratic in the infinitesimal rotation angles again.

The equation (3.173) implies that the correct way to combine infinitesimal rotations is by the addition of angle vectors, which justifies at the infinitesimal level a component-by-component discretization of the distortion field. However, the additivity rule does not in general hold for finite rotations. For example, we have observed in our numerical experiments, in which the solution of the distortion field is not particularly smooth, that simple averaging of the rotational matrices results in artificial stresses. This happened in tests such as the lid-driven cavity test, Section 4.2.5 if no special treatment is applied. In this test, the boundary conditions produce a velocity gradient singularity at the corners of the cavity, which results in a locally discontinuous distortion field. On the other hand, no issue arises in the double shear layer problem, Section 4.2.4. For this reason, a different approach would be required to describe the rotational component of the information encoded by $\mathbf{A}_a$, by means of a auxiliary mathematical representation of these quantities that allows a component-by-component treatment even for rotations of finite amplitude.

Thus, in this paper, we propose a simple but effective approach to address this issue. It employs the efficiency of the Chiocchetti semi-analytical solver [34] in the infinitely stiff relaxation regime, $\tau_a^{\mathrm{e}} \to 0$. In particular, in this limit, the strains encoded in the metric tensor $\mathbf{G}_a$ dissipate almost instantaneously, resulting in a distortion field that is represented by a pure rotation matrix, i.e. $\mathbf{A}_a = \boldsymbol{R}_a$ and $\mathbf{G}_a = \mathbf{I}$.

Therefore, the idea of decoupling of the evolution of the two types of information encoded in $\mathbf{A}_a$ (at least numerically) is straightforward. This can be done by adding an auxiliary evolution equation (3.161) for a new auxiliary distortion field $\widetilde{\mathbf{A}}_a$ subject to a relaxation timescale $\tilde{\tau}_a^{\mathrm{e}} \to 0$. This auxiliary distortion field $\widetilde{\mathbf{A}}_a$ carries only the information about the rotational component of the original distortion $\mathbf{A}_a$, i.e. $\widetilde{\mathbf{A}}_a = \widetilde{\boldsymbol{R}}_a$. Moreover, thanks to this almost instantaneous relaxation (numerically we use $\tilde{\tau}_a^{\mathrm{e}} = 10^{-14}$), the artificial stresses that may arise from the combination of finite amplitude rotations are dissipated instantaneously, both at the level of the predictor, Section 3.2.3, and at the level of the final solution at each time-step, Section 3.2.4 and Section 3.2.5.

On the other hand, due to this decoupling, the original distortion field $\mathbf{A}_a$ at each time step carries only the information about the strains, i.e. $\mathbf{A}_a = \mathbf{G}_a^{1/2}$ and $\boldsymbol{R}_a = \mathbf{I}$, both at the level of the predictor and the solution updated at time t^{n+1}. Therefore, expression (3.168), in the source term integration process for the original distortion field $\mathbf{A}_a$, should be rewritten as

$$\mathbf{A}_a^{(2)} = \mathbf{I}\left(\mathbf{G}_a^{(2)}\right)^{1/2}. \tag{3.174}$$

3.2.7 Final solution for the complete problem

The final solution $\mathbf{Q}_{i,j}^{n+1}$ of the complete problem (3.102) can now be retrieved by considering the solution of the homogeneous problem, the contribution of the source terms, and the remarks on rotational matrices discussed above. Thus, including formally the auxiliary phase distortion field $\widetilde{\mathbf{A}}_a$ to the set of state parameters, the final solution of each phase $a = 1, 2, 3$ reads

$$\mathbf{Q}_{a,i,j}^{n+1} = \left(\varrho_a^{(1)}, \boldsymbol{u}_a^{(2)}, s_a^{(2)}, \alpha_a^{(1)}, \mathbf{A}_a^{(3)}, \widetilde{\mathbf{A}}_a^{(2)}\right)_{i,j}, \tag{3.175}$$

where the complete phase distortion field $\mathbf{A}_a^{(3)}$ is computed as

$$\mathbf{A}_a^{(3)} = \widetilde{\boldsymbol{R}}_a^{(1)} \left(\mathbf{G}_a^{(2)}\right)^{1/2}. \tag{3.176}$$

4 Numerical results

This chapter provides and discusses an extensive collection of numerical experiments in order to validate both numerical methods presented in Section 3. The results consist of a large set of validation benchmarks and application to multiphase problems.

The first section will present the computational results, published in [69, 70], obtained with the semi-implicit finite volume scheme presented in Section 3.1 for solving a simplified BN model. As we shall see, this numerical sheme can be applied for the solution of complex non-hydrostatic free-surface flows interacting with moving solid bodies.

The following Section will provide some rather unique results yet to be published [71], related to the behavior of multiphase flows for more than two phases, which make clear the potential inherent in a description of the continuum through a unified model of compressible multiphase fluid and solid mechanics, as well as constituting a step forward in terms of its applicability to real problems.

Throughout this chapter, unless explicitly noted, we adopt SI units for all quantities.

4.1 Semi-implicit FV schemes for incompressible two-phase flows

Throughout this section, the numerical scheme presented in Section 3.1 is validated on a set of classical benchmark problems for incompressible Navier-Stokes equations, ranging from the Blasius boundary layer, the Hagen-Poiseuille flow and the lid-driven cavity test to more challenging free-surface problems where the liquid phase interacts with moving solid bodies. It is interesting to note that, most of the tests are formulated in such a way that two phases, the solid and liquid phase, are always present. This is to test the ability of the method to automatically solve two-phase flows, i.e. two phases are simulated quite often in order to asses that the boundary conditions between phases are automatically well imposed by solving the PDE.

In all the tests, the time step Δt is computed according to the CFL condition expressed in (3.92), based on the liquid and solid velocity and on the kinematic viscosity, assuming a CFL number set to 0.9. Moreover, the gravity is assumed to be constant and equal to $\boldsymbol{g} = g\,(0,-1)^{\intercal}$ with $g = 9.81$, (unless where specified differently) and it is recalled that p was defined, in Section 3.1.1, as the normalised pressure, i.e. the pressure divided by the density, which is assumed to be constant and equal to $\rho = 1000$. Finally, after conducting various numerical tests, it was found that it is enough to assume the scale for the velocity relaxation kinetics equal to $\lambda = 10^{-4}$.

It should also be specified that, in the tests involving the solid phase, we choose a subgrid consisting of 2×2 subelements for each principal control volume $\Omega_{i,j}$ to evaluate the decoupled advection of the solid phase.

4.1.1 Dambreak problems

The so-called dambreak problem is a common test for numerical methods applied to the shallow-water equations. It consists of removing a vertical weir instantly, which separates two different piecewise constant states of water from each other. In the initial stages of dambreak flow, the shallow water assumption of small vertical velocities and accelerations does not hold. For this reason, it is of interest to apply a more complete model that is able to deal with non-hydrostatic flows. First, in this section the new numerical method proposed in this paper is run on a mesh that consists of only vertical layer and thus simplifies to a consistent and conservative discretization of the hydrostatic one-dimensional shallow water equations. The obtained results are compared against the exact solutions of the shallow water equations, both, for the wet bed and for the dry bed case. For exact solutions of the Riemann problem of the shallow water equations see [170].
Then, in 2D, it is interesting to compare the behavior at small times and at large times with each other. For an experimental study of the initial instants of dambreak flow, see e.g. [158].

Hydrostatic simulations with only one vertical layer

The two-dimensional conservative method is simplified to a discretization of the hydrostatic one-dimensional equations by taking the vertical resolution Δy as large as the maximum vertical flow height, as illustrated in Section 3.1.8. This one-dimensional resulting method is used to solve the following 1D Riemann problems, which represent the dambreak problem over a wet bed and over a dry one. The exact solution of the dambreak problem over a dry bed has been derived by Ritter [142] in 1892.

The tests are run over a fixed spatial domain $\Omega = [-1;1] \times [0;1]$ covered by a uniform grid consisting of 100×1 cells, with mesh spacing $\Delta x = 0.01$ in the x-direction, while in the vertical y-axis, oriented upward along the gravity direction, a single cell of size $\Delta y = 1$ is taken. The simulations are carried out using a CFL number of CFL $= 0.9$, based on the maximum eigenvalue of the system, until the final time. Wall friction and fluid viscosity are neglected. The initial conditions of the following Riemann problems are given by

$$\alpha^s(x, y, 0) = 0, \quad v^l(x, y, 0) = u^l(x, y, 0) = 0, \tag{4.1}$$

while initial volume fraction and pressure are defined as follows

$$\alpha^l(x, y, 0) = \begin{cases} \alpha^l_L & \text{if } x > 0, \\ \alpha^l_R & \text{if } x \leq 0, \end{cases} \quad p(x, y, 0) = \begin{cases} \alpha^l_L \beta & \text{if } x > 0, \\ (\alpha^l_R - 0.5)\, \Delta y\, g & \text{if } x \leq 0, \end{cases} \tag{4.2}$$

where $\beta = g\, \Delta y/2$, as defined in Section 3.1.2. For the first Riemann problem (RP1) the initial left and right volume fractions are $\alpha^l_L = 1$, $\alpha^l_R = 0.1$; for the second Riemann problem (RP2) are $\alpha^l_L = 1$, $\alpha^l_R = 0$.

The results obtained with the new method are depicted for RP1 in Fig. 4.1 and for RP2 in Fig. 4.2. These figures clearly show that the problems are solved correctly even in the numerically more complex case over a dry bed. In Fig. 4.1 it is possible to observe that the shock is located in the right position and the post-shock values are also correct. Furthermore, it is possible to note the typical numerical dissipation (numerical viscosity) at the waves, which, however, is reasonably low for the numerical method used here, since the shock wave is well resolved. In Fig. 4.2 the Riemann problem over a dry bed is shown and compared against the exact solution of the shallow water equations obtained by Ritter [142]. In this case, there are no shock waves involved and the flow can be considered as smooth.

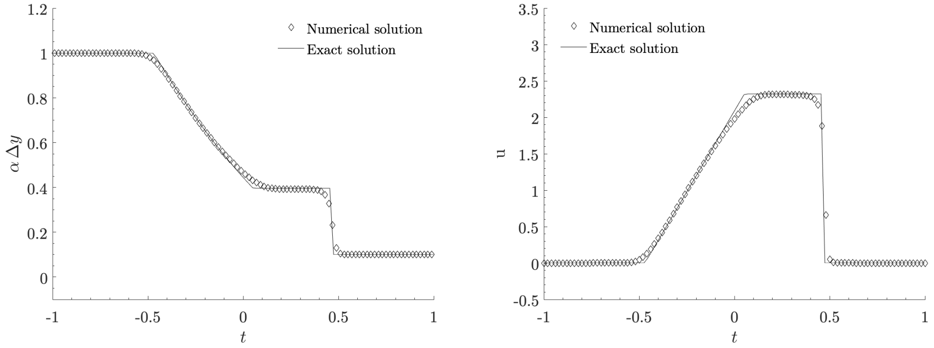

Fig. 4.1. Exact and numerical solutions evaluated with the conservative method for the (RP1), at time 0.25 s.

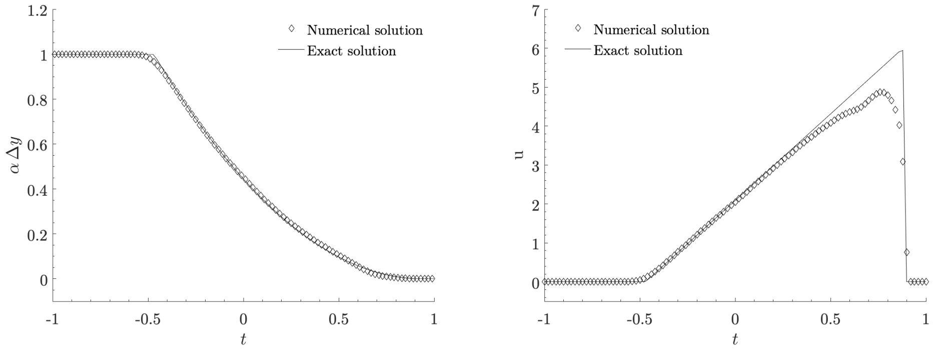

Fig. 4.2. Exact and numerical solutions evaluated with the conservative method for the (RP2), at time 0.2 s.

Non-hydrostatic simulations: dambreak over a dry bed

In order to preserve the non-hydrostatic behaviour of the flow, it is sufficient to take the vertical resolution Δy smaller than the maximum vertical flow height.

First, the classical dambreak over a dry bed is presented. As mentioned before, the exact solution to this problem, using the hydrostatic shallow-water model, is the Ritter solution. The rectangular computational domain is $\Omega = [-5; 5] \times [0; 2]$. For this test the initial conditions are given by

$$\begin{aligned} &\alpha^s(x,y,0) = 0, \quad v^l(x,y,0) = u^l(x,y,0) = 0, \quad p(x,y,0) = g\,y \\ &\alpha^l(x,y,0) = \begin{cases} 1 & \text{if } x \leq 0 \vee y < 1.5, \\ 0 & \text{otherwise,} \end{cases} \end{aligned} \tag{4.3}$$

The domain is covered by a uniform grid consisting of 1000×200 cells, with mesh spacing $\Delta x = 0.01$, $\Delta y = 0.01$ in both the x-direction and y-direction. The boundary conditions are reflective wall on all the borders of the computational domain Ω. Wall friction and fluid viscosity are neglected. The results obtained at time $t = 0.5$ with our new method proposed in this paper are presented in Fig. 4.3. The results are compared against the exact solution of the shallow water equations obtained by Ritter [142] for each time. At early times, the non-hydrostatic results are in good agreement with the previously computed results by Dumbser [49], which have been compared with the results obtained by the smooth particle hydrodynamics (SPH) scheme of Ferrari *et al.* [68]. It can be shown that the free-surface profile tends to be a good approximation of the analytical solution of the one-dimensional shallow water equations only as the spatial and the temporal domain increase. This is in total agreement with the fact that in the initial times, the vertical acceleration, as well as the

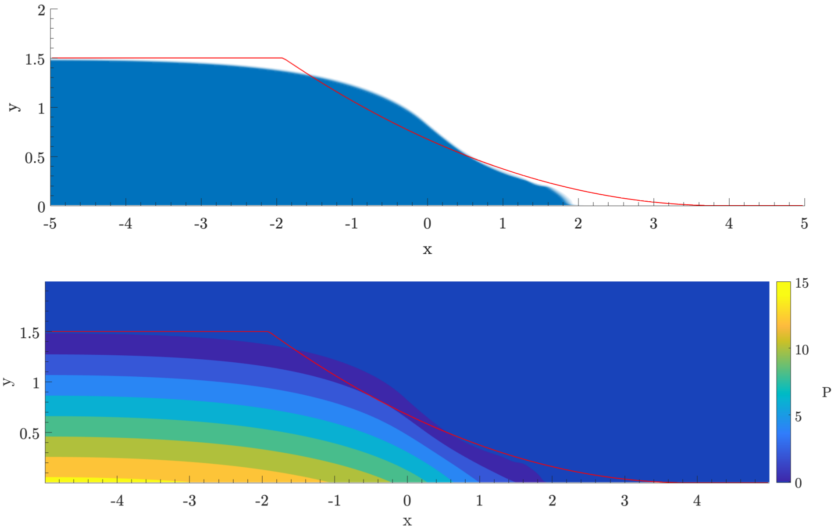

Fig. 4.3. Numerical solutions for free surface profile and pressure field, evaluated with the 2D non-hydrostatic conservative methods for the dambreak into dry bed problem, at time $t = 0.5$. The volume fraction is shown at the top and the pressure field contours at the bottom. A red line shows the solution obtained under the shallow water assumption.

pressure gradient in the vertical direction, are the main component of the flow, and thus the hydrostatic pressure assumption of the shallow water model is not verified. This initially strongly non-hydrostatic behaviour can also be seen in the pressure field depicted in Fig. 4.3. Here, the pressure field turns sharply to the x-axis until it becomes orthogonal to it.

Non-hydrostatic simulations: dambreak into a wet bed

Now, a dambreak into a wet bed case is considered. The rectangular computational domain is $\Omega = [-7.5; 5] \times [0; 2]$. The fluid is initially at rest and is confined in both the left and right parts of the domain, i.e. the the initial conditions are given by

$$\begin{aligned} &\alpha^s(x,y,0) = 0, \quad v^l(x,y,0) = u^l(x,y,0) = 0, \quad p(x,y,0) = g\,y \\ &\alpha^l(x,y,0) = \begin{cases} 1 & \text{if } \ x \leq 0 \vee y < 1.5 \ \text{ or } \ x > 0 \vee y < 0.75, \\ 0 & \text{otherwise,} \end{cases} \end{aligned} \tag{4.4}$$

The domain is covered by a uniform grid consisting of 1000×200 cells, with mesh spacing $\Delta x = 0.01$ in the x-direction, $\Delta y = 0.01$ in the y-direction and the computation is carried out until the final time $t_{end} = 1$.

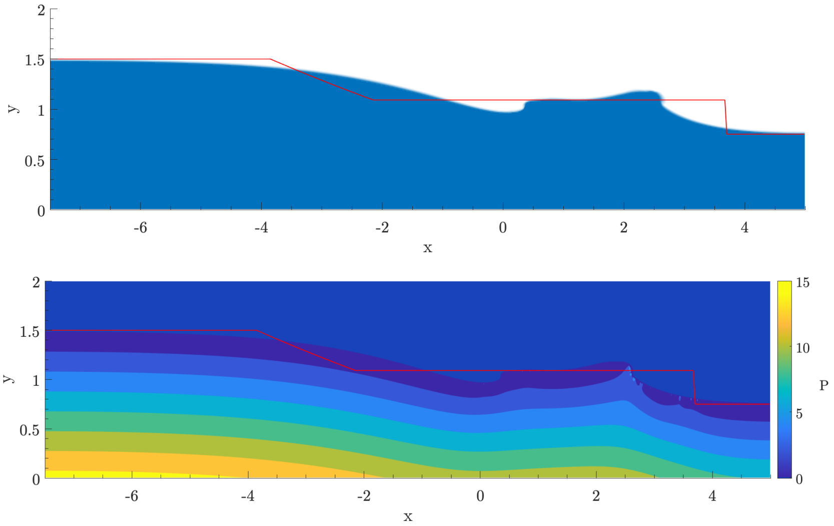

Fig. 4.4. Numerical solutions for free surface profile and pressure field, evaluated with the 2D non-hydrostatic conservative methods for the dambreak into wet bed problem, at time $t = 1.0$. The volume fraction is shown at the top and the pressure field contours at the bottom. A red line shows the solution obtained under the shallow water assumption.

Experimental observations [96] show that wave breaking can occur in a dambreak into a wet bed. However, the higher the water level on the right side of the dam, the smaller becomes the breaking wave. In this test case, the level of the right layer of water is quite high, so at most, a very small breaking wave can occur.

At the time $t = 1.0$, in Fig. 4.4, small-scale free surface waves are visible in the constant region between the shock and the rarefaction wave. Again, the results are in agreement with those previously obtained by the two-phase flow model of Dumbser [49] and by the SPH method of Ferrari *et al.* [68]-[67]. Furthermore, the solution is even closer to the one achieved with the SPH method. In fact, smaller surface waves are predicted by the latter and particularly it shows a small breaking of waves at the moving right front. In Fig. 4.4 the volume fraction shows a tendency for the crest of the wave to break via smaller volume fractions.

We emphasize that at the initial stages the obtained solution does not agree with the solution of the shallow-water model, represented by a red line in Fig. 4.4. This disagreement, for short times, is due to the fact that the hydrostatic shallow water model neglects vertical accelerations, which are quite important in the early stages of dambreak flow.

4.1.2 The first problem of Stokes

The first problem of Stokes [154] is one of the few test problems for which an exact analytical solution of the unsteady Navier-Stokes equations is known. This problem consists of the time-evolution of an infinite incompressible shear layer. The computational domain is $\Omega = [-0.5; 0.5] \times [-0.5; 0.5]$, with velocity imposed on the left and right boundaries and periodic boundary conditions along the y-direction. The initial conditions of the problem are given by

$$\begin{aligned} &\alpha^l(x,y,0) = 1, \qquad \alpha^s(x,y,0) = 0, \qquad p(x,y,0) = \beta, \\ &u^l(x,y,0) = 0, \qquad v^l(x,y,0) = \begin{cases} +0.1 & \text{if } x > 0, \\ -0.1 & \text{if } x \leq 0, \end{cases} \end{aligned} \tag{4.5}$$

where $\beta = g\,\Delta y/2$ as defined in Section 3.1.2. Simulations are performed assuming three different kinematic viscosities $\nu = 10^{-2}$, $\nu = 10^{-3}$ and $\nu = 10^{-4}$.

The exact analytical solution of the incompressible Navier-Stokes equations for the velocity component u is given by the following error function

$$v(x,y,t) = v(x,y,0)\,\mathrm{erf}\left(\frac{1}{2}\frac{x}{\sqrt{\nu t}}\right) \tag{4.6}$$

The computational domain is covered by a uniform rectangular grid consisting of 100×100 elements, with mesh spacing $\Delta x, \Delta y = 0.01$ in both x and y directions. The comparison between the computational results along the line $y = 0$, up to the final time $t = 1.0$, and the exact solution of the first problem of Stokes for the Navier-Stokes equations are depicted in Fig. 4.5. Even with a quite coarse mesh the numerical solution is in good agreement with the exact solution, also by varying the kinematic viscosity.

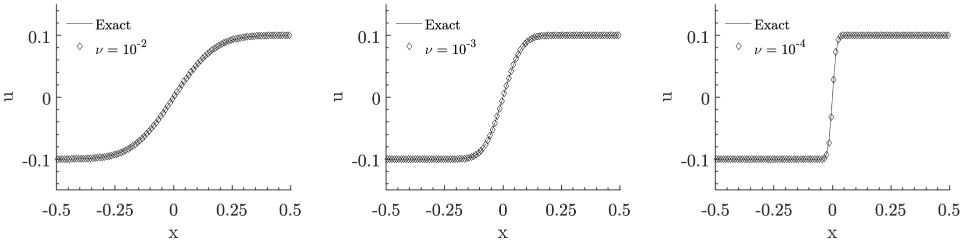

Fig. 4.5. 1D cut through the the computational domain at position $y = 0$. Exact (solid line) and numerical solution of the first problem of Stokes for the Navier-Stokes equations for the velocity component u at time = 1. Different viscosities are simulated, from left to right, $\nu = 10^{-2}$, $\nu = 10^{-3}$ and $\nu = 10^{-4}$.

4.1.3 2D Taylor-Green vortex

The Taylor-Green vortex is another test problem for which an exact solution of the incompressible Navier Stokes equations with periodic boundary conditions can be found. This test is widely used for testing the accuracy of numerical schemes, because it has a smooth unsteady analytical solution, which is a two-dimensional decaying vortex. In other words, the initial sinusoidal velocity field is smoothed over time by the viscous stresses. In a two-dimensional space, the analytical solution reads

$$\begin{aligned} u(x,y,t) &= \sin(x)\cos(y)e^{-2\nu t}, \\ v(x,y,t) &= -\cos(x)\sin(y)e^{-2\nu t}, \\ p(x,y,t) &= 1/4(\cos(2x)+\cos(2y))e^{-4\nu t}. \end{aligned} \tag{4.7}$$

The computational domain is $\Omega = [0;2\pi]^2$, with periodic boundary conditions on all the boundaries. In order to conduct a convergence study, the initial condition of the problem is given by the exact solution (4.7), assuming $t = 0$, and the kinematic viscosity is assumed to be $\nu = 10^{-1}$. The standard way to get the numerical order of accuracy is to refine the mesh spacing and to look at the ratio of the obtained numerical errors. Four simulations were carried out and Tab. 4.1 lists the meshes used, denoted by M_i with $i = 1, ..., 4$. For these tests a final time $t_{end} = 0.1$ is considered and the time step Δt is determined following the CFL condition.

The computational results, for the coarsest mesh M_1, are depicted in Fig. 4.6, where the pressure contour and the velocity field are represented. A comparison

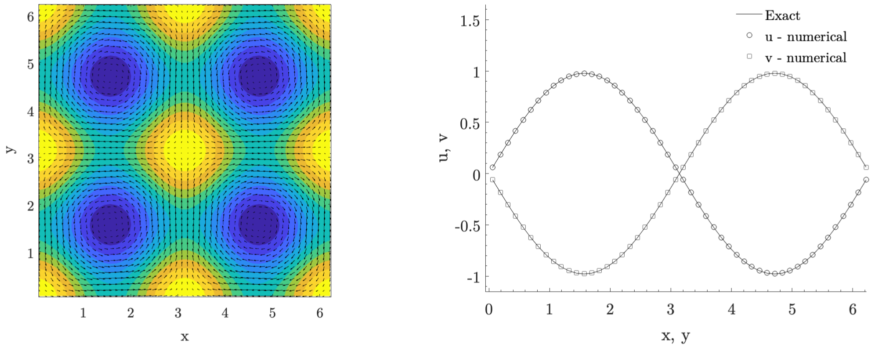

Fig. 4.6. Numerical solution for the Taylor-Green vortex at the final time $t = 0.1$, for the coarsest mesh M_1 and with a viscosity of $\nu = 10^{-1}$ (left). 1D comparison of the velocity components u, v, with the exact solution of the incompressible Navier-Stokes equations along the x and the y axis (right).

of the two velocity components with the exact solution of the incompressible Navier-Stokes equations is shown on the right. A simple qualitative observation shows excellent agreement between the numerical solution and the reference solution, for both velocity components.

The L_1 and the L_2 norms of the error and the corresponding convergence rates are presented in Tab. 4.1 for the variable u, and are defined as follows

$$E(u)=||u-u_{\mathrm{M}_i}||_{(L^p(\Omega))}, \quad \mathcal{O}_{L^p}(u_{\mathrm{M}_i/\mathrm{M}_j})=\log\left(\frac{E(u)_{\mathrm{M}_i}}{E(u)_{\mathrm{M}_j}}\right)/\log\left(\frac{h_{\mathrm{M}_i}}{h_{\mathrm{M}_j}}\right), \tag{4.8}$$

where p denotes the order of the norm. The calculated convergence rates, corresponding to the two norms, are also shown in the Tab. 4.1, and, as expected, the numerical scheme, here presented, essentially achieves second order of accuracy.

Mesh	Elements	E_{L^1}	$\mathcal{O}_{L^1}$	E_{L^2}	$\mathcal{O}_{L^2}$
M_1	50x50	4.5913e-02		8.8420e-03	
M_2	100x100	1.2508e-02	1.87	2.4232e-03	1.87
M_3	200x200	3.3405e-03	1.90	6.5442e-04	1.89
M_4	400x400	8.8514e-04	1.92	1.7394e-04	1.91

Tab. 4.1. Mesh name, mesh elements, L_1 and L_2-error norms and their respective numerical convergence rates, $\mathcal{O}_{L^1}$ and $\mathcal{O}_{L^2}$, for the variable u, applied to the 2D Taylor-Green vortex.

4.1.4 Blasius boundary layer

The boundary layer equations of Prandtl [137] were solved for the first time in the particular case of a steady laminar boundary layer over a flat plate by Blasius in [10]. For an overview of of boundary layer theory, see the textbook [154]. Blasius proposed a similarity solution that reduces the boundary layer equations to the solution of a third order non-linear ordinary differential equation, which reads

$$f''' + ff'' = 0, \tag{4.9}$$

where the prime denotes derivation with respect to η, which is the introduced self-similar variable $\eta = y\sqrt{\frac{U}{2\nu x}}$. Then the boundary conditions which have to be imposed are the no-slip condition, the impermeability of the wall and the free stream velocity outside the boundary layer, $u(x,0) = 0$, $v(x,0) = 0$ and $u(x,\infty) = U$, where U is the free stream velocity and it is a constant.

This ODE can be easily solved numerically, e.g. the reference solution in this paper is computed by a Runge-Kutta scheme of order 4 in combination with a classical shooting technique.

The computational domain is $\Omega = [-0.004; 0.1] \times [-0.5; 0.5]$, hence it includes the solid wall, and is discretized with 2000×208 rectangular elements. The initial condition of the problem for each phases, are given by

$$\begin{aligned}
&\alpha^l(x,y,0) = \begin{cases} 1 & \text{if } \; x > 0, \\ 1e^{-14} & \text{if } \; x \leq 0, \end{cases} \\
&\alpha^s(x,y,0) = \begin{cases} 1e^{-14} & \text{if } \; x > 0, \\ 1 & \text{if } \; x \leq 0, \end{cases} \qquad p(x,y,0) = p_{out}, \\
&u_i^s(x,y,0) = 0, \qquad v(x,y,0) = 0, \qquad u(x,y,0) = 1.
\end{aligned} \tag{4.10}$$

The kinematic viscosity is assumed to be very low $\nu = 10^{-5}$, which leads to a very thin boundary layer and then the Reynolds number of the flow is $\mathbb{R}\mathrm{e} = 10^5$. At the right and top outlet boundary condition are set by imposing a constant pressure $p_{out} = 50\beta$ while at $x = 0$ the inflow boundary condition is given by the initial conditions. It is important to note that it is not necessary to impose the no-slip boundary conditions along the flat plate, i.e. along the solid phase; the relaxation source term and the numerical method automatically impose these boundary conditions between the two phases in the correct way by solving the PDE. As the shape of the solid phase becomes more complex, this feature of the method will be of primary importance.

In Fig. 4.7 (left), the computational results obtained for the horizontal velocity field u, computed at time $t = 10$, are shown, together with a velocity profile at $x = 0.1$. A comparison of this numerical velocity profile against

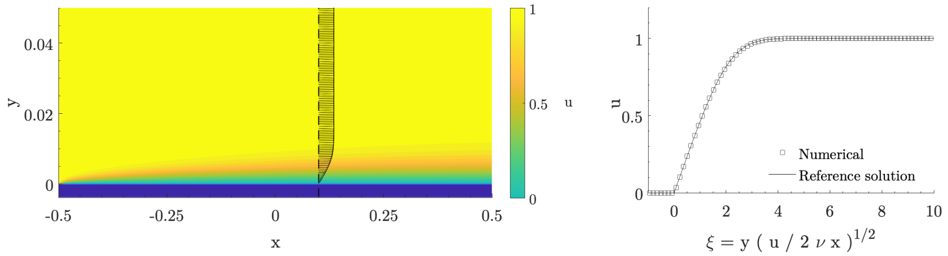

Fig. 4.7. Numerical solution for the laminar boundary layer over a flat solid plate (dark blue), with $\mathbb{R}\mathrm{e} = 10^5$, at the final time $t = 10.0$. The horizontal velocity u contours and a velocity profile in $x = 0.1$ are shown (left). Comparison of the numerical velocity profile at $x = 0.1$ against the Blasius reference solution (right).

the Blasius reference solution is made in Fig. 4.7 (right). The solid phase, characterized by $u^s(x,y,t) = v^s(x,y,t) = 0$, is shown in Fig. 4.7 in dark blue. A very good agreement between these two solutions can be observed, despite the fact that the no-slip boundary conditions along the flat plate is not imposed explicitly but just via the presence of a solid volume fraction for $y < 0$ and the stiff velocity relaxation source terms present in the PDE. This confirms the validity of the proposed numerical method to compute boundary layers correctly and thus to compute viscous incompressible two phase flows in a correct way.

4.1.5 Planar Hagen-Poiseuille flow

The Hagen-Poiseuille flow describes a steady-state velocity and pressure distribution for a viscous fluid in laminar flow between two plates whose length L is much greater than the constant distance d separating them. The flow is driven by a constant pressure gradient $-\Delta p$ prescribed by the boundary conditions, which is balanced by the viscous drag along both plates. This test, which satisfies the Hagen-Poiseuille flow, has a well known parabolic solution for the horizontal velocity profile u, given by

$$u = \frac{1}{2}\frac{\Delta p}{\nu L}\left(\frac{d^2}{4} - y^2\right). \tag{4.11}$$

This test is simulated on a domain $\Omega = [-2.5; 2.5] \times [-0.3; 0.3]$ which is discretized with 1000×120 rectangular elements, and the initial condition for each phases are given by

$$\begin{aligned}
&\alpha^l(x,y,0) = \begin{cases} 1 & \text{if } \ |x| \leq 0.25, \\ 1e^{-14} & \text{if } \ |x| > 0.25, \end{cases} \\
&\alpha^s(x,y,0) = \begin{cases} 1 & \text{if } \ |x| > 0.25, \\ 1e^{-14} & \text{if } \ |x| \leq 0.25, \end{cases} \\
&p(-2.5,y,0) = 10\beta + 2.4, \quad p(2.5,y,0) = 10\beta, \\
&u_i^s(x,y,0) = u_i(x,y,0) = 0.
\end{aligned} \tag{4.12}$$

The kinematic viscosity is assumed to be $\nu = 10^{-2}$. Therefore, the pressure gradient imposed between the left inflow and the right outlet is $\Delta p = 2.4$. These conditions, according to the Hagen-Poiseuille flow, result in a mean flow velocity of $\bar{u} = 1$ and a maximum flow velocity of $u_{max} = 1.5$. At the left inflow and at the right outlet the boundary condition are given by the initial conditions, whereas, again, it is not necessary to impose the no-slip boundary

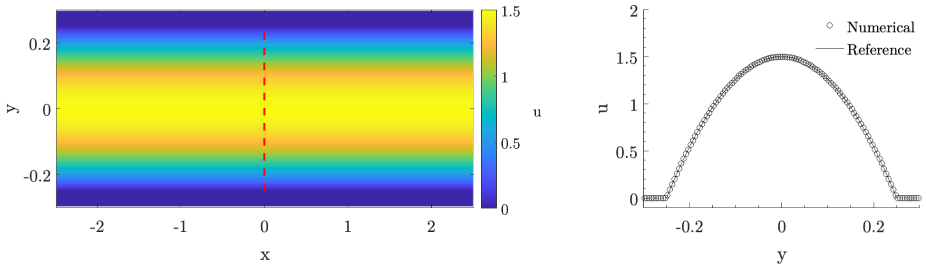

Fig. 4.8. Numerical solution for the laminar flow between two solid plates (dark blue) at a final time of $t = 50.0$. The horizontal velocity u contours is shown (left). Comparison of the numerical velocity profile at $x = 0.0$ against the reference solution of Hagen-Poiseuille flow (right).

conditions along the flat plates, i.e. along the solid phase. The boundary conditions are implicitly imposed via the stiff velocity relaxation source terms.

On the left-hand side of the Fig. 4.8 shows the computational results obtained for the horizontal velocity field u, computed at time $t = 50$, while in the right one a comparison of this numerical velocity profile against the parabolic reference solution is made. The numerical solution is in good agreement with the reference solution of the Hagen-Poiseuille flow. The laminar flow is very well reproduced and the boundary condition between the two phases are well resolved too.

4.1.6 Two dimensional lid-driven cavity problem

The lid-driven cavity is a fully two-dimensional classical reference problem for numerical methods applied to the incompressible Navier-Stokes equations, see [76], [161], [60]. In this test, a solid square cavity is considered, opened at the top and containing liquid which is driven by a lid imposed at the top.
This test is simulated on a domain $\Omega = [-0.55; 0.55] \times [-0.55; 0.5]$ which is discretized with 220×210 rectangular elements, and the initial condition for each phases are given by

$$\begin{aligned}
\alpha^l(x,y,0) &= \begin{cases} 1e^{-14} & \text{if } \ |x| > 0.5 \ \text{ or } \ y < 0.5, \\ 1 & \text{otherwise,} \end{cases} \\
\alpha^s(x,y,0) &= \begin{cases} 1 & \text{if } \ |x| > 0.5 \ \text{ or } \ y < 0.5, \\ 1e^{-14} & \text{otherwise,} \end{cases} \\
p(x,y,0) &= 10\beta, \qquad u_i^s(x,y,0) = 0, \qquad u_i(x,y,0) = 0,
\end{aligned} \tag{4.13}$$

where $\beta = g\,\Delta y/2$, as defined in Section 3.1.2. The kinematic viscosity is assumed to be $\nu = 10^{-2}$. The lid velocity is assumed to be equal to $u(x, 0.5, t) =$

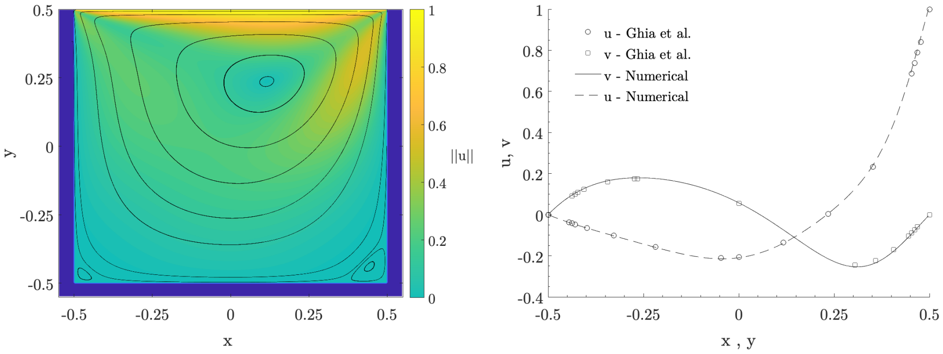

Fig. 4.9. Numerical solution for the lid driven cavity flow at time $t = 10$. The Reynolds number of the flow is $\mathbb{R}\text{e} = 100$. The velocity module $||u||$ contour plot and streamlines are shown (left). Comparison of 1D cuts of the velocity field against the Navier-Stokes reference solution of Ghia *et al.* [76] (right)

1. Therefore, the Reynolds number of the flow is $\mathbb{R}\text{e} = 100$. Also in this case it is not necessary to impose the no-slip boundary conditions along the solid phase square cavity explicitly, but they are automatically taken care of by the stiff velocity relaxation source term.

In Fig. 4.9, the computational results are shown and a comparison against the Navier-Stokes reference solution of Ghia *et al.* [76] is provided at time $t = 10$. In Fig. 4.9 (left) the velocity modulus contours are shown, while in dark blue the solid square cavity can be distinguished. It is important to emphasize that the description of the two phases has still been correctly resolved, automatically imposing the right boundary conditions. Again the numerical solution is in very good agreement with the reference solution.

4.1.7 Viscous flow over a circular cylinder

In this section, the viscous flow over a circular cylinder is considered for different Reynolds numbers. In previous work [69], an inviscid flow around the cylinder has been presented, in order to obtain a steady potential flow. Here, the viscous case is considered in order to observe the formation of the von Kármán vortex street.

The computational domain is taken sufficiently large $\Omega = [-3; 15] \times [-10; 10]$, to ensure that the boundary conditions affect the flow close to the cylinder the least. In order to obtain accurate results, unstructured meshes, see for instance as [161], are usually used to ensure a good representation of the geometry of the circular cylinder. However, in this work a simple uniform Cartesian grid is used and this leads to a particularly demanding test, since the geometry is only resolved via the diffuse interface approach. A rather large domain relative to the circular cylinder is required and at the same time a sufficiently refined grid is needed to represent the object correctly and to ensure that numerical viscosity is as low as possible. The domain is discretized with 720 × 800 rectangular elements. The initial condition for each phases are given by

$$\begin{aligned}
\alpha^l(x,y,0) &= \begin{cases} 1e^{-2} & \text{if } \sqrt{x^2+y^2} \leq 1, \\ 1 & \text{otherwise,} \end{cases} \\
\alpha^s(x,y,0) &= \begin{cases} 1-1e^{-2} & \text{if } \sqrt{x^2+y^2} \leq 1, \\ 0 & \text{otherwise,} \end{cases} \\
p(x,y,0) &= p_{out}, \quad u_i^s(x,y,0)=0, \quad v(x,y,0)=0, \quad u(x,y,0)=u_L,
\end{aligned} \tag{4.14}$$

where p_{out} is the pressure outside the domain while u_L is the inlet velocity, taken with the value 0.5. Different kinematic viscosity values are assumed to obtain simulations related to different Reynolds numbers, $\mathbb{R}\mathrm{e} = 75, 100, 125, 150$. At the upper, lower and right boundaries, the outlet boundary conditions are set by imposing a constant pressure $p_{out} = 50\beta$, while at the left boundary the velocity u_L is prescribed. It is not necessary to impose the no-slip boundary conditions along the solid phase circular cylinder.

As a first result, in Fig. 4.10 the von Kármán vortex street obtained at time $t = 300$ is shown for a $\mathbb{R}\mathrm{e} = 100$ flow. Here, to better visualize the typical structures of this viscous flow, the contour plot of a tracer added to the in-flow is shown. Moreover, to provide a qualitative comparison for this numerical

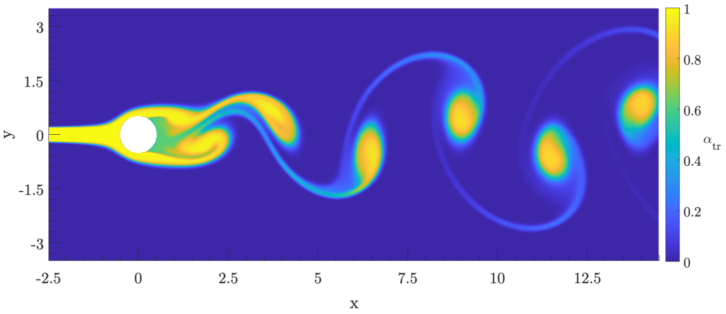

Fig. 4.10. Numerical solution for the laminar viscous flow past a circular cylinder at time $t = 300$, with $\mathbb{R}\mathrm{e} = 100$. The contour plot represents the concentration of the added tracer.

test, the Strouhal number of the vortex shedding can be computed as

$$St = \frac{fL}{u}, \tag{4.15}$$

where f is the frequency of the oscillating flow mechanisms, L is the characteristic length of the cylinder, namely the diameter and u is the modulus of the flow velocity. The vortex-shedding frequency can be evaluated from the time series of the drag and lift coefficients. In fact, for a solid phase immersed in a viscous liquid phase, a net force can be evaluated from the pressure differences due to the flow. The lift component of this force is the one perpendicular to the incoming flow and the drag is the one parallel to the flow direction. From these two components the lift and drag coefficients can be evaluated, which read

$$C_l = \frac{2F_l}{\rho A u^2} \qquad \text{and} \qquad C_d = \frac{2F_d}{\rho A u^2} \tag{4.16}$$

where F_d id the drag force, namely the resulting pressure force along the x-direction, and F_l the lift pressure force, A is the projected cylinder area and u again is the velocity of the oncoming flow.

In Fig. 4.12 the lift and drag coefficients are represented for $\mathbb{R}\mathrm{e} = 100$. It is interesting to see how this numerical method is able to evaluate in a smooth way the pressure forces acting on the solid phase, and how the von Kármán vortex street develops over time to reach a periodic signal with a constant frequency and amplitude. This is the vortex-shedding frequency from which the Strouhal number of this oscillating signal can be computed.

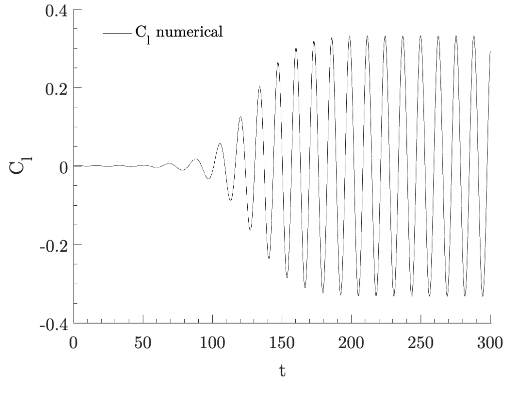

Fig. 4.11. The lift coefficient C_l for the solid circular cylinder immersed in a viscous flow. The Reynolds number of the flow is $\mathbb{R}\mathrm{e} = 100$.

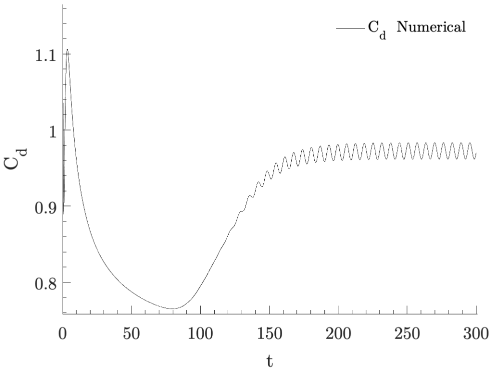

Fig. 4.12. The drag coefficient C_d for the solid circular cylinder immersed in a viscous flow. The Reynolds number of the flow is $\mathbb{R}\mathrm{e} = 100$.

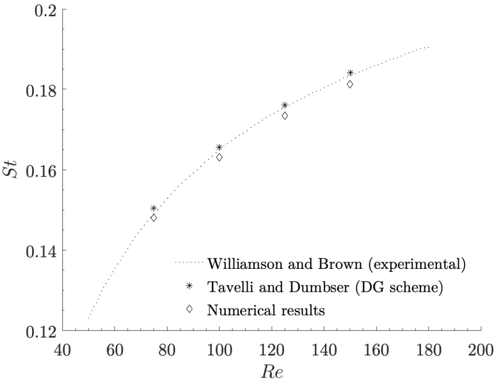

Fig. 4.13. Strouhal-Reynolds number relationship for the present numerical method compared with the experimental data of Williamson and Brown [175] and the numerical result of Tavelli and Dumbser [161].

Carrying out several simulations with different $\mathbb{R}\mathrm{e}$, it is possible to recover the Strouhal-Reynolds number relationship.

Figure 4.13 shows a qualitative comparison between the numerical results obtained and some reference solutions, which are those obtained with the staggered space-time DG method [161] and the experimental data of Williamson and Brown [175]. It is possible to see that the Strouhal-Reynolds number relationship obtained with the numerical method presented in this paper is in agreement with experimental data and other numerical method. However, a small discrepancy, which becomes more relevant as the Reynold number increases, can be seen from the reference solutions. This is due to numerical viscosity, in fact achieving mesh convergence is computationally expensive for such a large domain using a uniform Cartesian grid.

4.1.8 Sloshing in a moving tank

In these last tests, some computational results are shown for incompressible two-phase flow problems, such as water flows interacting with moving solids and vacuum. In particular, this test considers the sloshing motion of a liquid phase in a partially filled solid tank, i.e. a free-surface flow problem in a moving solid geometry. The resulting flow is quite complex, characterized by the presence of high-amplitude oscillations and wave breaking, thus the non-hydrostatic effects cannot be neglected. Furthermore, in order to solve such a problem, a numerical method is required that is able to deal with the motion and interaction of two phases or with moving geometries. Actually, the most common method to solve this kind of problem is to use mobile geometries, i.e. to move the mesh according to the movement of the sloshing tank, as it has been done, for example, in [21, 50]. A thorough description of the testcase, as well as references to analytical studies and numerical results can be found in [21, 50] and references therein. Laboratory measurements of the wave height and hydrodynamic pressure have also been collected and reported, such as those carried out by Faltinsen *et al.* [59].

As introduced earlier, to solve this problem through the numerical method presented in this paper, the dynamics of the liquid phase and the solid phase motion are decoupled. By solving the solid advection equation (3.1), with a prescribed solid velocity field u_k^s, one obtains the new solid volume fraction α^s distribution, which is needed in costitutive relationship of the liquid phase volume (3.22) and in the relaxation source term. From the solution of (3.1) it is therefore possible to solve the system for the liquid phase (3.10).

The simulations presented in this paper refer to the numerical solutions obtained in [21, 50], which in turn refer to the tests presented in the work of Shao *et al.* [157], who presented an improved SPH method for the modelling liquid sloshing dynamics. The numerical methods presented in these papers, although different, include some kind of turbulence model in order to properly describe the effects of turbulence, since in the tests that will be addressed, the Reynolds number is of the order of $\mathbb{R}\mathrm{e} = 10^6$. However, in the semi-implicit finite volume scheme presented in this paper, a turbulence model has not been implemented, assuming that the eddy viscosity, as a rough approximation, is proportional to the numerical viscosity (ILES).

In this article, an idealized two-dimensional case is considered, where the tank, i.e. the solid phase, moves with a purely horizontal sinusoidal velocity and the vertical component of the velocity is zero, namely

$$u_s = (-\omega \delta x_A \sin(\omega t), 0) \tag{4.17}$$

where $\omega = \frac{2\pi}{T}$ is the frequency of the oscillation and T is the period, while δx_A represent the amplitude of the horizontal tank displacement which is assumed constant for all the tests and equal to $\delta x_A = 0.032$. The computational domain is taken large enough to include the experimental material and its displacements used for the laboratory measurements carried out by Faltinsen *et al.* [59], and large enough to describe the tank with a solid phase distribution, thus is taken equal to $\Omega = [-1 + \delta x_A; 1 + \delta x_A] \times [-0.1; 1.2]$.

The initial condition for each phases are given by

$$\begin{aligned}
&\alpha^l(x,y,0) = \begin{cases} 1 & \text{if } \ y \le h_w, \\ 1e^{-4} & \text{otherwise,} \end{cases} \\
&\alpha^s(x,y,0) = \begin{cases} 1 - 10^{-4} & \text{if } \ |x - \delta x_A| \ge 0.865 \ \vee \ y < 0, \\ 0 & \text{otherwise,} \end{cases} \\
&p(x,y,0) = \beta \left(\frac{2 \ \alpha^l}{(1 - \alpha^s)} - 1 \right), \qquad u_i(x,y,0) = 0,
\end{aligned} \tag{4.18}$$

therefore the fluid and the tank are set to be initially at rest and h_w is the initial free surface elevation. We emphasise that in all free-surface tests, a two-phase flow containing a liquid phase, a solid phase and the surrounding void is considered, thus the sum of the volume fractions is not equal to 1. The kinematic viscosity is assumed to be $\nu = 10^{-6}$.

The domain is discretized with 720 × 800 rectangular elements. Also in this test, the classical no-slip wall boundary conditions for the liquid phase, on the solid one, is automatically well imposed via the stiff velocity relaxation source terms. Three simulations were carried out with three different parameter pairs, namely the first pair of parameters $T = 1.3$ and $h_w = 0.6$, the second one $T = 1.5$ and $h_w = 0.6$ and the last pair $T = 1.875$ and $h_w = 0.5$.

The sloshing dynamics, for the parameter pairs $T = 1.5$ and $h_w = 0.6$, is depicted in Fig. 4.14 by nine instants representing a period of oscillation of the solid phase, namely the solid tank. Here, it is possible to see the presence of high-amplitude oscillations of the free surface occurring as the solid geometry moves, and the solid phase motion is also clearly detectable. Figure 4.15 shows a comparison, for the first pair of parameters $T = 1.3$ and $h_w = 0.6$, between the computed numerical solution, the experimental data provided by Faltinsen *et al.* [59] and the numerical results of Dumbser *et al.* in [50]. ΔH is the perturbation of the free surface elevation with respect to the initial at rest

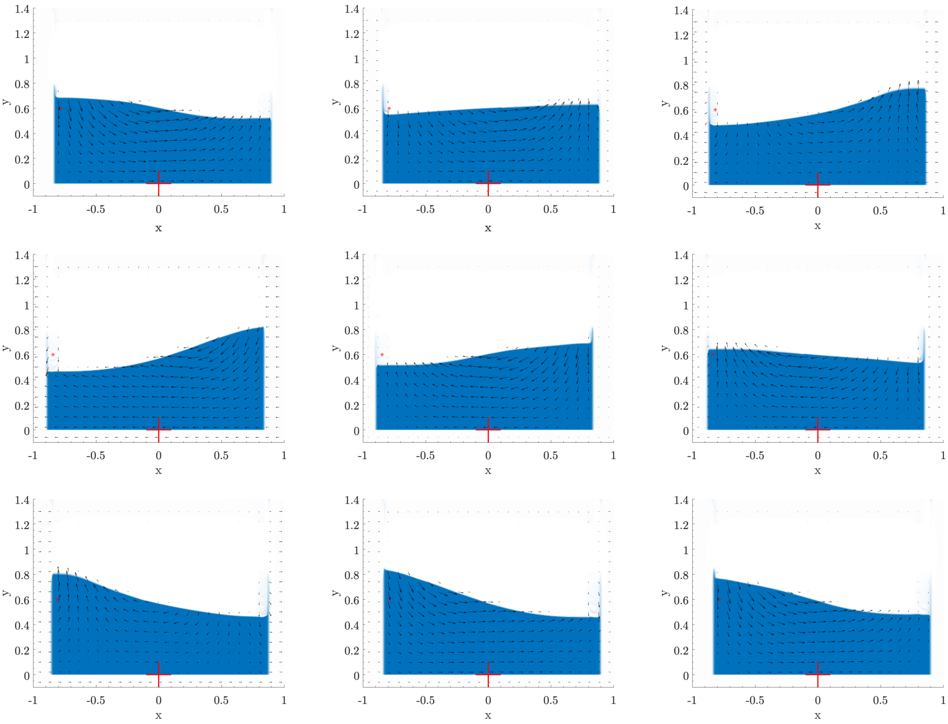

Fig. 4.14. The sloshing dynamics represented with the aid of the liquid volume fraction contours, for the parameter pairs $T = 1.5$ and $h_w = 0.6$, at times 3.0, 3.2, 3.4, 3.6, 3.8, 4.0, 4.2, 4.4 and 4.5 s. The vector lines, shown as arrows, show the velocity field of the mixture. A red asterisk on the left indicates the probe point.

condition. The numerical results were collected at the same probe point used in the two reference papers, which is fixed with respect to the solid phase, hence it moves together with the tank. This point is located 0.05 m away from the left wall and ΔH is evaluated at each time step as

$$\Delta H = \left(\sum_j \alpha^l_{i_p,j} dy \right) - h_w \tag{4.19}$$

where i_p is the discrete index, in the x-direction, associated to the probe point which is moving horizontally according to the solid phase. It can be seen that the liquid phase reacts with a certain inertia to the movement of the solid phase. As the solid phase starts to move towards the left, the free surface on the left tends to decrease and then increase as the solid phase slows down to change direction around 1.2 s. The liquid phase keeps moving following the described periodic cycle of the solid phase with a free surface perturbation which is

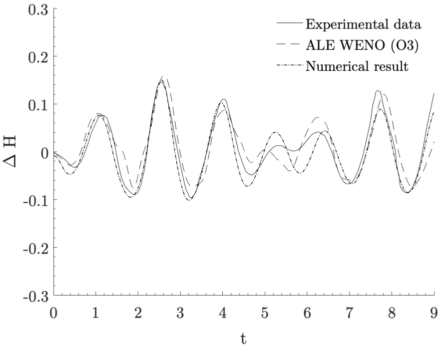

Fig. 4.15. Comparison for the sloshing in a moving tank test between the computed numerical solution, the experimental data provided by Faltinsen *et al.* [59] and the numerical results of Dumbser *et al.* in [50]. For the first pair of parameters $T = 1.3$ and $h_w = 0.6$.

in overall good agreement with the experimental data and the numerically computed results of Dumbser *et al.* in [50].

Two more comparisons, for the second pair $T = 1.5$ and $h_w = 0.6$ and the last pair $T = 1.875$ and $h_w = 0.5$ of parameters, are depicted in Fig. 4.16. Here it can be noticed how the amplitude of the wave progressively increases over time, due to a resonance effect. Again, the results are in good agreement with the experimental data, and it can be seen that the resonance phenomenon is well captured in the case of the test on the left in Fig. 4.16 compared to that obtained by an explicit method in [50].

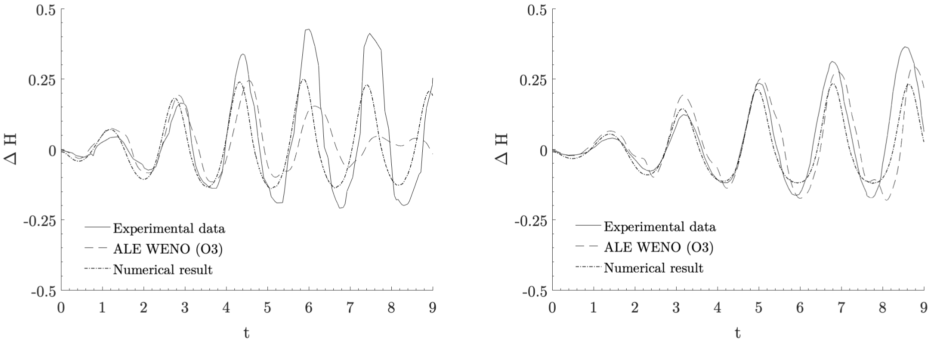

Fig. 4.16. Comparison for the sloshing in a moving tank test between the computed numerical solution, the experimental data provided by Faltinsen *et al.* [59] and the numerical results of Dumbser *et al.* in [50]. For the second pair of parameters $T = 1.5$ and $h_w = 0.6$ and the last pair $T = 1.875$ and $h_w = 0.5$.

4.1.9 Water entry of a symmetric wedge with prescribed velocity

In this last numerical simulation, a solid-fluid coupling problem is treated again in a free-surface flow context. In this test case a symmetric wedge impacting the free surface with prescribed velocity is considered. Indeed, the water entry of a solid through the free surface is also a widely investigated field in the literature, since the knowledge of the pressure field acting on objects is a fundamental criterion for their design. In addition, being able to evaluate the pressure field acting on an object with sufficient accuracy could, in future method development, allow the dynamics of the solid phase to be evaluated directly, rather than imposing an *a priori* kinematic law.

As for the sloshing phenomena studied in the previous section, the water entry of a two-dimensional symmetric wedge has been investigated both through analytical studies and numerical simulations, which are validated by comparing with experimental data, see e.g. the experiment which has been carried out by Zhao *et al.* [180] and the SPH method of Oger *et al.* [123]. Actually, this test case of a symmetric wedge impacting the free surface, refers to the experiment carried out by Zhao *et al.* [180], for which the motion of the wedge, i.e. the solid phase, was experimentally recorded and reported in Fig. 4.17.

The resulting flow and the solid-liquid interaction in general is even more complex in this test than in the previous one. Here, the wedge impact against calm water generates a large free surface deformation, which is followed by the formation of two jets running out along the edges of the wedge. An important feature is that the flow separates in a fixed separation point, which corresponds to the end of the edge, and it can be shown that the flow leaves the edge tangentially in the initial stages of the flow separation. Then, at a later stages

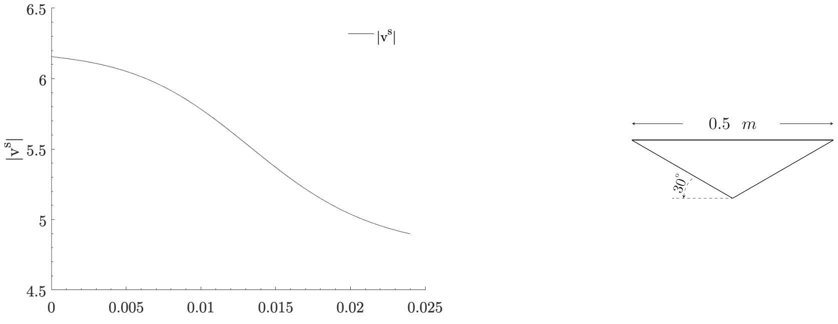

Fig. 4.17. The vertical drop velocity of the wedge recorded experimentally and prescribed numerically (left). The geometry of the wedge section having a deadrise angle of 30 degrees (right).

it will no longer be a jet, gravity will start to play a role and as the wedge penetrates the liquid the flow separation will also no longer be tangent to the edge.

Considering pressure, as the wedge enters the water the maximum pressure will be located along the side at the highest wetted point, whereas after the flow separates, the pressure value near the separation point drops rapidly and the maximum pressure moves towards the bottom of the wedge. It is expected that the numerical method will be able to reproduce these resulting flow characteristics qualitatively.

The computational domain is taken large enough to include the experimental material used for the laboratory measurements carried out by Zhao *et al.* [180], thus the domain is taken equal to $\Omega = [-0.5; 0.5] \times [-0.5; 0.5]$. The initial condition for each phases, according to the the geometry of the experimental section, which consider a wedge with a dead-rise angle of 30° illustrated in Fig. 4.17, are given by

$$
\begin{aligned}
&\alpha^l(x,y,0) = \begin{cases} 1 & \text{if } \; y \leq 0, \\ 1e^{-2} & \text{otherwise,} \end{cases} \\
&\alpha^s(x,y,0) = \begin{cases} 1 - 1e^{-2} & \text{if } \; |x| \leq 0.25 \; \wedge \; y \geq |x \tan(\frac{\pi}{6})| \; \wedge \; y \leq 0.25 \tan(\frac{\pi}{6}), \\ 0 & \text{otherwise,} \end{cases} \\
&p(x,y,0) = \beta \left(\frac{2 \; \alpha^l}{(1-\alpha^s)} - 1 \right), \qquad u_i(x,y,0) = 0,
\end{aligned}
\tag{4.20}
$$

therefore, the fluid is set to be initially at rest while the wedge is entering the water free surface with an initial vertical velocity of $v^s(x,y,0) = 6.15$ m/s. In this test, the motion of the wedge, i.e. the motion of the solid phase, is the drop velocity experimentally recorded by Zhao *et al.* [180] and reported in Fig. 4.17; while the horizontal velocity component is assumed to be zero, i.e. $u^s(x,y,t) = 0$ m/s. The domain is discretized with 720 × 800 rectangular elements and periodic boundaries condition are set. The kinematic viscosity is assumed to be $\nu = 10^{-6}$.

The numerical results, for this impact test, are represented in Figure 4.18. From the top to the bottom results for three different instants are shown, namely for $t = 0.00437$ s, $t = 0.0158$ s and $t = 0.02021$ s. From the left to the right, the liquid volume fraction α_l, the pressure field p and a comparison with the analytical local pressure profile along the wedge boundary of Zhao *et al.* [180] are shown. The free-surface evolution, during the water entry of a wedge, illustrated in Figure 4.18 on the left, shows quite well the formation of two jets

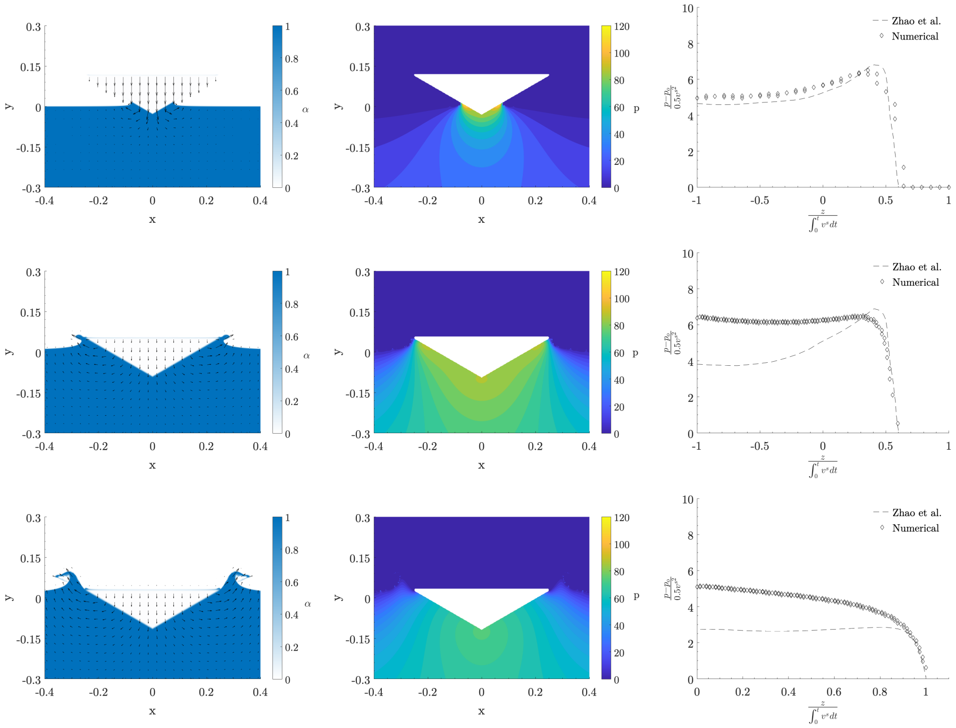

Fig. 4.18. From the left to the right, the liquid volume fraction α_l, the pressure field p and a comparison with the analytical local pressure profile along the wedge boundary of Zhao *et al.* [180] are shown. From the top to the bottom results for three different instants are shown, namely for t=0.0043 s, t=0.0158 s and t=0.0202 s.

running out along the edges of the wedge. At time $t = 0.0158$ these two jets reach the separation point, which corresponds to the end of the edge. It can be seen that the flow leaves the edge tangentially at this initial stage of flow separation. Then, at $t = 0.0202$ it is possible to see that the flow separation is no longer tangent to the edge and a sort of breaking wave is developed. This shape of jet is substantially different from the one obtained through the SPH method of Oger *et al.* [123], however, it is qualitatively similar to the experimental illustration given in the article of Zhao *et al.* [180].

Considering instead the pressure evolution, represented at the centre of figure 4.18 it is possible to observe how the numerical method presented in this article succeeds in evaluating a much more uniform, symmetrical and smooth pressure field than the one obtained with the SPH method of Oger *et al.* [123].

Furthermore, unlike SPH methods, where the estimation of the pressure field is a complex procedure, mainly in near boundary areas, in this pressure-based scheme the pressure field is obtained as directly and naturally as possible, in every part of the domain. A comparison is shown in the right-hand column of figure 4.18 with the Zhao's analytical results, represented with a dash line. The notation is the same as the one used in the article of Zhao *et al.* [180], p denotes the local pressure, p_o is the reference pressure assumed to be equal to β, $v^s(t)$ is the vertical velocity of the solid phase, z is the vertical coordinate on the wedge edge, z_k the vertical coordinate of the keel and z_d of the highest part of the solid phase. With respect to the first instant $t = 0.0043$, the pressure profile along the edge is in good agreement with Zhao's analytical ones, then for later time frames the numerical results over-estimate the pressure values especially in the lower part of the wedge. However, the values are still qualitatively comparable. As the wedge enters into the water the maximum pressure values are located along the side at the highest wetted point, whereas after the flow separates, the pressure value near the separation point drops rapidly and the maximum pressure moves towards the bottom of the wedge.

4.2 Explicit FV scheme for compressible multiphase fluid and solid mechanics

This section provides results that will be published in [71], obtained with the numerical scheme presented in Chapter 3.2 addressing the reduced SHTC three phase BN-type model described in Section 3.2.1. The numerical scheme presented in this work considers the entropy inequalities of each phase, instead of the energy conservation laws explicitly. This choice was made in order to make the mathematical model less complex, in fact entropy has a much simpler dynamics, however, it should be emphasised that the future intention is to develop a numerical scheme more suited to the model under consideration, i.e. thermodynamically compatible (HTC) scheme where the fully-discrete energy conservation is obtained as a mere consequence of the thermodynamically compatible discretization of the PDEs, see e.g. [1, 25, 168]. Therefore, the following numerical test problems will also aim to prove that considering the conservation of phase entropy rather than phase energy leads to a negligible error and that the scheme is capable of calculating correct solutions for problems with relatively *weak shocks*.

Furthermore, the results consist of a wide range of validation benchmarks and applications to problems involving several phases. Results are shown for multiphase flows in the limit behaviour of the Newtonian inviscid and viscous fluid, as well as in the limit of nonlinear hyperelasticity for phases behaving as elastic and elasto-plastic solids. In both cases the numerical results are comparable with results obtained from established standard models, i.e. the Euler or Navier-Stokes equations for fluids, or the classical hypo-elastic model with plasticity, but, notably, everything within a unified multi-phase model of continuum mechanics.

In all the tests, the time step Δt is computed according to the CFL condition expressed in (3.154), in order to guarantee the stability of the explicit FV time-stepping. Furthermore, the initial conditions for volume fractions are defined with respect to a minimum value $\alpha_{\min} = \epsilon = 10^{-6}$; i.e. when a phase is not present, a minimum tolerance is imposed.

4.2.1 Numerical convergence study

First, a numerical convergence study is presented by solving the isentropic vortex problem proposed in [4, 92], considering the one-phase limit of the model: $\alpha_1 = 1 - 2\epsilon$, $\alpha_2 = \epsilon$, $\alpha_3 = \epsilon$. For this problem there is an exact analytical solution for the compressible Euler equations, i.e. in the stiff inviscid limit $\tau_1^{\mathrm{e}} \to 0$ of the SHTC BN-type model considered in this work.

The initial condition consists of a linear superposition of a homogeneous background field and some δ perturbations, which in terms of primitive variables for the first phase read

$$\mathbf{V}_1 = (1 + \delta\rho_1, 1 + \delta v_{1,1}, 1 + \delta v_{1,2}, 1 + \delta p_1, 1 - 2\epsilon, \mathbf{I}), \tag{4.21}$$

where the phase distortion field is initially set equal to the identity, while the quantities for the absent phases are set in the same way except for the volume fractions. The computational domain is $\Omega = [0;10] \times [0;10]$ and periodic boundary conditions are applied everywhere. In this domain, the perturbations of velocities $\delta v_{1,k}$ and temperature δT_1 are given by

$$\begin{pmatrix} \delta v_{1,1} \\ \delta v_{1,2} \end{pmatrix} = \frac{5}{2\,\pi}\, e^{0.5(1-r^2)} \begin{pmatrix} 5 - y \\ x - 5 \end{pmatrix}, \qquad \delta T_1 = -\frac{(\gamma_1 - 1)\, 5^2}{8\,\gamma_1 \pi^2} e^{1-r^2}, \tag{4.22}$$

then, since we are considering an isentropic vortex, we assume that the perturbation of the entropy δs_1 is zero, hence the perturbations for density and pressure result

$$\delta\rho_1 = (1 + \delta T_1)^{\frac{1}{\gamma_1 - 1}} - 1, \qquad \delta p_1 = (1 + \delta T_1)^{\frac{\gamma_1}{\gamma_1 - 1}} - 1. \tag{4.23}$$

The exact analytical solution of the problem represented by these initial conditions, for the compressible Euler equations, is represented simply by the time-shifted initial condition (4.22), (4.23), convected following the mean velocity $\bar{\mathbf{v}} = (1, 1)$. The physical parameters that remain to be defined are assumed to be $\gamma_1 = 1.4$, $\mathrm{Cv}_1 = 1$, $\mathrm{Cs}_1 = 0.5$, $\tau_1 = 10^{-14}$.

This test is performed up to a final time of $t = 1.0$ using a sequence of successively refined equidistant meshes composed of $\mathrm{N}_x \times \mathrm{N}_y$ control volumes. The L^1 and L^2 error norms at the final time for the density ρ_1, the velocity component $v_{1,1}$ and the phase entropy s_1 are shown in Tab. 4.2 and Tab. 4.3

$\mathrm{N}_x \times \mathrm{N}_y$	$L^1_{\rho_1}$	$L^1_{v_{1,1}}$	$L^1_{s_1}$	$\mathcal{O}_{\rho_1}$	$\mathcal{O}_{v_{1,1}}$	$\mathcal{O}_{s_1}$
32	2.5094E-1	5.1290E-1	1.3009E-2			
64	5.2676E-2	1.1826E-1	5.4240E-3	2.25	2.11	1.26
128	1.0012E-2	2.7041E-2	9.9400E-4	2.39	2.12	2.44
256	1.8412E-3	6.3160E-3	1.5781E-4	2.44	2.09	2.65

Tab. 4.2. Mesh elements, L^1-error norms and their respective numerical convergence rates for the density ρ_1, the velocity component $v_{1,1}$ and the phase entropy s_1, applied to the isentropic vortex problem.

$\mathrm{N}_x \times \mathrm{N}_y$	$L^2_{\rho 1}$	$L^2_{v_{1,1}}$	L^2_{s1}	$\mathcal{O}_{\rho 1}$	$\mathcal{O}_{v_{1,1}}$	$\mathcal{O}_{s_1}$
32	6.6187E-2	1.3959E-1	4.4700E-3			
64	1.4075E-2	3.4710E-2	2.3585E-3	2.23	2.01	0.93
128	2.6702E-3	8.5657E-3	4.9292E-4	2.40	2.02	2.26
256	4.8569E-4	2.0754E-3	7.6455E-5	2.46	2.05	2.69

Tab. 4.3. Mesh elements, L^2-error norms and their respective numerical convergence rates for the density ρ_1, the velocity component $v_{1,1}$ and the phase entropy s_1, applied to the isentropic vortex problem.

together with the corresponding convergence rates. From the results shown in the tables, it can be seen that second-order accuracy is achieved for this inviscid problem, i.e. in the stiff limit of the governing PDE system.

4.2.2 Shear motion in solids and fluids

In the context of this work, this test has a twofold purpose of showing that the unified model for fluid and solid mechanics and the developed numerical scheme can indeed model the behavior of viscous fluids and elastic solids at once. We consider a simple shear motion in solids and fluids in the single-phase limit of the entire multiphase model: $\alpha_1 = 1 - 2\epsilon$, $\alpha_2 = \epsilon$, $\alpha_3 = \epsilon$.

Similar to the previous numerical test in Section 4.2.1, the time evolution of an incompressible shear layer is one of the few test problems for which the exact analytical solution of the non-stationary Navier-Stokes equations is known, and for the velocity component $v_{1,1}$ is given by the following error function

$$v_{1,1}(x, y, t) = v_{1,1}(x, y, 0)\,\mathrm{erf}\left(\frac{1}{2}\frac{x}{\sqrt{\nu_1 t}}\right). \tag{4.24}$$

However, because we are discretizing compressible equations with an explicit scheme, the best we can do is to simulate the problem at sufficiently low Mach number, e.g. $\mathrm{M}_1 = 0.1$ was sufficient to obtain an almost incompressible behavior.

The computational domain is $\Omega = [-0.5; 0.5] \times [-0.0625; 0.0625]$, with the opposite velocities imposed on the left and right halfs of the domain in the x-direction, while we use periodic boundary conditions in the y-direction. The initial conditions of the problem for the first phase, are given by

$$\begin{aligned} &\alpha_1 = 1 - 2\epsilon, \quad \rho_1 = 1, \quad p_1 = \frac{1}{\gamma_1}, \quad \mathbf{A}_1 = \mathbf{I} \\ &v_{1,1} = 0, \quad v_{1,2}(x,y) = \begin{cases} +0.1 & \text{if } \; x > 0, \\ -0.1 & \text{if } \; x \leq 0. \end{cases} \end{aligned} \tag{4.25}$$

with the physical parameters set to $\gamma_1 = 1.4$, $\mathrm{Cv}_1 = 1$, $\mathrm{Cs}_1 = 1$. The strain relaxation time $\tau_1^{\mathrm{e}} = 6\nu_1/\mathrm{Cs}_1^2$ is chosen for various values of the fluid kinematic viscosity ν_1, while for the elastic solid limit is set to $\tau_1^{\mathrm{e}} = 10^{14}$. For the elastic solid limit, this initial condition leads to two shear waves travelling to the left and right with the shear sound speed. In this case, a reference solution for the solid limit was obtained for the single-material GPR model using a classical second-order MUSCL-Hancock scheme [171] on a fine mesh of 32000 cells.

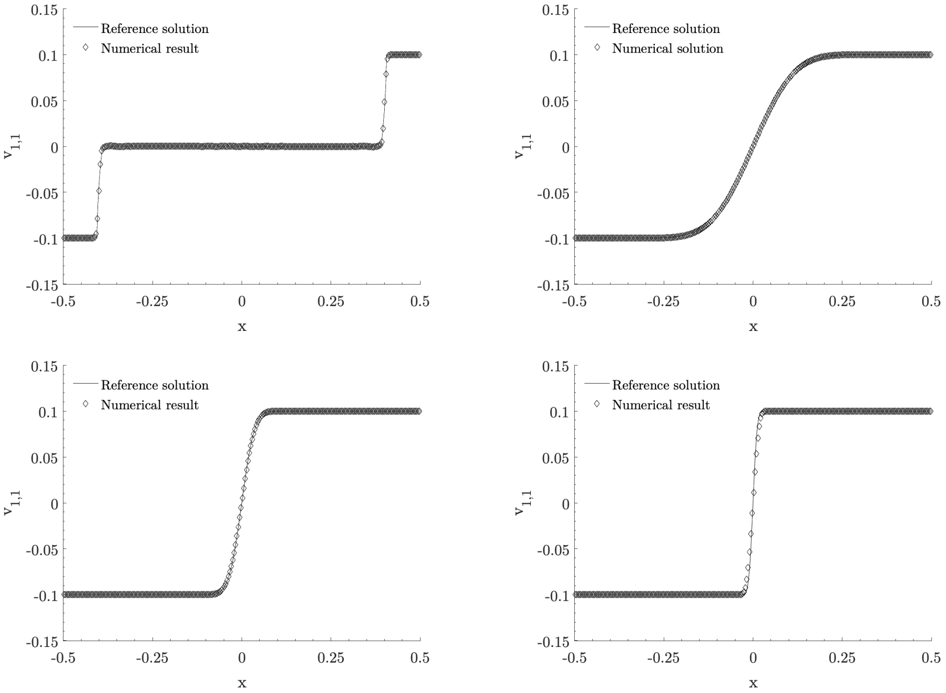

Fig. 4.19. Numerical solution at time $t = 0.4$ obtained with the explicit FV scheme for compressible multiphase fluid and solid mechanics applied to a simple shear flow in fluids and in an elastic solid. Results for the solid limit (top left) and for fluids with different viscosities $\nu_1 = 10^{-2}$ (top right), $\nu_1 = 10^{-2}$ (bottom left) and $\nu_1 = 10^{-2}$ (bottom right). For fluids, the analytical solution of the first problem of Stokes is used as the reference solution.

Simulations are carried out on a grid composed of 256 × 32 control volumes up to a final time of $t = 0.4$. The comparison between the numerical results and the previously mentioned reference solutions is presented in Fig. 4.19, where an excellent agreement between the two can be observed for both solid and liquid behaviour.

4.2.3 Riemann problems

We continue the validation of our numerical scheme with a set of Riemann problems to quantify the error encountered by considering the conservation of phase entropy rather than phase energy and to see that the correct wave structure can still be reproduced for problems with relatively weak shocks. In this section, we solve a series of Riemann problems with initial data according to Tab. 4.4, for the Euler equations of compressible gas dynamics, which can be retrieved in the stiff relaxation limit $\tau_1^{\mathrm{e}} \to 0$.

RP	ρ_1^L	$v_{1,1}^L$	$v_{1,2}^L$	p_1^L	ρ_1^R	$v_{1,1}^R$	$v_{1,2}^R$	p_1^R
RP1	1.0	0.0	0.0	1.0	0.125	0.0	0.0	0.1
RP2	1.0	0.75	0.0	1.0	0.125	0.0	0.0	0.1
RP3	1.0	0.0	-0.2	1.0	0.5	0.0	0.2	0.5

Tab. 4.4. Left initial state (L) and right initial state (R) for the quantities related to the first phase. In particular the density ρ_1, velocity $\boldsymbol{v} = (v_{1,1}, v_{1,2}, 0)$ and pressure P are defined for three different Riemann problems. These Riemann problems (RP1), (RP2) and (RP3) can be referred to the solution of the Euler equations, i.e. $\tau_1^{\mathrm{e}} = 10^{-14}$.

The computational domain $\Omega = [-0.5; 0.5] \times [-0.0625; 0.0625]$ is partitioned into two regions with constant states, left (L) and right (R), separated by a discontinuity normal to the x-direction, located at x_d. The distortion field is initially set equal to the identity $\mathbf{A}_1 = \mathbf{I}$, while the equation of state parameters are taken as $\gamma_1 = 1.4$, $\mathrm{Cv}_1 = 1.0$, $\mathrm{Cs}_1 = 1.0$ and Riemann problems. Simulations are carried out on a grid composed of 512 × 64 control volumes up to a final time of $t = 0.2$.

In Figure 4.20, the one-dimensional profiles of the density ρ_1, the x-component of the velocity field $v_{1,1}$ and pressure p_1 for the Riemann problems RP1 ($x_d = 0$) and RP2 ($x_d = -0.2$) are shown. The results are compared with the exact solution of the compressible Euler equations. From the results it can be observed that the correct wave structure is overall reproduced properly for the Riemann problem RP1, while as the shock wave becomes stronger, as for RP2, the error introduced due to the use of phase entropy balance laws increases.

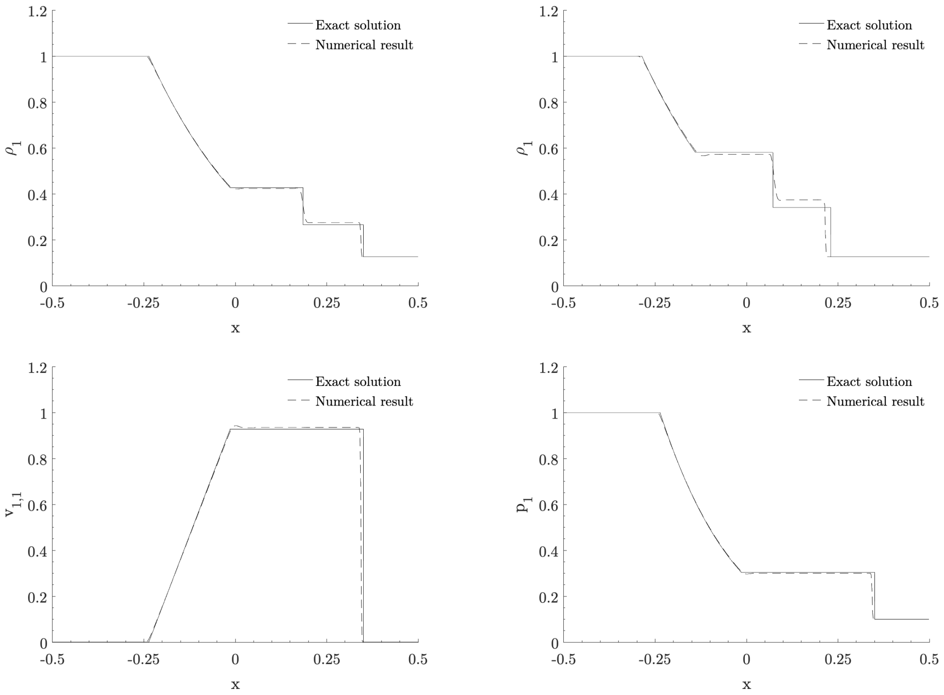

Fig. 4.20. Numerical results (dashed line) for density ρ_1, velocity component $v_{1,1}$ and pressure P_1 in the inviscid limit $\tau_1 = 10^{-14}$, for the Riemann problem RP1 ($x_d = 0$) (top left, bottom left and right), for the Riemann problem RP2 ($x_d = -0.2$) (top right). The exact solution of the compressible Euler equations (black solid line).

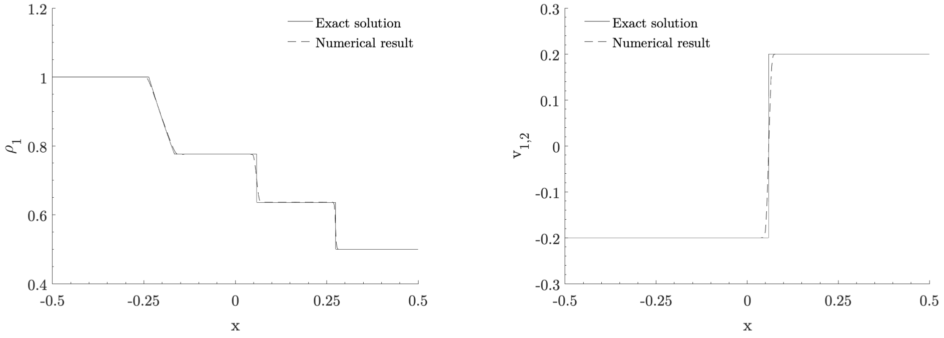

Fig. 4.21. Numerical results for density ρ_1 and velocity component $v_{1,2}$ in the inviscid limit $\tau_1 = 10^{-14}$, at time $t = 0.2$, for the Riemann problem RP3 ($x_d = 0$) (dashed line). The exact solution of the compressible Euler equations (black solid line).

This is why we limit ourselves to sufficiently low Mach number flows, and RP2 clearly demonstrates the well-known fact that satisfying the conservation of energy is essential to correctly solve problems involving shock waves. RP2 was proposed by Toro in [171] and includes a sonic rarefaction, however this test cases is well resolved and does not present any sonic glitches.

The numerical results obtained for the Riemann problem RP3 ($x_d = 0$) is shown in Fig. 4.21. In this case, the shock present is even weaker, the solution is very close to an isoentropic one, and therefore the numerical solution is in very good agreement with the exact one.

4.2.4 Double shear layer problem

The numerical scheme is now applied to solve the double shear layer test problem, see e.g. [8, 25, 34, 54, 162]. It is another classical benchmark problem which is useful for the validation of the viscosity model and the numerical algorithm. Again, here a single phase is considered, therefore the volume fractions are $\alpha_1 = 1 - 2\,\epsilon$, $\alpha_2 = \epsilon$, $\alpha_3 = \epsilon$. For this test the computational domain is $\Omega = [0;1]^2$, with periodic boundary conditions imposed everywhere. The initial conditions contain a sharp velocity gradient and are defined as follows

$$\begin{aligned}
&\alpha_1 = 1 - 2\epsilon, \quad \rho_1 = 1, \quad p_1 = \frac{100}{\gamma_1}, \quad \mathbf{A}_1 = \mathbf{I}, \\
&v_{1,1}(x,y) = \begin{cases} \tanh\big((y - 0.25)\bar{\rho}\big), & \text{if} \ \ x \leq 0.5, \\ \tanh\big((0.75 - y)\bar{\rho}\big), & \text{if} \ \ x > 0.5, \end{cases} \\
&v_{1,2}(x,y) = \delta \sin(2\pi x),
\end{aligned} \tag{4.26}$$

where the parameters that determine the shape of the velocity field are set to $\delta = 0.05$ and $\bar{\rho} = 30$. The other physical parameters are assumed to be $\gamma_1 = 1.4$, $\mathrm{Cv}_1 = 1$, $\mathrm{Cs}_1 = 8.0$ while two different viscosity coefficients were set in two separate runs of the test problem, $\nu_1 = 2 \times 10^{-3}$ ($\mathbb{R}\mathrm{e} \simeq 1000$) and $\nu_1 = 2 \times 10^{-4}$ ($\mathbb{R}\mathrm{e} \simeq 10000$) respectively, which result in $\tau_1^{\mathrm{e}} = 1.875 \cdot 10^{-4}$ and $\tau_1^{\mathrm{e}} = 1.875 \cdot 10^{-5}$, respectively.

Simulations are carried out up to a final time of $t = 1.8$ on a grid consisting of 1280×1280 control volumes. Figure 4.22 shows the time evolution of the $A_{1,12}$ component of the distortion field at times $t = 1.2$ (top), $t = 1.6$ (center) and $t = 1.8$ (bottom), for the two different viscosity coefficients considered (left) and (right), respectively. The dynamics of the flow, as already described in [8, 25, 34, 54, 162], is represented by the evolution of the initially perturbed shear layers into different vortices, which exhibit particularly complex flow structures.

The results in Fig. 4.22, highlight the incredible capability of the distortion field to describe the details of the flow structures, which in particular are encoded in the rotational component $\mathbf{R}_1$ of the distortion field $\mathbf{A}_1$. The results obtained are in excellent agreement with those obtained in [25], where a thermodynamically compatible scheme is used and with those in [34] obtained through a semi-implicit structure-preserving scheme, despite the fact that in these works a four times finer grid was used.

4.2.5 Lid-driven cavity

As a last numerical test considering a single-phase liquid, we present the lid-driven cavity problem, see [76]. It is a classical benchmark problem for numerical methods applied to incompressible Navier-Stokes equations, see [161], however it can be used to validate compressible flow solvers in the low Mach number regime [9, 51, 164].

Moreover, it has already been successfully solved with the GPR model in [14, 54] and with a thermodynamically compatible scheme in [25]. However, in these works, high-order schemes or schemes that make use of particular discretizations have been used, e.g. on staggered grid or thermodynamically compatible discretization. These could be the reasons why it would appear that the problem associated with the discretization, i.e. the combination, of purely rotational fields presented in Section 3.2.6 does not arise in these works, whereas it does for the classical MUSCL-Hancock discretization, specifically in this test where the boundary conditions produce a velocity gradient singularity in the corners.

The computational domain is given by $\Omega = [-0.5; 0.5] \times [-0.5; 0.5]$ and the initial condition are simply

$$\alpha_1 = 1 - 2\epsilon, \quad \rho_1 = 1, \quad \boldsymbol{v}_1 = \mathbf{0}, \quad p_1 = \frac{100}{\gamma_1}, \quad \mathbf{A}_1 = \mathbf{I}. \tag{4.27}$$

The fluid flow inside the cavity is driven by lid velocity on the upper boundary, which is set to $v_{1,1} = 1$, with respect to which, therefore, the Mach number of this test problem reads $\mathrm{M}_1 = 0.1$. On all the other boundaries a no-slip wall boundary condition with $\mathbf{v}_1 = 0$ has to be imposed. Furthermore, the parameters of the model are set to $\gamma_1 = 1.4$, $\mathrm{Cv}_1 = 1$, $\mathrm{Cs}_1 = 8.0$ and the dynamic viscosity is chosen as $\nu_1 = 10^{-2}$ so that the Reynolds number of the test problem is $\mathbb{R}\mathrm{e} = 100$.

Simulations are carried out up to a final time of $t = 10$ on a grid consisting of 512×512 control volumes. To correctly set the no-slip wall boundary conditions, it is necessary to compute and prescribe a specific distortion field $\boldsymbol{A}_{BC}$ using

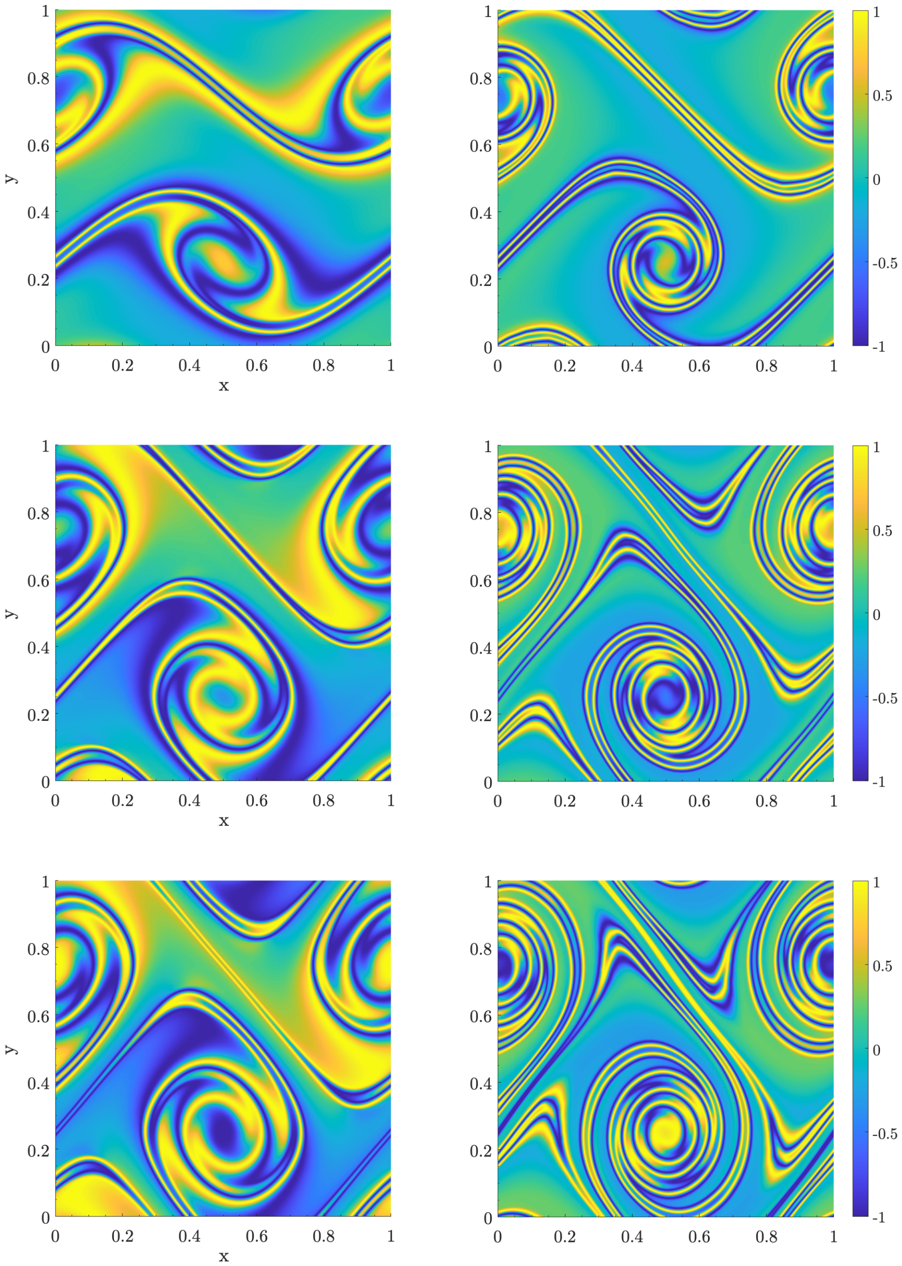

Fig. 4.22. Filled contours of one component of the distortion field $\mathbf{A}_1$, namely of the $A_{1,12}$ component, for the double shear layer problem at times $t = 1.2$ (top), $t = 1.6$ (center) and $t = 1.8$ (bottom); for two values of kinematic viscosity $\nu_1 = 2 \times 10^{-3}$ ($\mathbb{R}\mathrm{e} \simeq 1000$) (left) and $\nu_1 = 2 \times 10^{-4}$ ($\mathbb{R}\mathrm{e} \simeq 10000$) (right).

the values taken in the edge-adjacent cell. First, the information encoded by the distortion field is expressed through $\boldsymbol{R}_{BC\,(1)}$ and $\boldsymbol{G}_{BC\,(1)}$, by means of a polar decomposition. Subsequently, the inverse of the rotational component can be easily evaluated as $\boldsymbol{R}^{-1}_{BC\,(1)} = \boldsymbol{R}^{\mathsf{T}}_{BC\,(1)}$. At this point the information can be mapped back to obtain the boundary condition for the distortion field as

$$\boldsymbol{A}_{BC} = \boldsymbol{R}^{\mathsf{T}}_{BC\,(1)} \, \mathbf{G}^{1/2}_{BC\,(1)}. \tag{4.28}$$

Figure 4.23 shows the computational results obtained using the approach described in Section 3.2.6. This approach separates the evolution of the two types of information encoded in $\mathbf{A}_a$ and leverages the capabilities of a semi-analytical solver to efficiently solve the equations in the stiff relaxation regime. Excellent agreement between the numerical solution and the Navier-Stokes reference solution of Ghia et al. [76] was obtained.

Also for this test, Fig. 4.24 shows the time evolution of the $A_{1,12}$ component of the distortion field. It can again be seen that the distortion field components are excellent candidates for flow visualisation, revealing in detail the evolution of the flow and keeping track of the rotations that the fluid element undergoes over time.

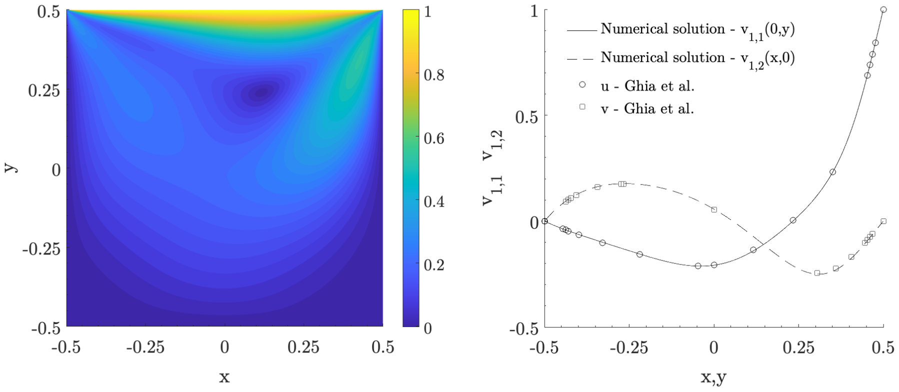

Fig. 4.23. Lid driven cavity at Reynolds number $\mathbb{R}\mathrm{e} = 100$. Numerical results obtained at time $t = 10.0$. Colour contours of the velocity module (left), and a comparison with the reference solution of Ghia *et al.* [76] of the velocity components $v_{1,1}$ and $v_{1,2}$ for 1D cuts along the x and y axis.

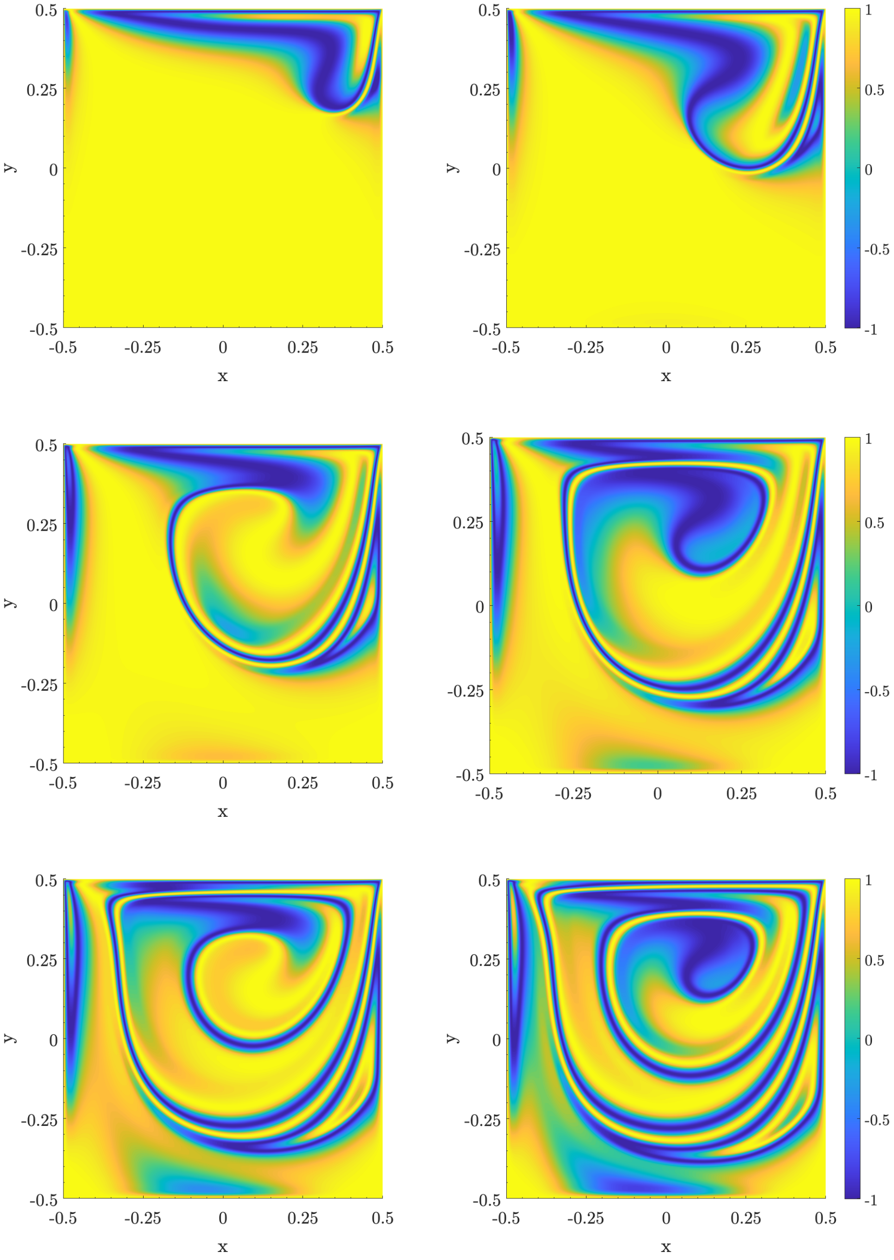

Fig. 4.24. Filled contours of one component of the distortion field $\mathbf{A}_1$, namely of the $A_{1,12}$ component, for the lid-driven cavity problem at $\mathbb{R}\mathrm{e} = 100$, at times $t = 1.0$, $t = 2.0$, (top), $t = 4.0$, $t = 6.0$, (center) and $t = 8.0$, $t = 10.0$ (bottom).

4.2.6 Elastic vibrations of a beryllium plate

Finally, we begin to test a further element of the mathematical model, namely its ability to describe the two main branches of continuum mechanics, i.e. fluid mechanics and solid mechanics, in a single PDE. Moreover, this represents the first test in which two phases are genuinely simulated. This test consists of simulating the purely elastic vibrations of a beryllium plate subjected to an initial velocity distribution. The setup follows [13, 20, 106, 133, 151], but with the notable modification that, instead of initialising a single solid surrounded by vacuum, we define two separate density fields, thus initialising a gas and a solid phase via their respective volume fractions.

Compared to the Lagrangian setup, used in the previously mentioned works, the computational domain considered here is larger, as in [26], and is assumed to be $\Omega = [-4.0; 4.0] \times [-2.0; 2.0]$ and the initial conditions for the first phase are

$$\begin{aligned} &\alpha_1(x,y) = \begin{cases} 1-2\epsilon & \text{if } \boldsymbol{x} \in \Omega_1, \\ \epsilon & \text{if } \boldsymbol{x} \notin \Omega_1, \end{cases} \qquad \boldsymbol{v}_1(x,y) = \begin{cases} (0, \boldsymbol{v}_{1,2}) & \text{if } \boldsymbol{x} \in \Omega_1, \\ (0,0) & \text{if } \boldsymbol{x} \notin \Omega_1, \end{cases} \\ &\rho_1 = 1.845, \quad p_1 = 10^{-4}, \quad \mathbf{A}_1 = \mathbf{I}, \end{aligned} \tag{4.29}$$

while the second phase (the gas) is initialised as follows

$$\begin{aligned} &\alpha_2(x,y) = \begin{cases} \epsilon & \text{if } \boldsymbol{x} \in \Omega_1, \\ 1-2\epsilon & \text{if } \boldsymbol{x} \notin \Omega_1, \end{cases} \\ &\rho_2 = 10^{-3}, \quad \boldsymbol{v}_2 = \mathbf{0} \quad p_2 = 10^{-4}, \quad \mathbf{A}_2 = \mathbf{I}, \end{aligned} \tag{4.30}$$

where $\Omega_1 = [-3.0; 3.0] \times [-0.5; 0.5]$ is the subdomain that defines the initial geometry of the beryllium bar, and the initial vertical velocity component $\boldsymbol{v}_{1,2}$, according to Boscheri et al. [13], is given as

$$\begin{aligned} \boldsymbol{v}_{1,2}(x) = C_1\omega(C_2(\sinh(C_3(x+3)) + \sin(C_3(x+3))) \\ - C_4(\cosh(C_3(x+3)) + \cos(C_3(x+3)))) \end{aligned} \tag{4.31}$$

with $C_3 = 0.7883401241$, $C_2 = 0.2359739922$, $C_1 = 0.004336850425$, $C_4 = 57.64552048$ and $C_2 = 56.53585154$. The third phase has $\alpha_3 = \epsilon$. The other parameters and physical quantities that define the properties of the beryllium material and that are required to use the stiffened-gas EOS (2.72) are chosen as $\gamma_1 = 1.4$, $\mathrm{Cv}_1 = 1000$, $\mathrm{Cs}_1 = 0.905$, $\rho_{\mathrm{o}_a} = 1.845$, $\mathrm{Co}_1 = 1.287$ and $p_{\mathrm{o}1} = p_1$. Additinally, to have an ideal elastic material we set $\tau_1^{\mathrm{e}} = 10^{14}$. For the gas phase surrounding the solid phase, the EOS of ideal gases is used and the physical parameters are $\gamma_2 = 1.2$, $\mathrm{Cv}_2 = 1000$, $\mathrm{Cs}_2 = 1.0$ and $\nu_2 = 10^{-4}$.

The simulation is carried out, according to [20], up to the final time $t_f = 53.2$ which corresponds approximately to two complete periods of vibration and the computational domain is discretized with an uniform Cartesian mesh composed of 1024×512 control volumes. In contrast to Lagrangian schemes, it is not necessary to impose boundary conditions on the surface of the solid, as the solid-gas boundary condition is directly taken into account within the governing PDE system. Hence, in our simulation, periodic boundaries are set everywhere.

In Fig. 4.25 we represent the contour map of the volume fraction function α_1, which represents the geometry of the bar at time $t = 8$ and in the same figure, we also depict the time evolution of the vertical velocity component $v_{1,2}(0, 0, t)$ at $\bar{\mathbf{x}} = (0, 0)$, i.e. in the barycenter of the bar. For comparison, we also show the results obtained with a third-order ALE ADER-WENO scheme (black line), against which our numerical solution (red line) is in good agreement.

In Fig. 4.26, the first component of the stress tensor $\sigma_{1,11}$ and the vertical component of the velocity $v_{1,2}$ are shown on the left and right panels respectively for the intermediate times $t = 8$, $t = 15$, $t = 23$ and $t = 30$, covering approximately one bending period. Note that the colour scales for both quantities are different depending on the time instant, depending on whether or not the bar has returned to its original position. Our computational results compare visually well with the reference solutions available in the literature, see [13, 20, 106, 133, 151], which have all been realised with pure Lagrangian or arbitrary Lagrangian-Eulerian schemes on moving meshes, despite the fact that in our case we use a diffuse interface approach on a fixed Cartesian grid, as in [26].

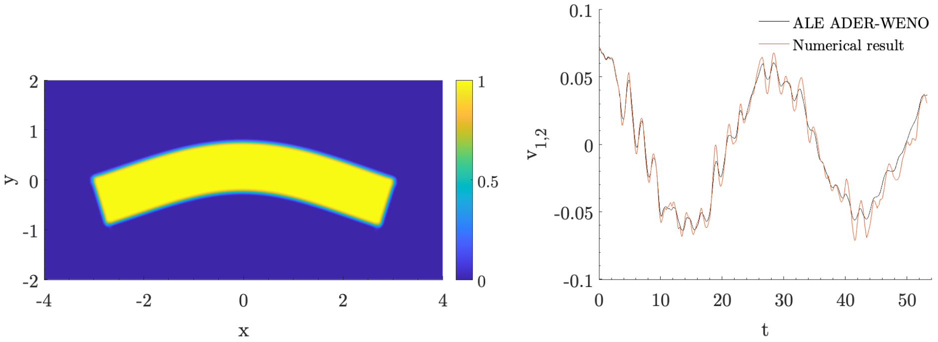

Fig. 4.25. Filled contour map of the volume fraction function α_1 for the first phase, which represents the geometry of the beryllium bar at time $t = 8$ (left). The time evolution of the vertical velocity component $v_{1,2}(0, 0, t)$ at $\bar{\mathbf{x}} = (0, 0)$, i.e. in the barycenter of the bar (right).

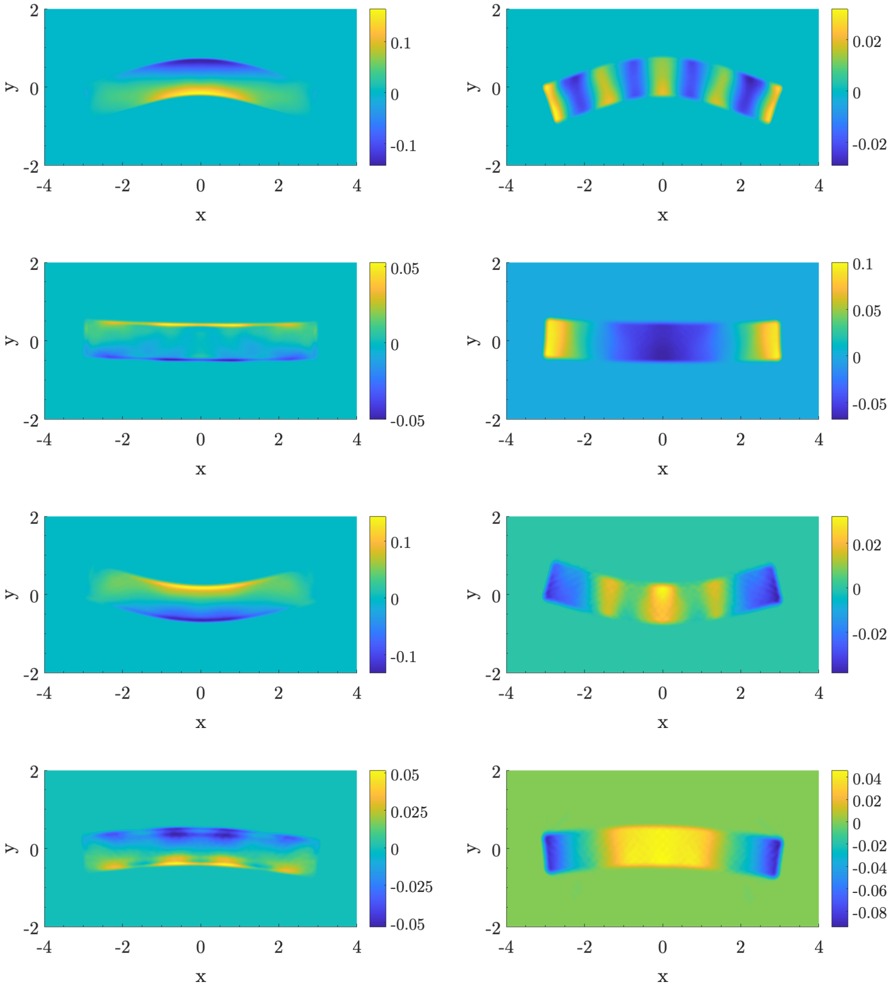

Fig. 4.26. Results for the elastic vibrations of a beryllium plate, at times $t = 8$, $t = 15$, $t = 23$ and $t = 30$ (from top to bottom), for the first component of the stress tensor $\sigma_{1,11}$ (left) and the vertical component of the velocity $v_{1,2}$ (right).

A final remark concerns the second phase, which was on purpose chosen three orders of magnitude less dense than the solid one, in order not to affect the dynamics of the beryllium bar and also according to physics, since air is much less dense than any solid material. However, this gaseous phase has its own fully resolved viscous dynamics, in subsequent tests more space will be given to the multiphase dynamics.

4.2.7 Taylor bar impact

In the previous test, we considered an ideal elastic material, which is the solid limit case for $\tau_1^{\mathrm{e}} \to \infty$. In this test, we show how a material can also exhibit non-linear elastic-plastic behaviour. Here we consider the Taylor bar impact problem, which is a classical benchmark for an elasto-plastic target that impacts on a rigid solid wall, see [13, 46, 106, 151] for pure Lagrangian or ALE schemes on moving meshes and [26] for an Eulerian diffuse interface approach.

As with the previous test, we define two separate density fields, initialising a gas and a solid phase through their respective volume fractions. The computational domain considered here is larger than in the Lagrangian setup in order to include the space occupied by the gas phase around the solid. The computational domain under consideration, as in [26], is $\Omega = [-150, +150] \times [0, 600]$ and the initial conditions for the first phase are

$$
\begin{aligned}
&\alpha_1(x,y) = \begin{cases} 1-2\epsilon & \text{if } \ \boldsymbol{x} \in \Omega_1, \\ \epsilon & \text{if } \ \boldsymbol{x} \notin \Omega_1, \end{cases} \qquad \boldsymbol{v}_1(x,y) = \begin{cases} (0, \boldsymbol{v}_{1,2}) & \text{if } \ \boldsymbol{x} \in \Omega_1, \\ (0,0) & \text{if } \ \boldsymbol{x} \notin \Omega_1, \end{cases} \\
&\rho_1 = 2.785, \quad p_1 = 10^{-4}, \quad \mathbf{A}_1 = \mathbf{I},
\end{aligned}
\tag{4.32}
$$

where $\Omega_1 = [-50, +50] \times [0, 500]$ is the subdomain that defines the initial geometry of the solid bar and the initial vertical velocity component is $\bar{v}_{1,2} = -0.015$; while the second phase is initialised as follows

$$
\begin{aligned}
&\alpha_2(x,y) = \begin{cases} \epsilon & \text{if } \ \boldsymbol{x} \in \Omega_1, \\ 1-2\epsilon & \text{if } \ \boldsymbol{x} \notin \Omega_1, \end{cases} \\
&\rho_2 = 10^{-3}, \quad \boldsymbol{v}_2 = \mathbf{0} \quad p_2 = 10^{-4}, \quad \mathbf{A}_2 = \mathbf{I}.
\end{aligned}
\tag{4.33}
$$

According to [13, 46, 106, 151], the first phase, i.e. the solid one is assumed to be an aluminium bar, then the other parameters and physical quantities that define the properties of such a material using the stiffened-gas EOS are $\gamma_1 = 1.4$, $\mathrm{Cv}_1 = 1000$, $\mathrm{Cs}_1 = 0.305$, $\rho_{\mathrm{o}a} = 2.785$, $\mathrm{Co}_1 = 0.533$ and $p_{\mathrm{o}1} = p_1$. To obtain a non-linear elasto-plastic material behaviour the relaxation time τ_1^{e} has to be choosen as a non-linear function of an invariant of the shear stress tensor as follows [133]

$$
\tau_1 = \tau_{\mathrm{o}} \left(\frac{\sigma_{\mathrm{o}}}{\bar{\sigma}_1} \right)^m, \tag{4.34}
$$

where $\tau_{\mathrm{o}} = 1$ is the scaling constant, $\sigma_{\mathrm{o}} = 0.003$ is the yield stress of the material under quasi static conditions, the exponent parameter is chosen equal to $m = 20$ (the higher m is the less rate-dependent the effective yield strength is [6, 133]) and the von Mises stress $\bar{\sigma}_1$ is given by

$$\begin{aligned}\bar{\sigma}_1 = \bigg(\frac{1}{2}\big(\,(\sigma_{1,11} - \sigma_{1,22})^2 + (\sigma_{1,22} - \sigma_{1,33})^2 + (\sigma_{1,33} - \sigma_{1,11})^2 \\ + 6(\sigma_{1,21}^2 + \sigma_{1,31}^2 + \sigma_{1,32}^2)\,\big)\bigg)^{1/2} .\end{aligned} \tag{4.35}$$

For the gas phase surrounding the solid phase, the EOS of ideal gases is used and the physical parameters are $\gamma_2 = 1.2$, $\mathrm{Cv}_2 = 1000$, $\mathrm{Cs}_2 = 1.0$ and $\nu_2 = 10^{-4}$.

The simulation is carried out, according to [26, 106], up to the final time $t_f = 5000$ and the computational domain is discretized with a uniform Cartesian mesh composed of 2048×1024 control volumes. In contrast to Lagrangian schemes, it is not necessary to impose boundary conditions on the surface of the solid; in our simulation, periodic boundaries are set in x-direction while reflective slip wall boundary conditions are set in y-direction.

In Fig. 4.27 we present the results computed at output times $t = 2500$ and $t = 5000$. The volume fraction (left), the density distribution (center) and the plastic rate $\eta_1 = \bar{\sigma}_1/\sigma_o$ (right) are depicted. It can be observed that the numerical solution is reasonably in agreement with that presented in [13, 106], although the models used are significantly different. Moreover at time $t = 5000$, the final length of the aluminium bar is $L_f = 455$, which fits the results achieved in [13, 106] within a 2% error.

4.2.8 Multiphase Rayleigh-Taylor instability

The two previous tests focused mainly on the validation of the unified model for elasto-plastic solid mechanics, thus not much emphasis was placed on the dynamics of the second phase. In this test, however, we will finally put to the test one of the main features of the model and the numerical scheme, namely the ability to describe several interacting phases. To this end, we will simulate a true *two-phase* relatively low-Mach, $M_1 \simeq M_2 \simeq 0.1$, viscous Rayleigh–Taylor instability.

The approach follows [34, 102], but with the notable modification that instead of initialising a single fluid with a jump in the density, we define two fluids through the volume fraction each with constant phase densities. This makes the problem more challenging because the quasi-vacuum states of either phase are introduced almost throughout the entire computational domain, however it introduces much more freedom in defining the material characteristics of each phase. The computational domain under consideration, as in [34], is

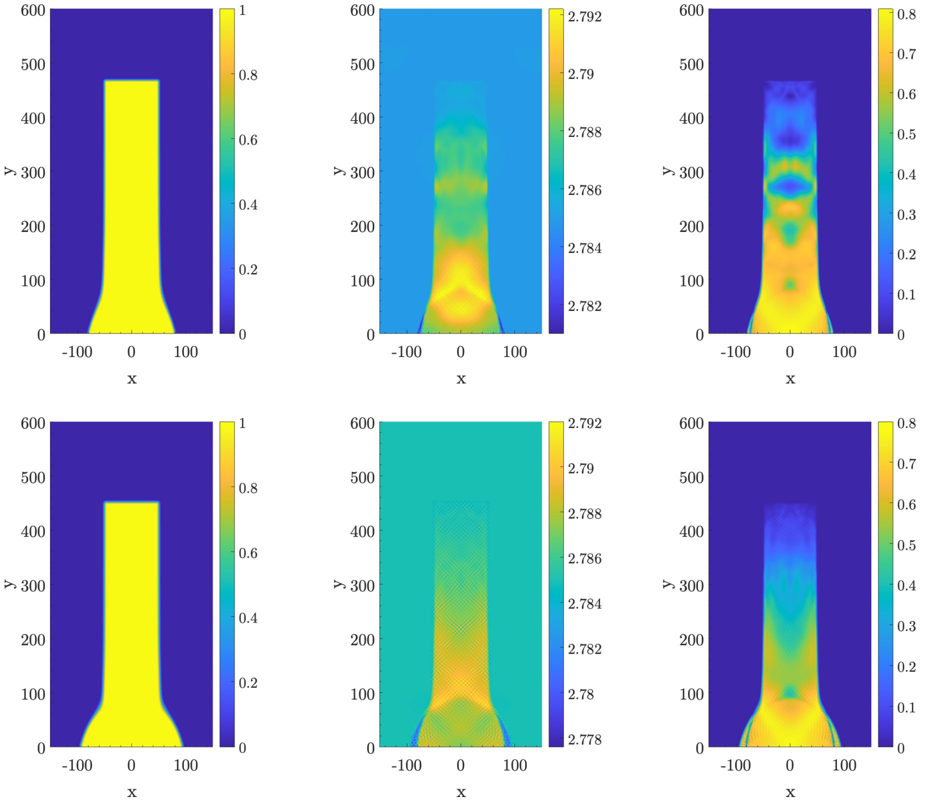

Fig. 4.27. Results for the non-linear elasto-plastic Taylor bar impact, at times $t = 2500$ and $t = 5000$ (from top to bottom): the volume fraction (left), the density distribution (center) and the plastic rate $\eta_1 = \bar{\sigma}_1/\sigma_0$ (right).

$\Omega = [0, 1/3] \times [0, 1]$ and the initial conditions for the first phase, the upper and heavier one, are

$$\begin{aligned} &\alpha_1(x,y) = \bar{s}(1-2\epsilon) + (1-\bar{s})\epsilon, \qquad \rho_1 = 2.0, \qquad \boldsymbol{v}_1 = \mathbf{0}, \\ &p_1 = \bar{s}p_t + (1-\bar{s})p_b, \qquad \mathbf{A}_1 = \mathbf{I}, \end{aligned} \tag{4.36}$$

and for the lighter fluid (at the bottom) are

$$\begin{aligned} &\alpha_2(x,y) = 1 - \alpha_1 - \epsilon, \qquad \rho_2 = 1.0, \qquad \boldsymbol{v}_2 = \mathbf{0}, \\ &p_2 = \bar{s}p_t + (1-\bar{s})p_b, \qquad \mathbf{A}_2 = \mathbf{I}, \end{aligned} \tag{4.37}$$

where $\bar{s}$ is a switch function introduced to impose a smooth transition between the two states and avoid an inaccurate representation of the initial condition on the discrete Cartesian grid. This function $\bar{s}$ is defined as

$$\bar{s} = \frac{1}{2} + \frac{1}{2}\mathrm{erf}\left(\frac{y - y_{\mathrm{I}}}{\delta}\right), \tag{4.38}$$

where $y_{\mathrm{I}} = 0.5 + 0.01\cos(6\,\pi\,x)$ is the initially perturbed interface between phases and $\delta = \max(\,0.004,\, 6\Delta x\,)$ can be seen as the thickness of this interface. The initial phase top and bottom pressures, in (4.36), (4.37), are defined as

$$\begin{aligned} p_t &= 1 + \rho_1\,(1-y)\mathbf{g}\,\hat{n}_y, \\ p_b &= 1 + 0.5\,\rho_1\,\mathbf{g}\,\hat{n}_y + \rho_2\,(0.5-y)\,\mathbf{g}\,\hat{n}_y. \end{aligned} \tag{4.39}$$

where the gravity vector is $\boldsymbol{g} = (0, -0.1, 0)^{\intercal}$. The other parameters and physical quantities are equal for the two gas phases and using the ideal-gas EOS are set as $\gamma = 1.4$, $\mathrm{Cv} = 1000$, $\mathrm{Cs} = 0.3$ and the dynamic viscosity $\mu = 6 \times 10^{-5}$, which translates to $\tau_1^{\mathrm{e}} = 2 \times 10^{-3}$ and $\tau_2^{\mathrm{e}} = 4 \times 10^{-3}$ so that the Reynolds number of the test problem is $\mathbb{R}\mathrm{e} \simeq 2000$ for the both phases.

Two simulations are carried out up to the final time $t_f = 10$ on two different uniform Cartesian meshes in order to verify mesh convergence of the solution algorithm. In these simulations, periodic boundaries are set in x-direction while reflective slip wall boundary conditions are set in y-direction. Fig. 4.28 shows on the left the result for the mixture density $\bar{\alpha} = \alpha_1\,\rho_1 + \alpha_2\,\rho_2 + \alpha_3\,\rho_3$ obtained with a mesh consisting of 512×1536, while on the right the result obtained by doubling the mesh resolution, both at time $t = 7$. It is possible to

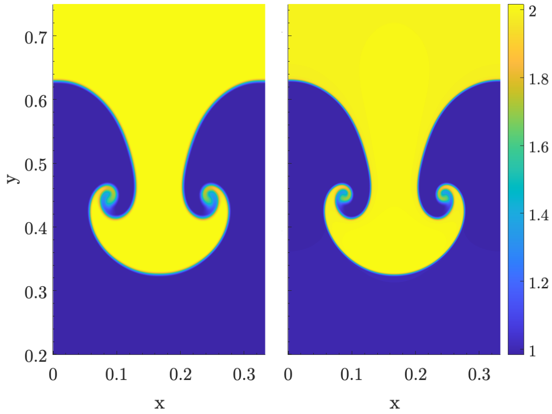

Fig. 4.28. Mesh convergence test for the Rayleigh-Taylor instability problem, at times $t = 7$; on the left the result obtained with a mesh consisting of 512×1536 is shown, and on the right the result obtained by doubling the mesh resolution.

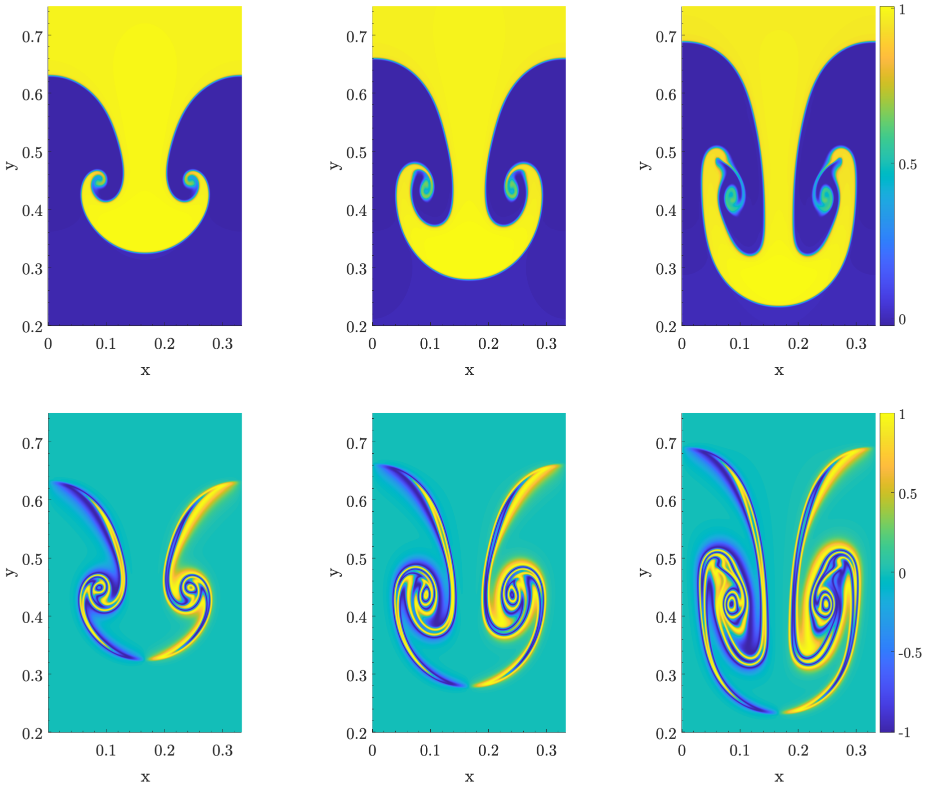

Fig. 4.29. Results for the multiphase Rayleigh-Taylor instability problem, at times $t = 6$, $t = 7$ and $t = 8$ (from left to right); the volume fraction α_1 (top) and the $A_{1,12}$ component of the distortion field for the first phase (bottom) are represented.

see that mesh convergence has already been achieved with the coarsest mesh, since the macroscopic structure of the flow does not depend on mesh size.

Fig. 4.29 shows the time evolution of both the volume fraction function α_1 and the $A_{1,12}$ component of the distortion field, for the first phase.

It is interesting to note that for a sufficiently low Mach number test, mixture density, depicted in Fig. 4.28 is macroscopically proportional to the volume fraction structure in Fig. 4.29. Moreover, due to velocity relaxation, both distortion fields encode the same flow structure, except that they satisfy two different algebraic constraints, so that each phase mass conservation equation is the consequence of the time evolution of each phase distortion field.

Our computational results, in particular the temporal evolution in Fig. 4.29, compare visually well with the reference solutions available in the literature, see [102], obtained in this case with ALE schemes on moving meshes.

4.2.9 Multi-phase and multi-material triple point problem

Finally, in this section, we will test all the capabilities of the model and the numerical scheme developed, i.e. the ability to describe several, up to three, interacting phases. The problem that will be addressed is a typical test of the ALE community, namely the so-called triple point problem. This test is a three state, two material, 2D Riemann problem in a rectangular domain that generates vorticity, which is why it is very popular in the ALE community for testing the ability of a code to handle the motion of a complex mesh. It was introduced in [103] and was used to compare ALE approaches in the case of a two-material Riemann problem in [17, 101, 102] or the simplified one-material case in [11, 15, 73]. In the Eluerian context, this problem has been addressed with an interface-capturing approach considering three immiscible compressible fluids in [179]. In the context of this thesis, the main aim of this problem is to verify the ability of the code and model to correctly propagate shock waves over multi-phase and multi-material regions.

Specifically, in this thesis, we follow the setting presented in [103], but with the significant modification that instead of initialising a two-material Riemann problem, we set up an initial problem involving three phases, where two of them have the same material parameters. The computational domain of the triple point problem $\Omega = [0; 7] \times [0; 3]$ is divided into three subdomains filled with three phases describing different perfect gases, thus yielding a three-phase, two-material problem. The initial condition, in our diffuse interface framework, can be easily set by means of jumps in volume fraction as follows. The first phase, with a state of high pressure and high density, is initialized as

$$\begin{aligned} &\alpha_1(x,y) = \begin{cases} 1-2\epsilon & \text{if } \ \boldsymbol{x} \in \Omega_1, \\ \epsilon & \text{if } \ \boldsymbol{x} \notin \Omega_1, \end{cases} \qquad \text{with} \qquad \Omega_1 = [0;1] \times [0;3] \\ &\rho_1 = 1.0, \quad \boldsymbol{v}_1 = \mathbf{0}, \quad p_1 = 1.0, \quad \mathbf{A}_1 = \mathbf{I}, \end{aligned} \tag{4.40}$$

the second phase, with a state of low pressure high density, as

$$\begin{aligned} &\alpha_2(x,y) = \begin{cases} 1-2\epsilon & \text{if } \ \boldsymbol{x} \in \Omega_2, \\ \epsilon & \text{if } \ \boldsymbol{x} \notin \Omega_2, \end{cases} \qquad \text{with} \qquad \Omega_2 = [1;7] \times [0;1.5] \\ &\rho_2 = 1.0, \quad \boldsymbol{v}_2 = \mathbf{0}, \quad p_2 = 0.1, \quad \mathbf{A}_2 = \mathbf{I}, \end{aligned} \tag{4.41}$$

and the third, with an initial low pressure and low density state, is initialized as

$$\begin{aligned} &\alpha_3(x,y) = \begin{cases} 1-2\epsilon & \text{if } \ \boldsymbol{x} \in \Omega_3, \\ \epsilon & \text{if } \ \boldsymbol{x} \notin \Omega_3, \end{cases} \qquad \text{with} \qquad \Omega_3 = [1;7] \times [1.5;3.0] \\ &\rho_3 = 0.125, \quad \boldsymbol{v}_3 = \mathbf{0}, \quad p_3 = 0.1, \quad \mathbf{A}_3 = \mathbf{I}. \end{aligned} \tag{4.42}$$

All the phases represent ideal inviscid gases, thus we are in the stiff limit of the model and the relaxation times are $\tau_1^e = \tau_2^e = \tau_3^e = 14^{-14}$. Furthermore, according to [103], since the first phase and the third phase represent the same material, the other parameters and physical quantities for these phases are $\gamma_1 = \gamma_3 = 1.5$, $\mathrm{Cv}_1 = \mathrm{Cv}_3 = 1$, $\mathrm{Cs}_1 = \mathrm{Cs}_3 = 1.0$. Finally, the other parameters and physical quantities for second phases, which represent a different perfect gas, are $\gamma_2 = 1.4$, $\mathrm{Cv}_2 = 1$, $\mathrm{Cs}_2 = 1.0$.

The simulation is carried out up to the final time $t_f = 5$ discretizing the computational domain with a uniform Cartesian mesh composed of 3584×1536 control volumes; reflective slip wall boundary conditions are set in all the directions.

In Fig. 4.30 and 4.31 we present the results obtained for the multi-phase and multi-material triple point problem at time $t = 3$ and $t = 5$, respectively. In particular, we illustrate the evolution of the different volume fractions (top), where the first phase is shown in blue, the second in yellow and the third in blue-green. These contour levels clearly show that the vortex shape is well resolved and a zoom is shown on the right to better visualise the vorticity formation resulting from the initial contact discontinuity. From these results, it is clear how suitable a modelling and numerical description via an Eulerian diffuse interface approach is for describing these mixing areas characterised by high vorticity.

From the representation of the density field, in Fig. 4.30 and 4.31, the entire dynamics of the problem can be well understood. The fluid flow after the initial discontinuity has broken is characterised by a rarefaction wave pointing to the left and two shock waves pointing to the right, separated by a horizontal contact discontinuity. Moreover, these two shock waves have different velocities, as the densities of the materials are different, and this leads to the formation of a strong vortex. Our computational results compare visually well with reference solutions available in the literature [73, 102, 103], proving the ability of the code and model to correctly propagate shock waves over multi-phase and multi-material regions, despite the results being obtained on a simple fixed Cartesian grid.

Additionally, in Fig. 4.30 and 4.31, we present the evolution of the $A_{1,12}$ component of the first phase distortion field. However, as emphasised in the previous test case, the distortion fields of all phases encode the same flow structure, except that they satisfy three different algebraic constraints (3.169), thus the representation in Fig. 4.30 and 4.31 is indicative of the flow structure of all phases. We note once again an extremely useful ability of the distortion field (encoded in its rotational component $\boldsymbol{R}_1$) to demonstrate the details of the flow structures hidden otherwise. Thus, thanks to this ability of the distortion field, it is possible to identify a strong shear zone along a contact discontinuity inside the second phase (the yellow one) that otherwise would not have been visible using the other state variables.

4.2.10 Water entry of a symmetric wedge

In all the previous test cases all three phases were formally considered, but some of them had identical material parameters. In this sense, the test addressed in this section is more general, and all three phases will be considered having

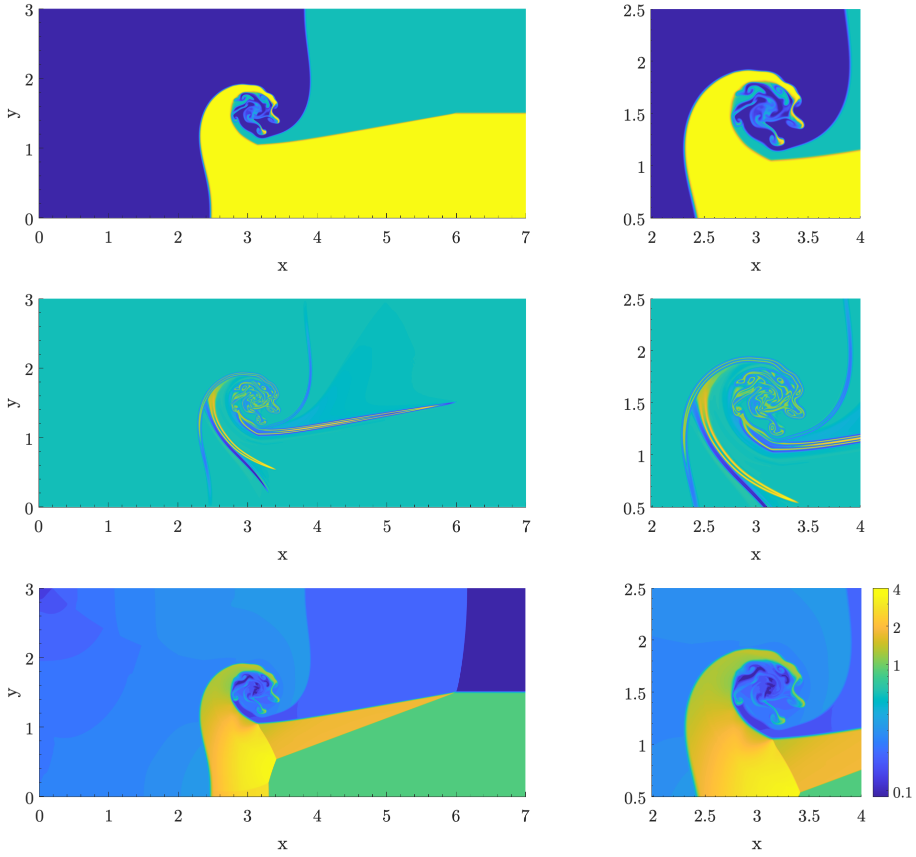

Fig. 4.30. Results for the multi-phase and multi-material triple point problem at time $t = 3$: the contour plots of the volume fractions (first phase in blue, second phase in yellow and the third one in blue-green) (top), the $A_{1,12}$ component of the distortion field for the first phase (center) and the mixture density (bottom). A zoom in the region $[2.0, 4.0] \times [0.5, 2.5]$, which illustrates the formation of vorticity resulting from the initial contact discontinuity, is shown (right).

very different material parameters. Namely, we consider one solid, one liquid and one gaseous phase.

The aim of this numerical test is to reproduce, as fully as possible, the experiment conducted by Zhao *et al.* [180], which we have already considered in the validation of the semi-implicit numerical method in Section 4.1.9 and which consists of the impact of a symmetrical wedge with a free surface. Unlike the previous work, using the explicit FV scheme developed in this paper for the compressible multiphase fluid and solid mechanics, we have a possibility to reproduce the experimental setup [180] in its completeness. Namely, by

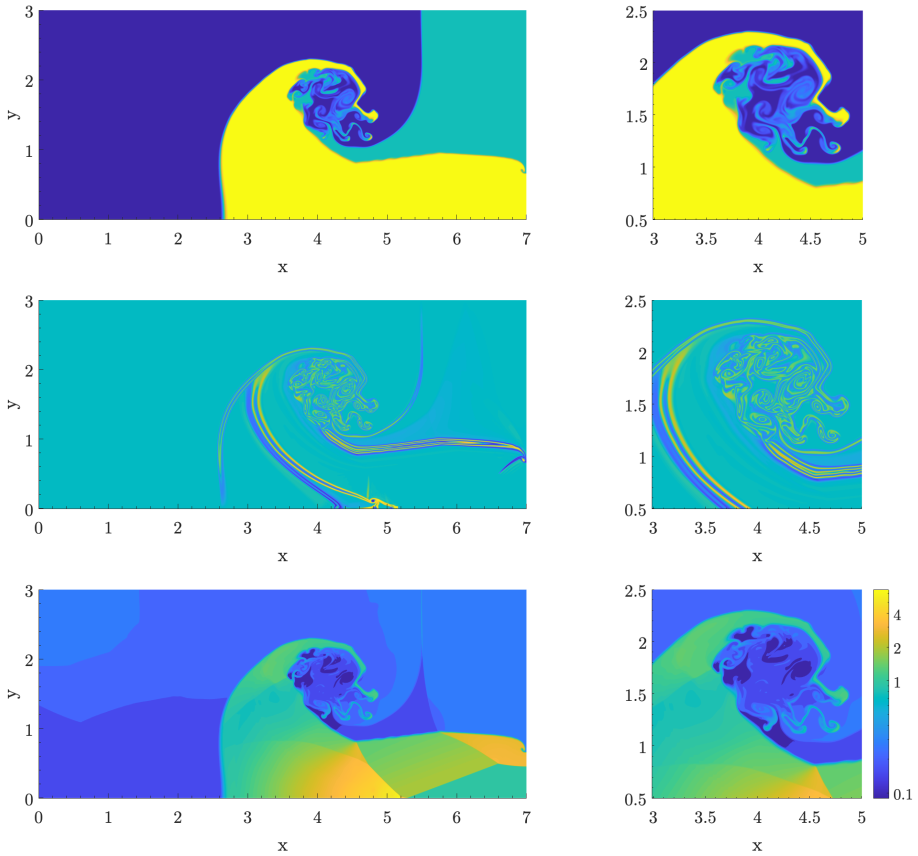

Fig. 4.31. Results for the multi-phase and multi-material triple point problem at time $t = 5$: the contour levels of the volume fractions (first phase in blue, second phase in yellow and the third one in blue-green) (top), the $A_{1,12}$ component of the distortion field for the first phase (center) and the mixture density (bottom). A zoom in the region $[3.0, 5.0] \times [0.5, 2.5]$, which illustrates the formation of vorticity resulting from the initial contact discontinuity, is shown (right).

imposing only the initial velocity of the solid wedge, we can now evaluate the complete dynamics of the three phases resulting from their interaction. Therefore, the vertical velocity of the wedge recorded experimentally by Zhao et al. [180] and reported in Fig. 4.32, which was *prescribed* in the previous work [70] and in the numerical test by Oger et al. [123], now becomes an excellent indicator to judge about the validity of the multiphase simulation presented here.

In this numerical experiment, we follow the geometric setup used previously in Section 4.1.9, which traces the setup of the laboratory measurements carried out by Zhao *et al.* [180], but with the significant modification of defining an initial problem involving three phases. The computational domain $\Omega = [-0.5; 0.5] \times [-0.5; 0.5]$ is divided into three subdomains occupied with three phases describing an ideal elastic solid, a viscous liquid phase and a viscous gaseous phase. The initial condition for each phases are set by means of jumps in volume fraction. The first phase, the solid one, is defined according to the the geometry of the experimental section, which consider the wedge with a dead-rise angle of 30° illustrated in Fig. 4.17; specifically the initial conditions for this phase are set

$$\alpha_1(x,y) = \begin{cases} 1-2\epsilon & \text{if} \quad |x| \le 0.25 \ \wedge \ y \ge |x\tan(\frac{\pi}{6})| \ \wedge \ y \le 0.25\tan(\frac{\pi}{6}), \\ \epsilon & \text{if} \quad \text{otherwise}, \end{cases}$$
$$\rho_1 = 7{\times}10^3, \quad \boldsymbol{v}_1 = (0,-6.15), \quad p_1 = 10^3, \quad \mathbf{A}_1 = \mathbf{I}, \tag{4.43}$$

where the density is evaluated to obtain the total weight of the measuring section used in the experiment by Zhao et al. [180], which corresponds to 255.5 *kg*; thus the density is calculated as the weight of the instrumental tools divided by the effective area described by the wedge in this numerical setup. The initial condition for the second phase, defining the viscous liquid phase, are

$$\alpha_2(x,y) = \begin{cases} 1-2\epsilon & \text{if} \quad \boldsymbol{x} \in \Omega_2, \\ \epsilon & \text{if} \quad \boldsymbol{x} \notin \Omega_2, \end{cases} \quad \text{with} \quad \Omega_2 = [-0.5; 0.5]{\times}[-0.5; 0.0]$$
$$\rho_2 = 10^3, \quad \boldsymbol{v}_2 = \mathbf{0}, \quad p_2 = 10^3, \quad \mathbf{A}_2 = \mathbf{I}, \tag{4.44}$$

while the third one, defining the gaseous phase, is initialized as

$$\alpha_3 = 1 - \alpha_1 - \alpha_2, \quad \rho_3 = 1, \quad \boldsymbol{v}_3 = \mathbf{0}, \quad p_3 = 10^3, \quad \mathbf{A}_3 = \mathbf{I}. \tag{4.45}$$

For the solid and liquid phase, the stiffened gas EOS is used; the other material parameters are $\gamma_1 = \gamma_2 = 1.4$, $\mathrm{Cv}_1 = \mathrm{Cv}_2 = 1$, $\mathrm{Cs}_1 = 120$, $\mathrm{Cs}_2 = 100$, $\mathrm{Co}_1 = \mathrm{Co}_2 = 120$ and $p_{o1} = p_{o2} = p_1$. For the viscous gas, the ideal gas EOS is used with the following parameters $\gamma_3 = 1.4$, $\mathrm{Cv}_3 = 1$, $\mathrm{Cs}_3 = 60.0$ and $\nu_3 = 10^{-1}$. To consider an ideal elastic material, the relaxation time for the first phase is chosen to be $\tau_1^{\mathrm{e}} = 10^{14}$, while a kinematic viscosity $\nu_1 = 10^{-6}$ is adopted for the viscous liquid phase.

Two simulations are carried out up to the final time $t_f = 0.025$ on two different uniform Cartesian meshes composed of 1024 × 1024 and 2048 × 2048 control volumes, in order to verify qualitatively the mesh convergence of the solution. In these simulations, reflective slip wall boundary conditions are set in all the directions.

Fig. 4.32 (left) shows the distribution of the different volume fractions in accordance with the initial conditions describing the geometric and experimental setup of the test water entry of a symmetric wedge. The solid phase is shown in yellow, the liquid phase in blue-green and the gas phase in blue. Moreover, in Fig. 4.32 (right) we present a comparison that verifies the validity of the results obtained. In this comparison, the vertical velocity of the wedge experimentally recorded by Zhao et al. [180] is compared with the purely elastic solid body velocity computed in this test by evaluating an averaged vertical velocity using the volume fraction, in accordance with the following definition

$$|\boldsymbol{v}_{1,2}| = \frac{|\sum_{ij}^{N_1 N_2} \alpha_{1,ij} v_{1,2}|}{\sum_{ij}^{N_1 N_2} \alpha_{ij}}, \tag{4.46}$$

N_1 and N_2 are the discrete elements in the first and in the second directions, respectively. It is possible to observe how qualitatively the dynamics of the impact is well represented, in particular the deceleration over time follows the correct trend, i.e. deceleration increases in modulus until about half the simulation time and then tends to decrease. Furthermore, both the results obtained with a 1024 × 1024 mesh and that obtained by doubling the mesh resolution are represented, and it can be seen that the numerical solution is getting closer to that recorded experimentally by Zhao et al. [180] as mesh is getting more finer. The main reason for the discrepancy from the experimental result has to be found in the low Mach nature of the test. Indeed, this impact, in which the solid must maintain a particularly rigid behaviour, represents a complex test for an explicit numerical scheme. Moreover, it should be noted that this is the first time this test has been solved by considering the interaction of three phases through a monolithic mathematical model for compressible multiphase fluid and solid mechanics.

In Fig. 4.33 the temporal evolution of volume fractions obtained with the explicit FV scheme for compressible multiphase fluid and solid mechanics is represented in the left-hand column. For the sake of comparison, the results previously obtained in Section 4.1.9 for the validation of the semi-implicit

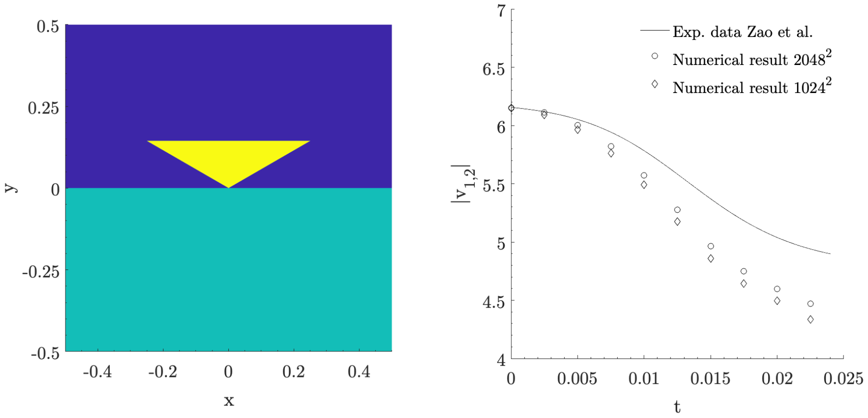

Fig. 4.32. Filled contour map of the different volume fractions of the constituents to represent the initial test condition (left). Comparison with the reference vertical wedge fall velocity experimentally recorded by Zhao *et al.* [180] of the average components of the vertical velocity of the solid wedge $v_{1,2}$ evaluated with the explicit FV scheme for the complete compressible multiphase fluid and solid mechanics on two different uniform Cartesian meshes (right).

numerical method are shown too, in the right-hand column. From the top to the bottom the results for three different instants are shown, namely for $t = 0.005$, $t = 0.015$ and $t = 0.020$. Again, it can be observed that the phenomenological evolution of the free surface during the entry of water into a wedge, obtained with the new numerical method that solves the entire three-phase dynamics, is in agreement with what was previously obtained in Section 4.1.9. The first time instant shows quite well the formation of two jets escaping along the edges of the wedge. At time $t = 0.015$ these two jets reach the point of separation, which corresponds to the end of the edge. It can be seen that the jet leaves the edge almost tangentially at this initial phase of flow separation. Then, at $t = 0.020$ the jets tend to develop more vertically as well as breaking. This shape is qualitatively similar to the experimental illustration in the article by Zhao *et al.* [180].

Furthermore, Fig. 4.33 shows the velocity fields obtained with both numerical methods. One can see that the gas phase was not considered in [70] presented in the left column, while the dynamics of all three phases is taken into account in this paper. The interraction of the liquid jets and the gas phase might in particular be responsible for the slight differences in jets shape between the two simulations.

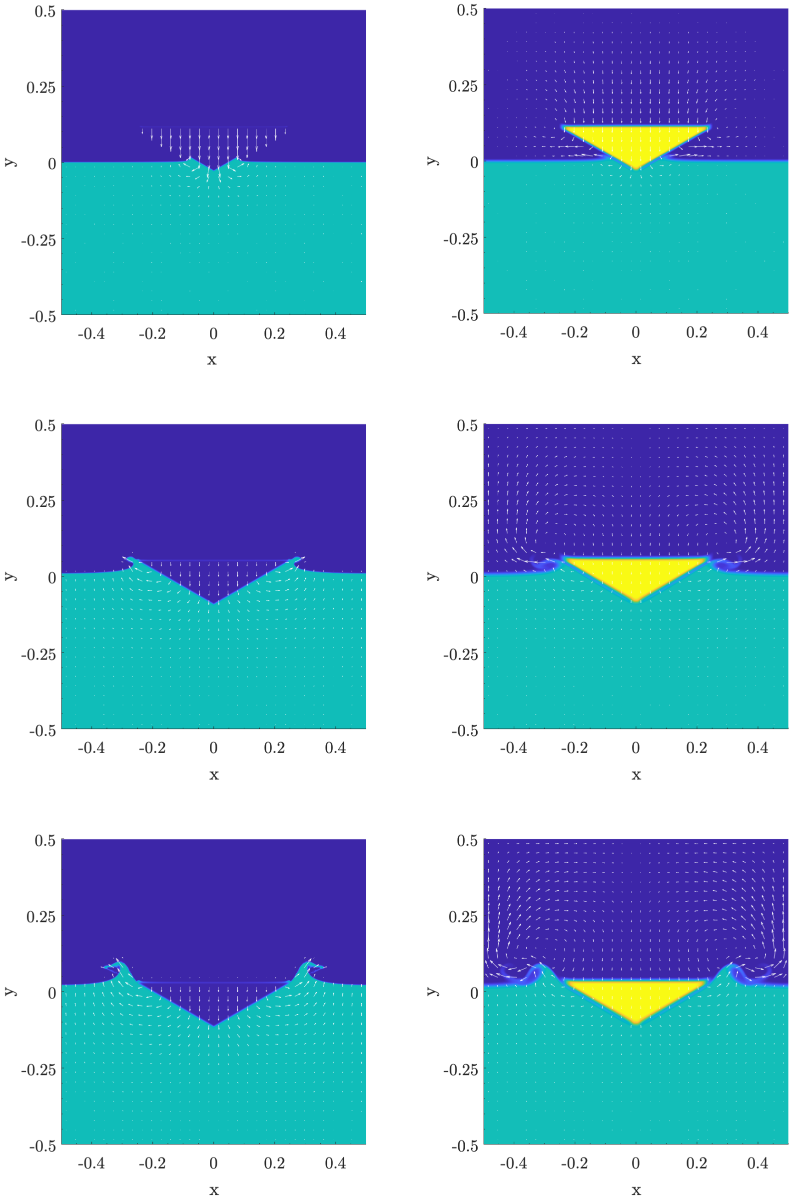

Fig. 4.33. Filled contour map of the different volume fractions of the constituents and velocity field of the mixture, the solid phase is shown in yellow, the liquid phase in blue-green and the gas phase in blue. Results obtained with the explicit FV scheme for compressible multiphase fluid and solid mechanics (right), with the semi-implicit numerical method in Section 4.1.9, [70] (left). From the top to the bottom results for three different instants are shown, namely for $t = 0.005$, $t = 0.015$ and $t = 0.020$.

4.2.11 Multi-phase and multi-material solid impact

This is the last test presented in this thesis, the aim of which is to show from a qualitative point of view the wide applicability of the model and numerical scheme presented. As in the previous test, all the capabilities of the developed model and numerical scheme are tested in the problem that will be tackled, namely the dynamics of three phases with different material properties. To this end, an impact of true multi-material *three-phases* will be simulated, which exhibits elastic and also elasto-plastic behaviour in a inviscid fluid environment.

In this test, we roughly follow the approach presented in [16, 41], which has been modified by not paying particular attention to physical material characteristics, as the interest is in qualitatively verifying the method's ability to solve such a complex test. Thus, while maintaining a geometry similar to the tests in the literature, the parameters and physical quantities that define the properties of the aluminium bar in Section 4.2.7 are used. Therefore, this test case is relative to an aluminium ball moving toward a aluminium plate on the east boundary and the surrounding fluid is a perfect gas. The computational domain $\Omega = [-0.5; 0.5] \times [-0.5; 0.5]$ is divided into three subdomains filled with three phases describing two solids with the same properties and a perfect gas. As for the previous test, the initial conditions are set by means of jumps in volume fraction; the first phase, that defines the aluminium ball, is initialized as

$$\begin{aligned} &\alpha_1(x,y) = \begin{cases} 1-2\epsilon & \text{if} \quad ((-0.125-x)^2+(0.5-y)^2)^{0.5} \leq 0.075, \\ \epsilon & \text{if} \quad \text{otherwise}, \end{cases} \\ &\rho_1 = 2.785, \quad \boldsymbol{v}_1 = (0.002, 0), \quad p_1 = 10^{-6}, \quad \mathbf{A}_1 = \mathbf{I}, \end{aligned} \tag{4.47}$$

the second phase, defining the aluminium plate, as

$$\begin{aligned} &\alpha_2(x,y) = \begin{cases} 1-2\epsilon & \text{if} \quad \boldsymbol{x} \in \Omega_2, \\ \epsilon & \text{if} \quad \boldsymbol{x} \notin \Omega_2, \end{cases} \quad \text{with} \quad \Omega_2 = [0.05; 0.225] \times [-0.35; 0.35] \\ &\rho_2 = 2.785, \quad \boldsymbol{v}_2 = \mathbf{0}, \quad p_2 = 10^{-6}, \quad \mathbf{A}_2 = \mathbf{I}, \end{aligned} \tag{4.48}$$

and the third, defining the surrounding perfect gas, is initialised as

$$\alpha_3 = 1-\alpha_1-\alpha_2, \quad \rho_3 = 10^{-3}, \quad \boldsymbol{v}_3 = \mathbf{0}, \quad p_3 = 10^{-6}, \quad \mathbf{A}_3 = \mathbf{I}. \tag{4.49}$$

Since the first and second phases represent the same material, i.e. aluminium, the other parameters and physical quantities that define the properties of such a material using the stiffened gas EOS are $\gamma_1 = \gamma_2 = 1.4$, $\mathrm{Cv}_1 = \mathrm{Cv}_2 = 1000$,

$\mathrm{Cs}_1 = \mathrm{Cs}_2 = 0.305$, $\mathrm{Co}_1 = \mathrm{Co}_2 = 0.533$ and $p_{\mathrm{o}1} = p_{\mathrm{o}2} = p_1$. For the inviscid gas phase surrounding the solid phases, the ideal gas EOS is used and the physical parameters are $\gamma_3 = 1.2$, $\mathrm{Cv}_3 = 1000$, $\mathrm{Cs}_3 = 0.0$ and $\tau_3^{\mathrm{e}} = 10^{-14}$. In a first simulation, the solid materials are assumed to have purely elastic behaviour, so the relaxation time is assumed to be $\tau_1^{\mathrm{e}} = \tau_2^{\mathrm{e}} = 10^{14}$ for both phases. Subsequently, to obtain a non-linear elasto-plastic behaviour of the material, the relaxation time $\tau_1^{\mathrm{e}}, \tau_2^{\mathrm{e}}$ is chosen as a non-linear function of an invariant of the shear stress tensor as done in the previous test, see (4.34). In this case, however, the yield stress of the material is set to a lower number, i.e. $\sigma_{\mathrm{o}} = 2.5 \times 10^{-4}$, for the sake of making the plastic deformations more visible.

Two simulations are carried out up to the final time $t_f = 200$ discretizing the computational domain with a uniform Cartesian mesh composed of 2048×2048 control volumes; periodic boundary conditions are set in all the directions.

Fig. 4.35 shows the volume fraction of the first and second phase at times $t = 60$, $t = 100$ and $t = 140$ from left to right, respectively. The first time instant represents the moment of impact with the plate. As one can see from the subsequent instants the behavior of an elastic collision is qualitatively well represented by the numerical solution. It should be emphasized that, in a diffuse interface approach, and if both the solid objects are represented by the same volume fraction function, it is not obvious that the two solids would bounce instead of sticking to each other. The results for multibody problems in which the solids are carrying their own volume fractions is, therefore, of considerable interest. Additionally, Fig. 4.34 shows the A_{12} component of the

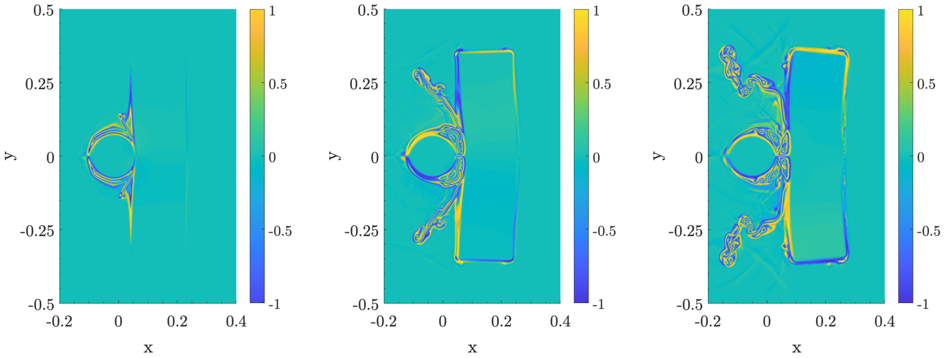

Fig. 4.34. Results for the multi-phase and multi-material elasto-plastic solid impact, the contour levels of one component of the distortion field $\mathbf{A}$ of the mixture, namely of the A_{12} component, at times $t = 60$, $t = 100$ and $t = 140$ (from left to right), respectively.

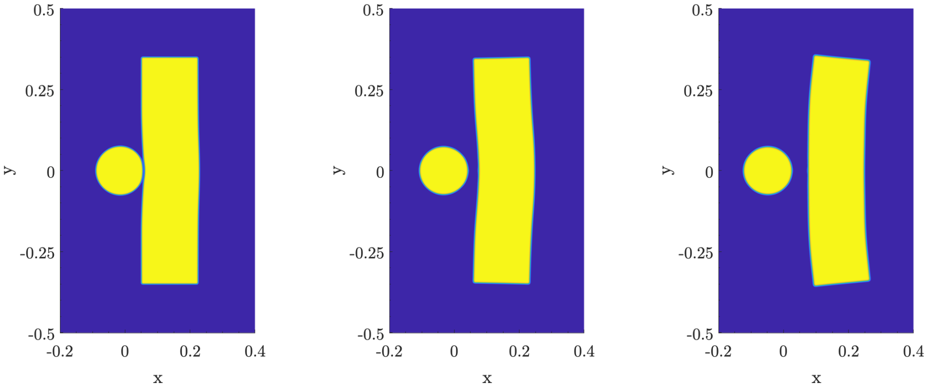

Fig. 4.35. Results for the multi-phase and multi-material elastic solid impact, the contour levels of the volume fractions of the first and the second phases at times $t = 60$, $t = 100$ and $t = 140$ (from left to right).

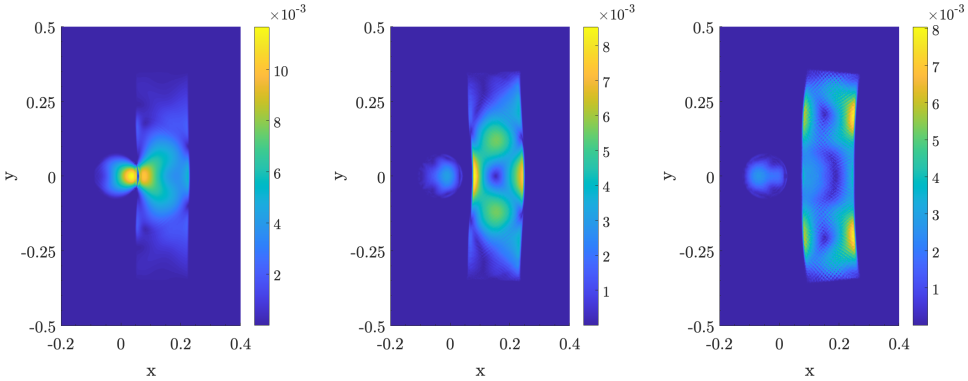

Fig. 4.36. Results for the multi-phase and multi-material elastic solid impact, the contour levels of the von Mises stresses of the first $\bar{\sigma}_1$ and the second $\bar{\sigma}_2$ phases are represented, at times $t = 60$, $t = 100$ and $t = 140$ (from left to right), respectively.

mixture distortion field, obtained through the following relation

$$A_{12} = \alpha_1 A_{1,12} + \alpha_2 A_{2,12} + \alpha_3 A_{3,12}. \tag{4.50}$$

This allows the dynamics of the gas phase to be clearly shown as well, making it evident that the dynamics of all three phases have been resolved through a distortion field for each phase. It is possible to see the two fluid jets with non-trivial vorticity being generated at the moment of impact.

Similarly, Fig. 4.37 shows a collision of the same solid objects but withe plasticity effect taken into account. The obtained results visually compare

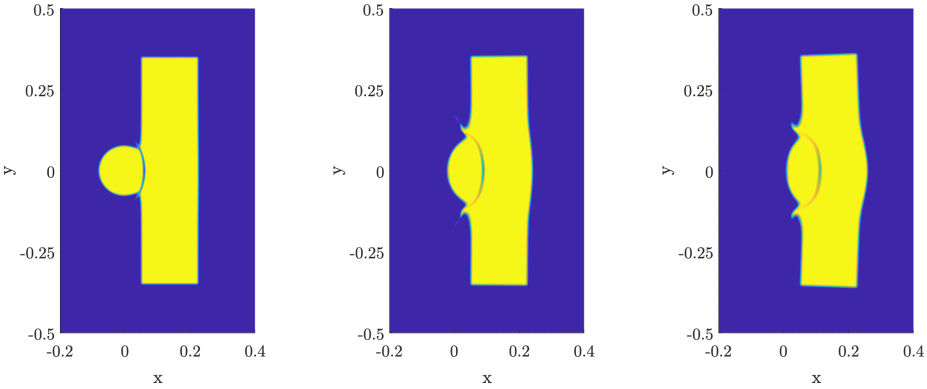

Fig. 4.37. Results for the multi-phase and multi-material elasto-plastic solid impact, the contour levels of the volume fractions of the first and the second phases at times $t = 60$, $t = 100$ and $t = 140$ (from left to right).

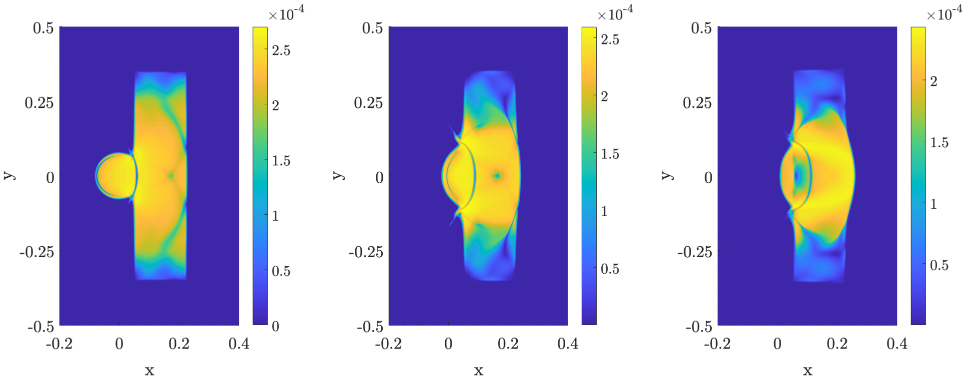

Fig. 4.38. Results for the multi-phase and multi-material elasto-plastic solid impact, the contour levels of the von Mises stresses of the first $\bar{\sigma}_1$ and the second $\bar{\sigma}_2$ phases are represented, at times $t = 60$, $t = 100$ and $t = 140$ (from left to right), respectively.

well with the one in [16]. To better understand how the different definitions of material properties in these two tests affect the behavior of solids, it is useful to observe the von Mises stress of the first phase $\bar{\sigma}_1$ and the second phase $\bar{\sigma}_2$, evaluated as in (4.35), and presented in Fig. 4.36 and 4.38. It can be seen that the stress in an ideal elastic material propagates through the body by means of waves, which are reflected over time from the body boundaries. On the contrary, in the case of an elasto-plastic material, it can be observed that the stress reaches a lower magnitude than in the ideal elastic case, due to the stress

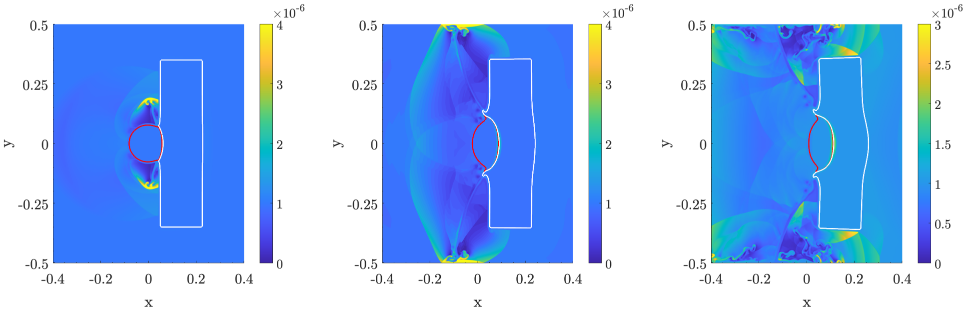

Fig. 4.39. Results for the multiphase and multi-material elastic-plastic solid impact. The contour levels of the the gas pressure p_3 and the contours of the solids presented at times $t = 60$, $t = 100$, and $t = 140$ (from left to right).

relaxation process in the inelastic deformations. Furthermore, it is evident that over time, the highest stress values are localised in the area undergoing plastic deformations, while the regions far from the impact, in this case, are less stressed.

Finally, to emphasize the multimaterial character of the test, Fig. 4.39 shows the gas pressure p_3 and the contours of the solid objects. One can see quite complicated flow structures consisting of multiple shock waves interracting with the boundaries of the solid bodies and with each other.

5 Conclusions and outlook

In one part of this thesis we have formulated a novel staggered, semi-implicit, finite-volume method for the solution of a simplified BN model for two-phase free-surface flows, derived starting from the works of Casulli *et al.* [29, 51], the results of which are published in [69, 70]. This method is the basis of a highly efficient Fortran MPI-parallel code that in terms of applicability is a step forward for the study of real-world problems related to complex non-hydrostatic free-surface flows interacting with solid moving obstacles.

However, the main work developed in this dissertation aims at the development and numerical solution of a set of hyperbolic partial differential equations capable of describing a generic multi-phase and multi-material continuum in a unified manner via a diffuse interface approach, after highlighting the problems inherent in the traditional formulation of multiphase flows through an excursus in the complex literature inherent in this topic. Thus, it can be said that this work presents novelties in both the theoretical aspects of modelling multiphase flows and the design of numerical algorithms for solving such models.

A reformulation of the multiphase SHTC model originally proposed by [143] is presented. In this reformulation of SHTC mixture theory, the unified continuum mechanics model introduced in [131], is included from the beginning, deriving the complete model as a whole from variational principles. Thus, a simplified, nonconservative reformulation of the model was derived and solved numerically by addressing the various challenges that this mathematical model poses from the numerical analysis standpoint. Finally, through an extensive collection of numerical experiments, the numerical method is validated, but more importantly, the very wide range of applicability of the derived theory and the numerical method developed to deal with it is shown.

Future work will cover further developments that can be made to the multiphase theory of fluid mechanics and compressible solids developed in this thesis, from both a modeling and numerical point of view, below we briefly introduce some of the research directions that will be sought.

Explicit structure-preserving numerical method. The original multi-phase unified model of continuum mechanics derived, as a whole, from variational principles in this thesis is an excellent starting point for future work. In fact, a simplified non-conservative reformulation of the model has been solved numerically in this thesis work. It lacks the energy conservation, thus, numerically addressing the complete multi-phase SHTC model, without making use of the BN-type reformulation, is now the natural next step. The complete multiphase and multi-material SHTC model derived in Section 2.2 is based on phase entropy inequalities as primary evolution equations, while the energy conservation law for the mixture is obtained as a consequence by a linear combination of the governing equations. Furthermore, dissipative processes, i.e. relaxation source terms, are defined in such a way as to satisfy the first and second laws of thermodynamics, i.e. entropy production and energy conservation. For the numerical scheme to be Hyperbolic Thermodynamically Compatible (HTC), it must fulfil these compatibility conditions at the discrete level. In this direction, recently, significant progress has been made in solving the entropy inequality instead of energy conservation, using so-called HTC schemes. Single-phase flow was considered in [1], while, for the first time, a full non-barotropic SHTC model of compressible two-fluid flow with *more than one entropy inequality* was numerically solved in [168]. Therefore, the development of a new thermodynamically compatible finite volume scheme based on this work to solve the complete model presented in this thesis will be of central importance in work in the near future.

Extension to additional physical processes The multiphase SHTC model presented in 2.2 can be further extended to include phenomena such as phase change and surface tension. Indeed, chemical kinetics phenomena, i.e. phase exchange, have already been considered in the SHTC mixture equations that has been presented. In fact, within the SHTC theory, the phenomenon of phase transformation can be mathematically described through dissipative processes proportional to a gradient of total potential energy. Specifically, it is necessary to introduce a source contribution into the true mass density equations. On the other hand, more attention should be paid to the further development of the unified first-order hyperbolic formulation for continuum mechanics in order to account for surface tension. In particular it will be preferable to include a first-order hyperbolic model for surface tension for reasons of consistency with the complete model and for several numerically interesting features that can be retrieved. An interesting strategy for modelling interface dynamics, presented in Schmidmayer *et al.* [155], is achieved by introducing a Galilean invariant evolution equation for a new interface vector field $\mathbf{b}$, representing the gradient of a colour function c. In this way, the governing equations can be written as a system of first-order PDEs, completely avoiding the calculation of local curvature values and interface normal vectors by including the geometric concept of interface at the PDE level. Thus, the surface tension tensor can be calculated directly from the state variables as a nonlinear algebraic function; the work done by Chiocchetti *et al.* in [34] is of considerable importance in this direction.

Extension of the structure-preserving properties of the scheme At this point, one will have a unified first-order hyperbolic multiphase model of continuum mechanics capable of capturing a wide range of physical phenomena, consistent with the first and second laws of thermodynamics, grounded on geometric principles and furthermore admitting a variational formulation [132]. The geometric origin, which gives such a general character to the unified model of continuum mechanics, can be identified in the involution constraints that arise in some of the governing equations. For instance, the last geometric concept introduced, is the interface vector field $\mathbf{b}$. Since it has been defined as a gradient of a scalar function, it must satisfy a curl-type involution constraint and from a numerical point of view, as pointed out in [36], the physical consistency of the numerical solution is completely lost if this involution constraint is violated. In the multiphase SHTC system considered so far, there are further involution constraints, specifically a curl involution on the relative velocity and a set of curls of the distortion matrix vectors. Consequently, the development of special structure-preserving numerical schemes will be crucial. For instance, to satisfy these geometric constraints, I can adopt special staggered discretizations, which guarantee curl-free condition at the discrete level, e.g. [14, 45] or suitable Generalized Lagrangian Multiplier (GLM) curl cleaning strategies, which are an extension to curl involutions of the successful GLM approach of Munz *et al.* [42, 115].

Efficient semi-implicit numerical scheme In many environmental or industrial applications, there is no interest in resolving acoustic waves, but rather the focus is on slow dynamics, such as related to convection transport phenomena. In these applications, the velocity of the flow is significantly slower than the sound speeds, and this difference in scale imposes a severe time-step stability restriction on explicit schemes, which enforce an all-wave resolution. This is the case for flows in the so-called low Mach number regime, i.e. weakly compressible regimes. Therefore, in order to obtain an accurate description of the slow waves only, the development of semi-implicit schemes will be important. In this perspective, a close collaboration with Dr. A. Thomann could lead to promising new results on incompressible limit systems and the development of asymptotic-preserving schemes.

List of Figures

List of Tables

References

[1] R. Abgrall, S. Busto, and M. Dumbser. A simple and general framework for the construction of thermodynamically compatible schemes for computational fluid and solid mechanics. *Applied Mathematics and Computation*, 440, 127629, 2023.

[2] N. Andrianov and G. Warnecke. The Riemann problem for the Baer-Nunziato two-phase flow model. *Journal of Computational Physics*, 212, 434–464, 2004.

[3] M. R. Baer and J. W. Nunziato. A two-phase mixture theory for the deflagration-to-detonation transition (DDT) in reactive granular materials. *International Journal of Multiphase Flow*, 12, 861–889, 1986.

[4] D. S. Balsara and C.-W. Shu. Monotonicity Preserving Weighted Essentially Non-oscillatory Schemes with Increasingly High Order of Accuracy. *Journal of Computational Physics*, 160, 405–452, 2000.

[5] P. Barton. An interface-capturing Godunov method for the simulation of compressible solid-fluid problems. *Journal of Computational Physics*, 390, 25–50, 2019.

[6] P. Barton, D. Drikakis, and E. Romenski. An Eulerian finite-volume scheme for large elastoplastic deformations in solids. *International Journal for Numerical Methods in Engineering*, 81(4), 453–484, 2010.

[7] J. B. Bdzil, R. Menikoff, S. F. Son, A. K. Kapila, and D. S. Stewart. Two-phase modeling of deflagration-to-detonation transition in granular materials: A critical examination of modeling issues. *Physics of Fluids*, 11, 378–402, 1999.

[8] J. Bell, P. Colella, and H. Glaz. A Second–Order Projection Method for the Incompressible Navier–Stokes Equations. *Journal of Computational Physics*, 85, 257–283, 1989.

[9] A. Bermúdez, S. Busto, M. Dumbser, J. Ferrín, L. Saavedra, and M. Vázquez-Cendón. A staggered semi-implicit hybrid FV/FE projection method for weakly compressible flows. *Journal of Computational Physics*, 421, 109743, 2020.

[10] H. Blasius. Grenzschichten in Flüssigkeiten mit kleiner Reibung. *Z. Math. Physik*, 56, 1–37, 1908.

[11] W. Bo and M. Shashkov. Adaptive reconnection-based arbitrary Lagrangian Eulerian method. *Journal of Computational Physics*, 299, 902–939, 2015.

[12] W. Boscheri, S. Chiocchetti, and I. Peshkov. A cell-centered implicit-explicit Lagrangian scheme for a unified model of nonlinear continuum mechanics on unstructured meshes. *Journal of Computational Physics*, 451, 110852, 2022.

[13] W. Boscheri, M. Dumbser, and R. Loubère. Cell centered direct Arbitrary-Lagrangian-Eulerian ADER-WENO finite volume schemes for nonlinear hyperelasticity. *Computers and Fluids*, 134–135, 111–129, 2016.

[14] W. Boscheri, M. Dumbser, M. Ioriatti, I. Peshkov, and E. Romenski. A structure-preserving staggered semi-implicit finite volume scheme for continuum mechanics. *Journal of Computational Physics*, 424, 109866, 2021.

[15] W. Boscheri, R. Loubère, and M. Dumbser. Direct Arbitrary-Lagrangian–Eulerian ADER-MOOD finite volume schemes for multidimensional hyperbolic conservation laws. *Journal of Computational Physics*, 292, 56–87, 2015.

[16] A. de Brauer, A. Iollo, and T. Milcent. A Cartesian Scheme for Compressible Multimaterial Hyperelastic Models with Plasticity. *Communications in Computational Physics*, 22, 1362–1384, 2017.

[17] J. Breil, T. Harribey, P. Maire, and M. Shashkov. A multi-material ReALE method with MOF interface reconstruction. *Computers & Fluids*, 83, 115–125, 2013.

[18] L. Brugnano and V. Casulli. Iterative solution of piecewise linear systems. *SIAM Journal on Scientific Computing*, 30, 463–472, 2007.

[19] L. Brugnano and V. Casulli. Iterative solution of piecewise linear systems and applications to flows in porous media. *SIAM Journal on Scientific Computing*, 31, 1858–1873, 2009.

[20] D. E. Burton, N. R. Morgan, T. C. Carney, and M. A. Kenamond. Reduction of dissipation in Lagrange cell-centered hydrodynamics (CCH) through corner gradient reconstruction (CGR). *Journal of Computational Physics*, 299, 229–280, 2015.

[21] S. Busto, M. Dumbser, and L. Río-Martín. An Arbitrary-Lagrangian-Eulerian hybrid finite volume/finite element method on moving unstructured meshes for the Navier-Stokes equations. *Applied Mathematics and Computation*, 437, 127539, 2023.

[22] S. Busto, M. Dumbser, and L. Río-Martín. Staggered semi-implicit hybrid finite volume/finite element schemes for turbulent and non-Newtonian flows. *Mathematics*, 9, 2972, 2021.

[23] S Busto, J. Ferrín, E. F. Toro, and M. E. Vázquez-Cendón. A projection hybrid high order finite volume/finite element method for incompressible turbulent flows. *Journal of Computational Physics*, 353, 169–192, 2018.

[24] S. Busto, L. Río-Martín, M. Vázquez-Cendón, and M. Dumbser. A semi-implicit hybrid finite volume/finite element scheme for all Mach number flows on staggered unstructured meshes. *Appl. Math. Comput.*, 402, 126117, 2021.

[25] S. Busto, M. Dumbser, I. Peshkov, and E. Romenski. On Thermodynamically Compatible Finite Volume Schemes for Continuum Mechanics. *SIAM Journal on Scientific Computing*, 44, A1723–A1751, 2022.

[26] S. Busto, S. Chiocchetti, M. Dumbser, E. Gaburro, and I. Peshkov. High Order ADER Schemes for Continuum Mechanics. *Frontiers in Physics*, 8, 2020.

[27] M. Castro, J. M. Gallardo, and C. Parés. High Order Finite Volume Schemes Based on Reconstruction of States for Solving Hyperbolic Systems with Nonconservative Products. Applications to Shallow-Water Systems. *Mathematics of Computation*, 75, 1103–1134, 2006.

[28] V. Casulli. A semi-implicit finite difference method for non-hydrostatic free-surface flows. *International Journal for Numerical Methods in Fluids*, 30, 425–440, 1999.

[29] V. Casulli. A semi–implicit numerical method for the free–surface Navier–Stokes equations. *International Journal for Numerical Methods in Fluids*, 74, 605–622, 2014.

[30] V. Casulli and R. Cheng. Semi-implicit finite difference methods for three-dimensional shallow water flow. *International Journal of Numerical Methods in Fluids*, 15, 629–648, 1992.

[31] V. Casulli and G. S. Stelling. Semi-implicit subgrid modelling of three-dimensional free-surface flows. *International Journal for Numerical Methods in Fluids*, 67, 441–449, 2011.

[32] V. Casulli and P. Zanolli. A nested Newton–type algorithm for finite volume methods solving Richards' equation in mixed form. *SIAM Journal on Scientific Computing*, 32, 2255–2273, 2009.

[33] V. Casulli and P. Zanolli. Iterative solutions of mildly nonlinear systems. *Journal of Computational and Applied Mathematics*, 236, 3937–3947, 2012.

[34] S. Chiocchetti and M. Dumbser. An Exactly Curl-Free Staggered Semi-Implicit Finite Volume Scheme for a First Order Hyperbolic Model of Viscous Two-Phase Flows with Surface Tension. *Journal of Scientific Computing*, 94, 24, 2023.

[35] S. Chiocchetti and C. Mueller. In: A Solver for Stiff Finite-Rate Relaxation in Baer–Nunziato Two-Phase Flow Models. 31–44. Mar. 2020.

[36] S. Chiocchetti, I. Peshkov, S. Gavrilyuk, and M. Dumbser. High order ADER schemes and GLM curl cleaning for a first order hyperbolic formulation of compressible flow with surface tension. *Journal of Computational Physics*, 2020.

[37] A. J. Chorin. Numerical solution of the Navier–Stokes equations. *Math. Comp.*, 22, 745–762, 1968.

[38] B. D. Coleman and W. Noll. The thermodynamics of elastic materials with heat conduction and viscosity. *Archive for Rational Mechanics and Analysis*, 13, 167–178, 1963.

[39] R. Courant, K. Friedrichs, and H. Lewy. Über die partiellen Differenzgleichungen der mathematische Physik. *Mathematische Annalen*, 100, 32–74, 1928.

[40] C. Crowe, M. Sommerfeld, and Y. Tsuji. *Multiphase Flows with Droplets and Particles.* Boca Raton: CRC Press, 1998.

[41] A. de Brauer, A. Iollo, and T. Milcent. A Cartesian scheme for compressible multimaterial models in 3D. *Journal of Computational Physics*, 313, 121–143, 2016.

[42] A. Dedner, F. Kemm, D. Kröner, C. Munz, T. Schnitzer, and M. Wesenberg. Hyperbolic Divergence Cleaning for the MHD Equations. *Journal of Computational Physics*, 175, 645–673, 2002.

[43] V. Deledicque and M. Papalexandris. An exact Riemann solver for compressible two-phase flow models containing non-conservative products. *Journal of Computational Physics*, 222, 217–245, 2007.

[44] S. Dellacherie. Analysis of Godunov type schemes applied to the compressible Euler system at low Mach number. *Journal of Computational Physics*, 229, 978–1016, 2010.

[45] F. Dhaouadi and M. Dumbser. A Structure-Preserving Finite Volume Scheme for a Hyperbolic Reformulation of the Navier Stokes Korteweg Equations. *Mathematics*, 11, 2023.

[46] V. A. Dobrev, T. V. Kolev, and R. N. Rieben. High order curvilinear finite elements for elastic-plastic Lagrangian dynamics. *Journal of Computational Physics*, 257, 1062–1080, 2014.

[47] D. Drew and S. Passman. *Theory of Multicomponent Fluids*. New York: Springer, 1999.

[48] D. A. Drew and L. A. Segel. Averaged Equations for Two-Phase Flows. *Studies in Applied Mathematics*, 50, 205–231, 1971.

[49] M. Dumbser. A simple two-phase method for the simulation of complex free surface flows. *Computer Methods in Applied Mechanics and Engineering*, 200, 1204–1219, 2011.

[50] M. Dumbser and W. Boscheri. High-order unstructured Lagrangian one–step WENO finite volume schemes for non–conservative hyperbolic systems: Applications to compressible multi–phase flows. *Computers and Fluids*, 86, 405–432, 2013.

[51] M. Dumbser and V. Casulli. A conservative, weakly nonlinear semi-implicit finite volume method for the compressible Navier-Stokes equations with general equation of state. *Applied Mathematics and Computation*, 272, 479–497, 2016.

[52] M. Dumbser, A. Hidalgo, M. Castro, C. Parés, and E. Toro. FORCE Schemes on Unstructured Meshes II: Non–Conservative Hyperbolic Systems. *Computer Methods in Applied Mechanics and Engineering*, 199, 625–647, 2010.

[53] M. Dumbser, O. Zanotti, R. Loubère, and S. Diot. A Posteriori Subcell Limiting of the Discontinuous Galerkin Finite Element Method for Hyperbolic Conservation Laws. *Journal of Computational Physics*, 2014.

[54] M. Dumbser, I. Peshkov, E. Romenski, and O. Zanotti. High order ADER schemes for a unified first order hyperbolic formulation of continuum mechanics: Viscous heat-conducting fluids and elastic solids. *Journal of Computational Physics*, 314, 824–862, 2016.

[55] M. Dumbser, I. Peshkov, E. Romenski, and O. Zanotti. High order ADER schemes for a unified first order hyperbolic formulation of Newtonian continuum mechanics coupled with electro-dynamics. *Journal of Computational Physics*, 348, 298–342, 2017.

[56] M. Dumbser, D. Balsara, M. Tavelli, and F. Fambri. A divergence-free semi-implicit finite volume scheme for ideal, viscous and resistive magnetohydrodynamics. *International Journal for Numerical Methods in Fluids*, 89, 16–42, 2019.

[57] K. Duraisamy, G. Iaccarino, and H. Xiao. Turbulence modeling in the age of data. *Annual Review of Fluid Mechanics*, 51, cited By 373, 357–377, 2019.

[58] P. Embid and M. R. Baer. Mathematical analysis of a two-phase continuum mixture theory. *Continuum Mechanics and Thermodynamics*, 4, 279–312, 1992.

[59] O. Faltinsen, O. Rognebakke, I. Lukovsky, and A. Timokha. Adaptive multimodal approach to nonlinear sloshing in a rectangular tank. *Journal of Fluid Mechanics*, 407, 201–234, 2000.

[60] F. Fambri and M. Dumbser. Spectral semi-implicit and space-time discontinuous Galerkin methods for the incompressible Navier-Stokes equations on staggered Cartesian grids. *Applied Numerical Mathematics*, 110, 41–74, 2016.

[61] F. Fambri and M. Dumbser. Semi-implicit discontinuous Galerkin methods for the incompressible Navier-Stokes equations on adaptive staggered Cartesian grids. *Computer Methods in Applied Mechanics and Engineering*, 324, 170–203, 2017.

[62] S. Fasoulas, C.-D. Munz, M. Pfeiffer, J. Beyer, T. Binder, S. Copplestone, A. Mirza, P. Nizenkov, P. Ortwein, and W. Reschke. Combining particle-in-cell and direct simulation Monte Carlo for the simulation of reactive plasma flows. *Physics of Fluids*, 31, 2019.

[63] N. Favrie and S. Gavrilyuk. Diffuse interface model for compressible fluid – Compressible elastic–plastic solid interaction. *Journal of Computational Physics*, 231, 2695–2723, 2012.

[64] N. Favrie, S. Gavrilyuk, and R.Saurel. Solid–fluid diffuse interface model in cases of extreme deformations. *Journal of Computational Physics*, 228, 6037–6077, 2009.

[65] R. Fedkiw, T. Aslam, B. Merriman, and S. Osher. A Non-oscillatory Eulerian Approach to Interfaces in Multimaterial Flows (the Ghost Fluid Method). *Journal of Computational Physics*, 152, 457–492, 1999.

[66] R. Fedkiw, T. Aslam, and S. Xu. The Ghost Fluid method for deflagration and detonation discontinuities. *Journal of Computational Physics*, 154, 393–427, 1999.

[67] A. Ferrari, M. Dumbser, E. Toro, and A. Armanini. A New Stable Version of the SPH Method in Lagrangian Coordinates. *Communications in Computational Physics*, 4, 378–404, 2008.

[68] A. Ferrari, M. Dumbser, E. F. Toro, and A. Armanini. A new 3D parallel SPH scheme for free surface flows. *Computers & Fluids*, 38, 1203–1217, 2009.

[69] D. Ferrari and M. Dumbser. A mass and momentum-conservative semi-implicit finite volume scheme for complex nonhydrostatic free surface flows. *International Journal for Numerical Methods in Fluids*, 93, 2946–2967, 2021.

[70] D. Ferrari and M. Dumbser. A Semi-implicit Finite Volume Scheme for Incompressible Two-Phase Flows. *Communications on Applied Mathematics and Computation*, 2023.

[71] D. Ferrari, I. Peshkov, E. Romenski, and M. Dumbser. A unified SHTC multiphase model of continuum mechanics. *arXiv preprint*, arXiv:2403.19298, 2024.

[72] E. Gaburro, M. J. Castro, and M. Dumbser. A well balanced diffuse interface method for complex nonhydrostatic free surface flows. *Computers & Fluids*, 175, 180–198, 2018.

[73] E. Gaburro, W. Boscheri, S. Chiocchetti, C. Klingenberg, V. Springel, and M. Dumbser. High order direct Arbitrary–Lagrangian–Eulerian schemes on moving Voronoi meshes with topology changes. *Journal of Computational Physics*, 407, 109167, 2020.

[74] S. Gavrilyuk, N. Favrie, and R. Saurel. Modelling wave dynamics of compressible elastic materials. *Journal of Computational Physics*, 227(5), 2941–2969, 2008.

[75] M. Germano, U. Piomelli, P. Moin, and W. Cabot. A dynamic subgrid-scale eddy viscosity model. *Physics of Fluids A*, 3, cited By 5489, 1760–1765, 1991.

[76] U. Ghia, K. N. Ghia, and C. T. Shin. High-Re solutions for incompressible flow using Navier-Stokes equations and multigrid method. *Journal of Computational Physics*, 48, 387–411, 1982.

[77] S. K. Godunov. An interesting class of quasilinear systems. *Dokl. Akad. Nauk SSSR*, 139(3), 521–523, 1961.

[78] S. K. Godunov. The problem of a generalized solution in the theory of quasilinear equations and in gas dynamics. *Russian Mathematical Surveys*, 17, 145–156, 1962.

[79] S. K. Godunov. Symmetric form of the equations of magnetohydrodynamics. *Numerical Methods for Mechanics of Continuum Medium*, 3, 26–34, 1972.

[80] S. K. Godunov. *Elements of Continuum Mechanics (in Russian).* Moscow: Nauka, 1978.

[81] S. K. Godunov, T. Y. Mikhailova, and E. Romenski. Systems of thermodynamically coordinated laws of conservation invariant under rotations. *Siberian Mathematical Journal*, 37, 690–705, 1996.

[82] S. K. Godunov and E. I. Romenski. Nonstationary equations of the nonlinear theory of elasticity in Euler coordinates. *Journal of Applied Mechanics and Technical Physics*, 13, 868–885, 1972.

[83] S. K. Godunov and E. I. Romenskii. *Elements of continuum mechanics and conservation laws.* Kluwer Academic/Plenum Publishers, 2003.

[84] S. Godunov and E. Romenskiî. *Elements of mechanics of continuous media.* Nauchnaya Kniga, 1998.

[85] S. Godunov and E. Romensky. Thermodynamics, conservation laws and symmetric forms of differential equations in mechanics of continuous media. In: *Computational Fluid Dynamics Review 1995.* Vol. 95. John Wiley, NY, 1995. 19–31.

[86] M. A. Goodman and S. C. Cowin. A Continuum Theory for Granular Materials. *Archive for Rational Mechanics and Analysis*, 44, 249–266, 1972.

[87] M. Grmela and H. Ottinger. Dynamics and thermodynamics of complex fluids. I. Development of a general formalism. *Physical Review E*, 56(6), 6620, 1997.

[88] F. Harlow and J. Welch. Numerical calculation of time-dependent viscous incompressible flow of fluid with a free surface. *Physics of Fluids*, 8, 2182–2189, 1965.

[89] C. W. Hirt and B. D. Nichols. Volume of Fluid (VOF) Method for Dynamics of Free Boundaries. *Journal of Computational Physics*, 39, 201–225, 1981.

[90] T. Hitz, M. Heinen, J. Vrabec, and C.-D. Munz. Comparison of macro- and microscopic solutions of the Riemann problem I. Supercritical shock tube and expansion into vacuum. *Journal of Computational Physics*, 402, 109077, 2020.

[91] T. Hitz, S. Jöns, M. Heinen, J. Vrabec, and C.-D. Munz. Comparison of macro- and microscopic solutions of the Riemann problem II. Two-phase shock tube. *Journal of Computational Physics*, 429, 110027, 2021.

[92] C. Hu and C.-W. Shu. Weighted Essentially Non-oscillatory Schemes on Triangular Meshes. *Journal of Computational Physics*, 150, 97–127, 1999.

[93] M. Ishii. Thermo-fluid Dynamic Theory of Two-phase Flow. *Eyrolles*, 1975.

[94] H. Jackson and N. Nikiforakis. A numerical scheme for non-Newtonian fluids and plastic solids under the GPR model. *Journal of Computational Physics*, 387, 410–429, 2019.

[95] H. Jackson and N. Nikiforakis. A unified Eulerian framework for multi-material continuum mechanics. *Journal of Computational Physics*, 401, 109–122, 2019.

[96] I. Janosi, D. Jan, K. Szabo, and T. Tel. Turbulent drag reduction in dam–break flows. *Experiments in Fluids*, 37, 219–229, 2004.

[97] F. Kemm, E. Gaburro, F. Thein, and M. Dumbser. A simple diffuse interface approach for compressible flows around moving solids of arbitrary shape based on a reduced Baer–Nunziato model. *Computers & Fluids*, 204, 104536, 2020.

[98] S. Klainermann and A. Majda. Singular Limits of Quasilinear Hyperbolic Systems with Large Parameters and the Incompressible Limit of Compressible Fluid. *Comm. Pure Appl. Math.*, XXXIV, 481–524, 1981.

[99] S. Klainermann and A. Majda. Compressible and incompressible fluids. *Communications on Pure and Applied Mathematics*, 35, 629–651, 1982.

[100] R. Klein. Semi-implicit extension of a Godunov-type scheme based on low Mach number asymptotics I: one-dimensional flow. *Journal of Computational Physics*, 121, 213–237, 1995.

[101] M. Kucharik and M. Shashkov. Conservative multi-material remap for staggered multi-material Arbitrary Lagrangian-Eulerian methods. *Journal of Computational Physics*, 258, 268–304, 2014.

[102] R. Loubère, P. H. Maire, and M. Shashkov. ReALE: A Reconnection Arbitrary-Lagrangian–Eulerian method in cylindrical geometry. *Computers and Fluids*, 46, 59–69, 2011.

[103] R. Loubère, P. H. Maire, M. Shashkov, J. Breil, and S. Galera. ReALE: A reconnection-based arbitrary-Lagrangian–Eulerian method. *Journal of Computational Physics*, 229, 4724–4761, 2010.

[104] M. Lukáčová-Medvid'ová, I. Peshkov, and A. Thomann. An implicit-explicit solver for a two-fluid single-temperature model. *Journal of Computational Physics*, 498, 112696, 2024.

[105] M. Lukáčová-Medvid'ová, G. Puppo, and A. Thomann. An all Mach number finite volume method for isentropic two-phase flow. *Journal of Numerical Mathematics*, 2022.

[106] P. Maire, R. Abgrall, J. Breil, R. Loubère, and B. Rebourcet. A nominally second-order cell-centered Lagrangian scheme for simulating elastic-plastic flows on two-dimensional unstructured grids. *Journal of Computational Physics*, 2012.

[107] P. J. Mason. Large-eddy simulation: A critical review of the technique. *Quarterly Journal of the Royal Meteorological Society*, 120, 1–26, 1994.

[108] C. Maxwell. The Dynamical Theory of Gases. *Philosophical Transactions of the Royal Society*, 157, 49–88, 1866.

[109] I. Men'shov and P. Zakharov. On the composite Riemann problem for multi-material fluid flows. *International Journal for Numerical Methods in Fluids*, 76, 109–127, 2014.

[110] W. Mulder, S. Osher, and J. Sethian. Computing Interface Motion in Compressible Gas Dynamics. *Journal of Computational Physics*, 100, 209–228, 1992.

[111] I. Müller and T. Ruggeri. *Rational Extended Thermodynamics.* Vol. 16. Springer, 1998.

[112] C.-D. Munz, S. Roller, R. Klein, and K. Geratz. The extension of incompressible flow solvers to the weakly compressible regime. *Computers & Fluids*, 32, 173–196, 2003.

[113] C. Munz. On the construction and comparison of two-step schemes for the Euler equations. *Notes Numer. Fluid Mech.*, 14, 195–217, 1986.

[114] C. Munz, M. Dumbser, and S. Roller. Linearized acoustic perturbation equations for low Mach number flow with variable density and temperature. *Journal of Computational Physics*, 224, 352–364, 2007.

[115] C. Munz, P. Omnes, R. Schneider, E. Sonnendrücker, and U. Voss. Divergence Correction Techniques for Maxwell Solvers Based on a Hyperbolic Model. *Journal of Computational Physics*, 161, 484–511, 2000.

[116] S. Ndanou, N. Favrie, and S. Gavrilyuk. Criterion of hyperbolicity in hyperelasticity in the case of the stored energy in separable form. *Journal of Elasticity*, 115, 1–25, 2014.

[117] S. Ndanou, N. Favrie, and S. Gavrilyuk. Multi–solid and multi–fluid diffuse interface model: Applications to dynamic fracture and fragmentation. *Journal of Computational Physics*, 295, 523–555, 2015.

[118] F. Nicoud and F. Ducros. Subgrid-scale stress modelling based on the square of the velocity gradient tensor. *Flow, Turbulence and Combustion*, 62, cited By 2295, 183–200, 1999.

[119] R. Nigmatulin. *Dynamics of Multiphase Media.* New York: Hemisphere, 1991.

[120] M. Nikodemou. *A unified multi-physics formulation for combustion modelling.* PhD thesis. University of Cambridge, 2023.

[121] M. Nikodemou, L. Michael, and N. Nikiforakis. A unified multi-phase and multi-material formulation for combustion modeling. *Physics of Fluids*, 33, 2021.

[122] J. W. Nunziato, E. K., and Walsh. On ideal multiphase mixtures with chemical reactions and diffusion. *Archive for Rational Mechanics and Analysis*, 73, 285–311, 1980.

[123] G. Oger, M. Doring, B. Alessandrini, and P. Ferrant. Two-dimensional SPH simulations of wedge water entries. *Journal of Computational Physics*, 213, 803–822, 2006.

[124] S. Osher and J. Sethian. Fronts Propagating with Curvature–Dependent Speed: Algorithms Based on Hamilton–Jacobi Formulations. *Journal of Computational Physics*, 79, 12–49, 1988.

[125] C. Parés. Numerical methods for nonconservative hyperbolic systems: a theoretical framework. *SIAM Journal on Numerical Analysis*, 44, 300–321, 2006.

[126] L. Pareschi and G. Russo. An introduction to Monte Carlo method for the Boltzmann equation. *ESAIM: Proc.*, 10, 35–75, 2001.

[127] J. H. Park and C.-D. Munz. Multiple pressure variables methods for fluid flow at all Mach numbers. *International Journal for Numerical Methods in Fluids*, 49, 905–931, 2005.

[128] S. Passman. Mixtures of granular materials. *International Journal of Engineering Science*, 15, 117–129, 1977.

[129] V. Patankar and B. Spalding. A calculation procedure for heat, mass and momentum transfer in three-dimensional parabolic flows. *International Journal of Heat and Mass Transfer*, 15, 1787–1806, 1972.

[130] M. Pavelka, V. Klika, and M. Grmela. *Multiscale Thermo-Dynamics.* Berlin, Boston: De Gruyter, 2018.

[131] I. Peshkov and E. Romenski. A hyperbolic model for viscous Newtonian flows. *Continuum Mechanics and Thermodynamics*, 28, 85–104, 2016.

[132] I. Peshkov, M. Pavelka, E. Romenski, and M. Grmela. Continuum mechanics and thermodynamics in the Hamilton and the Godunov-type formulations. *Continuum Mechanics and Thermodynamics*, 30, 1343–1378, 2018.

[133] I. Peshkov, W. Boscheri, R. Loubère, E. Romenski, and M. Dumbser. Theoretical and numerical comparison of hyperelastic and hypoelastic formulations for Eulerian non–linear elastoplasticity. *Journal of Computational Physics*, 387, 481–521, 2019.

[134] I. Peshkov, M. Dumbser, W. Boscheri, E. Romenski, S. Chiocchetti, and M. Ioriatti. Simulation of non-Newtonian viscoplastic flows with a unified first order hyperbolic model and a structure-preserving semi-implicit scheme. *Computers & Fluids*, 224, 104963, 2021.

[135] I. Peshkov, M. Grmela, and E. Romenski. Irreversible mechanics and thermodynamics of two-phase continua experiencing stress-induced solid–fluid transitions. *Continuum Mechanics and Thermodynamics*, DOI 10.1007/s00161–014–0386–1, 2014.

[136] J. Powers, D. Stewart, and H. Krier. Theory of two-phase detonation—Part I: Modeling. *Combustion and Flame*, 80, 264–279, 1990.

[137] L. Prandtl. Über Flüssigkeitsbewegung bei sehr kleiner Reibung. *Verhandlg. III. Intern. Math. Kongr. Heidelberg*, 484–491, 1904.

[138] B. Re and R. Abgrall. A pressure-based method for weakly compressible two-phase flows under a Baer–Nunziato type model with generic equations of state and pressure and velocity disequilibrium. *Int. J. Num. Meth. Fluids*, 94, 1183–1232, 2022.

[139] W. Reschke, M. Pfeiffer, and S. Fasoulas. Enabling Simulations of Droplets with the Direct Simulation Monte Carlo Method. *Fluid Mechanics and its Applications*, 121, cited By 0, 57–68, 2020.

[140] W. Reschke, T. Binder, J. Kleinert, A. Mirza, P. Nizenkov, M. Pfeiffer, S. Fasoulas, S. Copplestone, P. Ortwein, and C. D. Munz. Recent developments of DSMC within the reactive plasma flow solver PICLas. *AIP Conference Proceedings*, 1786, 130003, 2016.

[141] L. Rio-Martin and M. Dumbser. High-Order ADER Discontinuous Galerkin Schemes for a Symmetric Hyperbolic Model of Compressible Barotropic Two-Fluid Flows. *Communications on Applied Mathematics and Computation*, 2023.

[142] A. Ritter. Die Fortpflanzung der Wasserwellen. *Zeitschrift des Vereins Deutscher Ingenieure*, 36, 947–954, 1892.

[143] E. Romenski, A. A. Belozerov, and I. M. Peshkov. Conservative formulation for compressible multiphase flows. *Quarterly of Applied Mathematics*, 74, 113–136, 2016.

[144] E. Romenski, D. Drikakis, and E. Toro. Conservative Models and Numerical Methods for Compressible Two-Phase Flow. *Journal of Scientific Computing*, 42, 68–95, 2010.

[145] E. Romenski, A. Resnyansky, and E. Toro. Conservative hyperbolic formulation for compressible two-phase flow with different phase pressures and temperatures. *Quarterly of Applied Mathematics*, 65, 259–279, 2007.

[146] E. Romenski and E. F. Toro. Compressible two-phase flows: Two-pressure models and numerical methods. *Comput. Fluid Dyn. J*, 13, 1–30, 2004.

[147] E. Romenski, G. Reshetova, and I. Peshkov. Two-phase hyperbolic model for porous media saturated with a viscous fluid and its application to wavefields simulation. *Applied Mathematical Modelling*, 106, 567–600, 2022.

[148] E. Romenski, G. Reshetova, I. Peshkov, and M. Dumbser. Modeling wavefields in saturated elastic porous media based on thermodynamically compatible system theory for two-phase solid-fluid mixtures. *Computers & Fluids*, 206, 104587, 2020.

[149] E. I. Romensky. Hyperbolic systems of thermodynamically compatible conservation laws in continuum mechanics. *Mathematical and computer modelling*, 28, 115–130, 1998.

[150] E. I. Romensky. Thermodynamics and hyperbolic systems of balance laws in continuum mechanics. In: *Godunov Methods: Theory and Applications*. Ed. by E. Toro. New York: Springer US, 2001. 745–761.

[151] S. K. Sambasivan, M. Shashkov, and D. Burton. A finite volume cell-centered Lagrangian hydrodynamics approach for solids in general unstructured grids. *International Journal for Numerical Methods in Fluids*, 72, 770–810, 2013.

[152] R. Saurel and R. Abgrall. A multiphase Godunov method for compressible multifluid and multiphase flows. *Journal of Computational Physics*, 150, 425–467, 1999.

[153] R. Saurel, O. L. Metayer, J. Massoni, and S. Gavrilyuk. Shock jump relations for multiphase mixtures with stiff mechanical relaxation. *Shock Waves*, 16(3), 209–232, 2007.

[154] H. Schlichting and K. Gersten. *Boundary-Layer Theory.* Springer, 2018.

[155] K. Schmidmayer, F. Petitpas, E. Daniel, N. Favrie, and S. Gavrilyuk. A model and numerical method for compressible flows with capillary effects. *Journal of Computational Physics*, 334, 468–496, 2017.

[156] D. Schwendeman, C. Wahle, and A. Kapila. The Riemann problem and a high-resolution Godunov method for a model of compressible two-phase flow. *Journal of Computational Physics*, 212, 490–526, 2006.

[157] J. Shao, H. Li, G. Liu, and M. Liu. An improved SPH method for modeling liquid sloshing dynamics. *Computers and Structures*, 100-101, 18–26, 2012.

[158] P. K. Stansby, A. Chegini, and T. Barnes. The initial stages of dam-break flow. *Journal of Fluid Mechanics*, 374, 407–424, 1998.

[159] M. Sun and C. Ebner. Molecular-dynamics simulation of compressible fluid flow in two–dimensional channels. *Phys. Rev. A*, 46, 4813–4818, 1992.

[160] P. S.V. *Numerical Heat Transfer and Fluid Flow.* Hemisphere Publishing Corporation, Washington DC, 1980.

[161] M. Tavelli and M. Dumbser. A staggered semi-implicit discontinuous Galerkin method for the two dimensional incompressible Navier–Stokes equations. *Applied Mathematics and Computation*, 248, 70–92, 2014.

[162] M. Tavelli and M. Dumbser. A staggered space–time discontinuous Galerkin method for the incompressible Navier–Stokes equations on two–dimensional triangular meshes. *Computers and Fluids*, 119, 235–249, 2015.

[163] M. Tavelli and M. Dumbser. A staggered space-time discontinuous Galerkin method for the three-dimensional incompressible Navier-Stokes equations on unstructured tetrahedral meshes. *Journal of Computational Physics*, 319, 294 –323, 2016.

[164] M. Tavelli and M. Dumbser. A pressure-based semi-implicit space-time discontinuous Galerkin method on staggered unstructured meshes for the solution of the compressible Navier-Stokes equations at all Mach numbers. *Journal of Computational Physics*, 341, 341–376, 2017.

[165] M. Tavelli and M. Dumbser. Arbitrary high order accurate space-time discontinuous Galerkin finite element schemes on staggered unstructured meshes for linear elasticity. *Journal of Computational Physics*, 366, 386–414, 2018.

[166] M. Tavelli, S. Chiocchetti, E. Romenski, A. Gabriel, and M. Dumbser. Space-time adaptive ADER discontinuous Galerkin schemes for nonlinear hyperelasticity with material failure. *Journal of Computational Physics*, 422, 109758, 2020.

[167] F. Thein, E. Romenski, and M. Dumbser. Exact and Numerical Solutions of the Riemann Problem for a Conservative Model of Compressible Two-Phase Flows. *Journal of Scientific Computing*, 93, 83, 2022.

[168] A. Thomann and M. Dumbser. Thermodynamically Compatible Discretization of a Compressible Two-Fluid Model with Two Entropy Inequalities. *Journal of Scientific Computing*, 97, 9, 2023.

[169] S. Tokareva and E. Toro. HLLC–type Riemann solver for the Baer-Nunziato equations of compressible two-phase flow. *Journal of Computational Physics*, 229, 3573–3604, 2010.

[170] E. F. Toro. *Shock–Capturing Methods for Free–Surface Shallow Flows.* Wiley, 2001.

[171] E. F. Toro. *Riemann Solvers and Numerical Methods for Fluid Dynamics. A Practical Introduction, Third edition.* Berlin: Springer-Verlag, 2009.

[172] E. Toro and M. Vázquez-Cendón. Flux splitting schemes for the Euler equations. *Computers and Fluids*, 70, 1–12, 2012.

[173] C. Truesdell. Sulle basi della termomeccanica. *Rendiconti della Classe di Scienze Fisiche, Mathematiche e Naturali*, 22, 33, 1957.

[174] C. Truesdell and R. Toupin. *The Classical Field Theories. Handbuch der Physik.* Berlin: Springer-Verlag, 1960.

[175] C. Williamson and G.L.Brown. A series in 1/ Re to represent the Strouhal- Reynolds number relationship of the cylinder wake. *Journal of Fluids and Structures*, 12, 1073–1089, 1998.

[176] V. Yakhot and S. Orszag. Renormalization group analysis of turbulence. I. Basic theory. *Journal of Scientific Computing*, 1, cited By 3354, 3–51, 1986.

[177] O. Zanotti and M. Dumbser. Efficient conservative ADER schemes based on WENO reconstruction and space-time predictor in primitive variables. *Computational Astrophysics and Cosmology*, 3, 1, 2016.

[178] C. Zhang and I. Men'shov. Using the composite Riemann problem solution for capturing interfaces in compressible two-phase flows. *Applied Mathematics and Computation*, 363, 124610, 2019.

[179] C. Zhang and I. Men'shov. Eulerian Model for Simulating Multi-Fluid Flows with an Arbitrary Number of Immiscible Compressible Components. *Journal of Scientific Computing*, 83, 31, 2020.

[180] R. Zhao, O. Faltinsen, and J. Aarsnes. Water entry of arbitrary two-dimensional sections with and without flow separation. *21st Symposium on Naval Hydrodynamics*, 1997.